



**HAL**  
open science

# Search for antineutrino disappearance with the SoLi $\partial$ detector : novel reconstruction, calibration and selection

Mykhailo Yeresko

## ► To cite this version:

Mykhailo Yeresko. Search for antineutrino disappearance with the SoLi $\partial$  detector : novel reconstruction, calibration and selection. Nuclear Experiment [nucl-ex]. Université Clermont Auvergne, 2022. English. NNT : 2022UCFAC127 . tel-04433698

**HAL Id: tel-04433698**

**<https://theses.hal.science/tel-04433698>**

Submitted on 2 Feb 2024

**HAL** is a multi-disciplinary open access archive for the deposit and dissemination of scientific research documents, whether they are published or not. The documents may come from teaching and research institutions in France or abroad, or from public or private research centers.

L'archive ouverte pluridisciplinaire **HAL**, est destinée au dépôt et à la diffusion de documents scientifiques de niveau recherche, publiés ou non, émanant des établissements d'enseignement et de recherche français ou étrangers, des laboratoires publics ou privés.

UNIVERSITÉ CLERMONT AUVERGNE  
ÉCOLE DOCTORALE DES SCIENCES FONDAMENTALES

## THÈSE

présentée pour obtenir le grade de

### Docteur d'Université

Spécialité : PHYSIQUE DES DEUX INFINIS (particules, noyaux, évolution de l'univers)

Thèse présentée et soutenue à Clermont-Ferrand, le 19 décembre 2022, par

**Mykhailo YERESKO**

**Search for antineutrino disappearance with the SoLi $\partial$  detector: novel reconstruction, calibration and selection.**

<b>Examineurs :</b>	M.	Dirk RYCKBOSCH	Rapporteur
	M.	Yoshi UCHIDA	Rapporteur
	M.	Sergey BARSUK	
	M.	Claudio GIGANTI	
	Mme.	Ana Margarida TEIXEIRA	
<b>Directeurs de thèse :</b>	M.	Stephane MONTEIL	Directeur de thèse
	M.	Hervé CHANAL	Co-Directeur de thèse

# Contents

<b>1</b>	<b>The Standard Model of particle physics</b>	<b>5</b>
1.1	The brief neutrino history . . . . .	6
1.2	Hints for neutrino oscillations . . . . .	8
1.3	Theory of the neutrino oscillations . . . . .	11
1.3.1	The atmospheric term . . . . .	13
1.3.2	The solar term . . . . .	14
1.3.3	The reactor term . . . . .	15
1.3.4	The open questions . . . . .	16
1.4	Other neutrino anomalies . . . . .	19
1.4.1	The accelerator sector . . . . .	19
1.4.2	The gallium anomaly. Part 2 . . . . .	21
1.4.3	The reactor sector . . . . .	23
1.5	The sterile neutrino hypothesis . . . . .	27
1.5.1	NEOS . . . . .	29
1.5.2	Neutrino-4 . . . . .	30
1.5.3	PROSPECT . . . . .	30
1.5.4	STEREO . . . . .	31
1.6	Conclusion . . . . .	32
<b>2</b>	<b>The SoLi<math>\partial</math> experiment</b>	<b>33</b>
2.1	The BR2 site . . . . .	33
2.2	Detector design . . . . .	35
2.2.1	Detection cell . . . . .	35
2.2.2	Processing of the scintillation light . . . . .	36
2.2.3	Plane and module design . . . . .	37
2.2.4	Detector container . . . . .	38
2.2.5	CROSS calibration system . . . . .	39
2.2.6	DAQ system . . . . .	40
2.3	Detection principle . . . . .	43
2.4	Expected signal and background . . . . .	44
2.4.1	IBD predictions . . . . .	45
2.4.2	Atmospherics . . . . .	46
2.4.3	Natural radiation . . . . .	47
2.4.4	Accidentals . . . . .	48
2.5	Simulations . . . . .	49
2.5.1	SoLO generator . . . . .	49
2.5.2	Calibration sources . . . . .	50
2.5.3	Background . . . . .	50
2.5.4	ROSim software . . . . .	50
2.6	Conclusion . . . . .	51
<b>3</b>	<b>Reconstruction algorithm</b>	<b>52</b>
3.1	Event reconstruction software . . . . .	52
3.1.1	Muon clusters . . . . .	53
3.1.2	NS clusters . . . . .	54

3.1.3	The BiPonator . . . . .	55
3.1.4	ES clusters . . . . .	57
3.1.5	The NS-ES coincidence . . . . .	58
3.1.6	FPNT . . . . .	58
3.2	The CCube algorithm . . . . .	59
3.2.1	Reconstruction procedure estimators . . . . .	60
3.2.2	The regularisation approach . . . . .	62
3.2.3	The Bayesian approach . . . . .	64
3.2.4	The SoLi $\partial$ approach . . . . .	68
3.3	Conclusion . . . . .	70
<b>4</b>	<b>Electromagnetic energy calibration</b>	<b>71</b>
4.1	The relative calibration of the SoLi $\partial$ with horizontal muons . . . . .	71
4.1.1	Scintillating photons behaviour in the SoLi $\partial$ cube . . . . .	72
4.1.2	Geant4 MC simulation of muons . . . . .	73
4.1.3	The horizontal muons selection . . . . .	75
4.1.4	Upgraded track reconstruction . . . . .	76
4.1.5	Dead fibres and overflow channels . . . . .	77
4.1.6	KL divergence . . . . .	78
4.1.7	SM derivation. Light sharing . . . . .	79
4.1.8	SM derivation. Homogenisation of the response . . . . .	80
4.2	Absolute calibration . . . . .	82
4.2.1	Calibration with $^{22}\text{Na}$ . . . . .	83
4.2.2	Calibration with AmBe . . . . .	85
4.3	Crosschecks and validations . . . . .	92
4.3.1	Cosmogenic background determination . . . . .	95
4.4	Conclusion . . . . .	95
<b>5</b>	<b>IBD analysis</b>	<b>97</b>
5.1	Justification of the topologies . . . . .	98
5.2	Definition of the topologies . . . . .	100
5.2.1	Further search for the annihilation $\gamma$ contributions . . . . .	102
5.2.2	Cube level energy threshold . . . . .	105
5.2.3	CCube efficiency per topology . . . . .	106
5.3	Identification of the background sources . . . . .	107
5.3.1	Background sources distribution across topologies . . . . .	107
5.4	Preselection cuts . . . . .	109
5.4.1	Normalisation factor determination . . . . .	112
5.5	Discriminative variables . . . . .	113
5.6	Datasets . . . . .	117
5.6.1	BiPo enriched sample . . . . .	117
5.6.2	BiPo-enriched sample validation . . . . .	119
5.6.3	Atmospherics-enriched sample . . . . .	119
5.7	Multivariate analysis and 5D optimisation . . . . .	120
5.8	Simultaneous fit technique . . . . .	123
5.9	Systematic studies . . . . .	124
5.10	Construction of the predictions . . . . .	126

5.11 Unblinding strategy validation with the open data set . . . . .	128
5.11.1 BiPo component comparison . . . . .	130
5.11.2 Predictions versus ROn measurements . . . . .	131
<b>6 Summary and outlook</b>	<b>135</b>
<b>A Appendix</b>	<b>137</b>
<b>References</b>	<b>140</b>

## Acknowledgments

At the beginning, I would like to thank the reviewers: Dirk Ryckbosh and Yoshi Uchida for accepting, in a (very!) short notice, the duty to scrutinise my thesis. Many thanks for all the feedback, comments, and questions. Also, thanks to Sergey Barsuk for chairing the jury; as well as to the other jury members, Claudio Giganti and Ana Margarida Teixeira, for the time you have devoted to my thesis.

At the same time, I would like to express my deepest gratitude to my supervisors: Stephane and Hervé. Thanks Stephane for always keeping the enthusiasm in the system at the incredible level throughout all these years. Thanks for your guidance not only in the world of academia, research, and the art of scientific writing but also in the French culture and, more importantly, the French cuisine! Thanks a lot for all the fun, Tesla rides, Potinga nights, and infinite hours of discussions for which you have always magically managed to find time despite dozens (if not hundreds) projects you are orchestrating simultaneously and even if that meant leaving the lab when there is no sunlight outside anymore. Hervé, your ability to spot and fix any kind of bugs or problems is a real blessing. Compile the script, determine (I hope you have read this one right) the system matrix or (most impressively for me) deal with the French bureaucracy, turns into nothing as soon as you are involved. It was always a joy to start the day in your office exchanging jokes, and I am still disappointed that COVID has split us. I am also very thankful for your theatre initiative to support the people of Ukraine in these hard times. I hope one day we will witness your performance on Broadway (I would also bet they do really nice Long Islands in New York). Overall, I cannot imagine a better or more supportive environment to do a PhD and I am very grateful to you both for that.

I cannot avoid mentioning my SoLi $\delta$  colleagues. Despite the fact that most of the time we were interacting via Zoom or Mattermost, once we met at the collaboration meetings in Paris the feeling that we have met many times before was in the air. I would like to mention, in particular, Noë and David (and admit that it was always miraculous to be able to carry out the morning parts of the meetings after our prior evening reunions), Danny, Savitri, and Rijeesh. It was a pleasure to have such great collaborators. I also would like to thank Mathieu, Greg and Benoit for their time, help, and support on the thorny path of hunting antineutrinos.

The last, but not least I would like to thank all the friends I met during the PhD years and who made these years much smoother and funnier. It was an impressive ride full of hiking, visiting lakes, castles (and lakes with the castles of course), online cinema and bars during the pandemic, non-permanent events, birthday parties, pizza parties, and so many more. I would most likely forget someone; thus I apologise in advance, but thank you a lot to Ioan (the best jogging buddy and the guy who shares with me not only the name but also the sense of humour), Jonathan (my lieber Bruder with whom we are immortalised on the wall of fame in the best bar in Clermont (or even the whole France) Les Berthom), Lars (my accomplice in the battle against French language, with whom we will eventually figure out the deference between bonsoir and bonne soirée), Theo, Nicolas, Ema, Halime and Sofia (these two should go together even in the acknowledgements), Tristan (the best office mate), Andreas and Lennart. A more general thanks to all the other colleagues (Regis, Eric, Olivier, Vincent), personnel of the lab, and the Secretariat. In particular, I express my infinite gratitude to Geraldine, who always found the way to help me despite me not following any piece of advice to simplify my French administrative life.

Finally, I must thank all the people who made me who I am today, without whom this journey and the last 4 years in particular were not possible. I will always remember Andriy Mykolayovych Berezovskyi, who not only taught me physics at school, but has also shown that the world of science can be very fun and interesting (Знання - це сила!). I have kept this attitude with me to the university, where it was supported and enhanced by great Oleg Anatoliyovych Bezshyyko and Larisa Oleksandrivna Golinka-Bezshyyko. The need to always stay in the “motivated student” state, as well as the “gentleman pack” of skills and knowledge have made my life easier infinitely many times (and I could fill what “Ласкаво просимо в реальний світ” means). There will always be a place in my heart for my lifelong friends with whom we have passed through fire, water, snow, copper pipes, and under bridges. Andriy, Ihor, Ivan, Mykyta (who was always there to deal with my programming incompetence), Oles, Sasha, I hope we keep our link and keep the reunions either in Kyiv or in any other part of the world. And my family. Mom and Dad, I cannot thank you enough for all your support, time, resources, and belief that you have invested in me throughout my entire life. I am also grateful to my sister for being there, despite the fact that I am not always the most pleasant person to deal with (sorry and it will happen again). Thank you, Mom. Thank you, Dad. Thank you, Tamara.

Окремо хочу щиро подякувати кожному захиснику і захисниці України, що нині боронять нашу Батьківщину від російської навали. Лише завдяки Вам наша країна та наша нація досі існує, а люди можуть продовжувати жити та, зокрема, отримувати докторські ступені. Безмежна шана та низький уклін. Слава Україні!

## Abstract

This thesis presents the search for active-to-sterile antineutrino oscillations with the SoLi $\partial$  detector, which has an innovative concept based on a sandwich of composite polyvinyl-toluene and  $^6\text{LiF}:\text{ZnS}(\text{Ag})$  scintillators. Three main contributions to this search are reported. The first one describes the new reconstruction method based on the ML-EM algorithm. It is aimed at transformation of the raw detector response to the list of positions (with dedicated energies) where actual physics interaction in the detector took place. The second one describes the energy calibration of the detector. It includes both relative calibration with the cosmic horizontal muons and exploration of several options for the absolute energy scale derivation. Finally, the thesis presents a novel method for selecting antineutrino candidates based on the analysis of the electromagnetic part of the inverse beta decay signal and categorising them according to the geometry of the events in the detector (topologies). The analysis was developed blindly and the method was validated with a small fraction of the data sample.

Key words: Neutrino, SoLi $\partial$  detector, RAA, sterile, reconstruction, ML-EM, calibration, horizontal muons, topological selection.

## Résumé

Cette thèse présente la recherche d'oscillations d'antineutrinos actifs vers des antineutrinos stériles avec le détecteur SoLi $\partial$ . Ce détecteur promeut un concept innovant basé sur un sandwich de plastiques scintillant formé de polyvinyle-toluène composite et de scintillateurs  $^6\text{LiF}:\text{ZnS}(\text{Ag})$ . Trois contributions principales à cette recherche sont rapportées dans ce document. La première concerne une nouvelle méthode de reconstruction basée sur l'algorithme ML-EM. Elle vise à transformer la réponse brute du détecteur en une liste de positions (avec des énergies dédiées) où l'interaction physique réelle dans le détecteur a eu lieu. La seconde concerne l'étalonnage en énergie du détecteur. Elle comprend à la fois l'étalonnage relatif au moyen de muons cosmiques horizontaux et l'exploration de plusieurs options pour la détermination de l'échelle d'énergie absolue. Enfin, la thèse présente une nouvelle méthode de sélection des candidats antineutrinos basée sur l'analyse de la partie électromagnétique du signal de désintégration bêta inverse et leur classement en fonction de la géométrie des événements dans le détecteur (topologies). L'analyse a été développée en aveugle et la méthode a été validée avec une petite fraction de l'échantillon de données.

Mot clés : Neutrino, détecteur SoLi $\partial$ , AAR, stérile, reconstruction, ML-EM, calibration, muons horizontaux, sélection topologique.

# Introduction

It is not the path which is the difficulty;  
rather, it is difficulty, which is the path.

---

Sören Kierkegaard

Over the past century, neutrinos have provided a number of anomalous experimental results. Some were transformative for our understanding of the nature (*e.g.* neutrino masses), while some others are waiting for an explanation (which can be transformative as well!). In the list of enigmas to date, one can find the gallium anomaly, the accelerator anomaly, and the reactor antineutrino anomaly. The scientific scope of this thesis is in the Search for Oscillations with a  ${}^6\text{Li}$  detector (SoLi $\partial$ ) experiment frame. SoLi $\partial$  is aimed at searching for active-to-sterile antineutrino oscillations to discover the mentioned anomalies. The work I have done is related to the reconstruction, calibration, and design of the algorithm for the selection of anti-neutrino candidates. The structure of the thesis is as follows: Chapter 1 provides a brief historical overview and introduction to neutrino physics, Chapter 2 describes the experimental site and the setup of the SoLi $\partial$  experiment, Chapter 3 introduces the handling of the raw detector data and, in particular, the electromagnetic signal reconstruction algorithm (CCube), while Chapter 4 complements it with the description of the electromagnetic calibration techniques. Finally, Chapter 5 discusses the selection of signal candidates based on the geometrical (topological) properties of the signal signature. It is concluded with the proof of principle of the method based on the blind analysis of the open data set and the perspectives of the topological analysis summarised in the Chapter 6.

# 1 The Standard Model of particle physics

The Standard Model (SM) of particle physics describes the short-distance interactions between elementary particles. It accounts in a unified framework for three out of the four fundamental forces observed in nature (except gravity). While developing in the second half of the twentieth century, the SM was able not only to describe the already observed phenomena, but also provided a large list of predictions which found experimental confirmation later on (top quark, tau neutrino, Higgs, W, and Z bosons to cite few of them). Generally, the building blocks of the SM are summarised in the table like the one sketched in Figure 1. It consists of two groups of particles, fermions and bosons. The half-integer spin fermions are responsible for composing the matter. They include two families of three generations each: quarks, which are sensitive to all three types of interactions, and leptons, which are insensitive to the strong interaction. The second group of particles are integer-spin bosons, which act as the force carriers. The strong interaction is mediated by eight gluons, the electromagnetic by the photon, while weak interaction has two massive mediators, the Z and  $W^\pm$  bosons. The last fundamental particle to be mentioned is the Higgs boson associated with the Higgs field in the Brout-Englert-Higgs mechanism, the way massive particles acquire their masses.

Spin-1/2 fermions						Spin-1 bosons						
Quarks	Left	u	Right	Left	c	Right	Left	t	Right	Force carriers	g	Spin-0 Higgs boson
	Left	d	Right	Left	s	Right	Left	b	Right		$\gamma$	
	Left	$\nu_1$	Right	Left	$\nu_2$	Right	Left	$\nu_3$	Right		$Z^0$	
	Left	e	Right	Left	$\mu$	Right	Left	$\tau$	Right		$W^\pm$	

Figure 1: The table of elementary particles of the Standard Model. Extracted from [1]

The SM has withstood countless experimental cross-checks to date. Despite these immense successes, phenomena such as matter/antimatter asymmetry in the Universe, origin of dark matter, and origin of neutrino masses are left unexplained. If one tries to look for anything unusual in the table above, the set of leptons called neutrinos immediately catches the attention. To begin with, these are the only particles with squares that are not fully filled. They are missing not only the right-handed companions, but the only particles which have limits for their masses (not even considering the fact that they are massless according to the SM). Moreover, as has been stated above, leptons do not interact strongly. Since neutrinos do not carry any electrical charge, they also do not experience

electromagnetic interaction. Hence, they can only interact weakly, which in addition makes them really complicated particles to detect. But in order to explore the enigmas associated with neutrinos nowadays, we have to start from the beginning.

## 1.1 The brief neutrino history

In the beginning of the twentieth century, the newly discovered phenomena of radioactivity were under massive scrutiny. The energy spectrum of the  $\beta$  decay was among the most complicated questions. Although the electron energy was assumed to be well defined and to carry the whole energy of the interaction similarly to the  $\alpha$  and  $\gamma$  decays; instead, a continuous distribution was observed. To illustrate the level of perturbation in the physics society caused by this result, it is enough to say that within the leading explanations there was violation of the energy conservation proposed by Niels Bohr and existence of the invisible “neutron” particle proposed by Wolfgang Pauli in his famous letter to the dear Radioactive colleagues [2]. However, further scrutiny of the spectrum allowed Bohr’s idea to be discarded and the name neutron was claimed two years later by James Chadwick for another neutral particle he discovered. Hence, Enrico Fermi, who took on research on the Pauli idea, had to come up not only with a completed theory but also with a new name. Finally, in 1934 Fermi published his theory [3] (which was rejected by Nature as too remote from reality) of beta decays introducing neutrino (little neutron) via the reaction nowadays known as a neutron  $\beta$  decay:

$$n \longrightarrow p + e^- + \bar{\nu}_e . \quad (1)$$

Hence, it is neutrino, which becomes responsible for the missing energy and the continuous nature of the spectrum. The proposed theory triggered numerous discussions. For example, according to Pauli, both electron and neutrino are considered to not preexist in the nucleus but are created at the time of the decay. Hans Bethe and Rudolf Peierls [4], as a consequence of such an assumption, have pointed out that a creation process implies annihilation processes. In particular, a (anti)neutrino interacts with a nucleus and disappears, giving rise to a positron (electron) and a different nucleus with a charge changed by one unit. The so-called Inverse Beta Decay (IBD) remains one of the most employed tools to detect neutrinos up to now:

$$p + \bar{\nu}_e \longrightarrow e^+ + n . \quad (2)$$

The cross-section evaluation for this reaction has been provided in the same paper. It has been estimated to be less than  $10^{-44}$  cm<sup>2</sup>, which corresponds to a penetrating power of  $10^{14}$  km in solid matter. By that time, the conclusion was that it was highly improbable to observe the process even with cosmic rays. It has indeed taken about twenty years to come up with the design of an actual experiment, which will allow the neutrinos to be detected (and an additional forty to receive the Nobel prize). Probing such a low cross-section requires an enormous neutrino flux. It was even considered initially that the source of such a flux could be provided by an atomic bomb; the “Project Poltergeist” has even been approved in Los Alamos. Fortunately (or unfortunately) in late 1952, Clyde Cowan and Fred Reines were urged to reconsider the more practical idea of using antineutrinos from a nuclear reactor [5]. They had to think of additional background discrimination and additional signal signatures since the flux has been decreased by a few

orders of magnitude. That also results in a slight modification of the detector design. The final version sketched in Figure 2 was a sandwich with two layers of water with added cadmium chloride as a neutron and positron target and three layers of liquid scintillator for the annihilation gamma and delayed gamma from neutron capture detection. Such a design allowed one to employ the following extremely important features:

- Presence of the neutron capture signal
  - Making the signal signature more complex
  - Allows the time correlation to be used between prompt positron and delayed (due to the initial thermalization) neutron signal
- Utilize annihilation gammas back-to-back production nature

The experiment was successful [6] and the detection principle remains relevant more than sixty years later that it will be further used and discussed in the presented research.

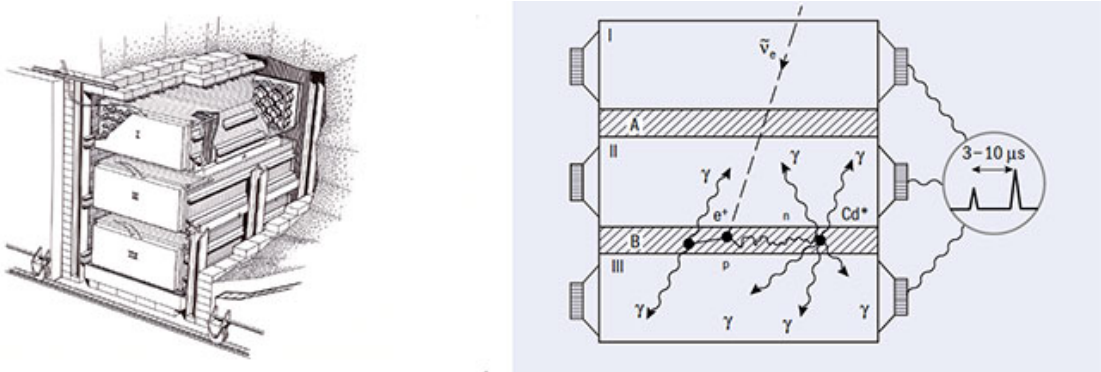


Figure 2: Sketch of the detector used at the Savannah River Plant. It consisted of three liquid scintillator tanks (I, II and III) and neutron targets (A and B) of water doped with cadmium (left). The detection principle based on the delayed coincidence employed in the Cowan and Reines experiment (right). Adapted from [7].

The particle discovered in the Cowan and Reines experiment was the electron antineutrino. Another neutrino flavour was detected in 1962 at Brookhaven National Laboratory (BNL) by Lederman, Schwartz, and Steinberger [8]. It also took around twenty years from the theoretical prediction to the experimental discovery. However, this time the neutrino flux was created by an accelerator. The idea was to collide a beam of 15 GeV protons from the Alternating Gradient Synchrotron (AGS) with a fixed Beryllium target to create charged pions. Pions are supposed to preferably decay via the channel:

$$\pi^{\pm} \longrightarrow \mu^{\pm} + (\nu/\bar{\nu}). \quad (3)$$

Twenty metres from the target, a 13.5 m thick iron shield has been installed. The purpose of that shielding was to stop the muons issued from the pion decay. The interactions of the remaining neutrinos were observed in a 10 tons aluminium spark chamber placed behind the shielding. It was not clear at that time whether these neutrinos have the same type as those observed by Cowan and Reines. However, the assumption that they are, was already leading to tension between some of the theoretical predictions and available data.

The neutrino-scattering experiment proposed by Lederman, Schwartz, and Steinberger brought an unambiguous response. Two neutrino scattering on matter are competing:

$$\begin{aligned}\nu + n &\longrightarrow p + e^- \\ \bar{\nu} + p &\longrightarrow n + e^+, \end{aligned} \tag{4}$$

$$\begin{aligned}\nu + n &\longrightarrow p + \mu^- \\ \bar{\nu} + p &\longrightarrow n + \mu^+ . \end{aligned} \tag{5}$$

If neutrinos would have been equivalent, then the same number of events listed in Equation 4 and Equation 5 should be observed. However, the result of the experiment clearly demonstrated the excess of muon events compared to the electron ones. The posited existence of a second neutrino flavour was hence acknowledged.

Once the tau lepton was discovered in 1975 at the Stanford Linear Accelerator Center [9], it became obvious that the hunting for the third neutrino flavour had just started. Further evidence came from the LEP experiment, which restricted the number of active light neutrinos to three after measuring the  $Z^0$  decay width [10]. Similarly to the case of the two previous flavours, it took about 20 years to experimentally probe the existence of the tau neutrino. It has been done by the DONUT collaboration at Fermilab [11]. Similarly to the muonic neutrino the idea was to create the beam of the tau neutrinos. In order to do that, 800 GeV proton beam from Tevatron collided with tungsten to produce the charm particles  $D_s^\pm$ . Their decay mode is the following:

$$\begin{aligned}D_s^- &\longrightarrow \tau^- + \bar{\nu}_\tau \\ D_s^+ &\longrightarrow \tau^+ + \nu_\tau . \end{aligned} \tag{6}$$

The  $\tau$ , which decays at least to a  $\nu_\tau$ , increases the final amount of neutrinos. If the  $\tau$  lepton is experiencing leptonic decay, two additional neutrinos are produced.

$$\begin{aligned}\tau &\longrightarrow \nu_\tau + \ell + \bar{\nu}_\ell \\ \tau^+ &\longrightarrow \nu_\tau + \ell^+ + \nu_\ell , \end{aligned} \tag{7}$$

where  $\ell$  represents the remaining light lepton ( $e$  or  $\mu$ ) and the corresponding neutrino. Since the operating energy is much larger than in case of the muon neutrino searches, a more elaborated system to reduce the backgrounds has been designed. It consisted of dipole and toroidal magnets and 17 m of steel passive shielding. Finally, processes similar to Equation 5 processes were used to spot the signal events:

$$\begin{aligned}\nu_\tau + n &\longrightarrow p + \tau^- \\ \bar{\nu}_\tau + p &\longrightarrow n + \tau^+ . \end{aligned} \tag{8}$$

As a final result, the DONUT collaboration reported 9  $\nu_\tau$  CC events for 1.5 background events [12] and as such completed the history of active neutrino flavour discoveries.

## 1.2 Hints for neutrino oscillations

Besides atomic bombs, nuclear reactors and accelerators, there is one more source of neutrinos that is used extensively. Around  $10^{11}$  solar neutrinos are crossing  $1 \text{ cm}^2$  of the Earth surface every second. The fact that they could provide insight into the core of the Sun and that the Standard Solar Model (SSM) was predicting the flux made solar

neutrinos desirable objects for experimental research since the 1960s [13]. Homestake, designed by Ray Davis, was the first experiment of this kind. A lot of ideas employed in this experiment remained distinguishing features for most of the neutrino experiments until now. To begin with, it took place in the Homestake Gold Mine in South Dakota situated 1.5km underground, hence reducing cosmic ray-induced background sources significantly. The second feature is the large size of the detector, which is another way to mitigate the low cross-sections. Homestake was a 600-ton tank filled with perchloroethylene or dry cleaning fluid. The idea was to use the radiochemical detection technique with the following reaction:



which allows one to estimate the neutrino rate by counting extracted  ${}^{37}\text{Ar}$  atoms on a periodic basis. The initial result reported a significant neutrino deficit with respect to the SSM. The neutrino signal extraction was performed 108 times during more than 20 years of experiment operation. All of them have reaffirmed the initial observation [14]. The discrepancy became known as “the solar neutrino problem”. Several scientific arguments were opposed to the interpretation of the results as an actual deficit of electronic neutrinos. The threshold level of the reaction was too high, leaving a significant part of the solar neutrino spectrum. The detector was neither capable of measuring the direction of the arrived neutrinos to claim the solar origin. The first issue was resolved by two gallium experiments concurrently running in the 90th. The 101 tons GALLEX experiment [15] installed at the Gran Sasso Underground Laboratory in Italy and the 50 ton SAGE experiment [16] hosted at the Baksan Neutrino Observatory in the Caucasus mountains. The technique remained the same as the one employed at Homestake:



This time, the threshold level was 233 keV (to be compared with 814 keV for  ${}^{37}\text{Cl}$ ), which significantly enhances the amount of neutrino that may be detected. However, the results obtained remained significantly lower than the SSM predictions (73 solar neutrino units (1 SNU =  $10^{-36}$  interactions per target atom per second) for GALLEX [17] versus 130 SNU predicted). The level of disagreement obtained with the SSM for the gallium experiments was different compared to the Homestake. It hinted that the magnitude of the deviation is energy dependent.

The inability to define the direction of the neutrinos arrived was solved by another experiment called Super-Kamiokande. This second generation solar-neutrino experiment inherited several features from its predecessors: underground position (at a depth of 2700 water-equivalent metres in the Kamioka Mozumi mine in Japan) and large dimensions (50 kton of water contained in a cylindrical steel tank of 39.3 m diameter and 41.4 m height). However, the detection technology differed. Super-Kamiokande is an imaging water Cherenkov detector. It relies on neutrino-electron elastic scattering and reading out the Cherenkov photons from the recoiled electrons by photomultipliers. The design of the experiment required a much larger threshold level, which was set at 5 MeV. Despite all the differences, the result was pretty similar - 47% of the flux predicted by the SSM [18]. On the other hand, it was possible to measure the angle between the reconstructed electron and the direction to the Sun at the time when the neutrino candidate occurred. Contrary to kinematic smearing and the fact that the recoiled electron could experience multiple

scattering, it is clearly possible to see the peak rising after the cosine value of 0.5 in the left plot of the Figure 3. At the same time, Super-Kamiokande was sensitive to one more source of neutrinos, the atmospheric ones. The atmospheric neutrinos originate as the secondary particles from the cosmic rays interaction with the nucleus in the atmosphere. The result of this interaction is cascades of mesons, primarily pions, that generate muon neutrinos in the decay mode as in Equation 3. The subsequently decaying muons also provide electron and muon neutrinos. Hence, the fraction of the muon atmospheric neutrino to electron is about 2 to 1. These neutrinos not only live in a drastically different energy regime (GeV versus MeV for the solar ones), they can also arrive from any part of the atmosphere, since it is not a problem for a neutrino to cross the Earth. That provides a range in the distance covered by the neutrino from 10 to 13000 km. The usual type of observable used is a double ratio:

$$R = \frac{(N_\mu/N_e)_{\text{DATA}}}{(N_\mu/N_e)_{\text{MC}}}, \quad \text{where } N_x = \nu_x + \bar{\nu}_x, \quad (11)$$

which is, here as well, another measurement way below the predicted value of 1. This discrepancy became known as the ‘‘atmospheric neutrino anomaly’’. It can be illustrated with the electron- and muon-like neutrino fluxes as a function of the zenith angle. This angle defines the direction of the neutrino, and hence measures the travelled distance. The muon-like neutrino distributions presented in the right plot of Figure 3 indicates that a global deficit of muon neutrinos is observed, as well as a modulation of the flux as a function of the inferred travelled distance.

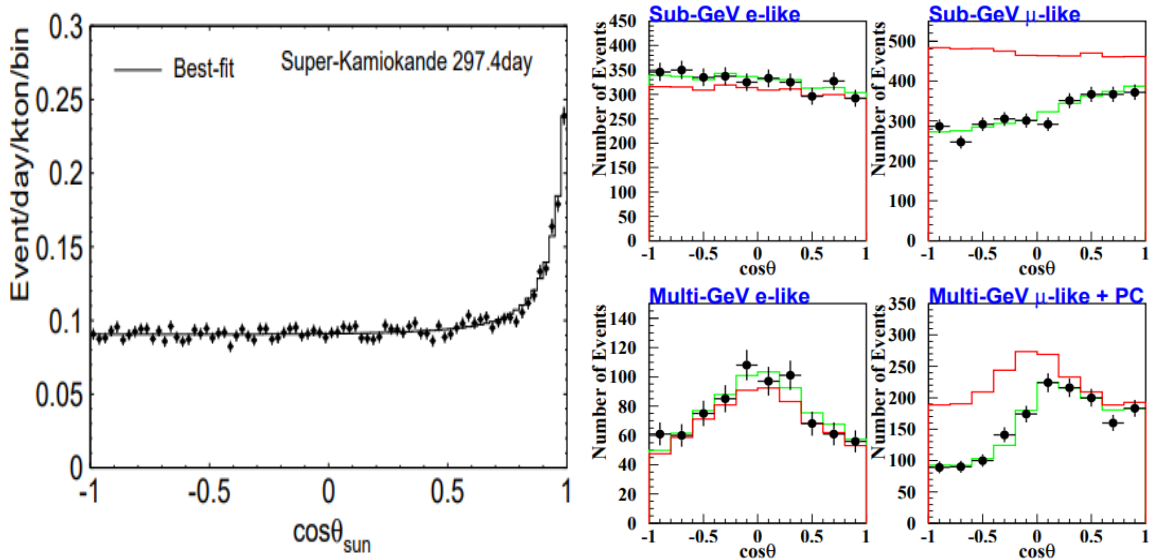


Figure 3: On the right: the cosine of the angle between the direction of the electron-like candidate and a radius vector from the Sun. On the left: the zenith angle distributions of the electron (left) and muon (right) like candidates detected at the Super-Kamiokande in the different energy regimes. The red solid line represents the prediction and black points represent the data. Extracted from [19] (left) and [20] (right).

Thus the puzzle remained unsolved. The discussed above results of the neutrino-physics experiments might be interpreted as pointing towards new phenomena of flavour conversions. That is the time when the idea of the experiment which detection method will be

independent of the neutrino flavour kicked in. The Sudbury Neutrino Observatory [21] became that ultimate experiment to solve both anomalies. SNO was located 2100 m underground in Vale's Creighton Mine in Sudbury, Canada, and was a 1 kton heavy water detector consisting of a transparent acrylic sphere 12 m in diameter. All the aforementioned neutrino detection techniques are employed:

- The elastic scattering channel:

$$\nu_x + e^- \longrightarrow \nu_x + e^- , \quad (12)$$

which is exactly the same process used by Super-Kamiokande. Although this channel is available for all neutrino flavours,  $\nu_e$  dominates it by a factor of about 7 due to the charged-current contribution. It can hence be used or contribute to probe the partial mixture of the fluxes.

- The charged current channel:

$$\nu_e + d \longrightarrow p + p + e^- , \quad (13)$$

which is similar to the radiochemical technique used in the Homestake and gallium experiments. Since the solar neutrino energy spectrum is not going higher than 30 MeV, this channel only probes the electron neutrino flux, since scattering reactions like  $\nu_\mu + X \rightarrow Y + \mu$  require at least 105 MeV to occur.

- The neutral current channel:

$$\nu_x + d \longrightarrow n + p + \nu_x , \quad (14)$$

This is the killer feature of the experiment. This channel is based on the deuterium dissociation by neutrino-induced neutral current scattering by neutrino, which is independent of the flavour and has a threshold of only 2.2 MeV. As such, it probes the total neutrino flux.

The elastic scattering and charged current channels allowed one to cross-check the direction of the detected neutrinos and compare the flux reduction to the one obtained in the other solar experiments. Finally, the flux measured by the neutral current channel matched the SSM [22]. The amount of muon and tau neutrinos obtained was three times larger than the electron. This is an unambiguous proof of neutrino flavour conversion.

### 1.3 Theory of the neutrino oscillations

The major outcome of the previous subsection is that neutrinos are experiencing flavour conversion. A natural candidate to explain this flavour conversion is the quantum phenomenon of oscillations. If neutrinos were to be massive, the flavour and mass eigenstates could be distinct and the rotation of their respective eigenbases would produce flavour transitions. The modelling of the phenomenon was composed in several stages. First, Bruno Pontecorvo in 1957 submitted the hypothesis [23] of neutrino oscillations to antineutrinos. Five years later, Ziro Maki, Masami Nakagawa, and Shoichi Sakata introduced a model to describe the mixing of neutrino flavours [24]. By the time, the

theory assumed the existence of only two kinds of neutrinos. However, the model can be extended straightforwardly to additional flavours and was indeed extended to account for the  $\tau$  neutrino. Similarly to the Cabibbo-Kobayashi-Maskawa matrix, which models the rotation of electroweak quark states to mass quark states in the quark sector, the Pontecorvo-Maki-Nakagawa-Sakata (PMNS) matrix relates the flavour and mass lepton states. It is commonly parameterized with three mixing angles and one charge-parity ( $CP$ ) violation phase. Before proceeding to a more detailed description of the PMNS matrix, the 1962 approach with two neutrino families is employed to introduce the oversimplified illustration of the oscillation scheme. Assuming that the flavour and mass eigenbases are rotated by an angle  $\theta$ , the two-flavour oscillation matrix can be written as follows:

$$\begin{pmatrix} \nu_e \\ \nu_\mu \end{pmatrix} = U \begin{pmatrix} \nu_1 \\ \nu_2 \end{pmatrix} = \begin{pmatrix} \cos \theta & \sin \theta \\ -\sin \theta & \cos \theta \end{pmatrix} \begin{pmatrix} \nu_1 \\ \nu_2 \end{pmatrix}, \quad (15)$$

where  $U$  is the prototype of the PMNS matrix. Under such notation, one can define the time evolution of the  $\nu_\mu$  state:

$$\begin{aligned} |\nu_e(t=0)\rangle &= |\nu_e\rangle = \cos \theta |\nu_1\rangle + \sin \theta |\nu_2\rangle \\ |\nu_\mu(t)\rangle &= \cos \theta |\nu_1\rangle e^{-i\frac{E_1 t}{\hbar}} + \sin \theta |\nu_2\rangle e^{-i\frac{E_2 t}{\hbar}}, \end{aligned} \quad (16)$$

where  $E_i = \sqrt{p_i^2 c^2 + m_i^2 c^4}$ . By assuming  $p_1 = p_2$ , natural units (*i.e.*  $\hbar = c = 1$ ) and neutrinos are ultra-relativistic:

$$\begin{aligned} E_i &= \sqrt{p^2 + m_i^2} = p \sqrt{1 + \left(\frac{m_i}{p}\right)^2} = |p \gg m_i| = p + \frac{m_i^2}{p} \\ |\nu_e(t)\rangle &= \cos \theta |\nu_1\rangle e^{-i(p + \frac{m_1^2}{2p})t} + \sin \theta |\nu_2\rangle e^{-i(p + \frac{m_2^2}{2p})t} \\ |\nu_\mu(t)\rangle &= e^{-i(p + \frac{m_1^2}{2p})t} (\cos \theta |\nu_1\rangle + \sin \theta |\nu_2\rangle e^{+i(p + \frac{m_1^2 - m_2^2}{2p})t}). \end{aligned} \quad (17)$$

For the sake of simplicity in the expression of the time evolution of the  $\nu_\mu$  state, further notation is introduced:

$$\Delta m^2 = m_1^2 - m_2^2, \quad t = \frac{x}{c} = x \quad \text{and} \quad e^{-iz} = e^{-i(p + \frac{m_1^2}{2p})t} \quad (18)$$

The time-dependent state vector becomes:

$$|\nu_e(t)\rangle = e^{-iz} (\cos \theta |\nu_1\rangle + \sin \theta |\nu_2\rangle e^{+i\frac{\Delta m^2}{2p}x}). \quad (19)$$

The probability of the oscillation of the state  $\nu_\mu$  to the state  $\nu_e$  corresponds to the squared amplitude that describes the transition:

$$\begin{aligned} P(\nu_e \longrightarrow \nu_\mu) &= |\langle \nu_\mu | \nu_e(t) \rangle|^2 \\ \text{where } \langle \nu_\mu | &= -\sin \theta \langle \nu_1 | + \cos \theta \langle \nu_2 |, \text{ defined similarly to Eq. 16} \end{aligned} \quad (20)$$

Then the amplitude for detecting a neutrino of muon flavour at the space-time point  $(t, x)$  given that it was generated with the electron flavour at space-time point  $(0, 0)$  is:

$$\langle \nu_\mu | \nu_e(t) \rangle = |\langle \nu_i | \nu_j \rangle = \delta_{ij}| = e^{-iz} (-\sin \theta \cos \theta + \sin \theta \cos \theta e^{+i\frac{\Delta m^2}{2p}x}). \quad (21)$$

Then the squared amplitude can be computed as follows:

$$\begin{aligned}
P(\nu_e \rightarrow \nu_\mu) &= |\langle \nu_\mu | \nu_e(t) \rangle|^2 = e^{+iz} e^{-iz} \sin^2 \theta \cos^2 \theta (-1 + e^{+i\frac{\Delta m^2}{2p}x}) (-1 + e^{-i\frac{\Delta m^2}{2p}x}) = \\
&= |\sin^2 \theta \cos^2 \theta = \frac{1}{4} \sin^2 2\theta; \frac{\Delta m^2}{2p}x = y| = \frac{1}{4} \sin^2 2\theta (2 - (e^{iy} + e^{-iy})) = \\
&= |e^{iy} + e^{-iy} = 2 \cos y| = \frac{1}{2} \sin^2 2\theta (1 - \cos y) = \frac{1}{2} \sin^2 2\theta (1 - \cos(\frac{\Delta m^2 x}{2p})).
\end{aligned} \tag{22}$$

The final transformation involves an additional trigonometric relation  $1 - \cos 2\theta = 2 \sin^2 \theta$ . Considering the ultrarelativistic nature of the neutrino and hence  $p = E_\nu$  and substituting  $x$  by the distance  $L$  travelled by the neutrino, one eventually obtains the following:

$$P(\nu_e \rightarrow \nu_\mu) = \sin^2 2\theta \sin^2\left(\frac{\Delta m^2 L}{4 E_\nu}\right). \tag{23}$$

That is the place to rewrite the second sinus argument back from the natural system of units, such that  $L$  is expressed in metres and  $E_\nu$  in MeV. It is done by introducing  $\hbar$  and  $c$  with  $\hbar c = 197.328 \text{ eV}\cdot\text{nm}$ :

$$\begin{aligned}
\frac{\Delta m^2 L}{4 E_\nu} &\Rightarrow \frac{\Delta(m c^2)^2 L}{4 \hbar c E_\nu} \Rightarrow \frac{\Delta m^2}{4 \cdot 197 \text{ eV} \cdot \text{nm}} \frac{L}{E_\nu} \frac{\text{eV}^2 \cdot 10^{-6} \frac{\text{MeV}}{\text{eV}}}{10^{-9} \frac{\text{m}}{\text{nm}}} = 1.27 \Delta m^2 \frac{L}{E_\nu} \\
P(\nu_\alpha \rightarrow \nu_\beta) &= \sin^2 2\theta \sin^2\left(1.27 \Delta m^2 \frac{L}{E_\nu}\right).
\end{aligned} \tag{24}$$

The factor 1.27 is unitless, and  $\frac{L}{E}$  is kept in  $\frac{\text{m}}{\text{MeV}}$  or in the equivalent  $\frac{\text{km}}{\text{GeV}}$  depending on the neutrino source used in the experiment. The value of the mixing angle  $\theta$  and the splitting of the mass  $\Delta m^2$  is defined by nature. Once these parameters are known, it is up to the experiment design to tune the  $\frac{L}{E}$  to maximise the oscillation probability. In order to understand the required ranges, the complete PMNS matrix has to be considered. It can be parameterised by 4 free parameters, which are usually defined as three mixing angles  $\theta_{12}$ ,  $\theta_{23}$  and  $\theta_{13}$  and  $\delta_{CP}$  phase, according to:

$$U_{PMNS} = \begin{bmatrix} 1 & 0 & 0 \\ 0 & c_{23} & s_{23} \\ 0 & -s_{23} & c_{23} \end{bmatrix} \begin{bmatrix} c_{13} & 0 & s_{13} e^{-i\delta_{CP}} \\ 0 & 1 & 0 \\ -s_{13} e^{i\delta_{CP}} & 0 & c_{13} \end{bmatrix} \begin{bmatrix} c_{12} & s_{12} & 0 \\ -s_{12} & c_{12} & 0 \\ 0 & 0 & 1 \end{bmatrix}, \tag{25}$$

with  $s$  and  $c$  denoting the sine and cosine functions. The PMNS matrix splitting conveniently reflects the phenomenological ordering of the leptonic couplings. Hence, the first matrix is generally referred to as atmospheric term, the second as reactor term, and the last one as solar term. Each of them is briefly discussed below.

### 1.3.1 The atmospheric term

With the oscillation probability defined by Equation 24 it is possible to explain the picture obtained for muon-like candidates shown in Figure 3. An average energy regime for the atmospheric neutrino is 1 GeV and there are two possible baselines of 10 km for the downgoing neutrino and 13000 km for the neutrino crossing the Earth. Then the  $\Delta m_{23}^2$  ( $\Delta m_{atm}^2$ ) value has to suppress the oscillation behaviour for the short distances and

increase the probability for the long baseline. Super Kamiokande has measured the mass splitting to be in the  $[1.5, 3.4] \cdot 10^{-3} eV^2$  [25]. Quantitatively, the oscillation probability is then described as:

$$\begin{aligned} 1.27 \cdot \Delta m^2 \cdot \frac{L}{E_\nu} &= 1.27 \cdot 10^{-3} \frac{10 \text{ km}}{1 \text{ GeV}} = 0.0127 \implies P_{\alpha \rightarrow \beta} \leq \sin^2(0.0127) = 10^{-4} \\ 1.27 \cdot \Delta m^2 \cdot \frac{L}{E_\nu} &= 1.27 \cdot 10^{-3} \frac{13000 \text{ km}}{1 \text{ GeV}} = 16.51 \implies P_{\alpha \rightarrow \beta} \leq \sin^2(16.51) = 0.52, \end{aligned} \quad (26)$$

which indicates that, in the first case scenario, the baseline is not long enough for the oscillations to occur. The atmospheric sector parameters can hence be validated with the accelerators. Typical accelerator neutrino energies are around 1 GeV. This defines the best baseline at 400 km, which is experimentally feasible. The usual setup of these so-called long-baseline experiments consists of two detectors - the near detector (ND) aimed at the measurement of the neutrino beam close to the production point, and the far detector (FD) aimed at the beam measurements where the oscillation probability is optimal. Accelerator experiments are further divided into disappearance and appearance types. The first one seeks for the same neutrino flavour in both ND and FD and, more specifically, their energy spectrum. The fraction of the spectrum FD to ND has to expose the oscillation pattern, that is, a dip, which position and depth are defined by the oscillation parameters. An example of the disappearance accelerator experiments is Tokai to Kamioka (T2K) [26], which employs 99.5% pure muon neutrino beam from the Japan Proton Accelerator Research Complex (J-PARC) facility in Tokai at the east coast of Japan and SK detector as FD. On the other hand, the appearance experiments are looking for a different neutrino flavour in the FD from the one generated in the initial neutrino beam. The Oscillation Project with Emulsion-tRacking Apparatus (OPERA) is an example of such an experiment. It used the CERN-to-Gran-Sasso (CNGS) beam with an average muon neutrino energy of 17 GeV. The FD was located 732 km away and employed the photographic emulsion technique similar to the DONUT experiment to observe the tau neutrino. The final results published by the OPERA experiment reported the observation of 10 tau neutrino candidates with  $6.8 \pm 0.75$  signal events and  $2.0 \pm 0.4$  background events expected, which corresponds to  $6.1\sigma$  significance [27]. The result of the combination of measurements including both atmospheric and accelerator data is the following [28]:

$$\Delta m_{atm}^2 = 2.5 \cdot 10^{-3} eV^2, \quad \theta_{atm} = 42.1^\circ. \quad (27)$$

### 1.3.2 The solar term

By considering the baseline for the solar neutrino of  $10^{11}$  m and the energy regime in the several MeV ballpark at face value, the determination of the value for  $\Delta m_{12}^2 \equiv \Delta m_{sol}^2$  from the Equation 24 gives around  $10^{-10} eV^2$ . Practically, Lincoln Wolfenstein showed in the end of 1970-th that the oscillation parameters in matter are different from the ones in vacuum. Few years later, his observation was complemented by Mikheyev and Smirnov, who predicted the resonant enhancement of the oscillation parameters in matter with a slowly decreasing density (as it is in the Sun if moving from the core towards the surface). The resulting Mikheyev-Smirnov-Wolfenstein (MSW) effect [29] has provided a solution

to the solar neutrino problem. Mathematically, it can be represented as an additional potential  $V$ , which modifies the Hamiltonian and hence the eigenstates and eigenvalues of the mass. The oscillation parameters are then connected as:

$$\begin{aligned}\Delta m_{matter}^2 &= \Delta m^2 \cdot \sqrt{(\Delta V/\Delta m^2 - \cos 2\theta)^2 + \sin^2 2\theta} \\ \sin 2\theta_{matter} &= \frac{\sin 2\theta}{\sqrt{(\Delta V/\Delta m^2 - \cos 2\theta)^2 + \sin^2 2\theta}} \\ P_{matter}(\nu_e \rightarrow \nu_\mu) &= \sin^2 2\theta_{matter} \cdot \sin^2(1.27 \cdot \Delta m^2 \cdot \frac{L}{E_\nu}),\end{aligned}\tag{28}$$

that directly transforms into the vacuum expressions in the absence of the potential (*i.e.*  $\Delta V = 0$ ) and enters the resonance mode once  $\Delta V/\Delta m^2 = \cos 2\theta$ , which is achievable with a specific electron number density in matter. The dedicated analysis of the solar data including the MSW effect provides a mass splitting value smaller by two orders of magnitude compared to the atmospheric one. Hence, it is not possible to validate it with accelerator experiments due to the required baseline of  $10^5$  km. On the other hand, the reactor neutrino has a typical energy of 5 MeV, which defines the best baseline of about 100 km. Furthermore, the amount of matter between the reactor and detector makes the determination of the oscillation insensitive to MSW effect. As such, the true solar vacuum oscillation parameters can be measured. The Kamioka Liquid Scintillator Antineutrino Detector (KamLAND) [30] belongs to this type of experiments. The 1 kton detector is situated in the mine shaft next to the Super-KamiokaNDE to the west of the Japanese Alps. The disappearance experiment profited from the prosperous Japanese nuclear power industry, which provides 53 commercial nuclear reactors as a MSW effect-free antineutrino source in KamLAND proximity. Since all of them have different baselines, the oscillation analysis is performed with respect to the averaged one. Finally, the solar experiments possess large statistics with a poor energy resolution, while the KamLAND conditions are reverted, which provides an additional synergy to the combined analysis. The best values obtained from Figure 4 are the following [28]:

$$\Delta m_{sol}^2 = 7.42 \cdot 10^{-5} \text{ eV}^2, \theta_{sol} = 33.45^\circ.\tag{29}$$

### 1.3.3 The reactor term

In principle, the information extracted from the solar and atmospheric sectors defines two necessary independent mass splitting (of which the third can be computed) and two out of three mixing angles, while the third one can be estimated out assuming the unitarity condition. Practically,  $\theta_{13}$  appeared to be the smallest mixing angle and hence plagued the most with the uncertainties on the other two angles measurements. Note that the unitarity of the PMNS matrix does not necessarily hold in models beyond the SM. Therefore, it is desirable to directly measure  $\theta_{13}$ . There are two ways to tackle the question: aim either at the survival probability of the electron neutrino or at the electron neutrino appearance in muon neutrino beams. The dedicated equations are the following:

$$\begin{aligned}P_{\nu_e \rightarrow \nu_e} &= 1 - \cos^4 \theta_{13} \sin^2 2\theta_{12} \sin^2(1.27 \Delta m_{12}^2 \frac{L}{E}) - \sin^2 2\theta_{13} \sin^2(1.27 \Delta m_{23}^2 \frac{L}{E}) \\ P_{\nu_\mu \rightarrow \nu_e} &= \sin^2 2\theta_{13} \sin^2 2\theta_{23} \sin^2(1.27 \Delta m_{23}^2 \frac{L}{E}),\end{aligned}\tag{30}$$

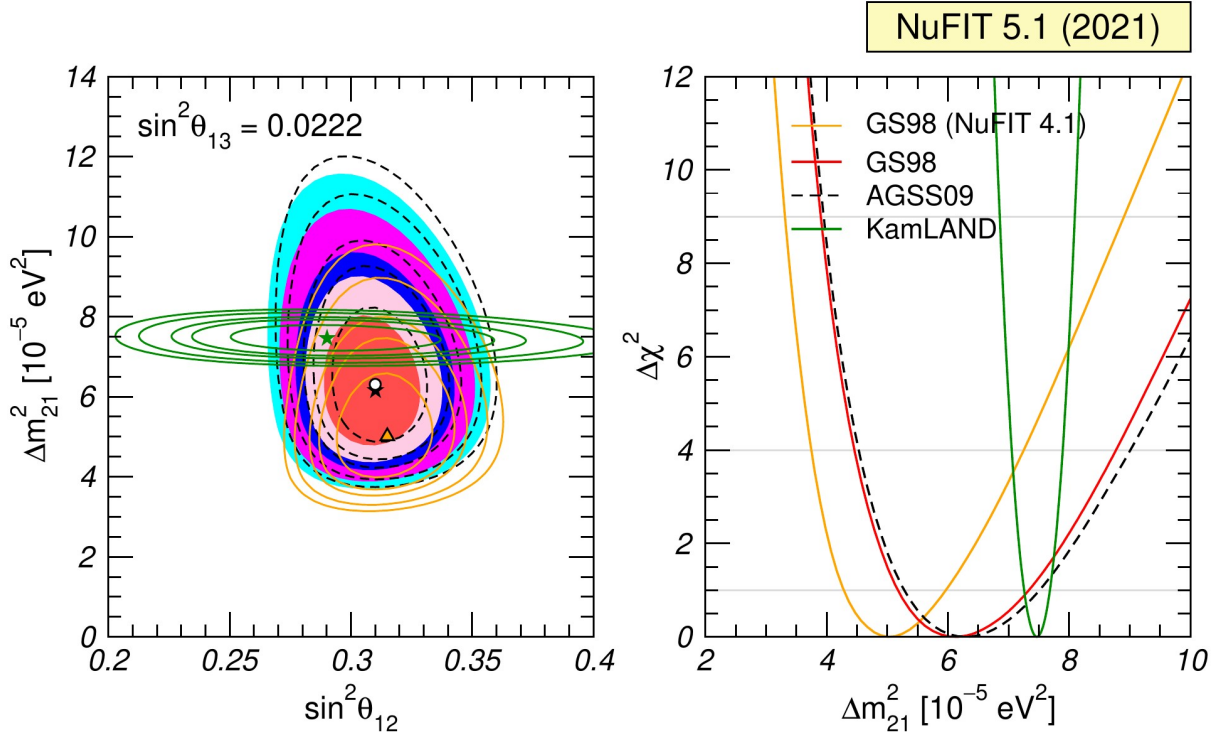


Figure 4: Left: Allowed parameters regions at 1, 2 and 3 $\sigma$  CL for the KamLAND data (solid green contours with the best fit point marked by green star) and three different solar models: AGSS09 (best fit as white dot), GS98 (best fit as black star) and previous version of the GS98 (best fit as yellow triangle). The discrepancy between solar and KamLAND data reduced from 2.2 to 1.1  $\sigma$  by including the latest data from Super-Kamiokande. Right:  $\Delta\chi^2$  versus  $\Delta m_{21}^2$  for the same four analyses after marginalizing over  $\theta_{12}$ . Extracted from [28].

The selection of the baseline within the kilometre for the reactor antineutrinos (which obey the same law if  $CPT$  is conserved) for the first equation allows the second term to be neglected (due to the value of the second sine) and, as such, eliminates interference with the solar mixing angle. This measurement was carried out by three reactor experiments: Daya Bay in China [31], Double CHOOZ in France [32] and RENO in South Korea [33]. The use of the second equation was the initial reason for building the T2K experiment. The publication in 2013 claimed 28 electron-like candidates with 5 background events predicted, which corresponds to more than 7 $\sigma$  significance [34]. Moreover, T2K can operate in the antineutrino mode, which allows the value of  $\delta_{CP}$  to be probed. The results of the reactor experiments agree with those obtained at T2K and provide the combined value of  $\theta_{13} = 8.62^\circ$  [28].

The combined analyses mentioned several times in the current subsection are performed by the NuFit group. Their objective is to provide the most accurate determination of the neutrino mixing parameters by combining the latest data from all experiments. The current state of the art is summarised in Figure 5.

### 1.3.4 The open questions

By construction, the neutrino oscillation experiments have access only to the mass-splitting values, and hence the absolute neutrino masses remain unknown. Moreover, the neutrino

		Normal Ordering (best fit)		Inverted Ordering ( $\Delta\chi^2 = 7.0$ )	
		bfp $\pm 1\sigma$	$3\sigma$ range	bfp $\pm 1\sigma$	$3\sigma$ range
with SK atmospheric data	$\sin^2 \theta_{12}$	$0.304^{+0.012}_{-0.012}$	$0.269 \rightarrow 0.343$	$0.304^{+0.013}_{-0.012}$	$0.269 \rightarrow 0.343$
	$\theta_{12}/^\circ$	$33.45^{+0.77}_{-0.75}$	$31.27 \rightarrow 35.87$	$33.45^{+0.78}_{-0.75}$	$31.27 \rightarrow 35.87$
	$\sin^2 \theta_{23}$	$0.450^{+0.019}_{-0.016}$	$0.408 \rightarrow 0.603$	$0.570^{+0.016}_{-0.022}$	$0.410 \rightarrow 0.613$
	$\theta_{23}/^\circ$	$42.1^{+1.1}_{-0.9}$	$39.7 \rightarrow 50.9$	$49.0^{+0.9}_{-1.3}$	$39.8 \rightarrow 51.6$
	$\sin^2 \theta_{13}$	$0.02246^{+0.00062}_{-0.00062}$	$0.02060 \rightarrow 0.02435$	$0.02241^{+0.00074}_{-0.00062}$	$0.02055 \rightarrow 0.02457$
	$\theta_{13}/^\circ$	$8.62^{+0.12}_{-0.12}$	$8.25 \rightarrow 8.98$	$8.61^{+0.14}_{-0.12}$	$8.24 \rightarrow 9.02$
	$\delta_{CP}/^\circ$	$230^{+36}_{-25}$	$144 \rightarrow 350$	$278^{+22}_{-30}$	$194 \rightarrow 345$
	$\frac{\Delta m_{21}^2}{10^{-5} \text{ eV}^2}$	$7.42^{+0.21}_{-0.20}$	$6.82 \rightarrow 8.04$	$7.42^{+0.21}_{-0.20}$	$6.82 \rightarrow 8.04$
	$\frac{\Delta m_{3\ell}^2}{10^{-3} \text{ eV}^2}$	$+2.510^{+0.027}_{-0.027}$	$+2.430 \rightarrow +2.593$	$-2.490^{+0.026}_{-0.028}$	$-2.574 \rightarrow -2.410$

Figure 5: The NuFit group three-flavour oscillation parameters values determined from the fit to global data as of October 2021. Extracted from [28].

mass ordering remains unknown as well. By convention, the  $\nu_1$  state is assumed to be lighter than  $\nu_2$ . Then depending on the sign of the  $\Delta m_{atm}$  the  $\nu_3$  state can either be the heaviest one, which results in the normal ordering (NO) assumption, or the lightest one, inverted ordering (IO). The two hypotheses are illustrated in Figure 6.

There are two main approaches to fix the ordering issue. The first one is an oscillation approach. The idea is to precisely measure the muon to electron neutrino oscillation, which is governed by  $\Delta m_{13}^2$  as defined in Equation 30. The leading order is not dependent on the mass ordering, however the sub-leading term is. It is caused by the matter effects briefly introduced in Chapter 1.3.2, which depend not only on the ordering but are also different for neutrinos and antineutrinos. As such, the combination of enough statistics from experiments capable of operating in both neutrino and antineutrino modes (T2K, NO $\nu$ A, DUNE, etc.) at different baselines under different conditions (to suppress degeneracies) can do the job. The second approach does not rely on the oscillation but on the assumption that neutrino are Majorana particles. If so, the ordering can be determined via the neutrino-less double  $\beta$  decay experiments. It also modifies the PMNS matrix by introducing an additional diagonal term with elements  $1$ ,  $e^{i\beta}$  and  $e^{i\gamma}$ , where  $\beta$  and  $\gamma$  are Majorana phases. The main concern is that the observable is not guaranteed to be there (*i.e.* neutrino are Dirac particles, thus  $\beta = \gamma = 0$  and hence the neutrino-less double  $\beta$  decay is not possible).

The last parameter of the PMNS matrix, which has not yet been touched on, is the  $\delta_{CP}$  phase. It is the analogue of  $\delta_{CKM}$  observed in the quark sector. To date, no valid mechanism has been brought forward to account for the observed matter-antimatter asymmetry in the universe, provided that the unique source of symmetry breaking comes from the quark sector. That is the place where leptogenesis [36] can take over. Not going too deep into the details, this is the class of scenarios where the baryon asymmetry of the Universe is produced from a lepton asymmetry generated in the decays of a heavy sterile

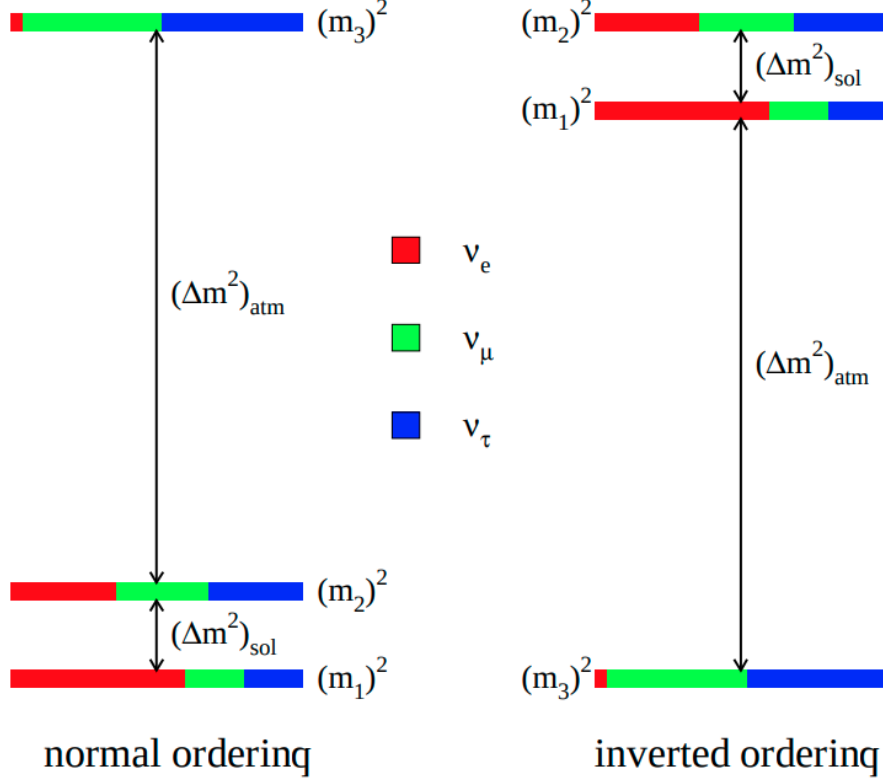


Figure 6: An illustration of the NO and IO assumptions. In addition, each mass eigenstate is color-coded with the indication of the fraction of each distinct flavour. Extracted from [35].

neutrino.

The necessary but not sufficient condition for leptogenesis to be possible is that the value of  $\delta_{CP}$  is different from 0 or  $\pi$  (closer to  $\pm\frac{\pi}{2}$  is better). Based on the flavour-change probability expression:

$$P_{\alpha\beta} = \delta_{\alpha\beta} - 4 \sum_{i>j} \Re(U_{\alpha i}^* U_{\beta i} U_{\alpha j} U_{\beta j}^*) \sin \Theta_{ij} + 2 \sum_{i>j} \Im(U_{\alpha i}^* U_{\beta i} U_{\alpha j} U_{\beta j}^*) \sin \Theta_{ij} \quad (31)$$

$$\Theta_{ij} = \sin^2(1.27 \cdot \Delta m_{ij}^2 \cdot \frac{L}{E}),$$

the disappearance experiments (*i.e.*  $\alpha = \beta$ ) are insensitive to  $\delta_{CP}$  measurement, since the third term equals zero. Once the mass ordering is resolved, there are, however, two possible options to estimate the  $CP$  phase from the appearance experiments. The first one relies on the same principle as the oscillation method of the ordering definition and therefore requires the precise measurement of  $\nu_\mu \rightarrow \nu_e$  versus  $\bar{\nu}_\mu \rightarrow \bar{\nu}_e$ . With 5 years of exposure, the Hyper-Kamiokande experiment is expected to determine the  $\delta_{CP}$  for better than 19 degrees for all possible values and determine the  $CP$  violation at the  $3\sigma$  significance for more than 76% of the data parameter space [37]. It will be complemented with the data obtained with other next-generation experiments such as DUNE in the USA and JUNO in China. In addition, DUNE will be sensitive to the approach, for which only one mode of measurement is enough. It relies on the probability measurement of either an electron neutrino or an antineutrino. Its energy dependence for the DUNE's baseline

of 1300 km is sketched in Figure 7. The approach aims at comparing the two peaks at around 2 and 1 GeV, the relative yield of which is sensitive to the  $\delta_{CP}$  phase value.

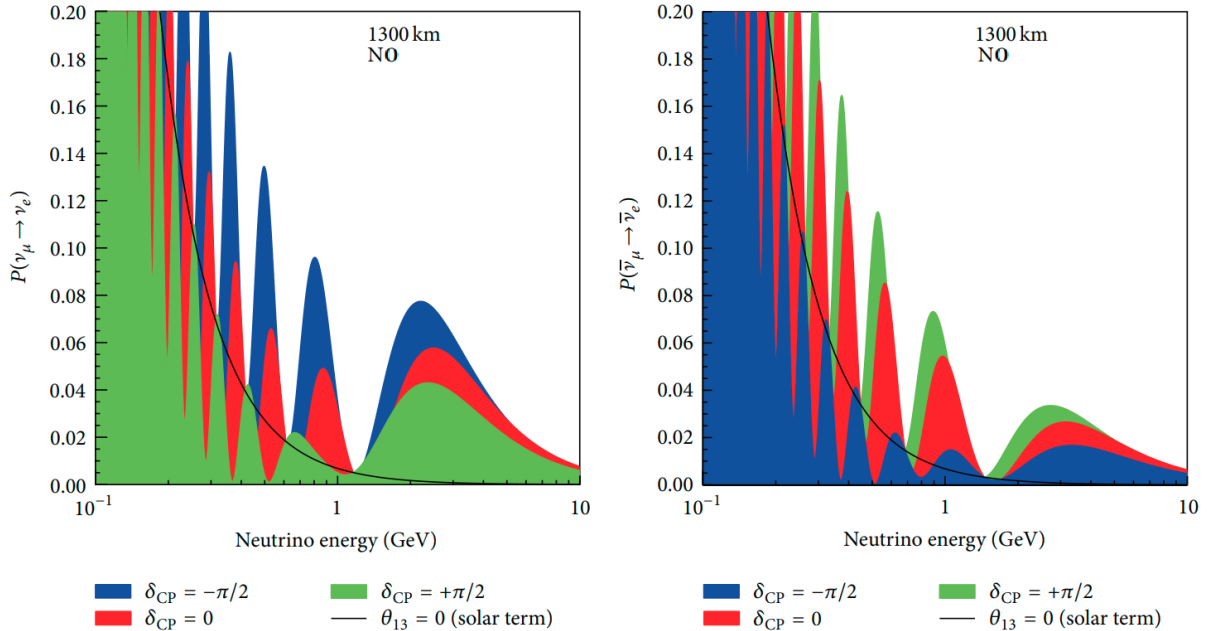


Figure 7: The appearance probability for the electron neutrino (left) and antineutrino (right) as a function of the energy of the beam energy of muon neutrino/antineutrino accordingly. The curves are calculated for the DUNE's baseline of 1300 km with respect to the three possible values of the  $\delta_{CP}$  for the Daya Bay best fit value of  $\theta_{13}$ . Extracted from [38]

## 1.4 Other neutrino anomalies

Both solar neutrino problem and atmospheric neutrino anomaly were solved with the introduction of the three-flavour neutrino oscillation model. However, further scrutiny of these elusive particles and the oscillation phenomena brought new challenges.

### 1.4.1 The accelerator sector

One of the anomalies in the accelerator sector comes from the Liquid Scintillator Neutrino Detector (LSND) experiment [39]. It was searching for the  $\bar{\nu}_\mu \rightarrow \bar{\nu}_e$  oscillations at the Los Alamos Meson Physics Facility (LAMPF). The way to create the muon antineutrino flux was the following - the proton beam of 800 MeV interacted with a water target. Due to the beam energy regime, mainly  $\pi^+$  and  $\pi^-$  were produced as a result of this interaction. Most of the  $\pi^+$  came to rest and decayed through the sequence:

$$\begin{aligned} \pi^+ &\longrightarrow \mu^+ + \nu_\mu \\ \mu^+ &\longrightarrow e^+ + \nu_e + \bar{\nu}_\mu, \end{aligned} \quad (32)$$

hence providing the neutrino signal events. At the same time, it was important to suppress the neutrino fluxes from negative pions. Here, the geometrical layout and the material composition of the beam stop were crucial. The target box consisted mainly of high  $Z$  materials. Therefore, most of the  $\pi^-$  were absorbed in the target and did not contribute

to the toxic  $\bar{\nu}_e$  event rate. In addition, this setup allowed one to reduce the rate of the  $\mu^-$  decaying in flight. In the end, the relative yield of  $\bar{\nu}_e$  versus  $\bar{\nu}_\mu$  was estimated to be around  $5 \times 10^{-4}$ . The observation of a  $\bar{\nu}_e$  rate significantly larger than the predicted background would be evidence for  $\bar{\nu}_\mu \rightarrow \bar{\nu}_e$  oscillations.

The electron antineutrinos were detected through the IBD process at a distance of around 30 m from the target box. The detector consisted of a tank filled with 167 tons of mineral oil. In the signal signature, the electron-like signal was completed by a 2.2 MeV gamma from the consecutively correlated in time neutron capture. Despite the fact that it was not possible to distinguish electrons from positrons, background processes due to  $\nu_e$  were eliminated by an energy cut and the request of a correlated neutron signal. A total excess of  $87.9 \pm 22.4 \pm 6.0$  events were reported above the expected background [40]. It was not the oscillation itself that was a problem, but the  $\Delta m^2$  value obtained by the LSND. From solar and atmospheric experiments, two squared mass differences are already known:  $\Delta m_{21}^2 = 7.4 \times 10^{-5} \text{ eV}^2$  and  $|\Delta m_{23}^2| = 2.5 \times 10^{-3} \text{ eV}^2$ . With  $N$  active neutrinos there must be  $N - 1$  mass splittings. It is also known from the LEP results that there are three light active neutrinos with a mass below 45 GeV. Since  $\Delta m_{LSND}^2$  has been measured to be in the range 0.2 - 10  $\text{eV}^2$ , it suggested at least one additional *sterile* neutrino.

It is all about cross-checks and validation once it comes to dramatic conclusions such as the one issued by the LSND experiment. Two experiments addressing the same phenomena are briefly discussed below. The first one is the KARlsruhe Rutherford Medium Energy Neutrino (KARMEN) experiment, which was extremely similar to LSND:

- The ISIS synchrotron accelerated the proton beam to the identical 800 MeV energy.
- The same sequence of decays was used to obtain the  $\bar{\nu}_\mu$  flux.
- The same target features were used to absorb  $\pi^-$  and prevent  $\bar{\nu}_e$  production.
- Electron antineutrinos were detected through the IBD process.

A rectangular tank filled with 56 tons of a liquid scintillator in combination with a  $\text{Gd}_2\text{O}_3$  coated paper were used in order to reconstruct respectively positron and neutron signals of the IBD. Despite the extremely similar setup, neither KARMEN nor slightly improved KARMEN2 saw any indication of the oscillations seen by LSND [41]. In the end, the neutrino oscillation parameters limits were set and they could not completely exclude the parameter space defined by the LSND. The difference in the distance at which neutrinos were measured (30 m for the LSND versus 18 m for KARMEN), which can cause the difference in sensitivity up to factor 3 at low values of  $\Delta m^2$ , was named as one of the most probable reasons for the discrepancy.

It became necessary to carry out a more definitive cross-check. The Booster Neutrino Experiment (MiniBooNE) [42] was designed to say the last word on the LSND anomaly. MiniBooNE is located at Fermi National Accelerator Laboratory (Fermilab) in the USA. The experiment setup and the production of the Booster Neutrino Beam (BNB) are sketched in Figure 8. The 8 GeV proton beam from the Fermilab Booster interacted with a beryllium target. Since the beam energy is 10 times larger than in the LSND experiment, it allows heavier mesons than pions to be created. More importantly, they are no longer created at rest. Therefore, it is not possible to employ the same technique of selecting positively charged mesons as in the experiments described above. Instead,

the target was placed inside a neutrino (magnetic) horn. It was initially introduced by Simon van der Meer in 1961 and was firstly operated at CERN two years later. Several shape modifications were developed further and adopted also by BNL, High Energy Accelerator Research Organisation (KEK) and J-PARC. The physics idea reads as: the configuration of the magnetic field allows one to focus particles with the selected charge and defocus particles with the opposite charge. The selection of the charge can be reversed by just switching the polarity of the field. It opens an additional opportunity to run the appearance experiment in both neutrino and antineutrino modes. The mesons from the secondary beam are decaying in a 50 m decay pipe. The pipe is followed by 4 m of absorber and 450 m of dirt. This was done to purify the tertiary neutrino beam from the leptons. Furthermore, the distance was chosen to match the same  $L/E$  and thus reach the same sensitivity region as the LSND. The composition of the neutrino beam is well known, since kaons are following the same decay mode as pions:

$$\begin{aligned} K^+ &\longrightarrow \mu^+ + \nu_\mu \\ \mu^+ &\longrightarrow e^+ + \nu_e + \bar{\nu}_\mu . \end{aligned} \tag{33}$$

In order to be efficient in the observation of oscillations, the MiniBooNE detector had to meet several conditions. The required target mass of the detector is around 1 kton to generate approximately 1000 neutrino-oscillation events from  $10^{21}$  protons on the target (POT). Obviously, such a detector had to perfectly discriminate events issued by the different neutrino flavours. Finally, it required a fully active volume and a  $4\pi$  veto to reject the cosmic ray events. A liquid Cherenkov detector is an economical choice which fits all the requirements listed above. In addition, such a detector design solution allowed one to use the phototubes and electronics from the LSND experiment, which decreased the construction price. The detector itself consists of a 12.2 m diameter sphere filled with 818 tons of pure mineral oil. A higher refractive index and lower density allowed electrons to produce more Cherenkov light in the mineral oil and increased the background rejection efficiency as a result of the lower Cherenkov threshold. The MiniBooNE results were published in several stages. Initially, in 2007, it was claimed that no significant excess is observed in the neutrino mode [45]. However, the conclusion was changed with more advanced analysis of the data. The polarity of the horn also changed since 2006. The most recent published result for 2021 reports a total excess of  $638 \pm 52 \pm 122$  electron-like events, which corresponds to an overall significance of  $4.8\sigma$ , limited by systematic uncertainties [46]. However, most of the excess lives in the low-energy range, which does not conform to the LSND results. The first liquid argon time projection chamber MicroBooNE was designed to further study the nature of this excess. Nevertheless, the first results, which started to pop out this year, do not see any excess in the  $\nu_e$  events [47].

#### 1.4.2 The gallium anomaly. Part 2

However, it is not necessary to build new experiments in order to extend the amount of enigmas related to the neutrino nature. The discussed above-line SAGE and GALLEX are further contributing to the list. This time the discrepancy came from the calibration runs. Both radiochemical experiments were carried out using calibration sources based on electron capture. The main advantage of this type of sources is the generation of the monoenergetic neutrinos:

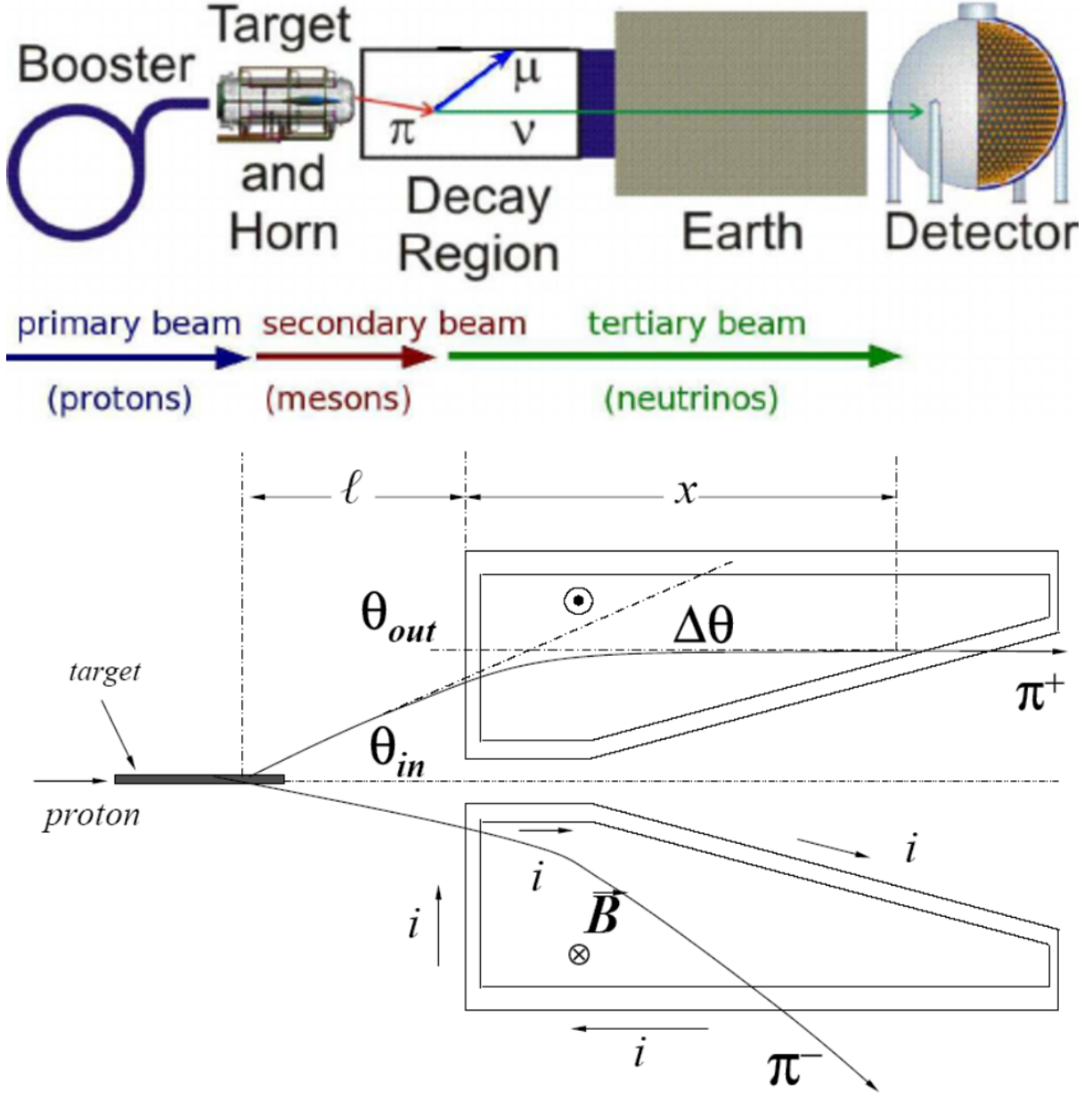


Figure 8: The experimental layout of the MiniBooNE (top). The principle of work of the neutrino (magnetic) horn (bottom). Extracted from [43] (top) and [44] (bottom).



For the GALLEX experiment, two  ${}^{51}\text{Cr}$  neutrino sources were produced at the Siloe reactor in Grenoble [48] for this purpose, while the SAGE experiment used both  ${}^{51}\text{Cr}$  and  ${}^{37}\text{Ar}$  sources. Both experiments observed a deficit of 15% with respect to the predicted neutrino signal of the sources. The deficit has a significance of  $3\sigma$  and is known as the gallium anomaly. It has recently been revisited by the Baksan Experiment on Sterile Transitions (BEST) [49], which used the gallium-germanium neutrino telescope of the SAGE experiment. BEST experiment employed two sensitive zones of a liquid Ga target

to probe the neutrino oscillations on the meter scale. It provides therefore two independent rate measurements that can be compared. Ten independent extractions were performed for each zone. Both exhibited a similar deficit with a  $4\sigma$  deviation from unity consistent with previously reported results. The measurements obtained from the three collaborations are summarised in Figure 9. The discrepancy can be addressed in different ways, *e.g.* questioning the predictions of the cross sections of the neutrino interactions or suggesting oscillations to a new sterile flavour. From the latter perspective, the measured deficit provides a best-fit oscillation parameters of  $\Delta m^2 = 3.3_{-2.3}^{+\infty} \text{ eV}^2$  and  $\sin^2 2\theta = 0.42_{-0.17}^{+0.15}$ . However, such a large mixing angle immediately finds itself in significant tension with the solar neutrino experiments [50].

### 1.4.3 The reactor sector

The last anomalies, which will be discussed in this chapter, come from the neutrino source that was used by the pioneers of neutrino explorations: nuclear reactors. Precise prediction of the reactor flux is an extremely complicated exercise. One of the attempts to improve the existing calculations was made in 2011 [51]. The updated version of the so-called *ab initio* approach (also known as the summation method) was introduced by Mueller *et al.*. The reference spectrum was composed out of the sum of all  $\beta$ -branches of all fission products. Initially, it was used to obtain the spectra for  $^{238}\text{U}$ ,  $^{235}\text{U}$ ,  $^{239}\text{Pu}$ , and  $^{241}\text{Pu}$ . More accurate computations for the last three isotopes were developed by adding missing contributions obtained from the conversion of the Institut Laue-Langevin (ILL)  $\beta$  spectra. These particular spectra were further corrected with an improved conversion method by Huber. Finally, the Huber-Muller (HM) model was composed. It consisted of  $^{235}\text{U}$ ,  $^{239}\text{Pu}$  and  $^{241}\text{Pu}$  spectra obtained by Huber with the conversion method and  $^{238}\text{U}$  obtained by Mueller *et al.* with the summation method. Together with the new reference antineutrino energy spectra, the flux was reported. It appeared to be on average 3% larger relative to the previous calculations. Consequently, this created a deficit of the same amount when the flux measurements at the reactors were compared with the new theory. The newly established discrepancy was called the Reactor Antineutrino Anomaly (RAA) [52]. Figure 10 illustrates the RAA as seen in 2011.

Since the deficit appeared after the reevaluation of the theory, it is natural to assume an error in it. The summation method is based on nuclear databases, which are incomplete and sometimes inaccurate. This can potentially cause large and unknown uncertainties. On the other hand, the conversion method was believed to be more reliable and with small uncertainties. That changed after the discovery of the so-called 5 MeV bump, which will be the last anomaly considered in this chapter. The 5 MeV bump is a disagreement between the predicted reactor antineutrino spectra and the measured one. It was first reported at the Neutrino 2014 conference by the Reactor Experiment for Neutrino Oscillation (RENO) collaboration [53]. The experiment used six aligned reactor cores at Hanbit nuclear reactors in Yonggwang, Korea. In addition, RENO had near- and far-detectors. For both of them, the bump was consistent within the uncertainties. Shortly after, the discrepancy was confirmed by two other commercial reactor experiments, Daya Bay and Double Chooz. Among the possible explanations one can list: an error in the calibration (since all three experiments used the same type of scintillators); the impact of the forbidden decays [54] on the spectra (this was later disfavored to be a unique explanation to the distortion); SM processes mimicking the signal event signature, such as high-energy (with

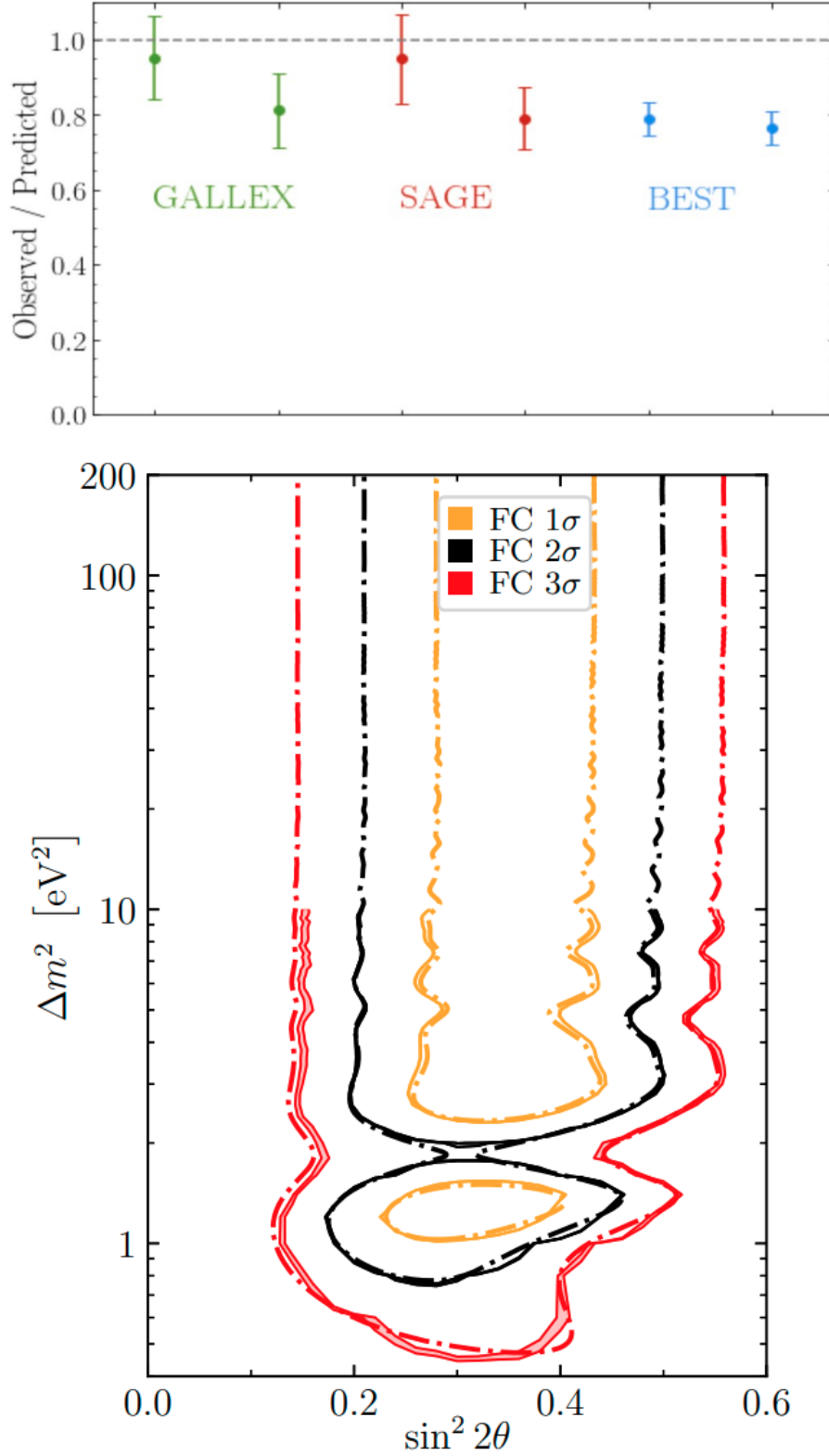


Figure 9: The ratio of the measured neutrino flux to the predicted one on the gallium experiments (top). The allowed regions of the parameter space for the sterile hypothesis derived from the gallium data at the 1, 2, 3 $\sigma$  C.L. (bottom). Extracted from [50].

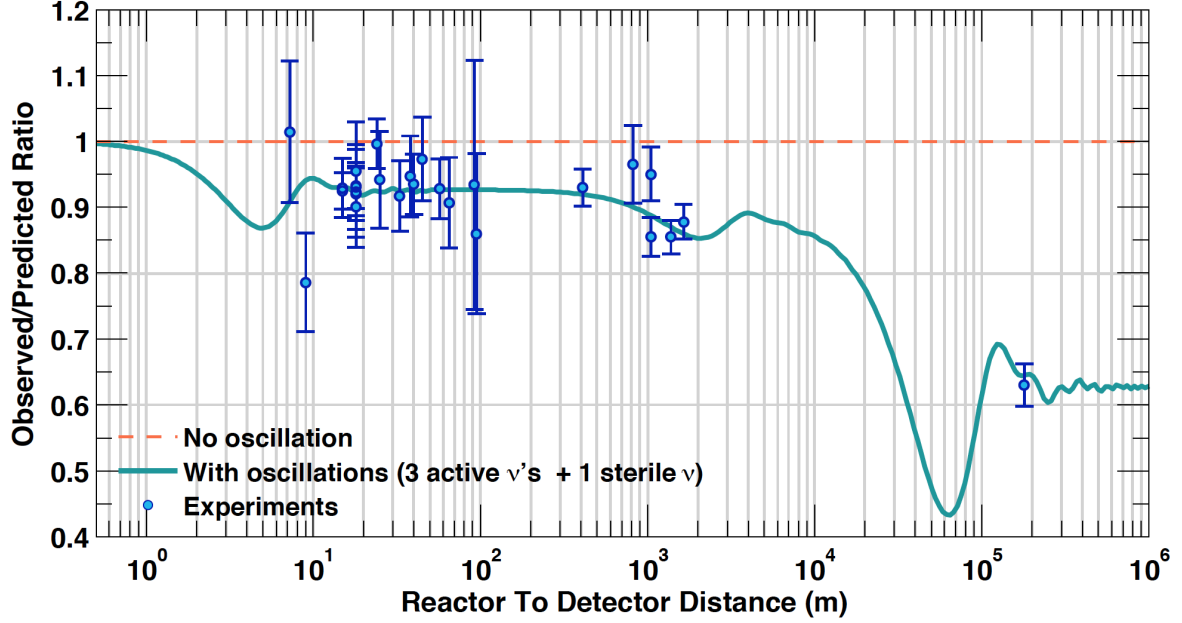


Figure 10: The ratio of the measured IBD yield to the predicted by the HM model as the function of the reactor to detector distance. The dashed red line represents the model with no considered oscillations and the solid green line represents the model with standard oscillation and additional one to the sterile state with  $\Delta m_{41}^2 = 1\text{eV}^2$ . Extracted from [52].

a 9.4 MeV threshold) neutrino interactions with the  $^{13}\text{C}$  in organic scintillator detectors; the miscalculation of the flux of the certain isotopes (or making one particular isotope responsible for the whole bump), etc. However, no satisfactory explanation has been established to date. Moreover, the latest results published by PROSPECT and STEREO (as well as their joint analysis) confirm the distortion [55]. The 5 MeV bump observations are summarised in Figure 11.

As far as nuclear models are concerned, they must be able to predict not only the flux, but also all the features of the spectra as well, including the 5 MeV bump. Progress in understanding the neutrino flux predictions is tentatively reported in the following lines. Several attempts have recently been made in this direction [57]. For example, nuclear databases were improved, in particular, thanks to the application of the Total Absorption Gamma-ray Spectroscopy (TAGS) technique for a better identification of the  $\beta$  decay branches. The updated nuclear database information was used in 2019 by Estienne, Fallot *et al.* (EF model). On the one hand, a lower neutrino flux was obtained from the  $^{235}\text{U}$  reactor, which was in better agreement with the experimental data. In addition, this model provided a better description of the Daya Bay antineutrino spectrum than the HM model. On the other hand, a lower flux may be the sign of residual incompleteness of the nuclear database and, furthermore, the EF model gave a worse fit of the 5 MeV bump. Another angle of improvement was related to the conversion method. The same year Hayen, Kostensalo, Severijns and Suhonen (HKSS model) tried to improve it by introducing the forbidden transitions calculated with the nuclear shell model. As mentioned above, such types of transition can partially explain the 5 MeV bump. The flux prediction calculated with the HKSS model increased the significance of the RAA. The last thing which can be improved are the spectra measured at ILL. A novel measurement

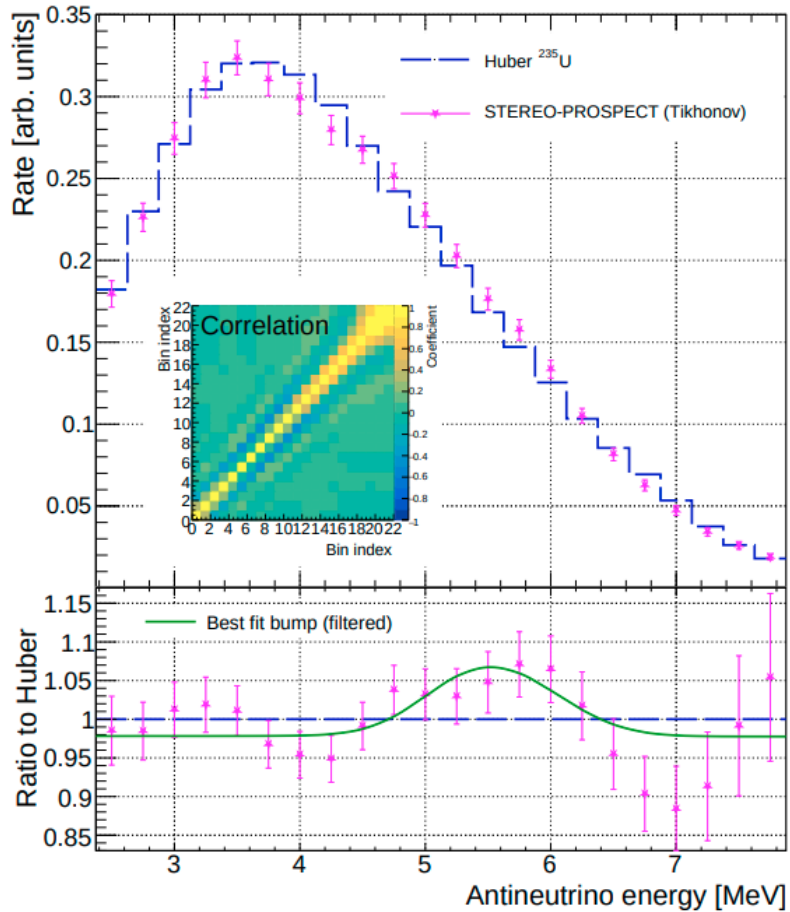
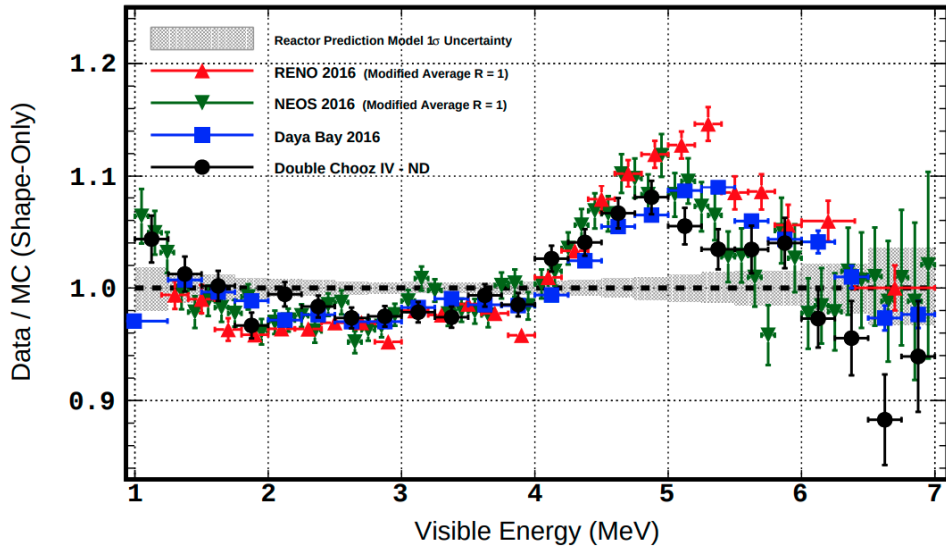


Figure 11: The measured to predicted spectral ratios. For the commercial reactors: Double Chooz Near Detector (in black), Daya Bay (in blue), RENO (in red) and NEOS (in green), with the last two re-scaled with respect to the published results in order to address the shape-only question (left). For the more recent joint analysis of the PROSPECT and STEREO experiments (right). Extracted from [56] (right) and [55] left.

was performed by Kopeikin *et al.* which has resulted in the Kurchatov Institute (KI) conversion model. According to it, the normalisation of the ILL  $^{235}\text{U}$   $\beta$  spectrum was overestimated, which results in a smaller flux w.r.t. the HM model. The same conclusion was obtained for  $^{238}\text{U}$ , which was recalculated with the conversion method. Finally, the Pu isotope flux predictions were estimated to be at a similar level. Therefore, the KI model leads to a decrease in the significance of the RAA. Since correction factors from the KI model improve the description  $^{235}\text{U}$  spectrum and since forbidden transitions from the HKSS model partially explain the 5 MeV bump, it is natural to combine these positive features in a unique description, referred to as the HKSS-KI model. The comparison of the experimental results with all the models described above is shown in Figure 12.

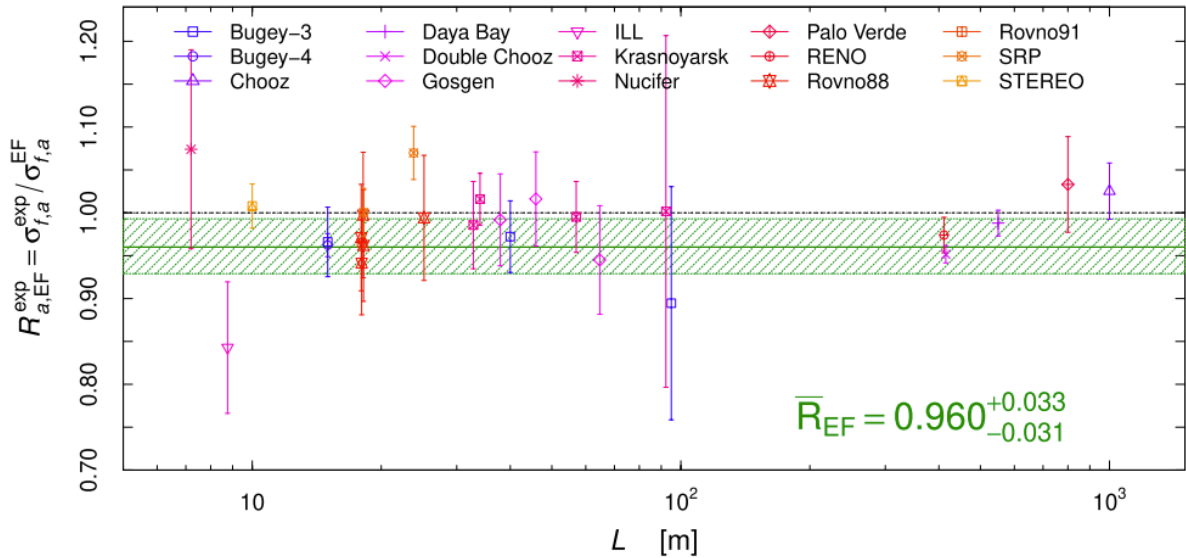


Figure 12: The ratio of the measured IBD yields with respect to the predicted by the model for the reactor experiments as a function of the distance  $L$  from the reactor core to the detector. The represented model is EF. Extracted from [57], where the comprehensive description of the other models (HKSS, KI and HKSS-KI) can be found.

## 1.5 The sterile neutrino hypothesis

There are several possible explanations [58] for the experimental deviations from the theoretical predictions discussed in the previous subsection. One of the most appealing is the sterile neutrino hypothesis, which can account for all the anomalies with the existence of an additional neutrino state with mass at the eV scale. It is also known as the 3+1 model. Obviously, there is absolutely no physical reasoning behind the existence of one single additional neutrino state. Hence, the 3+1 model has to be considered as a convenient minimal model, which helps in defining the direction to accumulate the experimental efforts to look for the deviations from the SM. With that being said, the possible directions are briefly described below. As discussed previously, the number of the light active neutrinos is fixed to be three in the SM to satisfy the  $Z^0$  boson decay width measurement. An additional neutrino state is not able to interact weakly with the matter (which justifies the name) and therefore cannot be directly observed. However,

this additional state might have mass-mixing couplings and can potentially modify the PMNS matrix. It could then be indirectly observed through oscillation patterns with active flavours. This behaviour can be addressed through several types of experiments. To begin with, the experiments, which are designed to probe the absolute mass scale of the neutrino, should see a kink-like signature in the energy spectrum  $E_0 - m_s$  (where  $E_0$  is the endpoint energy of the  $\beta$  decay and  $m_s$  is the mass of the sterile state). The Karlsruhe TRItium Neutrino (KATRIN) experiment is the world-leading effort in this field. It is sensitive to keV-like sterile neutrinos, whereas searches for a lighter state are limited by statistics. However, the projected final sensitivity indicates that KATRIN will be able to examine the entire large  $\Delta m_{41}^2$  parameter space defined by the gallium anomaly and a significant fraction of that of the RAA [59].

Moreover, the appearance/disappearance experiments for the active neutrino flavours can be employed. For the former, existence of a sterile state can cause an excess in the flux of the observed neutrinos due to, for example, the  $\bar{\nu}_\mu \rightarrow \bar{\nu}_s$  oscillation and subsequent re-coupling  $\bar{\nu}_s \rightarrow \bar{\nu}_e$ . This is the reason why accelerator experiments like LSND are sensitive to a sterile neutrino presence. As for the disappearance experiments, the additional state can alter the energy spectra. Neutrino observatories such as IceCUBE or ANTARES [60] are capable of measuring this effect. For example, an eV scale sterile neutrino will cause matter-enhanced resonance, which will be reflected as a dip in the spectra of TeV scale neutrinos coming from the Earth core. However, IceCUBE has not found any strong evidence of sterile neutrino in the recently published search, based on the eight years of atmospheric muon neutrino statistics [61]. Moreover, it has put stringent constraints, strongly excluding global preferred regions from appearance experiments at 99% C.L.

Finally, the experiment design can be based on measuring the modulation of the active neutrino flavour flux due to the oscillation towards the sterile state. The cleanest way to explore this idea is by measuring the reactor electron antineutrino flux modulation. The RAA indicated a probable mass difference of order  $\Delta m^2 = 1\text{eV}^2$ . This value implies that the reactor experiments have to be very short baseline in order to probe the region with the most pronounced oscillation behaviour. Of course, it is not the only parameter that is important for the experiment design. The covered parameter space depends on both reactor (power, size of the core, live-time) and detector (efficiency, cross section, length, and energy resolution) features. A wealth of very short baseline reactor experiments emerged in the past decade. Before some of them are described in more detail, it is important to mention that the sterile neutrino hypothesis has been heavily scrutinised over the past years. All available anomalies and experimental data were explored together to constrain the parameter space and identify accessible regions for the sterile. As mentioned before gallium data is in significant tension with the solar data, such that it is not possible to define the part of the parameter space which is satisfying all the requirements. In addition, the combination of reactor and solar data satisfy the hypothesis that there is no additional sterile. On the other hand, the best fit value resulting from the combination of gallium and reactor experiments is  $\Delta m^2 = 8.86\text{ eV}^2$  and  $\sin^2 2\theta = 0.32$  [50]. The current state of the art regarding parameter space constraints is summarised in Figure 13.

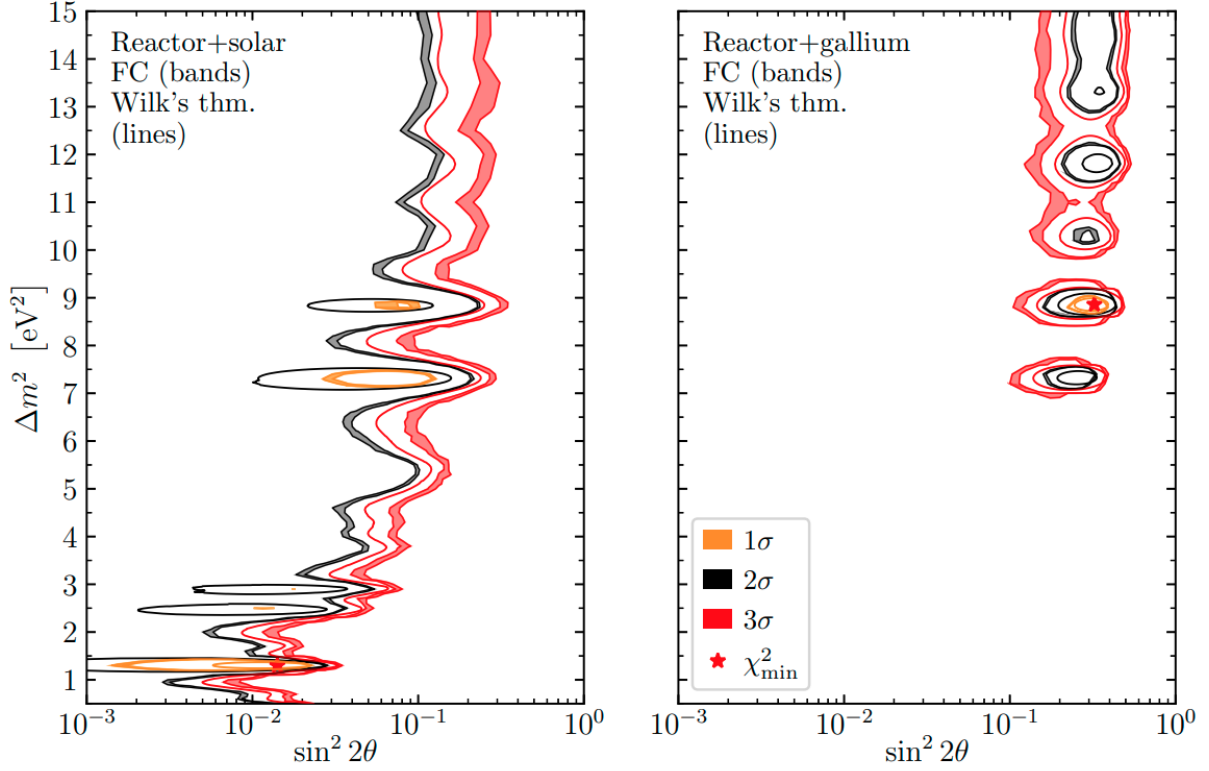


Figure 13: C.L. at 1, 2 and 3 $\sigma$  for the allowed sterile neutrino parameter space values in combinations of: reactor and solar data (left), reactor and gallium (right). The bands correspond to the Feldman-Cousins analysis, while the thin curves are obtained under the Wilk's theorem assumption. Extracted from [50].

### 1.5.1 NEOS

The NEOS experiment is located in the tendon gallery of Reactor Unit 5 of Hanbit Nuclear Power Plant (Yeonggwang, South Korea). The detector core has a thermal power of 2.8  $\text{GW}_{th}$  with a diameter of 3.1 m and a height of 3.8 m. The NEOS detector is measuring the flux at a distance of about 24 m from the reactor core with an overburden of around 20 metres water-equivalent. The detector consists of an active target filled with 1,000 L of gadolinium-loaded liquid scintillator, two buffer tanks filled with mineral oil, a shielding, and the muon detector. The size of the nuclear core and the fact that the detector is unmovable (hence the flux measurement is performed at a unique distance) make the oscillation analysis difficult. However, the difficulty is mitigated by the high detection efficiency (2,000 IBD events on a daily basis) with a signal-to-background ratio of over 20. In addition, a more advanced analysis is performed by combining data from the NEOS and RENO experiments. Since both detectors are located at the same reactor complex, the reactor-related systematic uncertainties are significantly suppressed. As a result, part of the parameter space region in the range  $0.1 < |\Delta m_{41}^2| < 7 \text{ eV}^2$  is excluded at the 95% confidence level (C. L.). The region  $|\Delta m_{41}^2| = 2.41 \text{ eV}^2$  and  $\sin^2 2\theta = 0.08$  are preferred by the data with 68% C.L. with a  $p$ -value of 8.2% [62]. Finally, the 5 MeV bump is observed in the spectra of both experiments.

### 1.5.2 Neutrino-4

The Neutrino-4 experiment has been operated with a full-scale detector for 5 years since 2016. It is located near the SM-3 compact reactor core ( $35 \times 42 \times 42 \text{ cm}^3$ ) with a reactor power of 90 MW. The  $1.8 \text{ m}^3$  Gd-doped liquid scintillator detector is divided into 50 sections gathered in 10 rows of 5 sections each. While the edge rows are used as an active veto, the active volume of the detector is  $1.42 \text{ m}^3$ . The detector is constructed with a movable platform, allowing the reactor antineutrino flux modulation to be measured at distances in the 6-12 m range. For today, it is the only very-short-baseline experiment which obtained a positive result, *i.e.* observed evidence of an oscillation pattern. The analysis of the full statistics yielded a significance level of the signal of about  $3 \sigma$  with the best fit parameters measured as  $\Delta m_{41}^2 = (7.3 \pm 0.13_{stat} \pm 1.16_{syst}) \text{ eV}^2$  and  $\sin^2 2\theta = 0.36 \pm 0.12_{stat}$  [63]. The complete Monte-Carlo statistical analysis gives an ultimate significance of  $2.7\sigma$ . The results obtained by Neutrino-4, in tension with other experiments, were controversial. Analysis techniques were in particular questioned [64]. An additional complexity is that very SBL experiments were not originally aimed at testing the parameter space region at a large  $\Delta m_{41}^2$  value. It requires indeed both excellent energy resolution and a closer placement with respect to the nuclear reactor. Future experiments, including the updated Neutrino-4, will further investigate this result.

### 1.5.3 PROSPECT

A PRecision Oscillation and SPECTrum Experiment (PROSPECT) was designed to measure the reactor antineutrino flux modulation and energy spectra at the highly enriched High Flux Isotope Reactor (HFIR) at Oak Ridge National Laboratory. The reactor core consists of two cylindrical concentric rings of 93% enriched  $^{235}\text{U}$  with an outer diameter of 43.5 cm and a height of 50.8 cm operating at the nominal thermal power of 85  $\text{MW}_{th}$ . The PROSPECT inner-detector consists of four tons of pulse-shape discriminating (PSD) liquid scintillator loaded with  $^6\text{Li}$  (which aims at the capture of IBD neutrons). The scintillator is subdivided into 154 optically isolated segments  $14.5 \times 14.5 \times 117.6 \text{ cm}^3$ . To perform the oscillation analysis, the detector segments are further split to be assigned to one of ten defined baseline ranges between 6.7 and 9.2 metres. During 96 calendar days, more than 50000 IBD events have been recorded by the PROSPECT experiment. Although the reactor facility operated on the Earth's surface and in a high-background reactor facility environment, it was possible to achieve a signal-to-background ratio above 1. The values of the best-fit parameter are found at  $(\sin^2 2\theta_{14}, \Delta m^2) = (0.11, 1.78 \text{ eV}^2)$  [65]. However, the preference level is insignificant with respect to the no-oscillation hypothesis. Furthermore, the RAA best fit point was disfavored at the  $2.5\sigma$  significance level. Finally, PROSPECT was able to probe the 5 MeV bump and disfavored at the  $2.4\sigma$  confidence level the hypothesis that the  $^{235}\text{U}$  antineutrino is solely responsible for it. More and more reactor neutrino experiments are publishing the results. Thus, it is natural that joint-experiment analyses occur. Earlier this year, PROSPECT together with Daya Bay published [66] a joint paper, scrutinising  $^{235}\text{U}$  and  $^{239}\text{Pu}$  antineutrino spectra. Combining the data allowed the degeneracy between the dominant isotopes to be reduced and reduced the uncertainty of the spectral shape of  $^{235}\text{U}$  to approximately 3%. Furthermore, it was the first time that experimental data from low- and highly enriched uranium reactors were combined. The unfolded spectra are consistent between experiments, and the discrepancy from the HM model increased throughout the energy range with a maximum deviation of

4.2 $\sigma$  significance around the 5 MeV prompt energy region.

#### 1.5.4 STEREO

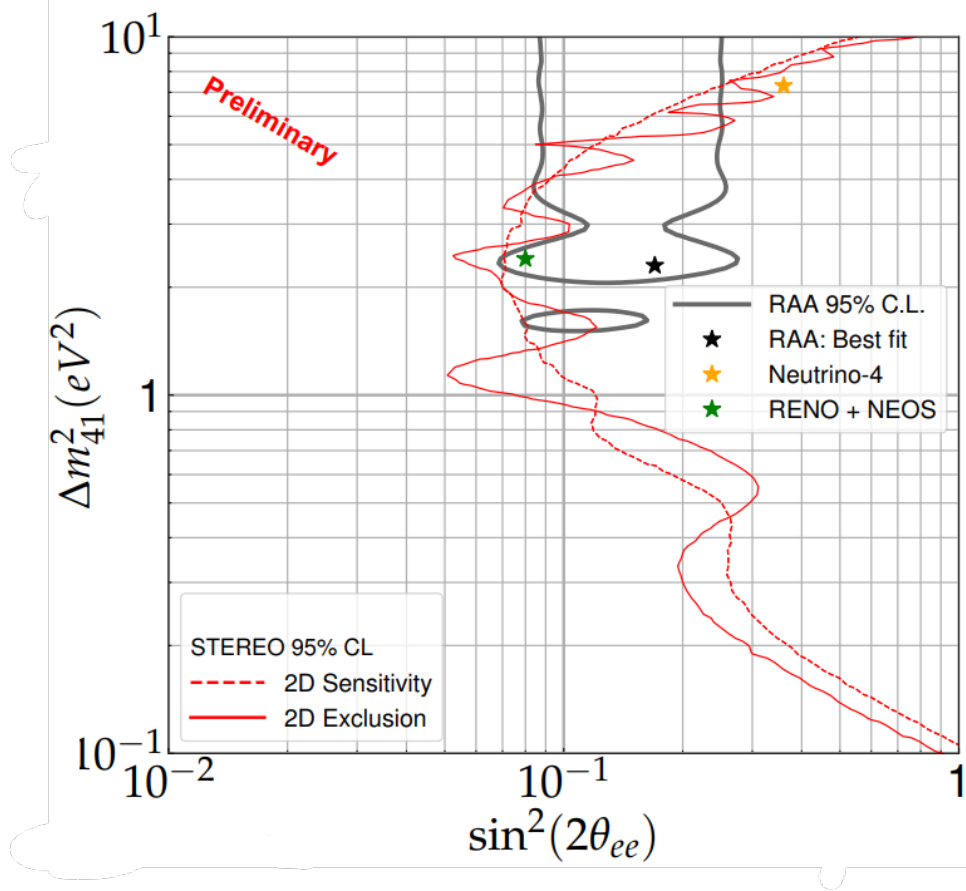


Figure 14: STEREO final sensitivity (dashed) and exclusion (solid) at the 95% C.L. sterile oscillation exclusion contours in red, with the RAA (reactor and gallium) allowed parameter space in grey and the excluded best fit parameter values from: Neutrino-4 in yellow (at 3.1 $\sigma$ ), RENO + NEOS in green (at 2.8 $\sigma$ ) and the global in black (at 4.0 $\sigma$ ). Extracted from [67].

The STEREO experiment is located in a historically significant place, where the reference beta spectrum was measured to predict the reactor antineutrino flux and spectrum - the Institut Laue Langevin in Grenoble, France. The research reactor provides a compact cylindrical fuel element with an external diameter of 40 cm and a height of 80 cm. The reactor is highly enriched (93%) in  $^{235}\text{U}$  fuel and has a nominal thermal power of 58.3 MW $_{th}$ . The STEREO experiment is able to measure reactor flux modulation at distances ranging from 9 to 11 m. The inner detector consists of an acrylic aquarium with dimensions  $L \times l \times h = 2.233 \text{ m} \times 0.889 \text{ m} \times 1.230 \text{ m}$ . It is longitudinally divided into six identical and optically independent volumes. The aquarium is also covered by a gamma catcher crown, which serves not only for the identification of the  $\gamma$  rays escaping from the aquarium, but also as an active veto against external background sources. In addition, the heavy passive shielding is composed to fulfil the same goal. The inner detector is filled with a liquid scintillator, capable of providing pulse shape discrimination, and doped with gadolinium to capture neutrons from IBD events. In the final results shown at ICHEP 2022 [67], the

STEREO collaboration claimed to exclude most of the parameter space allowed by RAA (RAA best fit at  $4.0\sigma$  significance, Neutrino-4 at  $3.1\sigma$  and NEOS+RENO at  $2.8\sigma$ ) and at the same time confirmed the deficit of 5% in reactor neutrino flux with respect to the model. As for the  $^{235}\text{U}$  antineutrino spectrum, STEREO provides its own unfolding and a joint analysis with the PROSPECT data. The latter finds an excess around the 5 MeV bump with a significance of  $2.4\sigma$  over the no-bump hypothesis.

## 1.6 Conclusion

In this chapter a brief history of experimental neutrino physics has been presented. Since their discovery (and even shortly before), these elusive particles have posed complicated questions for the physics community. Some of them were successfully fixed, but an extension of the SM is still required to account for, for example, the neutrino masses. The unresolved questions to date can be explained if additional sterile neutrino states exist. The very short baseline reactor experiments are one of the promising experimental approaches to address the sterile neutrino hypothesis. The SoLi $\partial$  experiment, which will be discussed in the following chapters, is one of this kind.

## 2 The SoLi $\partial$ experiment

A variety of neutrino-related anomalies were described in the Chapter 1. Their nature points towards further scrutiny of the oscillation behaviour of neutrino. This field is under intense scrutiny, and very short baseline reactor experiments were appearing globally over the past decade [68]. The precise measurement of the reactor antineutrino flux modulation at a very short distance is one of the cleanest ways to address the question of both the existence of the sterile state by putting the constraints on the parameter space in the low  $\Delta m^2$  region and the measurement of the antineutrino spectrum.

The Search for Oscillations with a  ${}^6\text{Li}$  detector (SoLi $\partial$ ) experiment belongs to this type. In this chapter, the experiment site, the detector design, and expected signal and background will be discussed. The following description is an executive summary of the full-scale detector referred to as Phase I. A more detailed overview can be found in [69].

### 2.1 The BR2 site

The first thing to decide while designing the very short baseline reactor experiment is the choice of construction site. As for the SoLi $\partial$  experiment, the Belgian Reactor 2 (BR2) was selected. The BR2 is a material testing reactor operated by the nuclear research center SCK • CEN in Mol, Belgium. Since its establishment in 1963, it has been among the most powerful and flexible research reactors in the world and enjoys an excellent international reputation. BR2 is widely known for the fuel R&D, production of the medical isotopes and neutron transmutation doped silicon [70]. This pressurised “tank-in-pool” reactor is moderated by its beryllium structure and water. Since the major overhaul, which has taken 1.5 years to complete in July 2016, the BR2 reactor operates in the 40-100 MW $_{th}$  power range with the nominal one of 65 MW $_{th}$ . It provides a neutron flux of up to  $10^{15}$  n/cm $^2$ /s which results in the intense antineutrino source of up to about  $2 \cdot 10^{19}$   $\bar{\nu}_e$ /s. The reactor is capable of operating with nominal power up to 210 days per year within cycles of up to four weeks (ON period). The ON periods are alternated with the maintenance periods of the same length (OFF period). The latter are employed for the calibration campaigns and scrutinising the background composition.

Beside that, the BR2 site provides many advantages. To begin with, it has a unique twisted design with inclined channels to obtain a compact core, which is represented in Figure 15. This means that both components of the  $\frac{L}{E}$  ratio are protected from large uncertainties, which is of utmost importance for oscillation analysis. Furthermore, it uses 93.5% enriched in fuel  ${}^{235}\text{U}$ , making the  ${}^{235}\text{U}$  isotope responsible for more than 99% of fission. Such a fuel composition greatly simplifies the prediction for the antineutrino spectrum. It allows a clean 5 MeV bump exploration given that it is not clear today whether it is one specific isotope causing the 5 MeV bump as it was discussed in the Chapter 1. Another advantage comes from the available position for the detector. The third level of the BR2 containment building is in direct line-of-sight of the nominal detector core. Construction allowed the baseline to be covered in the range of 6.3 - 8.9 m, where the oscillation behaviour with the  $\Delta m^2 = 1 \text{ eV}^2$  is the most pronounced. Last but not least, no other experiments are installed at the same level, while all neighbouring beam ports were shielded with the 20 cm thickness of lead. It creates an environment with a very low reactor-induced background together with moderate thermal power and properly shielded reactor irradiation (due to complete immersion in the water).

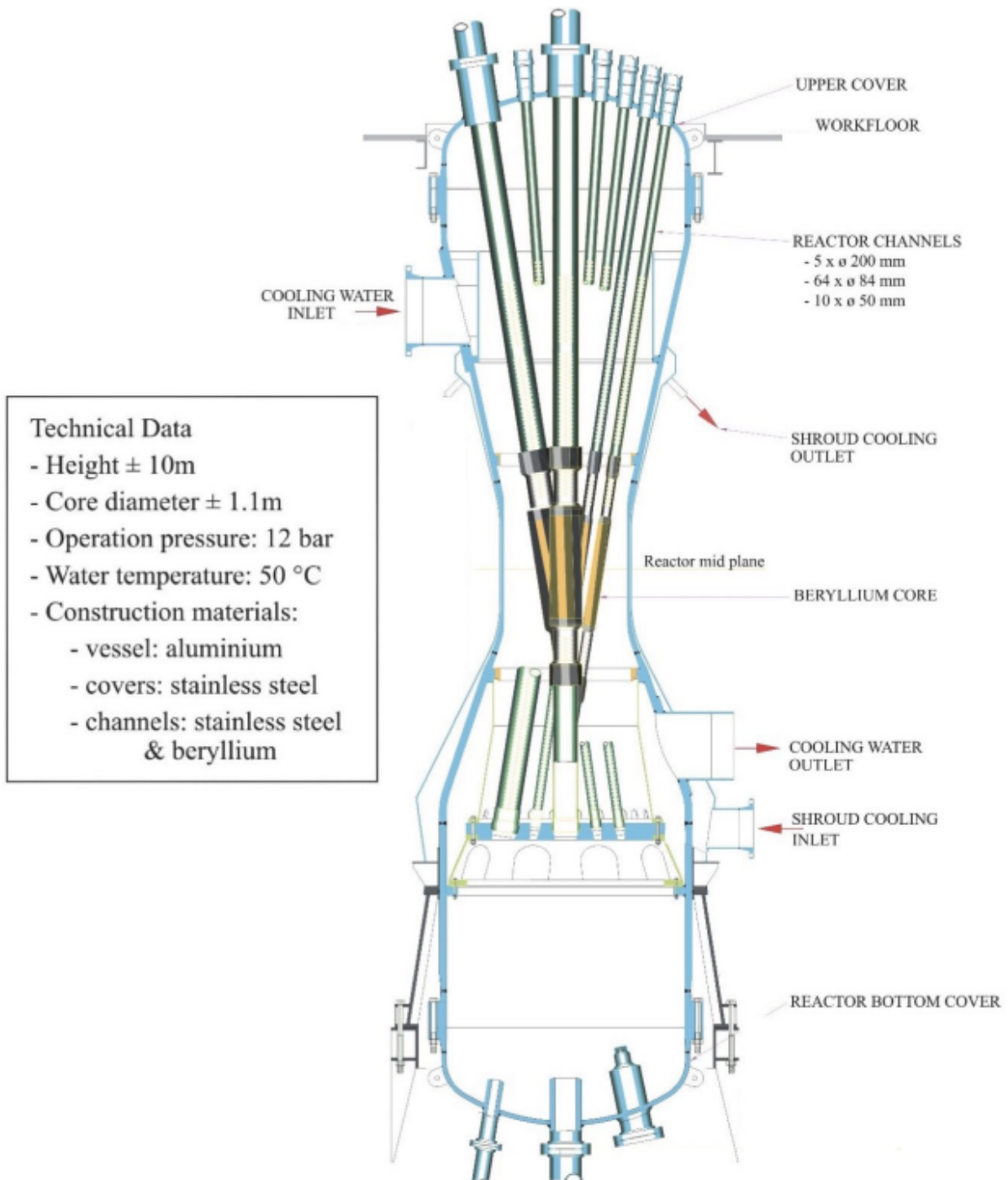


Figure 15: Twisted design and the technical data of the BR2 reactor core. It includes the beryllium matrix with hexagonal channels containing the nuclear fuel elements, control rods and the experimental channels. The core is confined in an aluminium vessel (blue) that is completely underwater (left). Picture of the upper cover of the reactor vessel (right).

However, since the BR2 is operating at the surface of the Earth, it is exposed to the atmospheric background. In that respect, the shielding comes from the 3 concrete floors and the steel roof of the building, corresponding to 8 meters-water-equivalent (m.w.e) and the reactor pool itself. Thus, it is up to the detector design to identify and reject the

atmospheric back. The geometry of the construction site and the positioning of the SoLi $\partial$  detector are sketched in Figure 16.

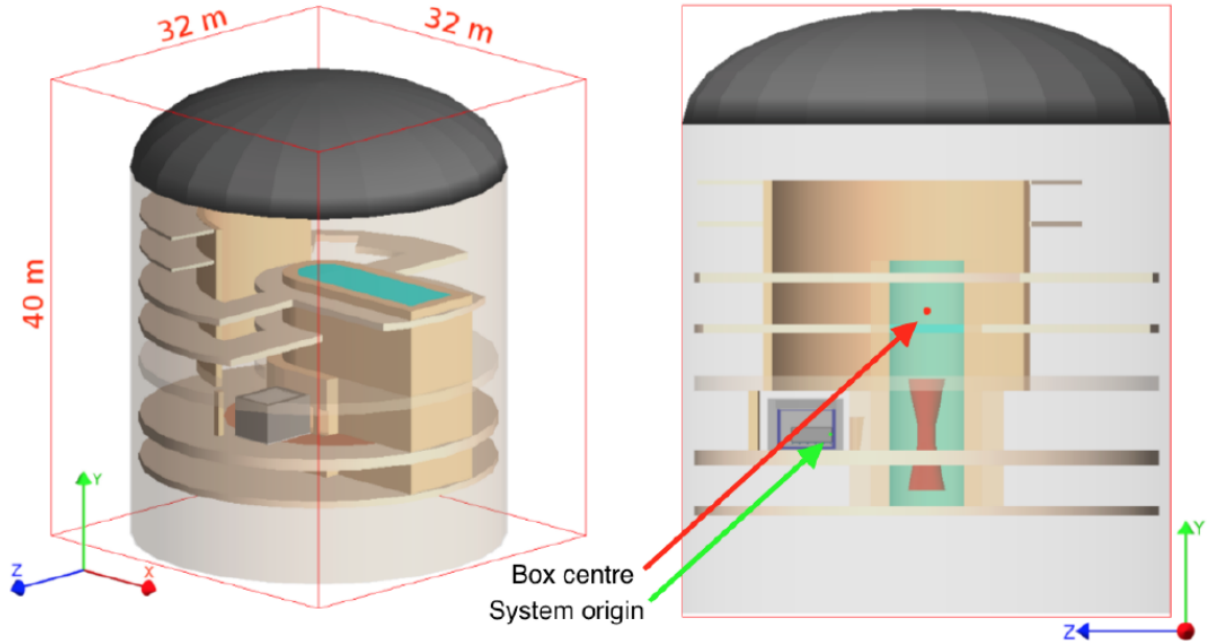


Figure 16: 3D representation of the BR2 site and positioning of the SoLi $\partial$  detector, which is based three Cartesian coordinates along perpendicular axes in a right-handed system. The Z-axis is perpendicular to the detector planes and point in the direction away from the reactor, Y-axis points upwards and X-axis points to the right side of the detector, when facing the reactor.

## 2.2 Detector design

The following subsection aims to describe the detector composition and design. It starts with the basic physical detection unit and goes up to full-scale detector geometry with the utility parts.

### 2.2.1 Detection cell

The basic detection cell in the SoLi $\partial$  detector consists of a 5 cm side polyvinyl toluene (PVT) cube. The PVT employed is of the type EJ-200 manufactured by ELJEN Technology [71]. The emitted scintillation photons are in the blue-violet wavelength band with a peak emission wavelength of 425 nm. The size of the cubes is motivated by the fact that a positron of 10 MeV travels no more than 48 mm in PVT. This size secures the energy contribution to a single cube for the majority of the IBD positrons. In addition, such a segmentation level makes it possible to distinguish the annihilation photons. The  ${}^6\text{LiF}:\text{ZnS}(\text{Ag})$  scintillator is produced by SCINTACOR in the form of thin screens with a peak emission wavelength of 450 nm, which is similar to PVT [72]. These screens are further cut into 5 cm size squares and placed, without glues or optical gels, on two adjacent faces of the PVT cube. The covered faces are the one along the Z- and X-axis, which are pointing from the reactor core and towards the electronic readout boxes, respectively. It

can be seen in more detail in Figure 17. Implementing such an asymmetric positioning increased the neutron capture efficiency by 30% with respect to the prototype detector. Another employed improvement was adding the 225  $\mu\text{m}$  thick MELINEX-339 reflecting backing to the neutron detection screens [73]. It resulted in a higher amplitude of the NS signal, which ensures better NS-ES waveform discrimination. Each detection unit is optically decoupled with a 270  $\mu\text{m}$  thick DuPont Tyvek wrapping of type 1082D to keep the scintillating light inside the cube where it was issued [74]. It decreased the impact of the neighbouring cubes; thus, the signal position and amount of the deposited energy can be determined more precisely.

Finally, each cell has 4 grooves machined in 4 different faces (two along the X and Y axes). These grooves have a square cross-section with a 5 mm side and made in order to accommodate the optical fibres, with a square cross-section of 3 mm side, that guides the scintillation light to an optical sensors at the edge of the detector.

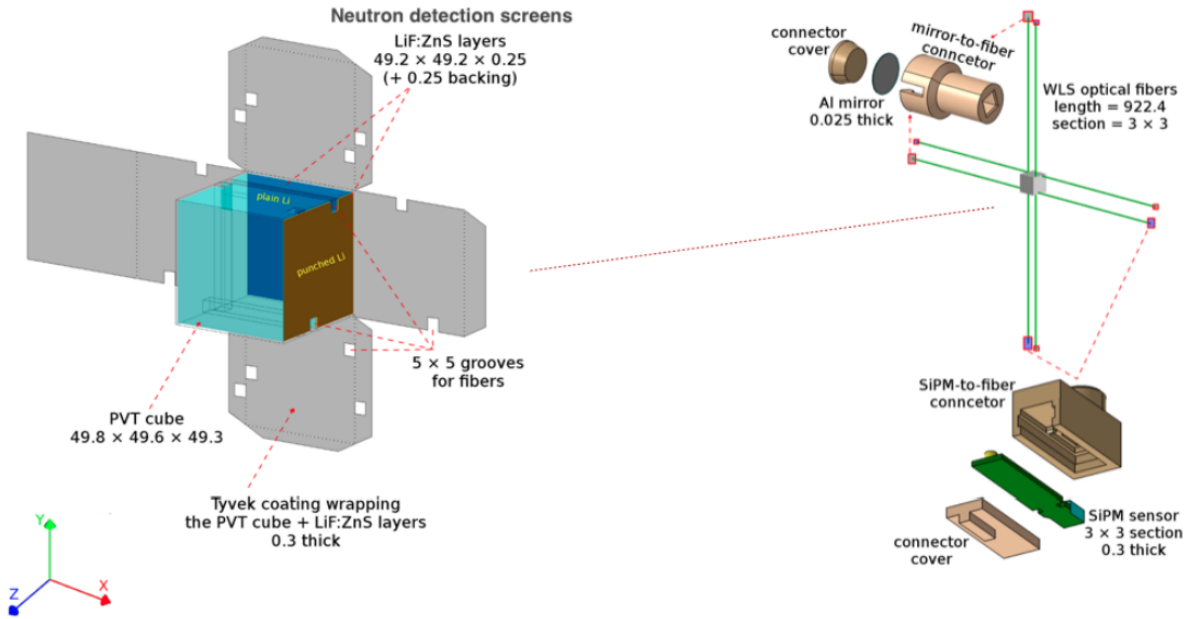


Figure 17: Sketch of the fundamental detection unit cell of the SoLi $\partial$  experiment. The PVT cube, with the positioning of the neutron detection screens, WLS fibre grooves and Tyvek wrapping (left). The coordinate system coincides with the one from Figure 16. The light transportation system consists of WLS fibres, 3D printed connection caps, Mylar mirror and MPPC (left).

## 2.2.2 Processing of the scintillation light

The readout of the scintillation light can be divided into two parts. First, it has to be transported to the edge of the detector. In the SoLi $\partial$  experiment it is done with the 92 cm long double clad BCF-91A wavelength shifting fibres (WLS) produced by Saint-Gobain [75]. One side of each WLS is covered with a Mylar foil with a reflective aluminium coating. It acts as a mirror to redirect the arrived light towards another side. The other side is coupled to a Hamamatsu type S12572-050P multipixel photon counter (MPPC) [76]. The positions of the mirrors and MPPCs alternate between the parallel fibres to mitigate the attenuation of light and ensure a more uniform detector response.

Since the detection cells are arranged in the detection planes of  $16 \times 16$  units each and there are two fibres per row and per column, the total number is 64 optical fibres per detection planes and an equivalent number of readout channels.

The selected WLS fibres shifts blue light to green with an emission peak wavelength of 494 nm, which corresponds to the region of the peak sensitivity of the MPPC used. For the MPPC, it has exactly the same cross-sectional surface as the WLS fibres. It is composed of a 3600-pixel matrix. Basically, each pixel is a p-n junction that can be activated by the arriving WLS photon and will result in a certain amount of electron generated, called a pixel avalanche (PA). Thus, the obtained readout is a quantised object corresponding to the integer number of PA triggered by the incoming photons. The amount of generated electrons and the photon detection probability are directly dependent on the operating voltage of the MPPC or, to be more specific, on the difference of the operating and the breakdown voltage of the p-n junction. This quantity is called the over voltage (OV). The increase of this difference provides larger photon detection efficiency but simultaneously increases the self-triggering rate from the thermal noise (dark count rate) and probability of the multiple pixels triggering from the secondary photons released during the avalanche (optical cross-talk). Both of the mentioned effects directly impact the energy resolution and , as such, have to be mitigated. These effects decrease with temperature and require the ability to monitor and control the environmental conditions at the experimental site. In the current state, the photon detection efficiency is 32%, a cross talk probability of 20% and a mean dark count rate of 110 kHz per channel. The digitised version of the MPPC readout is the raw input data from the detector, which is a fundamental piece of information for further analysis.

### 2.2.3 Plane and module design

The detection planes are made up of a matrix of  $16 \times 16$  of the detection units, resulting in a surface of  $0.8 \times 0.8 \text{ m}^2$ . Each plane is surrounded by two 46 mm thick high-density polyethylene (HDPE) sheets vertically and 46.8 mm horizontally. The HDPE sheets are used to increase the neutron detection efficiencies by acting as reflectors for the escaping ones, *e.g.* neutrons created at the edges of the detector. The first and last planes of the whole detector are also equipped with HDPE of 9 cm thick. The following layer is the structurally supporting frame of extruded aluminium. Each frame was chrome coated to act as a Faraday cage for the MPPCs and their wiring. The WLS fibres are capped with MPPCs and mirrors outside the HDPE and aluminium frames. The front-end electronics are self-contained in an aluminium encasing mounted on one side of each detection plane. The final layer of the detection plane is composed of two square Tyvek sheets on each of the light sensitive side to provide even better optical decoupling of the adjacent place. These construction features will have an interesting implication on the calibration procedure. Ten detection planes, with all the components discussed above, constitute a detector module. Each module is mounted on the movable platform and has independent power supply and trigger electronics. Thus, such a separate module is capable of operating as a standalone detector which can be further employed in the oscillation analysis strategy. In the current state, the SoLi $\theta$  detector consists of 5 detection modules, which result in 50 planes and 12800 PVT cubes with a fiducial mass of 1.6 ton. The composition of the detection plane and module is summarised in Figure 18.

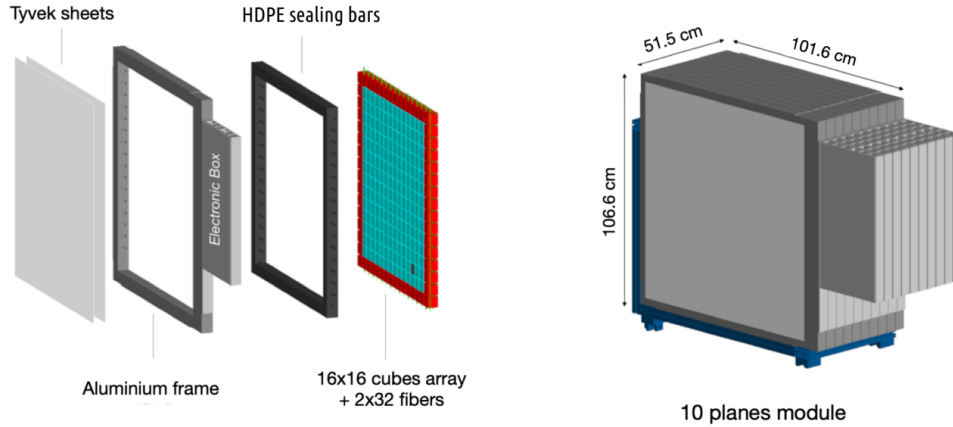


Figure 18: The composition of the detection plane (left) and detection module (right).

#### 2.2.4 Detector container

The SoLi $\vartheta$  detector is placed inside a cooled cargo container. It covers several objectives. The container has to provide protection from the atmospheric and cosmic background. Its size was maximised with respect to the cost, available space, and floor load versus suppression of the cosmic neutrons. The top of the container is shielded with a 50 cm PE layer made of the 2.5 cm thick PE slabs. The four sides of the container are further surrounded with a 50 cm thick water wall. It decreases the cosmic neutron flux by one order of magnitude and converts a small amount of them into slow neutrons. The latter captured with the 2 mm thick cadmium sheets, which are sandwiched between the passive shielding and the container housing. The cadmium sheets have a neutron capture efficiency of 88% and are constructed so that they result in 45% coverage of the experiment surface. Another important objective of the container is to secure the comfort environment for the detector. As such, the container was custom-made for thermal insulation and feed through of cooling lines. This allows one to keep the operating temperature at a fixed value of 11 degrees Celsius. It is continuously monitored with a precision of 0.2 degrees. In addition, the container is permanently flushed with dry air at a flow rate of 5 m<sup>3</sup> per hour. It secures the relative humidity at an acceptable level and removes the possible traces of the radon gas inside the detector. The concentration of airborne radon is monitored by the detector based on the RADONLITE and RADONPIX technology, developed at CERN [77]. Moreover, a PMT coupled with a NaI scintillator is located next to the radon detector to monitor the gamma background. As such, environmental characteristics are constantly monitored. Despite the ensuring the proper operating conditions, they can also be helpful for background explorations, *e.g.* correlation of the pressure with the rate of the atmospheric background. Monitoring is performed inside and outside the container with Raspberry-Pi devices. They are connected to the experiment readout. In addition, the BR2 building has its own monitoring sensors. Their observations are registered in the BR2 Integrated Data Acquisition System for Surveys and Experiments (BIDASSE) and used as a cross-check of the data received from inside the container.

### 2.2.5 CROSS calibration system

The last important component to be described within the detector container is the calibration robot mounted on top of the SoLi $\partial$  detector. As mentioned previously, each detector module is installed on a movable platform, which in turn is connected to a linear actuator. This actuator moves the module in the range of few centimetres and thus creates a place to insert a small radioactive source for calibration. For that purpose, a robot is equipped with a radioactive calibration source holder. It uses three capacitive sensors to control the longitudinal positioning of the robot, and a capacitive sensor to measure the distance between the modules in order to secure the proper positioning of the source. All measurements are done by detecting aluminium reference pins with stainless steel screws on the top located on the top of each module. Once CROSS (which stands for CalibRation On Site Solid) is properly positioned within the modules, it is capable to further move the source in the X- and Y-axis directions to increase the coverage of the detection cells. In total, there are six calibration air gaps between modules with nine different available source positions in each plane.

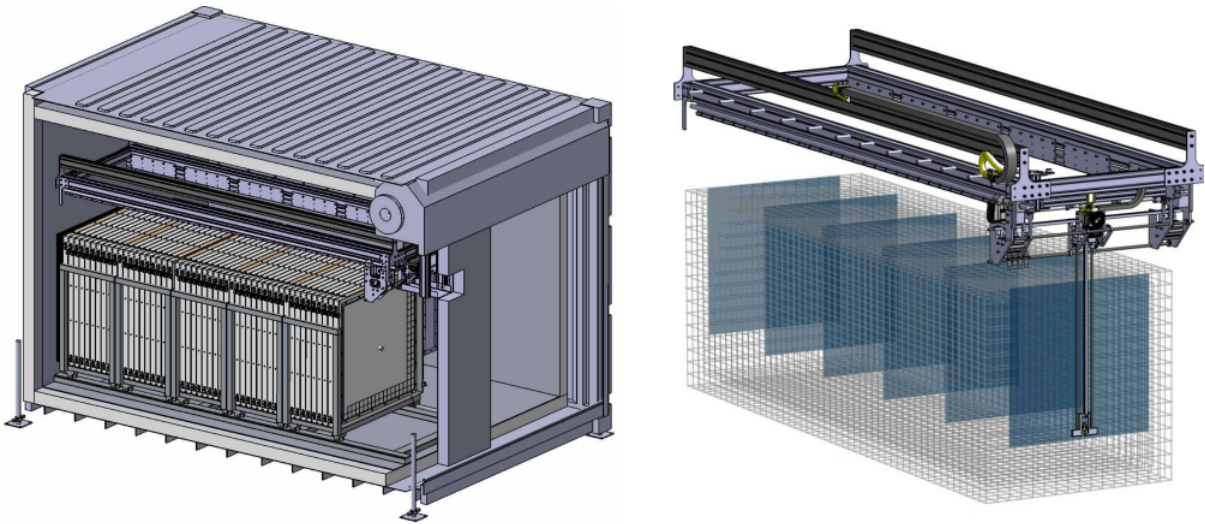
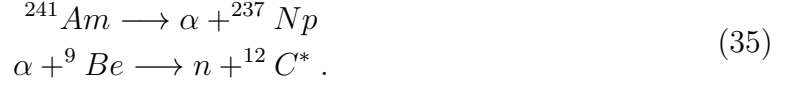


Figure 19: The 3D simulation of the CROSS calibration system geometry, showing the rail system, which provides the access to the whole detector surface (left) and the radioactive source holder placed in one of the six calibration air gaps, indicated in dark blue squares (right).

Both neutron and electromagnetic calibrations can be performed with CROSS. However, such a system created certain constraints on the sources that can be employed. For example, the source has to be penetrating enough to reach the detection cell units at least within 5 planes, since CROSS can be placed only in front and at the back of a module. The consequences for electromagnetic calibration together with the available sources and calibration techniques are covered in Chapter 4, while neutron calibration is outside the scope of this thesis. However, it cannot be completely ignored since the amount of IBD disclosed by the detector is directly dependent on the neutron detection efficiency. This efficiency is composed of two numbers, neutron reconstruction efficiency and capture efficiency. The latter one is determined to be 74% based on the Geant4 [78] simulation, while determination of the first value is the main objective of the neutron calibration. It was performed with  $^{252}\text{Cf}$  and americium-beryllium (AmBe) sources. The

first one produces on average 3.8 neutrons per spontaneous fission, while the second is the  $\alpha$  - neutron emitter, which works through the sequence:



The results of the calibration for both sources are in agreement and can be seen (together with the associated uncertainty) in Figure 20. The average detector value was estimated to be 71%. Provides an average neutron detection efficiency at the level of 52% when it is associated with the detection reconstruction efficiency. A more detailed and comprehensive description of the neutron calibration procedure can be found in the PhD thesis of Valentin Pestel [79].

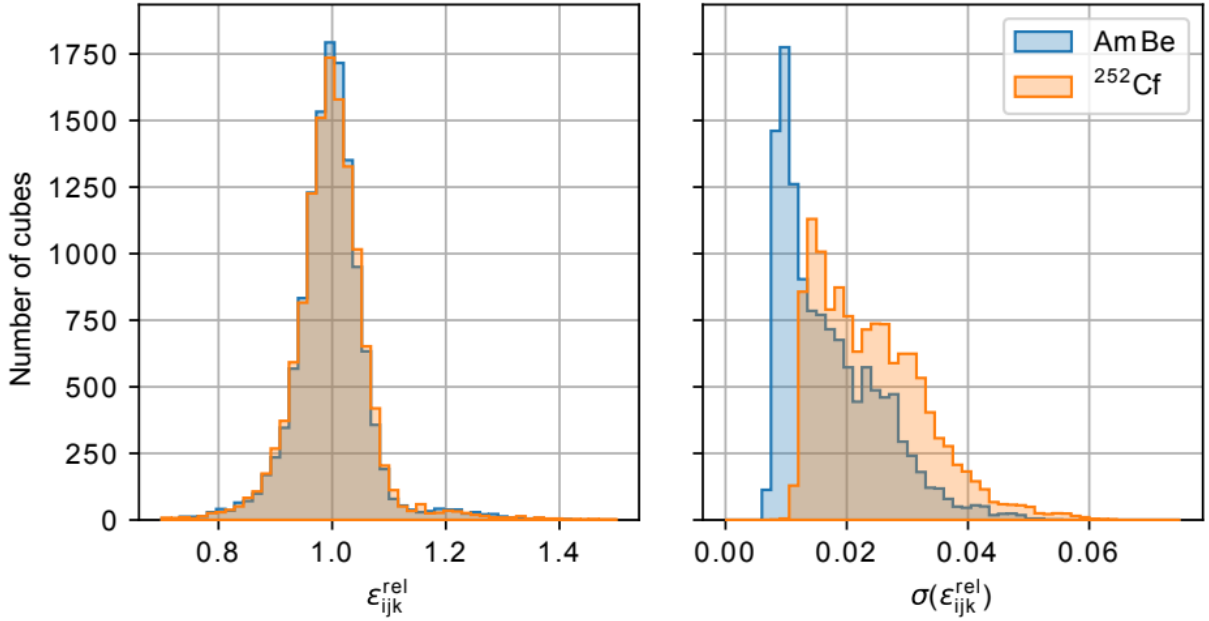


Figure 20: The results of the neutron reconstruction efficiency determination out of the neutron calibration procedure. The calibration is performed per each detection cell with two different neutron sources: Californium and Americium-Beryllium. The relative neutron capture efficiency (left) and its attached uncertainty (right) are in agreement in both cases.

### 2.2.6 DAQ system

The readout in the SoLi $\partial$  experiment is a custom-made system based on analogue / digital front-end electronics and Field-Programmable Gate Array (FPGA) chips. Such an approach optimised mechanical flexibility, compactness, and low power consumption at a low cost. The design of the readout system is similar to the composition of the detection volume *i.e.*, it operates on the same plane, module, and full detector levels. At the plane level, the aluminium frame accommodates the connections between WLS fibres and MPPCs. Then, an aluminium enclosure allows the MPPC connection to the remaining electronics. The next level is employed as an intermediate step to group the ten planes both mechanically and electronically. On top of each module, the so-called “service

box” is installed. It contains a clock-board that synchronises the ten planes, a DC-DC converter to power the module, and a fan system. A set of fans is installed between them and the service boxes. They push the air downward through the opening to keep the enclosures cool. The heat exchanger is installed below the enclosure to remove the heat generated and keep the temperature constant throughout the container. At the last level, all five service boxes are connected to the sixth one placed at the back of the container. A dedicated clock-board is used to synchronise the whole detector while running in the physics mode. The design discussed for the readout at the plane and module level is represented in Figure 21.

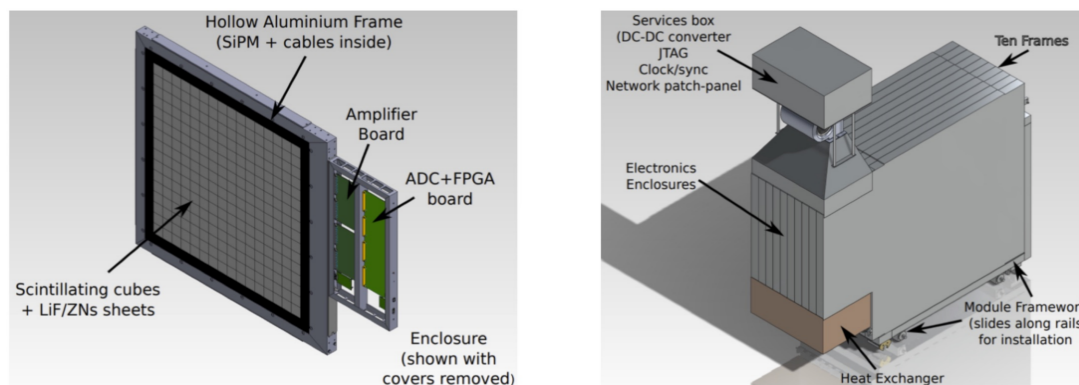


Figure 21: The readout system composition on the different levels: (left) the plane level consists of aluminium frames, MPPCs and enclosure with the front-end electronics inside and (right) module level consists of 10 planes, service box and the heat exchanger.

The front-end electronics of the single plane consists of two 32-channel analogue boards, a 64-channel digital board, a power distribution system and an environmental sensor reading module. The two analogue boards allow one to shape and amplify the analogue signal coming from the 64 MPPCs while providing the power supplies. The latter is performed in two steps. At first, a bias voltage of 70 V is supplied to all the channels called the High Voltage (HV). Then each channel has an individual trim voltage ranging from 0 to 4 V, called Low Voltage (LV). LV tuning is mandatory due to the spread in breakdown voltages between the different MPPCs. As was discussed above, the OV value is a crucial parameter for MPPC performance. Its optimisation can be performed using two different scan procedures. The first one maintains the same HV and modify LV, while the second one proceeds vice versa. The obtained results are used to individually tune the LV to equalise the MPPC gain. It is defined as the amount of charge carriers produced by the MPPC for a single photon. The pedestal value can be measured during the same calibration procedure. Characterises the number of counts in the absence of any signal. It varies by analogue board. The pedestals are used in the definition of the trigger thresholds and by the reconstruction software. These measurements are part of the MPPC equalisation procedure. They are performed several times a year to ensure the stability of the detector performance.

The two analogue boards are connected to the digital board. It digitises the signal and performs the online triggering. The digital boards use 8-channel 14-bit analogue to digital converters (ADCs) with an operating rate of 40 MHz (25 ns). The unit of the digital sample is called an ADC count. All in all, an energy deposit in the SoLi $\vartheta$  detector (in

MeV) is converted to PA by the MPPC and eventually digitised to an ADC count value. Therefore, one of the targets of the reconstruction procedure is to ensure the reverse transformation. The digitised output is then transferred to the FPGA, where the samples are composed in blocks of 256 (6.4  $\mu$ s). Commonly, the blocks consist only of random oscillating values around the pedestal level and MPPC noise. The dedicated triggering system was designed to ensure the readout of signals that contain useful information. It operates on a block-per-block basis. It is not solely the question of selecting waveforms suitable for the analysis, but the storage space. The final reduction factor for the triggers applied in the physics run is around 10,000, which results in 20 MB/s or 1.7 TB/day. The first step for any trigger is the application of a zero-suppression (ZS) algorithm. It is aimed at removing the wiggles around the pedestal and the dark count noise. For example, a ZS cut at 0.5 PA reduces the number of waveforms by factor 50. The zero-suppressed samples are further transferred to the window buffer. It contains 1536 of samples at maximum. The analog boards have to be periodically re-synchronized. Its occurs every 8 minutes for the normal data-taking conditions. Finally, the blocks are transferred to the derandomiser by the channel readout. This step also allows the records for the channels forbidden by the trigger to be discarded. The data which passed all the stages are grouped by the main readout buffer.

The last missing puzzle of the information is the actual trigger settings, which includes available channels (*e.g.* amount of planes around the trigger to read out) and timing characteristics (*e.g.* number of blocks to read out/skip before/after the trigger). There are three main trigger strategies in the SoLi $\partial$  experiment:

- **Periodic trigger.** This trigger is aimed at collecting the unbiased data. It is used for MPPC and noise stability monitoring, as well as for low-energy calibration, to avoid any threshold effects. The entire detector is read out without ZS at a constant trigger rate for a time window of 2 blocks/512 samples/12.8 $\mu$ s. The default trigger rate of 1.2 Hz results in a data rate of 3.9 MB/s.
- **Threshold trigger.** This trigger is also aimed at the background and detector stability explorations, but from the different angles of high-amplitude ES signals such as muons. As such, the ZS threshold is set at 1.5 PA and it requires a horizontal-vertical channel coincidence within 1 sample. Both channels have to be above an adjustable threshold (usual: 50 PA per channel or typical 2 MeV in total). If the trigger condition is met, the whole plane is read out for a time window of 1 block. The typical trigger rate during the reactor ON periods is 2.1 kHz, which results in a data rate of 2 MB/s.
- **Neutron trigger.** This is the most important trigger for the SoLi $\partial$  experiment physics runs. It is impossible to trigger on each ES due to the large rate and hence the large data rate and the ZS thresholds must keep the readout of the annihilation gamma caused waveforms. Thus, the only way to proceed is to tune the trigger for the detection of the NS signal. The dedicated algorithm based on the calculations of the peaks over a threshold (PoT) within one block was developed. The optimised values obtained for the ZS of 0.5 PA is 17 PoT [80]. All the discussed numbers were tuned to maximise the neutron trigger efficiency. The poor purity of this trigger (20%) is caused by muons. The dedicated offline analysis allows the purity to increase to 99%. It is discussed in more detail in Chapter 3.1.2. For each NS

trigger, three planes are read out on either side for an asymmetrical time window of -80 blocks ( $512 \mu\text{s}$ ) and +30 blocks ( $192 \mu\text{s}$ ). The large negative part ensures that all the ES information is included, while the positive one can be used as a proxy for the accidental background level. The final trigger rate of 80 Hz results in the data rate of 15 MB/s.

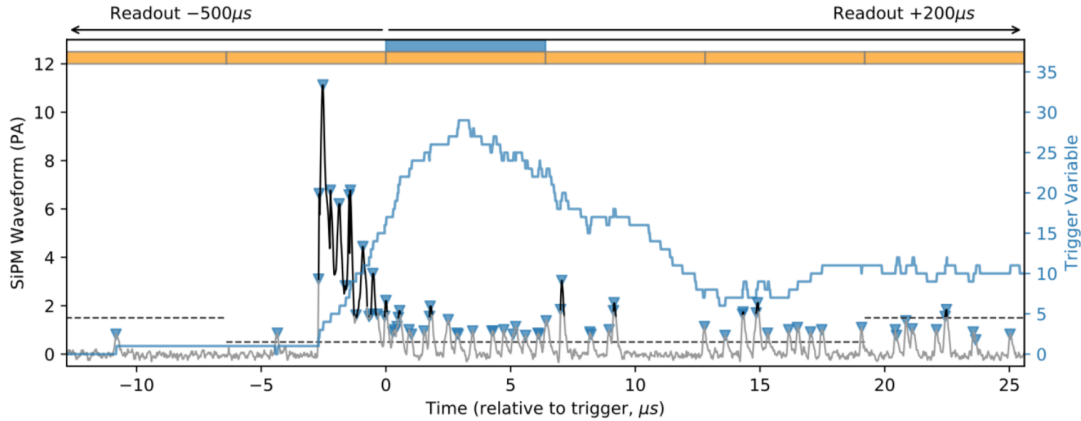


Figure 22: An example of the neutron trigger application. The NS waveform is in solid grey. The dashed black line represents the ZS of 1.5 PA for the regular data taking, which is lowered to 0.5 PA for the neutron signal. The blue triangles indicate the PoT, corresponding to the different de-excitation times for the excited states in the ZnS crystal. The solid blue line shows the amount of PoT within the time window of 1 block. The blue block at the top indicates the occurrence of the neutron trigger, resulting in the readout for the asymmetrical time window of -80 blocks and +30 blocks.

## 2.3 Detection principle

When it comes to detecting the electron antineutrino from the nuclear reactor, there was no better method set than the one used for an actual discovery by Cowan and Reines:

$$\bar{\nu}_e + p \longrightarrow e^+ + n . \quad (36)$$

In order to increase the probability of the interaction, the detector must contain a proton-rich target. Afterwards, the IBD provides two sources of signal, which need to be accurately tracked. The positron typically loses all of its energy within a few nanoseconds and subsequently annihilates with an electron, creating two back-to-back annihilation gamma photons of 511 keV each. The typical free path of such a photon in an environment with a density around  $1 \text{ g/cm}^3$  is 10 cm. The ability to identify the positron signal and the two annihilation photons determines the size of the unit element of the detector. Subsequent segmentation allows one to distinguish the signal from the backgrounds. On the other hand, the neutral neutron thermalises through the elastic collisions and can be captured by the nuclei with the dedicated high cross section. Such that, the neutron component of the signal is delayed. This feature allows the time-coincidence technique to be employed, once both of the signals are detected. The neutron moderation time is tunable via the choice of the capture element.

Commonly, the combination of the liquid scintillator (for positron) with gadolinium (for neutron) is used for the detection of IBD products. However, in the SoLi $\partial$  experiment, it was decided to use a novel approach based on the combination of the two scintillators. The PVT is used as the proton-enriched antineutrino target. It is also capable of detecting annihilation gammas. PVT is a relatively cheap plastic scintillator, easy to produce in the desired geometrical shape. As such, any reasonable level of segmentation can be achieved. It was also chosen due to the good light yield (10 000 emitted photons per MeV on average), the linear response over the wide range of energies from hundreds of keV to several MeV, and a long optical attenuation length of about 380 cm [71].

As for the antineutrino energy, the following estimator can be constrained:

$$\begin{aligned} E_\nu + E_p + m_p &= m_{e^+} + m_{e^+} + E_n + m_n \\ E_\nu &= E_{e^+} + m_{e^+} + m_n - m_p = E_{e^+} + 1.807 \text{ MeV} , \end{aligned} \quad (37)$$

in which the antineutrino mass,  $E_p$  and  $E_n$  were neglected. The latter is justified by the typical neutron energies involved in the IBD process, which are on average 10 keV and do not go higher than 50 keV. Since the selected neutrino energies considered in this document are above 3 MeV this sub-percent correction is safely absorbed within resolution effects. At the same time, it is possible to see already at this stage that the presence of the annihilation gammas will require modification of the estimator. The neutron is detected with the combination of the inorganic ZnS(Ag) scintillator and the  $^6\text{LiF}$  screens via reaction:



The high neutron capture cross section of the  $^6\text{LiF}$  screens ensures that only a small amount of neutrons are captured on hydrogen (936 barns versus 0.33). While tritium and  $\alpha$  particle are creating the subsequent scintillation signal in the ZnS(Ag). Both particles are highly ionising and hence cause many excited states in the ZnS crystal. Each state has an individual de-excitation time, which is averaged to 80  $\mu\text{s}$ . That results in a much longer signal compared to the one provided by the PVT. It has several peaks that match the dedicated excited state in time. Such a shape difference secures easy distinguishing between PVT and ZnS signals, but requires a specific triggering algorithm for the latter. The final neutron capture efficiency and moderation time depend on the number of capture screens. It was exhaustively studied during the SoLi $\partial$  prototype era. The current setup includes 2 neutron screens. This layout leads to a neutron capture efficiency of 74% and a moderation time of 65  $\mu\text{s}$  [69].

The detection principle is summarised in Figure 23. Due to the nature of the signal appearing in the dedicated scintillator, the component detected in the PVT is further denoted as ES (electromagnetic signal) and NS (nuclear signal) for  $^6\text{LiF}:\text{ZnS}(\text{Ag})$ .

## 2.4 Expected signal and background

Any event which is capable of reproducing the time-correlated NS and ES signature is considered an IBD candidate. IBD caused by the reactor antineutrino itself is an obvious candidate to meet the requirement. The prediction of the signal is the combination of the reactor input, *i.e.* antineutrino flux rate and the energy spectrum, with the detector features such as neutron detection efficiency, geometrical acceptance, etc. It provides an

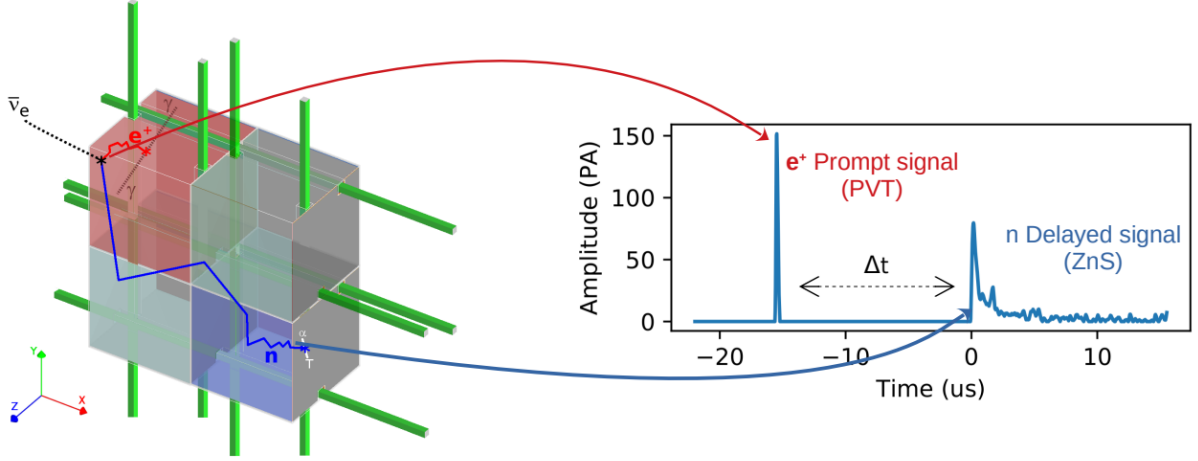


Figure 23: The left graphic summarizes the IBD detection principle of the SoLi $\theta$  detector. The electromagnetic part of the signal triggered in the PVT cube by positron and annihilation gammas represented in red. The NS signal triggered in the  ${}^6\text{LiF}:\text{ZnS}(\text{Ag})$  in blue. The right plot indicates the pulse-shape difference of NS and ES and their correlation in time.

estimation of the IBD events rate expected to appear in the detector per day. However, several sources of background can also mimic the signature. They can be categorised as correlated and accidental. The most common of them are further discussed in this subsection.

#### 2.4.1 IBD predictions

In the SoLi $\theta$  experiment, antineutrino flux modelling relies on the detailed simulation of the BR2 reaction core, HM conversion method and the summation method to mitigate the off-equilibrium effects coming from the long-lived fission products. The conversion method used as input the reference ILL  $\beta$  spectrum and the fission rate predictions extracted from the Monte Carlo n-code extended (MCNPX) [81] 3D model of the reactor core coupled to the MCNPX/CINDER90 evolution code [82]. The MCNP Utility for Reactor Evolution (MURE) is used to deal with the burning of nuclear fuel during the reactor ON cycle [83]. The missing piece is the IBD cross-section which can be calculated via [84]:

$$\sigma_{IBD} = \kappa \times E_{e^+} \times p_{e^+} , \quad (39)$$

where prefactor  $\kappa$  can be calculated using either of the two options:

$$\kappa = \frac{G_F^2 |V_{ud}|^2}{\pi} (1 + \Delta^R) (f^2 + 3g^2) \quad (40)$$

$$\kappa = \frac{2\pi^2}{m_e^5 f^R \tau_n} ,$$

where the first includes the Fermi coupling  $G_F^2$  and the mixing parameter  $V_{ud}$  of the Cabibbo-Kobayashi-Maskawa (CKM) matrix,  $\Delta^R$  responsible for the inner radiative corrections and  $f$  and  $g$  are, respectively, the vector and axial-vector coupling constants. While the second one contains positron mass  $m_e$ , a phase space factor  $f^R$  that includes all the relevant corrections, but the inner radiative corrections  $\Delta^R$  and finally the neutron

lifetime  $\tau_n$ . There is a slight tension between the  $\kappa$  values obtained by two different methods. It is a well-known issue that shall be cleaned out by future neutron experiments. However, with a ballpark value of  $\kappa = 0.9610^{-43}\text{cm}^2\text{MeV}^{-2}$  the expected energy spectrum is sketched in Figure 24. Its combination with geometrical acceptance gives an estimate of the expected daily IBD yield in the detector. Acceptance is defined as a fraction. The total number of antineutrinos produced by the reactor serves as a denominator. The number of antineutrino, which has interacted with the detector, acts as the nominator, respectively. Both values are obtained from the Geant4 simulation. Acceptance is evaluated as 0.11% in the SoLi $\partial$  experiment. Therefore, it is unreasonable to generate the antineutrinos isotropically for simulation studies. In order to save computational cost, only the events where the neutrino interaction has indeed taken place in the detector are kept for further simulation processing. Finally, one obtains around 1200 events per day [85], which are reducing to 600 once taking into account the neutron trigger efficiency.

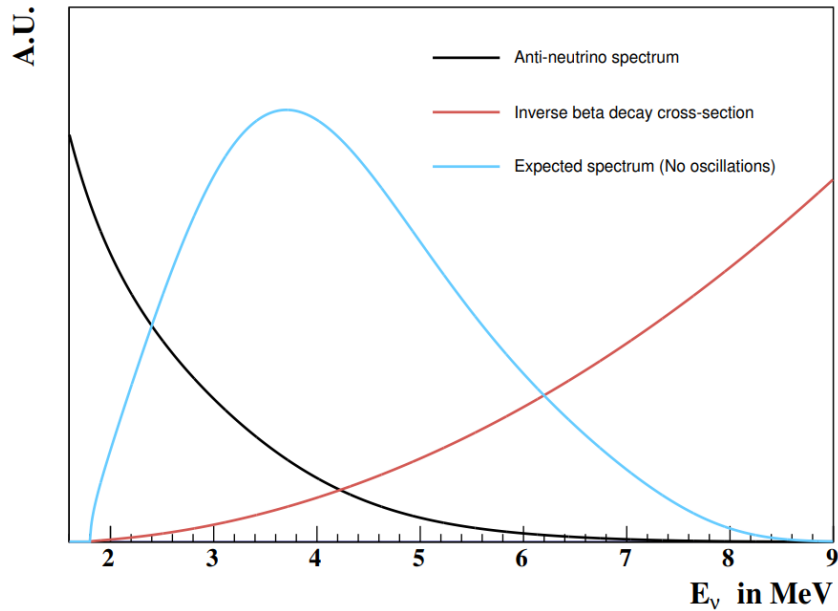


Figure 24: An illustration of the expected antineutrino spectrum (blue) obtained from combining the emitted reactor antineutrino spectrum (black) with the IBD cross-section (red).

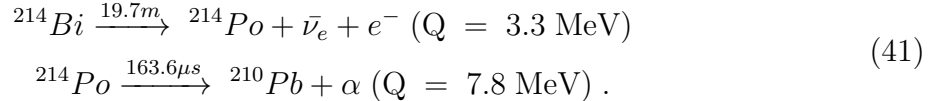
### 2.4.2 Atmospherics

The cosmic induced background was already mentioned in this chapter due to the location of the SoLi $\partial$  experiment on the surface of the earth and the poor protection (less than 10 m.w.e) provided by the construction site. This type of background has two different mechanisms to mimic the IBD signature in the detector. The first one directly involves neutrons that originated from cosmic rays that can penetrate the detector. Unlike the low-energy neutrons issued in the IBD, cosmic neutrons are capable of creating relatively high-energetic proton recoils. The SoLi $\partial$  detector does not possess the feature of distinguishing proton recoils from photons. Thus, the recoils will mimic the ES part of the signal, while the thermalised cosmic neutron, captured by the  $^6\text{LiF}$  screen, completes the signal signature. The fact that the neutron moderation time is exactly the same as in

the IBD event makes this background even more toxic. However, it is mitigated by the detector container design. The second mechanism employs other particles from the cosmic rays: muons. By interacting with the materials of the construction site in the vicinity of the detector or even the container itself, they can create spallation neutrons. Then, they can further undergo the same sequence discussed above. In addition, muons can leave the ES contributions directly in the detector. They can either contribute to the same ES cluster or create an additional one by a possible misidentification or by interacting just in the few cubes at the border of the detector. In both cases, they most likely fall into the accidental background category.

### 2.4.3 Natural radiation

The natural radioactivity of the detector and the construction site materials is an additional source of the correlated background. Long-lived isotopes with long decay chains such as  $^{238}\text{U}$  and  $^{232}\text{Th}$  are the most toxic ones. The NS contribution consists of the interaction of  $\alpha$  and tritium in ZnS. Therefore, the  $\alpha$  decay is able to mimic it. As discussed above, the SoLi $\partial$  detector is not capable of distinguishing the source of the ES, hence, any kind of the  $\beta$  decay mimics it. Thus, any radioactive source that has subsequent  $\alpha$  and  $\beta$  decays in the chain and its end-point energy comparable with the IBD positron energy regime within the reasonable half-life time (which is in the same ballpark as neutron moderation time) is a source of the correlated background. Fortunately, there are not that many candidates. One of the examples is the bismuth-polonium (BiPo) cascade. It is part of the  $^{238}\text{U}$  decay chain and can appear from the  $^{222}\text{Rn}$  emission from the concrete in the vicinity of the detector. Unluckily, the neutron detection screens were contaminated with elements from the same chain during production. Thus, this particular cascade is discussed further in more detail. The decay chain of the  $^{238}\text{U}$  presented in Figure 25. The undergoing sequence is the following:



The end-point energy of the primary  $\beta$  decay is in the left part of the IBD induced positron spectrum. The subsequent  $\alpha$  decay half-life time is  $163.6 \mu\text{s}$  which results in a time decay constant of around  $235 \mu\text{s}$ . Thus, the significant part of BiPo events matches the time window of interest defined by the neutron moderation time. However, the events with the larger correlation time provide a relatively pure region for further explorations of possible suppression of the background. In addition, the difference in the Q energy of the reaction (4.8 MeV for neutron capture in the  $^6\text{LiF}$  screens versus 7.8 MeV from the BiPo  $\alpha$  decay) provides a possibility to distinguish two types of events by reviewing the waveforms of candidates for NS. The pulse shape discriminating algorithm is continuously being developed within the collaboration. The first version, called ‘‘BiPonisher’’, was based on the fraction computation of the waveform integrals in the short and long time windows. An updated version relied on the convolution neural network (CNN) is predestined to provide the ultimate discrimination between the two types of signal on the neutron detection screens. It is called the ‘‘BiPonator’’ and is discussed in more detail in the dedicated Chapter 3.1.3.

Finally, additional radioactive isotopes are created via the interaction of cosmic-induced

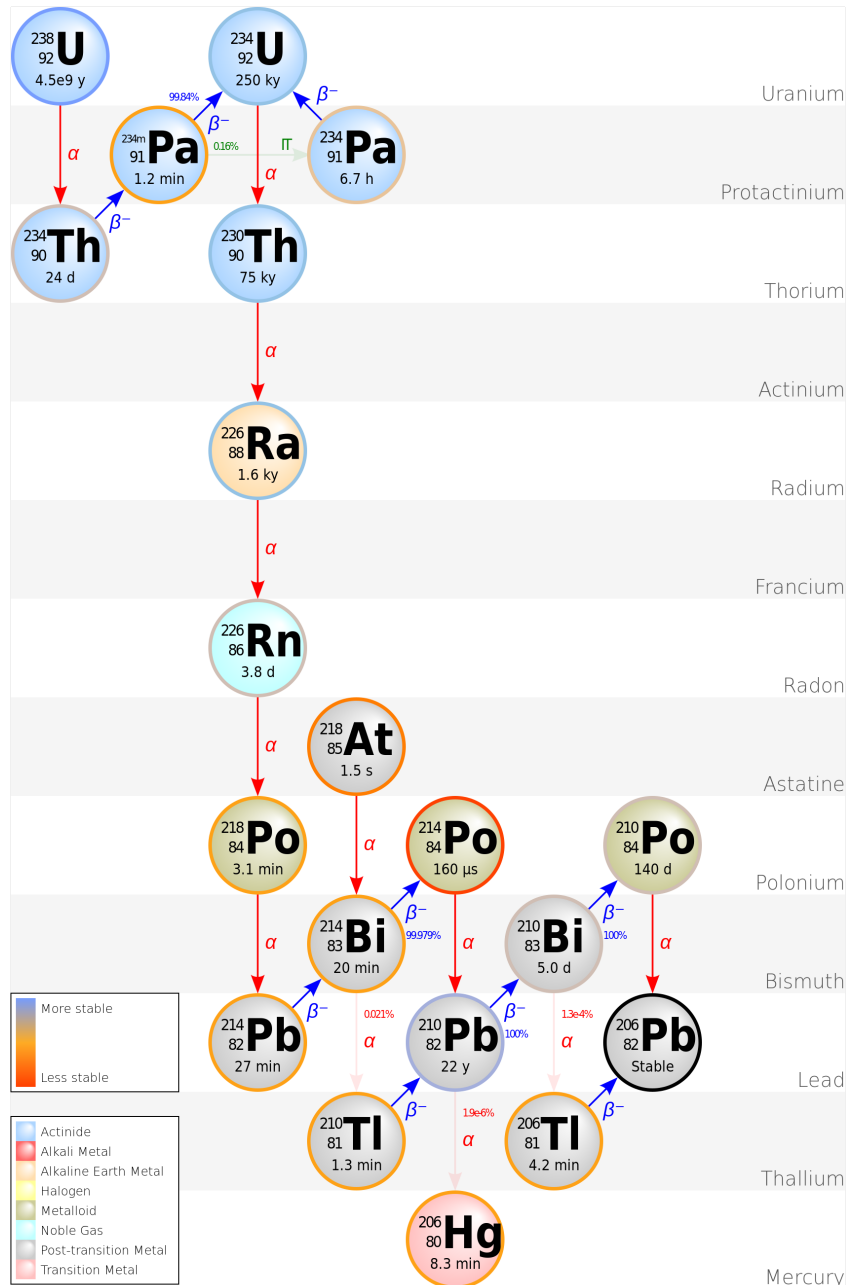


Figure 25: The decay chain of the  $^{238}\text{U}$ .

particles (both muons and neutrons) with the detector materials (mostly  $^{12}\text{C}$ ). The selected sample of this type of background provides an extremely well-established candle to evaluate the detector performance. An example of the use of the  $^{12}\text{B}$  sample for that purpose is presented in Chapter 4.3.1. The list of the isotopes created in the KamLAND experiments is presented in Figure 26.

#### 2.4.4 Accidentals

The accidental background emerges from the random coincidences of the NS and ES. The possible sources of the NS candidates were exhaustively discussed above, including

	Lifetime in KamLAND LS	Radiation energy (MeV)	Yield ( $\times 10^{-7} \mu^{-1} \text{g}^{-1} \text{cm}^2$ )			Fraction from showering $\mu$
			Ref. [10]	FLUKA calc.	This measurement	This measurement
$n$	207.5 $\mu\text{s}$	2.225 (capt. $\gamma$ )	—	2097 $\pm$ 13	2787 $\pm$ 311	(64 $\pm$ 5)%
$^{12}\text{B}$	29.1 ms	13.4 ( $\beta^-$ )	—	27.8 $\pm$ 1.9	42.9 $\pm$ 3.3	(68 $\pm$ 2)%
$^{12}\text{N}$	15.9 ms	17.3 ( $\beta^+$ )	—	0.77 $\pm$ 0.08	1.8 $\pm$ 0.4	(77 $\pm$ 14)%
$^8\text{Li}$	1.21 s	16.0 ( $\beta^- \alpha$ )	1.9 $\pm$ 0.8	21.1 $\pm$ 1.4	12.2 $\pm$ 2.6	(65 $\pm$ 17)%
$^8\text{B}$	1.11 s	18.0 ( $\beta^+ \alpha$ )	3.3 $\pm$ 1.0	5.77 $\pm$ 0.42	8.4 $\pm$ 2.4	(78 $\pm$ 23)%
$^9\text{C}$	182.5 ms	16.5 ( $\beta^+$ )	2.3 $\pm$ 0.9	1.35 $\pm$ 0.12	3.0 $\pm$ 1.2	(91 $\pm$ 32)%
$^8\text{He}$	171.7 ms	10.7 ( $\beta^- \gamma n$ )	} 1.0 $\pm$ 0.3	0.32 $\pm$ 0.05	0.7 $\pm$ 0.4	(76 $\pm$ 45)%
$^9\text{Li}$	257.2 ms	13.6 ( $\beta^- \gamma n$ )		3.16 $\pm$ 0.25	2.2 $\pm$ 0.2	(77 $\pm$ 6)%
$^{11}\text{C}$	29.4 min	1.98 ( $\beta^+$ )	421 $\pm$ 68	416 $\pm$ 27	866 $\pm$ 153	(62 $\pm$ 10)%
$^{10}\text{C}$	27.8 s	3.65 ( $\beta^+ \gamma$ )	54 $\pm$ 12	19.1 $\pm$ 1.3	16.5 $\pm$ 1.9	(76 $\pm$ 6)%
$^{11}\text{Be}$	19.9 s	11.5 ( $\beta^-$ )	< 1.1	0.84 $\pm$ 0.09	1.1 $\pm$ 0.2	(74 $\pm$ 12)%
$^6\text{He}$	1.16 s	3.51 ( $\beta^-$ )	7.5 $\pm$ 1.5	12.08 $\pm$ 0.83	—	—
$^7\text{Be}$	76.9 day	0.478 (EC $\gamma$ )	107 $\pm$ 21	105.3 $\pm$ 6.9	—	—

Figure 26: Summary of the isotope production via the muon-initiated spallation in KamLAND [86]

the nuclear signals induced by the IBD events as well. Additional sources for the electromagnetic signals emerge from the natural radiation decay chains (by contrast with BiPo, accidentals do not require two specific consecutive decays within IBD-like time window) and gamma ray contributions at the vicinity of the SoLi $\partial$  detector. Among those sources, one finds a reactor fission product  $^{60}\text{Co}$  and  $^{41}\text{Ar}$ , created by the reactor neutron capture on the natural  $^{40}\text{Ar}$ . The latter background sources are dependent on the activity cycle of the reactor and, in principle, are reduced before the ES sources because of the passive shielding of the detector container.

## 2.5 Simulations

The simulations available in the SoLi $\partial$  experiment are divided into the following categories:

- The geometry simulation of reactor core, detector and construction site vicinity;
- The generation of interactions taking place within the detector;
- The simulation of the detector response.

The geometry part is done with the Geant4 software. The full-scale Phase I SoLi $\partial$  detector together with fundamental volumes of the detector as PVT, ZnS screens, WLS fibres, Tyvek wrapping, etc. is accurately simulated with respect to both physics features and positioning. The detector container is simulated in a less detailed way. This was done to explore the interaction of the detector environment with cosmic particles. To make it even more complete, the whole BR2 construction site, with different floors and reactor pool, was reconstructed based on the blueprints. Finally, the precise simulation of the BR2 reactor core provides access to the accurate determination of the fission positioning. This part is crucial for the determination of the oscillation parameters.

### 2.5.1 SoLO generator

The isotropic generation of the reactor antineutrino can not be applied for simulation studies due to the poor geometrical acceptance. The dedicated SoLi $\partial$  Oscillation (SoLO)

analysis framework was developed to fix this problem. Practically, SoLO operates in several stages. It performs the intermediate connection between the fission inputs from the reactor core simulation and the simulation of the detector geometry. The first stage consists of the calculation of the signal event yield per isotope per 5 cm size voxel. Subsequently, the predicted yield is simulated hundred times per voxel to avoid statistical fluctuation. In the end, each generated event has its fission position in the core with its antineutrino energy and momentum associated with the interaction voxel position within the detector. Such an approach reduces the computation time, avoiding the impact of geometrical acceptance. The kinematic information of the neutron and positron issued by the IBD is generated in order to optimise the computation time even further. Neutron and positron inputs are used in the G4 simulation of the detector response. In addition, SoLO is capable of creating fake oscillation patterns in order to provide an important validation tool. The comprehensive description of the software can be found in the PhD thesis of Ianthe Michiels [85].

### 2.5.2 Calibration sources

The calibration sources simulation uses a highly detailed model of the CROSS geometry simulation. It uses the energy distribution inputs of the electromagnetic sources ( $^{22}\text{Na}$ ,  $^{137}\text{Cs}$ ,  $^{207}\text{Bi}$ ) and neutron sources ( $^{252}\text{Cf}$ , AmBe) combined with the available positioning of the sources in the air gaps to reproduce the real calibration conditions. These simulations are of uttermost importance in order to create the templates for the calibration procedure, described in the Chapter 4.

### 2.5.3 Background

Several background source generators are implemented in the simulation tool. The first one is responsible for the BiPo cascade. Since the contamination comes from the neutron detection screens, only the events generated within this specific physical volume are kept. This generator is used to create any other isotope generated in any specific detector volume. This feature is *e.g.* helpful in scrutinising muon-induced isotope interactions. The second background generator is used to determine the correlated background of cosmic origin. It can use two possible external tools as an input:

- The CRY generator checked with Guan parametrisation [87] for cosmic muons
- Gordon parametrisation [88] employed for the atmospheric neutron generation

The latter generators are very resource-consuming, and no optimisation procedure was derived. Thus, they are not used directly for background studies. However, the muon sample, generated with the CRY engine [89], is used for calibration purposes in Chapter 4.

### 2.5.4 ROSim software

The last piece of the simulation chain allows one to link the Geant4 simulation energy deposit with the actual detector readout. It is called read-out simulation software (ROSim) and is aimed at reproducing the detector response. It consists of several stages. In the first one, the energy deposit from the Geant4 simulation undergoes quenching corrections. It follows an empirical Birks' law [90]:

$$\frac{dL}{dx} = S \cdot \frac{\frac{dE}{dx}}{1 + kB \cdot \frac{dE}{dx}}, \quad (42)$$

which corrects the light yield ( $L$ ) depending on the scintillator type and its properties ( $S$ ), the particle type, hence the energy losses  $\frac{dE}{dx}$ , and the path length ( $x$ ). The quenching significantly impacts the neutrons and nucleus emerged within the detector, but it is mostly negligible for the positrons, electrons and gamma.

The second stage emulates the set of photons distributed in time from the corrected deposit that are reaching the MPPC. The conversion is not done with the ratio provided in the scintillator data sheet (10000 photons per MeV) but rather via applying an effective factor. This approach allows for actual optical simulation to be avoided. All the inefficiencies associated to each stage of the light collection (PVT, WLS, and MPPC) are embodied into the conversion ratio. It is determined by comparing the data coming from either the calibration sources or the BiPo enriched samples. The obtained amount of photons is shared between the WLS fibres (or more precisely directly between the associated MPPCs) of the main and neighbouring cubes. The latter effect is called light leakage and will be discussed later. The splitting is done according to the best knowledge of the detector acquired from the calibration procedure. The final amount of the photons for each MPPC is randomised according to the Poisson distribution, and each photon receives the time stamp based on the travelled distance and the scintillation constants. The emulated output is compatible with the reconstruction algorithm and thus secures the transition between them and the Geant4 level information. Finally, the ROSim also emulates the impact of neutron detection efficiency. The last stage generates the dedicated waveform amplitude. Ensures the correct operation of the trigger system for the generated events. Although, the variables used for the pulse-shape discrimination are not simulated. A more elaborate description of the development and tuning of ROSim software can be found in the PhD thesis of Maja Verstraeten [91].

## 2.6 Conclusion

The SoLi $\partial$  experiment is presented in this chapter. The detection principle and detector design ranging from the simplest detection unit cell to the full-scale geometry is discussed. It is complemented by a description of the electronics and the trigger system. The list of advantages and disadvantages provided by the experimental site of the BR2 was presented. Eventually, the expected signal and background and available simulations have been described.

## 3 Reconstruction algorithm

As discussed in Chapter 2 the raw data received from the detector (or ROSim) are the digitised MPPC readout values of the light collected by the WLS fibres crossing SoLi $\partial$  cubes. The signal candidates and, singularly, their electromagnetic parts must be defined from this raw information. The topological reconstruction at work in this thesis aims at optimally using the granularity of the detector response. The most natural and convenient way to present the data is hence to transform the fibre responses into an assignation of their readout values to the physical detection units: the scintillating cubes. The purpose of Chapter 3 and Chapter 4 is to report this transition. Chapter 3 describes the reconstruction software of the SoLi $\partial$  collaboration, developed to cluster the waveforms, categorise and describe the created clusters. It is followed by the introduction of the CCube algorithm, which is designed to convert the list of readout values joint to the ES clusters into the list of impacted (*i.e.* where the interaction took place) cubes with the associated energy deposits. The Chapter 4 complements the description of the reconstruction algorithm by providing the calibration procedure information, which accounts for the characteristics differences of the PVT cubes and completes the transformation of the MPPC readout into MeV units. Thus, the necessary knowledge to construct the signal definition will be established in the following two chapters.

### 3.1 Event reconstruction software

The SoLi $\partial$  analysis software framework (Saffron2) is a C++-based tool used for offline reconstruction and further description of SoLi $\partial$  data. The purpose of the software is to match the set of recorded waveforms, remained after the application of the triggers, with the physics interaction that took place in the detector, and distinguish it from the remained electronics noise. To pursue the latter objective, the waveforms with amplitude values below 2.5 PA are discarded, which is 1 PA above the ZS threshold. To simplify further processing of data and to reduce time and memory consumption, the waveforms are first grouped into cycles. A new cycle emerges once the time difference between two subsequent waveforms exceeds the threshold. The threshold value is adjustable and chosen based on the intensity of the analysed run (it is 350 blocks or 2.24 ms in the IBD regime and is significantly decreased for calibration campaigns). Such an approach allows obvious overlaps between the uncorrelated events to be avoided. The next stages of the analysis are performed per cycle.

The following step consists of gathering waveforms into clusters. The purpose of a cluster is to collect all the detector channels fired by the same particle. The waveforms are attached to a cluster under either of the following conditions:

- The waveform starts within a 7 samples (175 ns) coincidence window with respect to the start of the cluster's seed waveform.
- The channel that registered the waveform, is by default associated to the cluster and the waveform arrived within the time window. Its length is computed according to an empirical function dependent on the current cluster length and the number of channels involved. It is tuned so that the larger the length of the cluster, the larger the impact of the function. It allows one to take into account the lengthy nature of the NS, which consists of multiples peaks within the same waveform.

Simultaneously, it does not scale much for the clusters with the nanosecond scale length (ES and most of the muons). The operating principle of the clustering is sketched in Figure 27. An enhanced look at the development procedure and the tuning of the cluster time window can be found in [79].

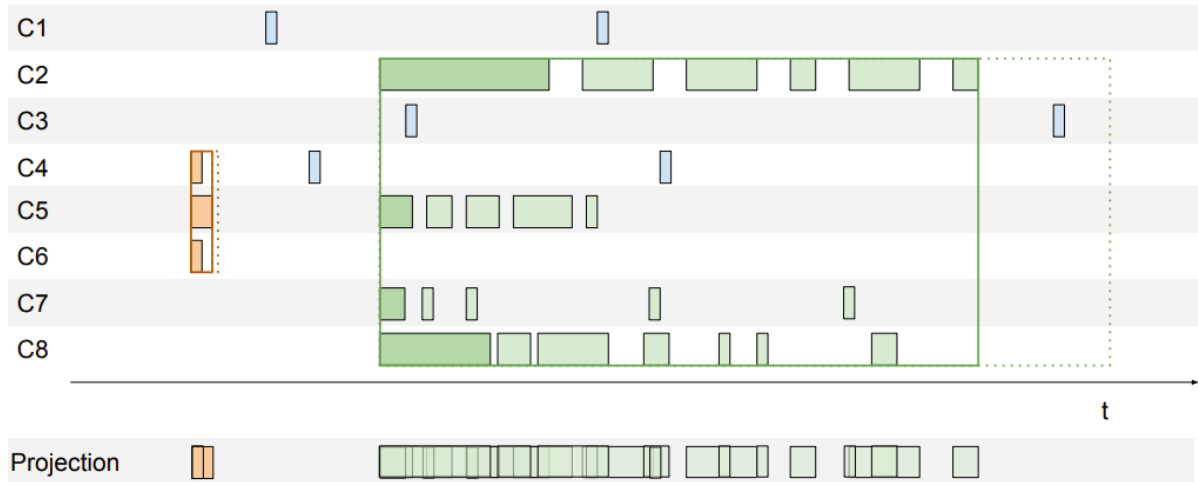


Figure 27: Simplified scheme of the cluster time window application. For the short orange waveforms, representing the ES expected signal, it does not scale significantly and thus does not bring additional waveforms to the initial collection. The green clusters, representing the NS expected signal, are experiencing the empirical function impact, on the contrary. The waveforms arrived with a delay to the same channels (which are actually part of the same NS waveform, but split due to the threshold effect) associated to the NS instead of creating additional clusters. This effect is further sketched at the projection of the clusters at the bottom line of the plot.

- The clusters obtained can be further combined. For clusters within the same plane with the overlapping channels, the coincidence time window can be extended up to a factor of three. The initial clustering is performed on the plane-by-plane level. Thus, it is possible to have clusters in different planes within the 7 samples window. Such clusters are also additionally gathered.

The list of created clusters is then categorised with the Saffron2 identification algorithms. Each of the clusters receives one of the three existing mutually exclusive categorisation types: muon, NS, or ES. The identification algorithms for each of them are summarised below.

### 3.1.1 Muon clusters

Each cluster with at least one horizontal and one vertical channel with an amplitude larger than 200 ADC is tagged muon. Depending on the muon features, they are further tagged in three subcategories. If the number of channels is low ( $< 11$  in either horizontal or vertical list), the cluster is tagged as Type 0 muon. In most cases, they correspond to the so-called clipping muons, which affect only a few cubes on the edge of the detector. Once the number of channels increases, it means that the muon candidate deposited energy in more cubes and most likely left a track in the detector. Muon tracks themselves as well as the muon rate derived from the number of reconstructed tracks are a valuable source

of information about the detector stability and overall response. Therefore, a dedicated algorithm for muon track reconstruction was developed. It splits the involved cluster channels into horizontal and vertical, performs the spatial clustering in each dimension, which allows outlier cubes to be excluded, and runs a linear track fit for each set of channels. Depending on the convergence of the fit, the muon candidates are further split into Type 1 (one of the fits has not converged, which, for example, can be caused by muons localised in one plane either vertically or horizontally) and Type 2 (the cleanest candidates, for which both fits have converged). An example of a reconstructed muon track in the SoLi $\vartheta$  detector can be seen in Figure 28. A more complete description of the reconstruction algorithm can be found in the PhD thesis of Giel Vandierendonck [92]. Since the identification algorithms are mutually exclusive, the clusters tagged as muons are not considered for the following identification algorithms.

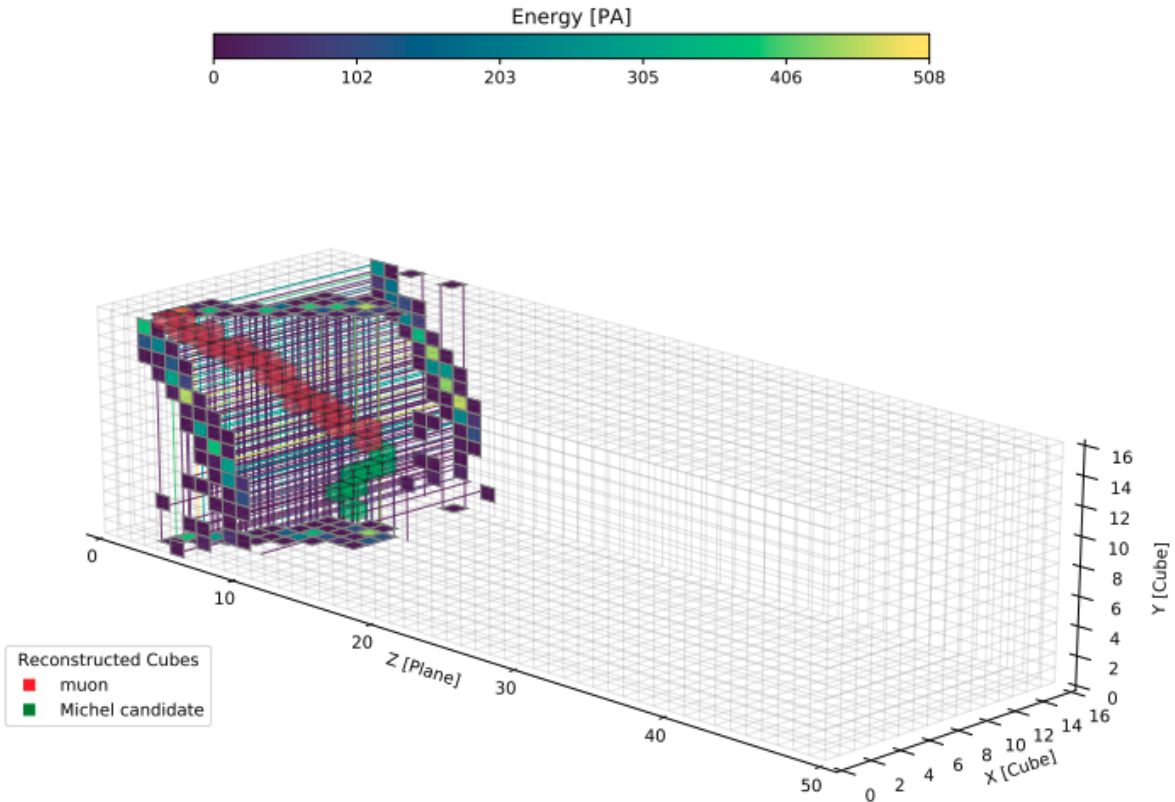


Figure 28: An example of the reconstructed Type 2 muon track in the SoLi $\vartheta$  detector (red squares) with the set of channel hits (violet, dark green and yellow squares). The further exploration potential of muons is illustrated by associating the reconstructed track of the Michel electron candidate (green cubes). The comparison to these well-known candles allows the detector performance to be evaluated.

### 3.1.2 NS clusters

The next opportunity for a cluster is to end up as the NS. The NS identification algorithm has two main purposes. The initial one is to improve the poor purity of the NS trigger. Most false triggers come from muon signals. These are so-called horizontal and vertical

muons. In this case, the muon track is following certain WLS fibres (unlike the case of the “diagonal” muon, which impacts different fibres in the different planes), and thus the scintillating photons are mainly distributed between these specific fibres. The amount of incoming photons is overwhelming to the electronics and causes after-pulse signals. The effect occurs on the  $\mu$  s scale and, as such, mimics the signature of the NS signal. Moreover, the amount of received photons can saturate the channel, which will not receive any data (*i.e.* will be “dead”) until the end of the 8-minute run, when the electronics buffers are cleared. The so-called dead fibre effect and methods to mitigate its impact are discussed in the next Chapter 4. The length of the after-pulses is on average shorter than that of the ZnS scintillating time. Therefore, NS candidates are required to have a cluster length larger than 1000 samples (25  $\mu$ s). The second part of the algorithm is applied only to the candidates who meet the cluster length condition. The goal is to localise the NS to a certain cube, since the online trigger uniquely provides the channel that caused the trigger. To do that, the trigger channel is first coupled to the correspondent channel at the other end of the row. The scan of the full plane is subsequently performed in order to find the pair with the largest combined PoT value, and hence to define the associated orthogonal channels. The characteristics of the selected channels are used to eliminate the remaining contamination of the false triggers:

$$\begin{aligned}\bar{A} &= \frac{1}{n_c} \sum_c^{n_c} \max(\text{ADC}_c) \\ \bar{Q} &= \frac{1}{n_c} \sum_c^{n_c} \sum_i^{\text{time}} \text{ADC}_c(i),\end{aligned}\tag{43}$$

where  $\bar{A}$  seeks the highest amplitude in channel  $c$  and  $\bar{Q}$  is the integral, which is computed over two different time windows: 30 (short) and 1000 (long) samples resulting in  $\bar{Q}_{short}$  and  $\bar{Q}_{long}$  respectively. Both features are averaged per channel ( $n_c$ ) and further combined into:

$$\begin{aligned}\text{IonA} &= \frac{\bar{Q}_{long}}{\bar{A}} \\ \delta_{X-Y} &= \frac{\overline{Q_{long}(X)} - \overline{Q_{long}(Y)}}{\overline{Q_{long}(X)} + \overline{Q_{long}(Y)}}.\end{aligned}\tag{44}$$

The integral over an amplitude value (IonA) is intended to eliminate the remaining mixed clusters originating from muon interactions. Unlike the NS-triggered damping waveforms, the muon after-pulses remain at the same level and hence populate the region with the high values of  $\bar{A}$ . The asymmetry  $\delta_{X-Y}$  is caused by the positioning of the neutron capture screens (see Figure 17). The WLS fibres positioned closer with respect to the  ${}^6\text{LiF}$  screens are expected to receive a larger amount of photons. Empirical dependencies between the established parameters (IonA,  $\bar{Q}_{short}$ ,  $\bar{Q}_{long}$  and  $\delta_{X-Y}$ ) are tuned to maximise the purity of neutron identification [79]. The impact of the cuts is shown in Figure 29.

### 3.1.3 The BiPonator

The NS identification algorithm ensures the selection of neutron triggers issued by the ZnS scintillator. There are two sources of these triggers: the BiPo cascade  $\alpha$  and the capture

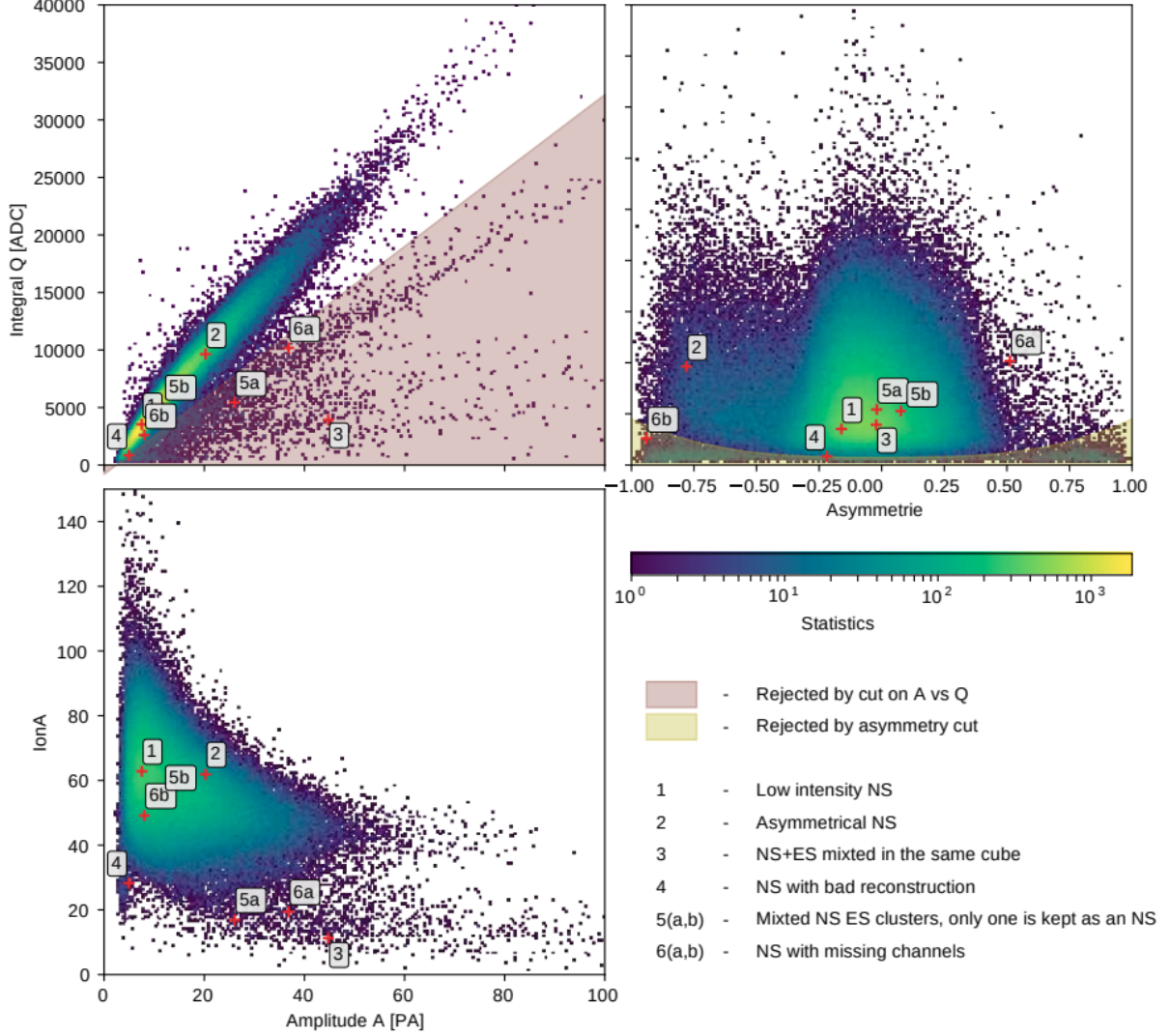


Figure 29: The distributions of the NS characteristic features. They include the amplitude value ( $\overline{A}$ ), the integrated sum of all triggered channels ( $\overline{Q_{short}}$ ), the ratio of the two (IonA) and the vertical-horizontal asymmetry ( $\delta_{X-Y}$ ). The red crosses represent the different types of recorded NSs. Their description is provided in the bottom right list. The two top-plots show the rejected areas defined in red and yellow in order to discard the ill-defined NSs.

of neutrons on the lithium screen. To distinguish them, a pulse-shaped discrimination technique was developed. It relies on the integration of the waveform in a short and long time window, similar to what was discussed previously. The differences in the waveform amplitudes, shown in the left plot in Figure 30, are caused by the different  $Q$  value of the corresponding reactions (4.8 versus 7.7 MeV). The discriminating variable, called BiPonisher, is constructed as the fraction of the integral in the long time window of 3500 samples ( $87.5 \mu s$ ) to the integral in the short time window of 300 samples ( $7.5 \mu s$ ). The BiPonisher distribution for two different trigger sources is presented in the middle plot of the Figure 30. The overwhelming level of BiPo background made it necessary to go beyond the performance of the BiPonisher tool. A 1 dimensional convolutional neural network (CNN) is employed to improve the BiPo rejection by a factor of three for a similar

neutron efficiency. Waveform information is prepared in several stages to be aligned with the commonly used CNN input format. First, the waveforms in the long time window are summarised for all the active channels. The largest and smallest amplitudes are defined in order to normalise the obtained waveform to unity. The set of values of the normalised amplitude for each of the 3500 samples defines the CNN input. In addition to being aligned with the required format, such handling of the waveform characteristics decreases the impact of the variations over time (*e.g.* caused by the baseline), making the response in principle more stable. The CNN score provides a new discriminating variable, denoted BiPonator. Its distribution is shown on the right plot of Figure 30. The CNN stability is validated with calibration campaigns data performed regularly during the whole Phase I of data taking. The development, tuning, and validation of the BiPonator is described in more detail in the PhD thesis of Savitri Gallego [93].

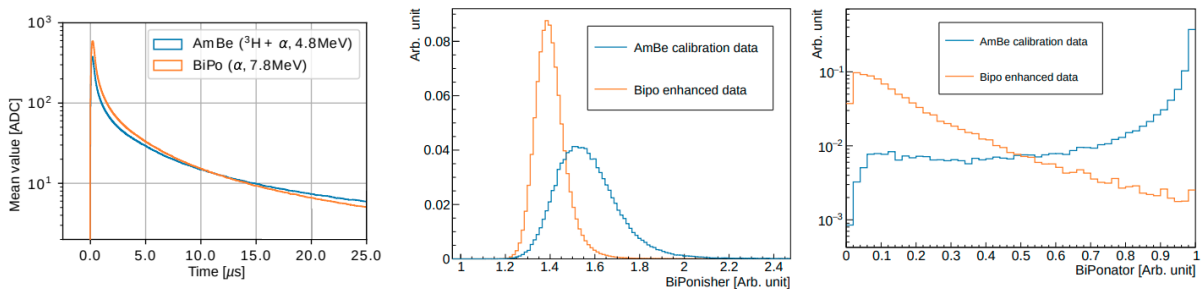


Figure 30: The discriminating variables distributions for the two sources of neutron triggers in the ZnS: the neutron from the AmBe calibration source in orange and  $\alpha$  from the BiPo cascade in blue. Left: the average shape of the neutron waveform. Middle: the BiPonisher distribution. Right: the BiPonator (BiPonisher improved with machine learning technique) distribution.

### 3.1.4 ES clusters

All remaining clusters are tagged as ES. However, unlike the algorithm for the muon clusters, which relies on the linear fit of the sequence of the cubes in the track, or the one for the NS, which relies on the identification of a unique cube where the trigger took place, the algorithm which processes the ES clusters has to be capable of reconstructing the list of the impacted PVT cubes (which can be scattered in the detector volume) based on the readout response. The efficiency and accuracy of the algorithm defines the limitation of the experiment in terms of the oscillation analysis. The precision of the positron annihilation cube placement is crucial for the antineutrino travelled distance approximation; the associated energy to this cube is in the core of the antineutrino energy estimator. In addition, the reconstruction of the additional cubes (*i.e.* potentially triggered by the annihilation gamma), involved in the event, provides supplementary information for the background suppression and thus increase signal-to-background ratio, which is another key parameter, when it comes to the sensitivity to the oscillations. Finally, the ES cluster is rejected if the total energy of the reconstructed cubes is below 1 MeV. It decreases the size of the output file by a factor of 7. A dedicated ES signal reconstruction algorithm was developed. It is called the CCube algorithm and described in more detail in the next Section.

### 3.1.5 The NS-ES coincidence

The final step of the identification algorithm is to compose the IBD candidates by creating the coincidence between the NS and all the ES clusters. At this stage, the initial information about the candidate is defined. It includes the spatial distance between the positron annihilation cube and the neutron capture cube ( $\Delta R$ ) and the time difference between the two ( $\Delta T$ ). The determination of the other features is detailed in the Chapter 5. The  $\Delta T$  quantity is used to reject ES clusters that do not fit the time window range of  $[-200, 500] \mu\text{s}$ . By construction, the positive part of the window corresponds to the correlated IBD candidates, while the negative part aims at the accidental level estimation.

### 3.1.6 FPNT

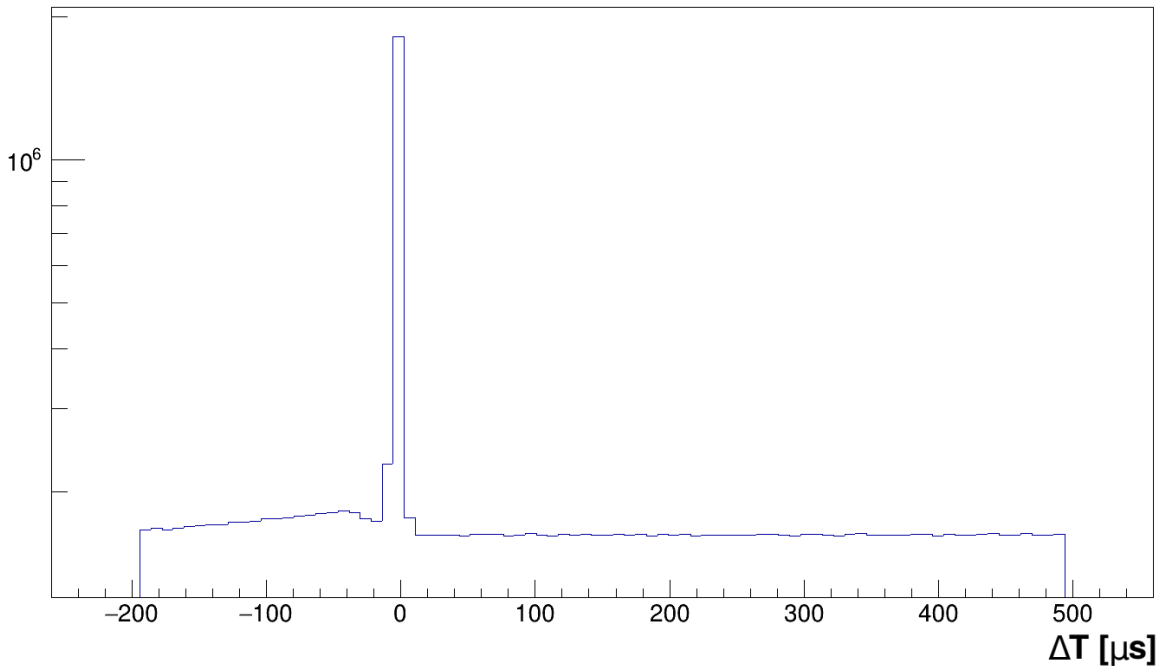


Figure 31: The time-difference distribution between the clusters attached to false positive neutron trigger and electromagnetic signal. It operates in three regimes: below zero (time-correlated background-induced), around zero (self-correlated induced) and above zero (purely accidental coincidences). The latter provides a sample of events to estimate the accidental background rate with an adequate statistical precision.

Let us note here that even rejected clusters are a source of valuable information. For example, the neutron triggers, which are not tagged as the NS cluster after the identification procedure, but associated with the reconstructed muon-track instead, can serve as an alternative way to estimate the accidentals. Such neutron triggers are called false positive neutron triggers (FPNTs). The need (beyond completeness) for introducing an alternative way to measure accidentals comes on one hand from the fact that the negative time window for the NS cluster has a reduced statistics, compared to the positive one (30 blocks versus 80); it furthermore experiences a small correlated candidate contamination (most likely coming from the 2.2 MeV  $\gamma$  from the neutron capture on hydrogen), which results in inaccuracies in the estimation of the accidental rate. The only additional requirement

placed on the FPNT is that it occurs in the same plane as one of the true reconstructed NS clusters. Once this requirement is met, the same procedure of creating the NS-ES coincidences is applied with the FPNT being a fake neutron cluster. Although the FPNT rate is twice the NS rate, some of the true triggers remained unmatched. Those are called “orphans”, and the final FPNT yield is corrected to take them into account. The  $\Delta T$  distribution of these coincidences is shown in Figure 31 and is divided into three different regimes. The negative time-window, which is still slightly contaminated with the correlated after-muon events, induced, for example, by interactions with the detector materials (see Figure 26) is therefore discarded. The peaking region around 0, which is induced by the ES triggered by the muon itself and, hence, causing the self-correlated events, is also discarded. And finally, the positive time-window is used to determine the actual accidental rate. It is used to describe the yield and EM features of the accidental background with an improved statistical precision and less potential biases compared to the prior method (negative time-window).

### 3.2 The CCube algorithm

The purpose of the Clermont-Cubes (CCubes) algorithm is to perform a reverse engineering procedure and to transform the list of digitised MPPC readout into a list of cubes, where physics interactions took place. Let us mathematically define the problem. The communication between the PVT cubes and MPPCs is provided with the WLS fibres. In other words, the fibres act as projectors from the cubes to the electronics. The projection is linear with respect to the deposited energy. The detector planes are optically decoupled in the SoLi $\partial$  design, which means that only cubes in the same plane as the fired fibres shall be considered. This simplifies the 3D reconstruction problem to 2D. By defining  $a_{ij}$  as the projector from cube  $j$  to MPPC  $i$ , the readout value can be computed as follows:

$$a_{i,1} \cdot E_1 + a_{i,2} \cdot E_2 + \dots + a_{i,256} \cdot E_{256} = p_i , \quad (45)$$

where 256 corresponds to the number of PVT cubes in the plane (composed of  $16 \times 16$ ). The number of projections is twice the sum of the number of cubes in rows and columns, so, for the SoLi $\partial$  geometry, there are 64 of them. Thus, the reconstruction problem can be written as a system of 64 equations:

$$\begin{aligned} a_{1,1} \cdot E_1 + a_{1,2} \cdot E_2 + \dots + a_{1,256} \cdot E_{256} &= p_1 \\ a_{2,1} \cdot E_1 + a_{2,2} \cdot E_2 + \dots + a_{2,256} \cdot E_{256} &= p_2 \\ &\dots \\ a_{64,1} \cdot E_1 + a_{64,2} \cdot E_2 + \dots + a_{64,256} \cdot E_{256} &= p_{64} , \end{aligned} \quad (46)$$

which can be rewritten in matrix form as:

$$AE = p , \quad (47)$$

where  $p$  is the column vector of the readout projections.  $E$  is a column vector of unknown energy deposits. Thus, the aim of the calibration procedure is to find it. The CCube algorithm only assesses the energy to the cube if and only if at least one fibre in horizontal and vertical directions has been hit. The typical amount of cubes in a physics event is below 20 (and not necessarily all of them are in the same plane). The reconstruction

algorithm is hence only dealing with a small subset of detector planes, that solely contains the cubes in which the light could have occurred. Finally,  $A$  is a matrix of  $64 \times 256$  dimension. It is called the System Matrix (SM)<sup>1</sup> and embodies the best of our knowledge about the detector behaviour at each stage, from the light generation to the digitisation. Moreover, it also includes the absolute energy scale. The derivation of the SM is beyond the scope of this chapter and is exhaustively presented in Chapter 4. For now it is assumed that all the elements of the SM and the absolute energy scale can be determined. The latter is kept the same, as well as the ROSim version, to ensure identical conditions while solving Equation 47. This matrix equation is a linear discrete inverse problem. It is well posed if it fits certain requirements:

- Existence of the solution,
- Uniqueness of the solution,
- Stability of the solution with respect to the small shifts.

In the case of the current reconstruction problem, the second requirement is violated. It is illustrated with a simple example provided in Figure 32. In this example, the PVT cube communicates individually through the fibres, crossing the cube, and all the elements of the SM are set to 1. It shows that two energy deposits in the same plane are enough to allow the algorithm to fulfil the readout in several ways, by creating false cubes at the intersection of the fibres of the true ones. Moreover, false cubes introduce an energy bias to the initial energy deposits, almost always lowering the true energies. As such, the initial problem is ill-posed. Thereby, there are two main approaches to solve it: the regularisation and the Bayesian. Several methods are proposed, discussed, and compared further in the chapter. Before proceeding to it, the set of estimators used to assess the performance is defined.

### 3.2.1 Reconstruction procedure estimators

In order to evaluate the performance of the selected reconstruction approaches, a set of estimators has to be established. These estimators are divided into two categories. The first one relates to the performance of the algorithms per se. It computes the deviations of the derived solution from the actual measurements. This value is also denoted as *data fidelity*. The least squares norm ( $L2$ ) and Kullback-Leiber divergence ( $KL$ ) were both selected to obtain it:

$$T_{L2}(E) = \|AE - p\|_2^2 \quad (48)$$

$$T_{KL}(E) = AE - p + p \cdot \log p - p \cdot \log AE. \quad (49)$$

The employment of these two estimators provides the opportunity to perform an immediate cross-check and helps to track the behaviour outliers. Moreover, some of the estimators are more suitable depending on the physical model of the measurement process ( $L2$  prefers a Gaussian nature, while  $KL$  prefers the Poisson one). The data-fidelity value can be

---

<sup>1</sup>Such a designation unfortunately introduces the confusion with the Standard Model acronym. However, the latter one is never employed further; hence SM has to be solely interpreted as the System Matrix.

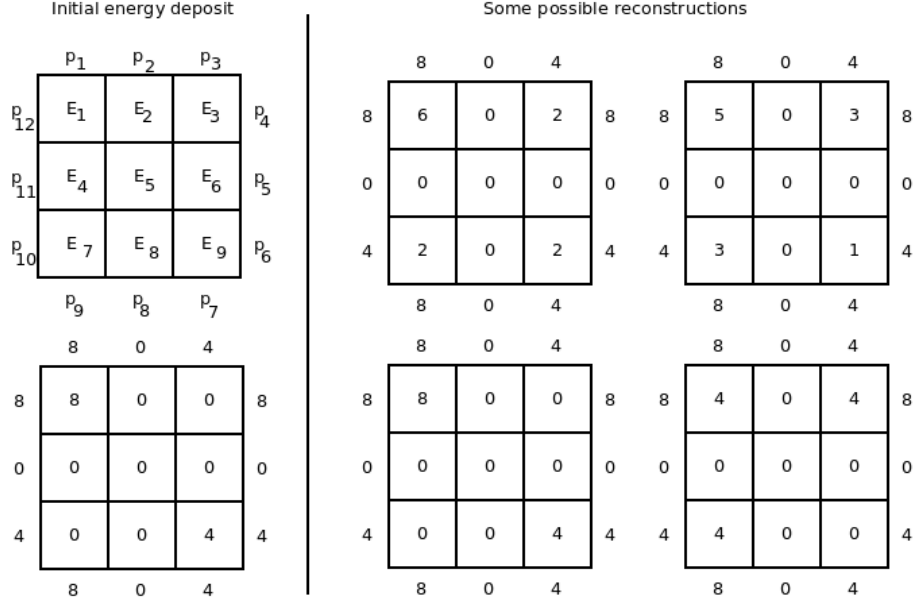


Figure 32: An illustration of the non-uniqueness of the reconstruction problem. The initial digitized readout interpreted in multiple ways in the sense of the attached energy contributions.

computed for both the data and the simulation (it has been implemented in ROSim). This is of utmost importance, since the only way to address the physics performance of the methods is to compare their outputs with the Geant4 level information. The comparison relies on the per-event list of cubes, their coordinates, and associated energy contributions. The obvious variable to track is the total number of cubes at each level:

- $n_{\text{cubes}}^{G4}$  representing the number of involved cubes at the Geant4 level,
- $n_{\text{cubes}}^{RO}$  representing the number of involved cubes at the ROSim level.

The further scrutiny of the positions of the cubes in the lists has three possible outcomes. The cube is present in both lists, which means it was properly reconstructed. The total number of these cubes makes up the counter  $n_{\text{cubes}}^{G4}(RO)$ . The next option is when the cube is only present in the Geant4 list, which means that it was not reconstructed. Finally, the cube can only be present in the ROSim list. These are the false reconstructed cubes introduced in Figure 32. Since they appear only after reconstruction out of nowhere, they are called *ghosts*. The total number of ghosts is denoted as  $n_{\text{cubes}}^{RO}(\overline{G4})$ . The newly defined counters combined with the initial multiplicity compose the final estimators:

- The cube reconstruction efficiency:

$$\epsilon_{\text{RECO}} = \frac{n_{\text{cubes}}^{G4}(RO)}{n_{\text{cubes}}^{G4}} \cdot 100\% \quad (50)$$

- The ghost cube rate:

$$G_{\text{RATE}} = \hat{\mathcal{G}} = \frac{n_{\text{cubes}}^{RO}(\overline{G4})}{n_{\text{cubes}}^{RO}} \cdot 100\% . \quad (51)$$

The number of unreconstructed cubes is an energy-dependent parameter. The lower the energy of the cube, the higher the probability that it will not be reconstructed. The situation is similar to that of the ghost cubes, which generally have very low energies. If in the example in Figure 32 the attached  $E_1$  and  $E_9$  do not satisfy the projection, the algorithm is forced to assign the energy to  $E_3$  and  $E_7$ . Such that the data fidelity is optimised. To mitigate this impact, the physics estimators are evaluated for several different energy threshold levels. The threshold cuts all the cubes at both ROSim and Geant4 levels, which have a related energy below the threshold. For now, the cut values are selected arbitrarily; however, it will be discussed in the analysis chapter that these values can be optimised for selection purposes in Chapter 5.2.2. The last estimator is the energy resolution. It is evaluated only for the cubes that were properly reconstructed. Moreover, the energy resolution has the highest importance for the cubes, where positron annihilation was supposed to happen. This estimator is determined solely for the cubes with the energy  $> 1$  MeV:

$$E_{\text{SPREAD}} = \frac{E_{\text{TRUE}} - E_{\text{RECO}}}{E_{\text{TRUE}}} = \frac{E_{G4} - E_{RO}}{E_{G4}}. \quad (52)$$

Consequently, the energy resolution is defined as the full width at half-maximum of the  $E_{\text{SPREAD}}$  distribution. Each of the three following subsections is an executive summary for one highly relevant approach to solve Equation 47. Thus, it does not contain a detailed technical explanation of the employed method. A more enhanced look at each of them will be available in the upcoming reconstruction note.

### 3.2.2 The regularisation approach

The first method is not aimed at explicitly solving the initial equation. Its purpose is to obtain a well-posed problem, similar to the starting ill-posed one, and solve it instead. The obtained solutions are therefore an approximation. An example of such an approach is a Tikhonov regularisation ( $TR$ ) [94]:

$$E_{TR} = \min_E \{ \|AE - p\|_2^2 + \lambda \|LE\|_2^2 \}, \quad (53)$$

where the second part of the expression is known as a regularisation term, and  $\lambda$  is the regularisation parameter, accordingly. It is important to understand that the solution to the regularised problem is biased with respect to the desired one. In other words, the  $A^{-1}p$  expression (assuming that  $A$  is of even dimensions and invertible) does not satisfy Equation 53. The level of deviation is controlled by the regularisation parameter  $\lambda$ . This is the price to pay for obtaining a unique solution. In Equation 53 the regularisation term is quadratic; however, the choice of it heavily depends on the nature of the initial problem. It is known [95] that for sparse problems (and SoLi $\partial$  reconstruction is like this due to the low multiplicity of cubes per plane) the so-called  $l_1$  approach [96] can be employed. It uses the absolute values of the target value (energies) as the regularisation term. The following loss function therefore reads as:

$$E_{L1} = \min_E \{ \|AE - p\|_2^2 + \lambda \|E\|_1 \}. \quad (54)$$

Most frequently the given equations are met in medical imaging, which deals with a large amount of data. Thus, the most popular methods to solve it are gradient-based since it

allows the computational resources to be significantly decreased, in particular the iterative shrinkage-thresholding algorithms (ISTA). Gradient-based algorithms, in general, use the iterative approach, which relies on improving the current knowledge of the solution with an additional information provided by the gradient of the initial function. In the ISTA approach, the iterative step is completed by the shrinkage-soft-threshold step, which provides:

$$\begin{aligned} E_n &= T_{\lambda\eta}(E_{n-1} - \eta \cdot \nabla F(E_{n-1})) \\ T_\alpha(x) &= \text{sgn}(x) \cdot (|x| - \alpha)_+, \end{aligned} \quad (55)$$

where  $\eta$  is a stepsize,  $\text{sgn}$  is a sign function and  $T$  is a shrinkage operator. Recently, an upgraded version of the ISTA algorithm was developed [97]. It has an improved complexity result of  $O(1/k^2)$ , which is achieved by using the specific linear combination of the two previous iteration values inside the shrinkage operator, called FISTA (for the fast ISTA). The FISTA was implemented in Saffron2 and tested.

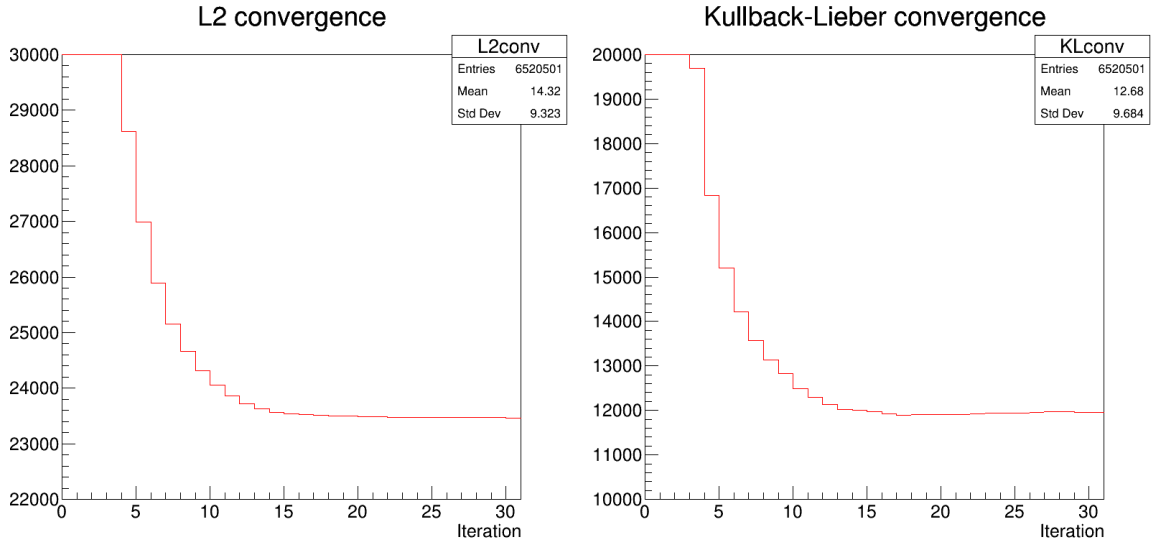


Figure 33: The performance of the fast ISTA algorithm versus the number of executed iterations. It was obtained from 300k simulated IBD events and evaluated with two different data fidelity estimators, that are employed to show the divergence of the derived answer from the true one. The results for both estimators are in agreement and also show the required number of iterations, which can be used to optimise the computational cost.

The method was tested with a ROSim sample of 300k IBD events generated with SoLO. The convergence development is presented in Figure 33. With either of the calculation methods, it is improving with the number of iterations and comes to a plateau. The high data fidelity value is explained by the fact that it is the sum of all the generated events. The number of iterations was arbitrarily selected to 30 and the physics estimators were obtained after this condition. The energy spread distribution, presented in Figure 34, is manually shifted to centre at zero, in order to rule out the impact of absolute calibration. The ghost rate and the reconstruction efficiency for several cube energy threshold values are summarised in Table 1. As expected, the first value is drastically decreasing with larger energy cut values. However, it can be observed that an excessive increase in the cut significantly suppresses the information from the IBD annihilation gammas. Together

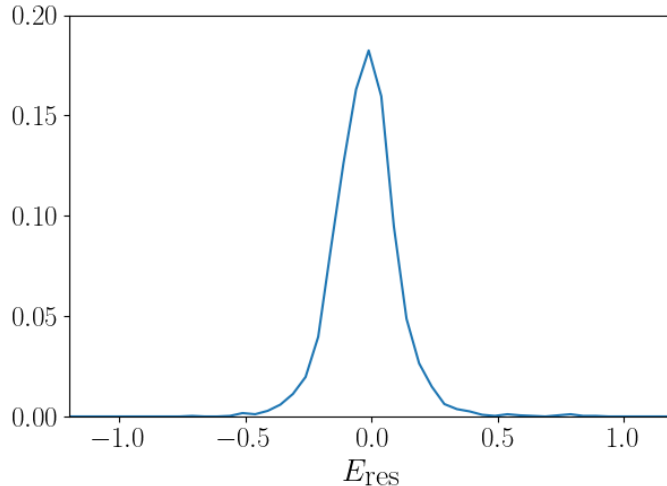


Figure 34: The energy spread distribution obtained by applying 30 FISTA algorithm iterations to 300k simulated IBD events. Since the positron energy is used as an estimator for the anti-neutrino energy, the energy spread is derived only for the cubes with an energy larger than 1 MeV. It secures the presence of the positron in the cube. The distribution is manually shifted to 0 to exclude the impact of the absolute calibration. The value of the energy resolution is determined to be about 13%.

with the reduction of the multiplicity of ghosts, the reconstruction efficiency improves with a larger threshold. This is a further illustration that the algorithm is coping much easier with the high-energy cubes.

Cut (keV)	50	100	150	200	250	300	350	400	450	500
$\hat{\mu}$ (%)	23.7	15.8	10.6	7.0	4.7	3.1	2.2	1.6	1.2	1.0
$\epsilon$ (%)	66.9	75.3	81.2	85.9	89.8	92.7	95.6	96.7	97.2	97.3

Table 1: The ghost cubes rate and the cube reconstruction efficiency after 30 iterations of the FISTA algorithm, obtained for the ROSim of the IBD events generated with SoLO.

### 3.2.3 The Bayesian approach

Bayesian statistics can be used alternatively. It will not provide a unique solution, and different initial guesses can result in different response outputs. However, it presents advantageous attributes that are discussed in this subsection. The method par se is based on the assumption that both energy deposits  $E$  and the measured projections  $p$  are stochastic variables, with the following characteristics:

- $\pi_{\text{data}}(p|E)$  - is a probability density function (p.d.f.), which describes the likelihood of measuring  $p$  given the knowledge of  $E$ ;
- $\pi_{\text{prior}}(E)$  - describes the nature of the considered signal;
- $\pi_{\text{posterior}}(E|p)$  - is a posterior distribution, *i.e.* the p.d.f., which describes the probability to have  $E$  given  $p$ .

By considering the Bayes master formula, the following relation between the three is obtained:

$$\pi_{\text{posterior}}(E|p) \propto \pi_{\text{prior}}(E) \cdot \pi_{\text{data}}(p|E), \quad (56)$$

where  $\propto$  denotes proportionality. In this approach,  $\pi_{\text{posterior}}(E|p)$  is the solution to Equation 47. The measured projections in SoLiD obey the Poisson law. Thereby, the selection of the Maximum-Likelihood Expectation-Minimization (ML-EM) method is one of the most adapted. It is widely used in medical imaging and lately in particle physics, *e.g.* in the NEXT experiment. The ML-EM method has the following set of features:

- accurate modeling of the Poisson noise distribution;
- the solution is constrained to be positive without regularization;
- the number of photons (which is in the core of the projected values) is conserved.

Similarly to FISTA, it is an iterative approach, which is improving the knowledge of the solution at each step. But in order to do that, it does not rely on the gradient of the initial function. Instead, it generates the projected values based on the current approximation of the solution and compares them with the actual measurement. Finally, the difference between the two defines the subsequent approximation. The whole scheme is sketched in Figure 35. At the same time, according to the scheme, the initial guess for the answer is required as input to launch the iterative process. And this is exactly the place where the condition of the uniqueness of the solution can be violated for ML-EM. There are several approaches to choosing a starting point. A *democratic* one supposes the initialisation of the cubes in each and every position, where it is possible (*i.e.* every intersection of at least one vertical and one horizontal fibre) and equal sharing of the total energy between them. Alternatively, it is possible to employ FISTA to derive the first guess. It has been shown [98] that this choice significantly improves ML-EM performance for sparse problems. Thus, it was chosen as the baseline of the algorithm: FISTA and ML-EM are reconciled in a combined approach.

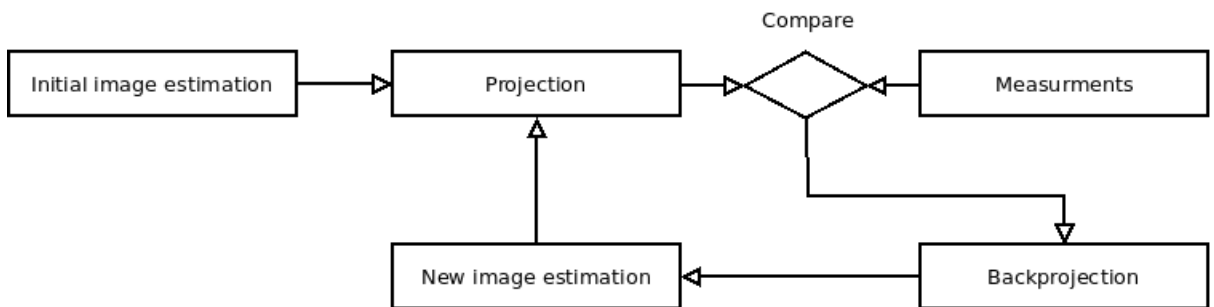


Figure 35: An illustration of the ML-EM iterative part working principle.

$$E_j^{m+1} = \frac{E_j^n}{\sum_i a_{ij}} \sum_i a_{ij} \frac{p_i}{\sum_k a_{ik} E_k^n} \quad (57)$$

The Equation 57 defines the master formula of the ML-EM algorithm. The detailed derivation of the formula is beyond the scope of the thesis, but generally speaking, the

procedure relies on the maximisation of the probability to retrieve a measurement  $p$ , by setting the derivative of it with respect to the current approximation  $E_j^n$  to zero.

Cut (keV)	50	100	150	200	250	300	350	400	450	500
$\hat{\mu}$ (%)	21.3	11.4	7.3	5.2	3.8	2.8	2.1	1.5	1.2	1.0
$\epsilon$ (%)	66.4	76.4	82.6	87.0	90.0	92.7	95.4	96.5	97.0	97.2

Table 2: The ghost cubes rate and the cube reconstruction efficiency after 30 iterations of the FISTA algorithm, followed by 30 iterations of the ML-EM algorithm, obtained for the ROSim sample of IBD events generated with SoLO.

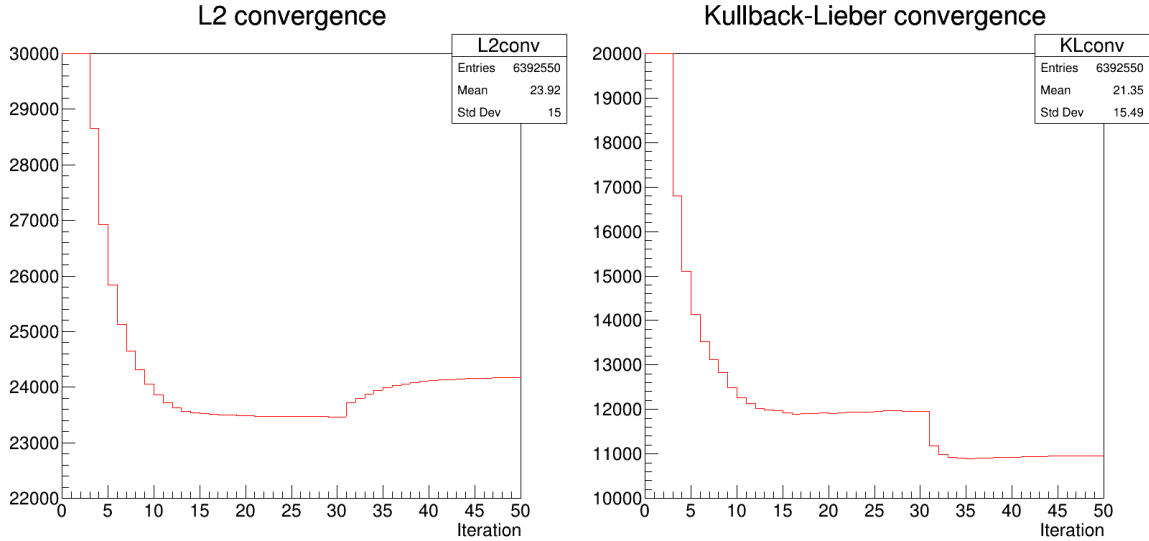


Figure 36: The performance of the FISTA + ML-EM algorithm versus the number of executed iterations (30 iterations for each algorithm). It was obtained from 300k simulated IBD events and evaluated with two different data-fidelity estimators, that are employed to show the divergence of the derived answer from the true one. The results for both estimators are in agreement and also show the required number of iterations, which can be used to optimise the computational cost.

The combined FISTA and ML-EM method was implemented and tested using the same ROSim sample. Subsequently, the same 30 iterations of the FISTA were followed by additional 30 iterations of the EM-LM. The physics estimators are summarised in Table 2. The overall trend with respect to the cut value highlighted in the previous subsections remains the same for both observables. However, this composite approach improved overall performance for all the thresholds considered. The comparison of the energy spread for the high-energy cubes is presented in Figure 37. An extracted energy resolution value remains at the same level: 13%. The most interesting change appears in the data fidelity distributions displayed in Figure 36. Indicates the difference in the nature of the two approaches. Since the ML-EM algorithm is aimed at reproducing the Poisson behaviour of the measured signal, the KL data fidelity is improving after ML-EM takes over. On the contrary, the importance of the L2 algorithm is less prioritised. Taking the result of the current approach at face value implies that taking into account the physics features of the

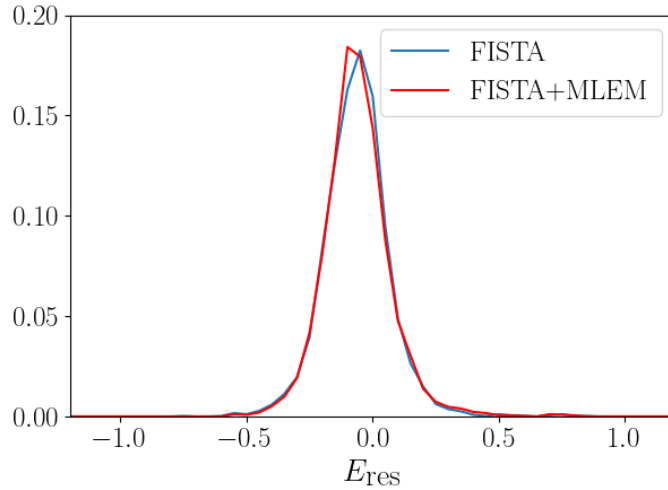


Figure 37: The energy spread distribution obtained by applying 30 FISTA and 30 ML-EM iterations to 300k simulated IBD events. Since the positron energy is used as an estimator for the anti-neutrino energy, the energy spread is derived only for the cubes with an energy larger than 1 MeV. It secures the presence of the positron in the cube. The distribution is manually shifted to 0 to exclude the impact of the absolute calibration. The determined value of the energy resolution is 13%. The performance is at the same level as for the regularization approach.

performed measurement improves the performance of the reconstruction algorithms. At the same time, the performance achieved is not the finest. For example, just based on the projected values, the algorithm cannot claim which of the two configurations presented in Figure 38 is better. The purpose of the next subsection is to explore the opportunities to employ additional information about the signal and ways to implement it inside the algorithm.

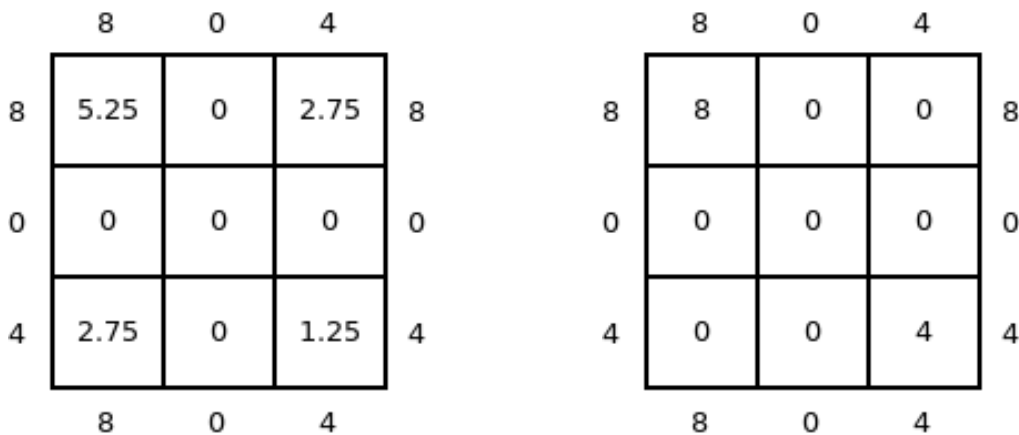


Figure 38: The two possible solutions to the simplified reconstruction problem posed in Figure 32, which are equally favored by the ML-EM approach.

### 3.2.4 The SoLi $\partial$ approach

In the list of cubes where an IBD event has deposited energy, some cubes contain more important information than others. They are ranked in average along the following hierarchy: the cube in which the positron annihilation takes place; the cubes where the first Compton scatterings of the annihilation photons occur. Thus, the reconstruction algorithm, seeking primarily cubes with larger energies, is aligned with the underlying physics of the IBD process. The Orthogonal Matching Pursuit (OMP) algorithm is a perfect candidate for this role. At each stage, it looks for the best pair, the available cube in the plane and the deposited energy, which improves the L2 norm (see Equation 48) the most. By construction, it means that the OMP is trying to attach the largest possible energy and keeping  $E$  sparse simultaneously. The working principle is summarised in the following pseudocode:

```

Define an empty support set  $E$ 
while  $T_{L2}(E) < \text{threshold}$  do
  Find an element  $E_i$  minimizing  $T_{L2}(E)$ 
  (All elements which are not in  $E$  are kept at 0)
  Add  $E_i$  to  $E$ 
end while

```

For the simplified problem in Figure 32, this algorithm will perform the following steps:

1. iteration 1: assigning  $E_1 = 8$  minimizes the  $T_{L2} \implies$  add it to  $E$ ;
2. iteration 2: assigning  $E_9 = 4$  minimizes the  $T_{L2} \implies$  add it to  $E$ ;
3.  $T_{L2} = 0 \implies$  done.

As far as implementation is concerned, the idea is to compose a novel approach, which combines the OMP with the ML-EM algorithm. Likewise FISTA, OMP will be used as the initializer. The full capacity of the OMP is not required in that case, and in order to reduce the computational cost, a simplified OMP (sOMP for simplified OMP) is derived. The main difference between the two is that the simplified version allows one to assign the energy to the cube only once. Hence, once a cube is accessed, it is removed from the list of options. Furthermore, the number of iterations is the multiplicity of cubes in the plane and is small. Finally, the algorithm stops when there are no more available cubes, which defines the exit condition for the while loop. Considering all the modifications, the updated pseudocode transforms into:

```

Input: cubes available for the energy assignment  $E^{input}$ 
while  $E^{input}$  is not empty:
  Find the best pair  $(E_i^{input}, E_i)$  minimizing  $T_{LS}(E)$ 
  (All elements which are not in  $E$  are kept at 0)
  Assign  $E_i$  to  $E_i^{input}$ 
  Remove  $E_i^{input}$  from  $E^{input}$ 
end while

```

The method was implemented and tested with the same ROSim IBD sample as the other methods. The sOMP is performed beforehand and then followed by 50 iterations of the

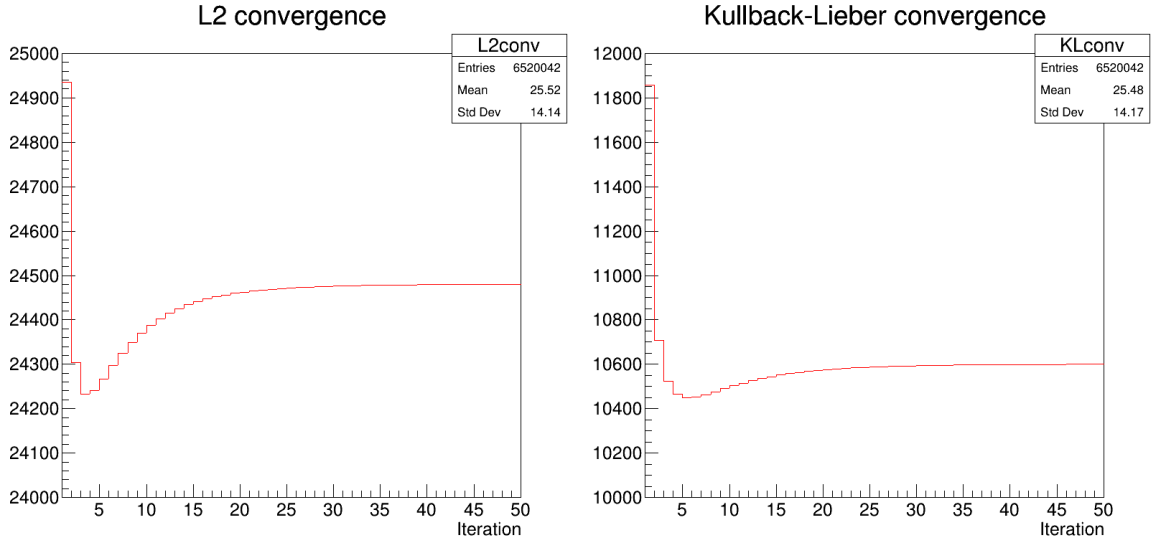


Figure 39: The performance of the simplified OMP + ML-EM algorithm versus the number of executed iterations. It was obtained from 300k simulated IBD events and evaluated with two different data fidelity estimators, that are employed to show the divergence of the derived answer from the true one. The results for both estimators are in agreement and also show the required number of iterations, which can be used to optimise the computational cost.

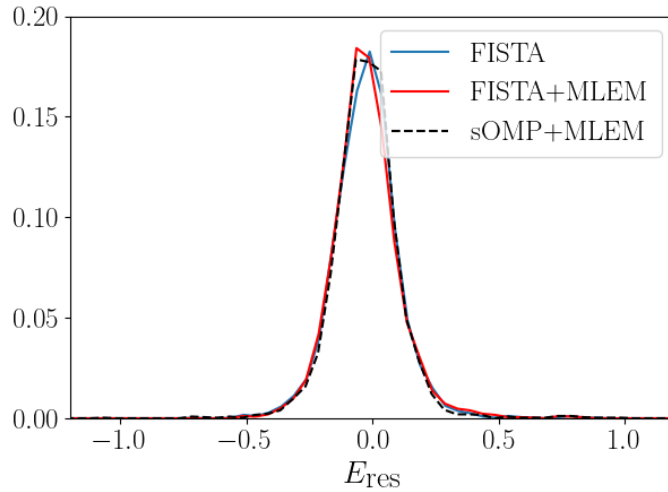


Figure 40: The energy spread distribution obtained by applying sOMP and 30 ML-EM iterations to 300k simulated IBD events. Since the positron energy is used as an estimator for the anti-neutrino energy, the energy spread is derived only for the cubes with an energy larger than 1 MeV. It secures the presence of the positron in the cube. The distribution is manually shifted to 0 to exclude the impact of the absolute calibration. The determined value of the energy resolution is 13%. The performance for all three approaches is equivalent.

ML-EM algorithm. The data-fidelity distributions displayed in Figure 39 show that this method converges faster than the previous two. The degradation of performance after reaching the best point is a known feature of the ML-EM. The energy spread shown in Figure 40 and the energy resolution of the correspondent remains unchanged. However,

a dramatic improvement can be seen for the physics estimators summarised in Table 3. For an energy threshold of 100 keV, the ghost rate was reduced by a factor of two for a comparable cube reconstruction efficiency. A similar performance enhancement is observed for all energy cut values.

Cut (keV)	50	100	150	200	250	300	350	400	450	500
$\hat{\mathcal{L}}$ (%)	15.3	6.9	3.7	2.3	1.5	1.1	0.8	0.7	0.6	0.6
$\epsilon$ (%)	65.1	77.8	85.0	89.1	91.9	93.9	95.9	96.6	97.0	97.0

Table 3: The ghost cubes rate and the cube reconstruction efficiency after 50 iterations of the sOMP + ML-EM algorithm, obtained for the ROSim of the IBD events generated with SoLO.

### 3.3 Conclusion

The Saffron2 reconstruction software was introduced in this chapter. It takes care of the whole path of transforming the waveforms into objects appropriate for physics analysis. Several fundamental tools were presented, including the muon track reconstruction, BiPonator, FPNT, and the CCube algorithm. The latter is central to characterising ES clusters and is therefore the cornerstone of the definition and selection of IBD candidates. Three different methods to solve the reconstruction problem were considered. A superior performance is reached for the one that is maximally profiting from the additional information about the nature of the performed measurement and the underlying physics of IBD. The final comparison between the three is detailed in Table 4. The results presented are obtained for an energy threshold level of 100 keV and illustrate the dominant performance of the combined sOMP and ML-EM method. The choice of the 100 keV threshold was dictated by the original energy threshold in the anti-neutrino selection analysis. Further improvements in reconstruction that will be discussed in Chapter 5.2.2 led to a reduction in this threshold. Though the actual values of the performance estimators (ghost rate, efficiency, resolution) are changing, it has been checked that the hierarchy between the methods is preserved. The combined sOMP + ML-EM algorithm is implemented in Saffron2 and used as a baseline in the SoLi $\partial$  collaboration.

Method	FISTA	FISTA+ML-EM	sOMP+ML-EM
$\hat{\mathcal{L}}$ (%)	15.8	11.4	6.9
$\epsilon$ (%)	75.3	76.4	77.8
$E_{res} \sigma$	0.13	0.13	0.13

Table 4: The performance comparison of the three reconstruction methods.

## 4 Electromagnetic energy calibration

In Chapter 3, the algorithm that solves the SoLi $\partial$  reconstruction problem was introduced. Performance was evaluated with respect to a given system matrix  $A$  and the absolute scale. The purpose of the following chapter is to complement it with the derivation of the SM, which embodies best of our knowledge about the detector response. Also, to explore the most relevant options to use as the absolute energy scale. In other words, the detector has to be calibrated, and, practically, this task splits into two:

1. Relative calibration of the detector:
  - Provides the system matrix knowledge;
  - Homogenises the detector unit (cubes) responses;
2. Absolute energy calibration.

The first part is completed using only the sample of horizontal muons described in Chapter 3, while several options are discussed for the determination of the absolute energy scale.

### 4.1 The relative calibration of the SoLi $\partial$ with horizontal muons

To be selected, the calibration procedure has to meet several requirements. First, it must account for the differences in characteristics of the individual cubes. Hence, it has to be performed at least at the per-cube level. An additional layer of detail, *i.e.* calibration performed on the per-fibre level, is preferable to improve the understanding of the detector behaviour, but is not essential. Secondly, the detector is a dynamic system, *e.g.* the PVT is exposed to ageing, which decreases the number of the generated photons, and thus modifies the energy response during the data taking. Therefore, the calibration procedure must be performed regularly, with a frequency defined by the precision of the method (*i.e.* there is no need to calibrate more often if the uncertainty is at the same level or larger than the variation caused by the time evolution). This in turn provides the third requirement: the precision of the approach has to be at the percent level, which requires enough statistics for all the cubes/fibres. In summary, the accurate measurement of the light-sharing features contributes to the precise reconstruction of the impacted cube in the detector. In its turn, it makes possible the design of the event signature according to its topological characteristics.

The horizontal muons are capable of meeting all the requirements listed above, even the optional ones. Generally speaking, only a subset of the horizontal muons are considered for calibration purposes. It consists of muons that are horizontal enough to only cross one cube in a detector plane. Therefore, each cube crossed by the reconstructed track has a unique  $z$  coordinate. For the sake of simplicity of the notation, this subset is referred to in the following as horizontal muons. An example of a reconstructed horizontal muon track crossing the SoLi $\partial$  detector is shown in Figure 41. Selection of the horizontal muons only simplifies the calibration problem from 3D to 2D similarly to the case of solving the matrix equation for the reconstruction procedure in the previous chapter. As a reminder, the detector planes are optically decoupled with Tyvek sheets, hence each separate plane can be treated as a separate calibration problem. It is therefore possible to evaluate within

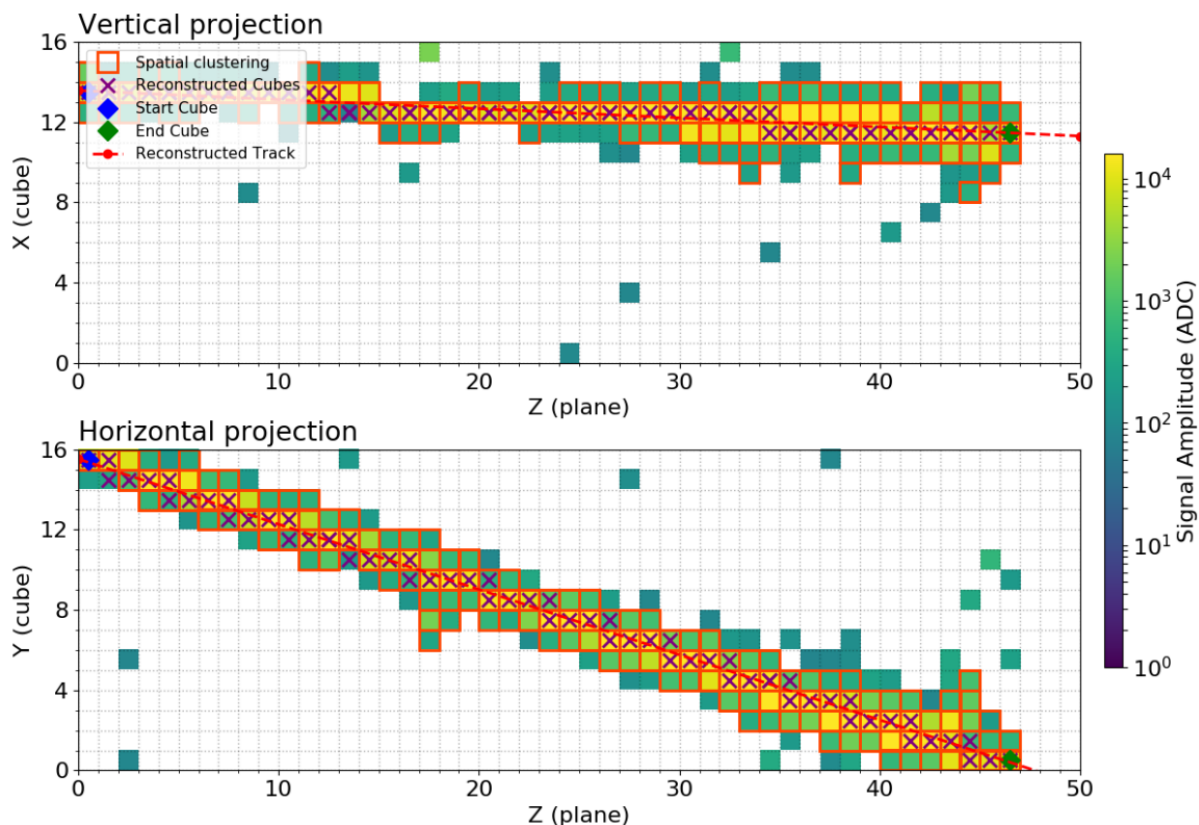


Figure 41: An example of the horizontal muon track (obtained from ROff data) crossing the SoLi $\partial$  detector in  $x - z$  and  $y - z$  planes. The purple crosses indicate the reconstructed cubes through which muon has made its path. The coloured cubes around the dotted red line, which represents the reconstructed track, are showing the cubes impacted by the light produced by the muon. This feature is further referred to in the text as the light leakages.

one plane the light sharing within the fibres from a unique energy deposit, as well as the light leakages towards the fibres from the neighbouring cubes. The total energy registered in the plane hence corresponds to the energy deposited by the muon candidate in this plane. Knowledge of the reconstructed muon path also offers information about the muon path length within the same plane. Therefore, the energy loss observable per cube  $\frac{dE}{dx}$  can be measured. Its measurement will be used to homogenise the detector response. It can be used as well, in principle, to provide an absolute energy-scale calibration if one can rely on external knowledge to predict its average value. The horizontal muon sample is composed of Type 2 muons tagged by the correspondent identification algorithm presented in Chapter 3.1.1, which was slightly modified and improved. The changes made to obtain the dedicated data set and the relative calibration procedure itself are described in more detail below.

#### 4.1.1 Scintillating photons behaviour in the SoLi $\partial$ cube

The initial understanding of the detector behaviour is gained from a simplified Geant4 optical simulation. It consists of one row of 16 PVT cubes without neutron detection screens, but wrapped with the reflective Tyvek paper and emulating the electronics read-

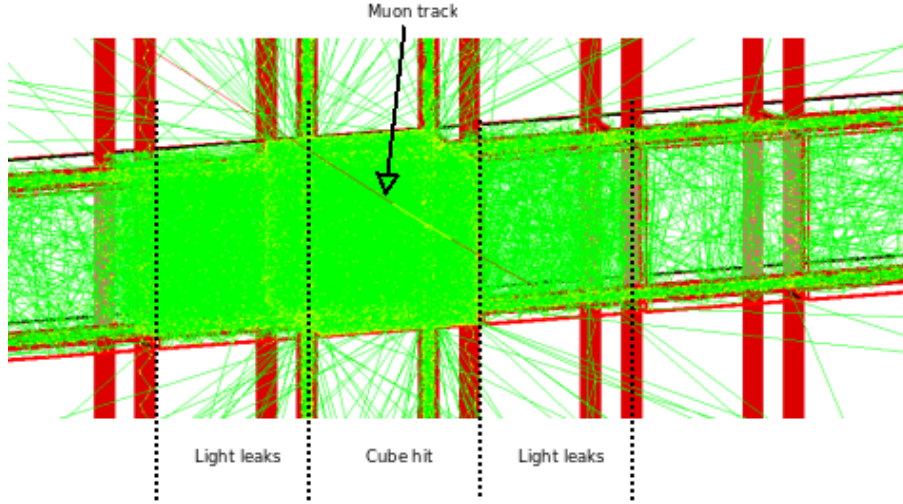


Figure 42: An illustration of the Geant4 optical simulation, obtained for a single photon launched into a row of simulated PVT SoLi $\partial$  cubes. The propagation of the scintillation photons to the neighboring cubes (the Light Leakages effect) is clearly seen.

out response. Both horizontal and vertical WLS fibres are paired with MPPCs, which read out the number of arrived photons. A single muon is generated such that it crosses the central cube of the system. The setup is sketched in Figure 42. It provides the picture of the scintillation photons that share space among the cubes and fibres of the apparatus. Firstly, it shows that the light sharing is not limited to the hit cube and a non-negligible fraction of scintillating photons are propagating to the neighbouring cubes, in particular via the holes created by the WLS positioning tolerances. This effect will be referred to as Light Leakages (LL) in the following. Accurate knowledge of this effect will decrease the level of ghost-cubes rate during the reconstruction. The fraction of photons that end up in the next to neighbouring cube, is at the sub-percent level and can be considered negligible. It is comparable to electronics noise (zero suppression is applied to remove it). The LL effect (and its assessment) is then limited to  $\pm 1$  cube. Secondly, the simulation reveals asymmetries in light sharing between the fibres. These asymmetries are observed not only for the horizontal and vertical fibres but also between the co-directional fibres as well. A per-fibre calibration is, therefore, desirable. Finally, the simulation output changes significantly if the WLS groove size is modified (it was originally set as  $3 \times 3 \text{ mm}^2$  WLS in a  $5 \times 5 \text{ mm}^2$  groove). This modification was done by changing the optical index of the volume between the WLS and the cube to be identical to that of PVT (emulating that the size of the groove is smaller or that the empty space is filled with an optical gel). This observation reveals that a very detailed simulation of the scintillating photon collection and detection would be necessary in order to describe the miscalibrations due to the actual geometry of the detector. Since these information are not available, the data must be used instead, and the horizontal muon samples is invaluable in that respect.

#### 4.1.2 Geant4 MC simulation of muons

A crucial input for the validation of the calibration method is the simulation of the detector response to an incoming signal in the full-scale detector geometry. It is operational to cross-check the track reconstruction algorithm, the LL level, both  $dE$  and  $dx$  components of the

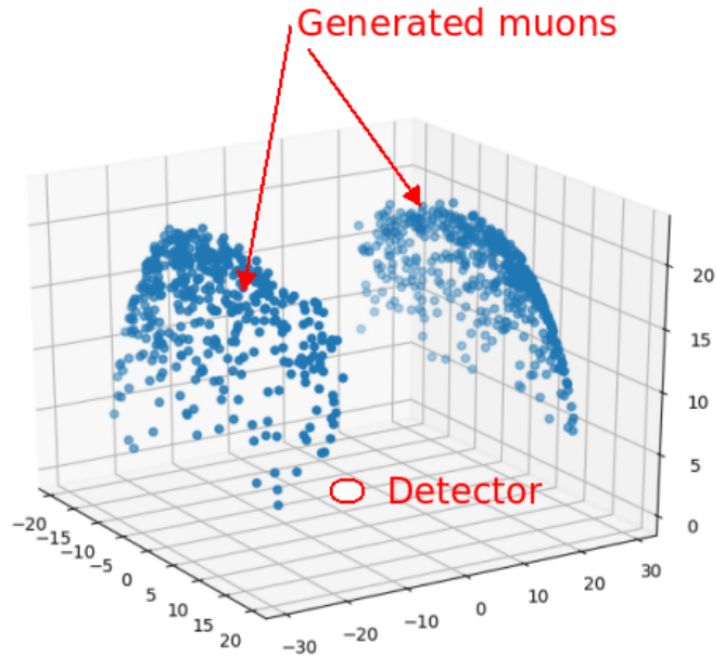


Figure 43: An illustration of the original strategy to obtain the muon Geant4 MC simulation. It includes the random muon generation in the 30 meters side square surface above the detector. This approach provides a sub-percent level efficiency for the events in which the muon is interacting with the detector.

energy losses, etc. As mentioned in Chapter 2.5.3, such a simulation is available via the CRY engine, but it is very resource-consuming out of the box. Therefore, simplifications were made to make it practical.

The default strategy implies a random generation of muons in a  $30 \times 30$ -meter square window on top of the BR2 building as shown in Figure 43. The number of muons that actually interact with the detector is low, since their trajectories are random. It is even more critical for horizontal muons. The total efficiency (fraction of useful events) after passing the Saffron2 processing is at the sub-percent level. This effect is mitigated by keeping for each muon the generated directions and energies, but applying to those that do not cross the detector the following changes:

1. shift the muon in the generation plane, until it crosses the detector volume;
2. the distance between the detector and the shifted muon (especially the horizontal one) can increase significantly. To decrease the computation resources required, the following simplification is considered:
  - assume a 30m radius sphere around the detector;
  - assume, that muon was initially generated on the sphere and hence cut the track at the surface;
  - the muon is supposed to have the initial direction and energy, since it is only air around the BR2 building;

The horizontal muons are selected by applying cuts at the tracks angles. The total efficiency after passing the Saffron2 processing increased to 45% with the modified strategy. An example of a simulated horizontal muon is shown in Figure 44

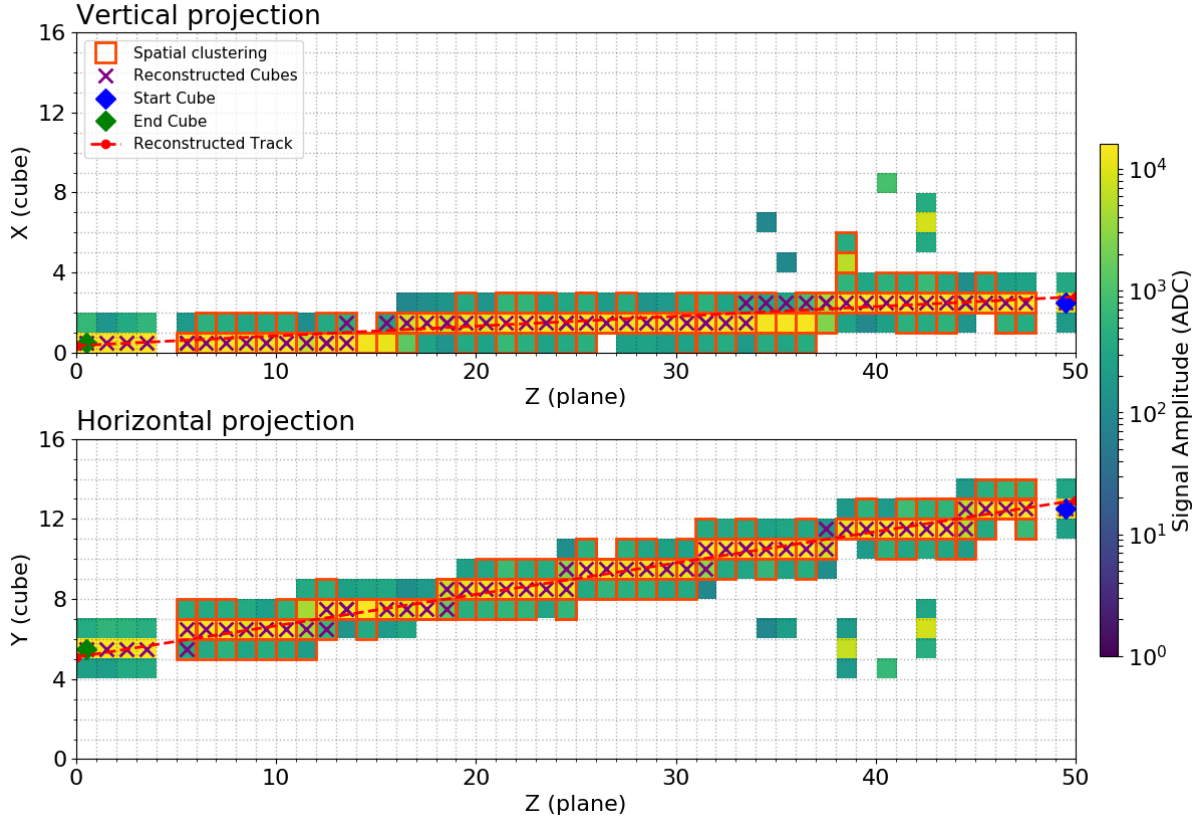


Figure 44: An example of the horizontal muon track (obtained from the MC simulation) crossing the SoLiD detector in  $x - z$  and  $y - z$  planes. The purple crosses indicate the reconstructed cubes through which muon has made its path. The coloured cubes around the dotted red line (reconstructed muon track) are showing the cubes impacted by the light produced by muon. It is used to perform the crosscheck of light leakages,  $dE$  and  $dx$  being obtained from ROFF data.

### 4.1.3 The horizontal muons selection

The initial muon selection corresponds to the definition of Type 2 muon implemented in Saffron. It requires only more than 11 horizontal and 11 vertical channels with an amplitude greater than 200 ADC counts. The tracks are obtained from the raw data, which is another advantage of using muons as the calibration tool. Additional conditions are placed on the characteristics of the track:

- The track has to enter each cube through a fiducial window (10% far from each cube's border as shown in the Figure 45);
- $x/z$  and  $y/z$  slopes have to provide  $\cos \theta < 0.8$  where  $\theta$  is the polar angle of the muon track (approximately  $40^\circ$ );

- the muon track length has to be  $\geq 7$  cubes. This allows one to reject for instance electrons misidentified as muons;
- start and end cubes of the track have to be on the border of the detector; this requirement allows stopping muons to be rejected, which can have in principle larger  $\frac{dE}{dx}$  values.

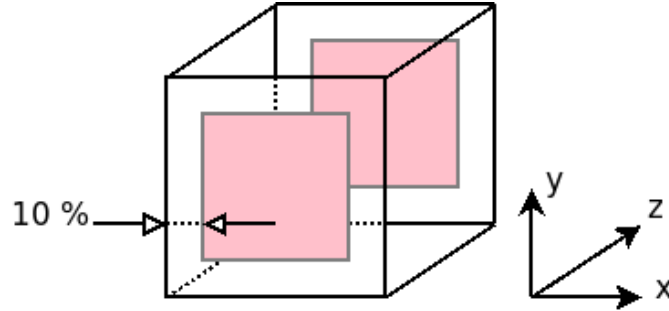


Figure 45: An illustration of the entrance and exit windows (shown in pink), that the muon reconstructed track has to enter for each cube of the track.

#### 4.1.4 Upgraded track reconstruction

The horizontal muon sample obtained with the initial set of conditions listed above corresponds to the first attempt to use them as a calibration sample [92]. It has been further improved to match the calibration purpose of this work. Let us begin with the muon track reconstruction algorithm. A precise evaluation of the length of the path covered by the muon is important for the determination of  $\frac{dE}{dx}$ . The strategy presented in Chapter 3.1.1 includes two additional steps:

- spatial clustering of the fibers (to remove outliers);
- performing a least square linear fit to the selected cubes in  $y-z$  and  $x-z$  projections;

The considered fit method is optimised for the “diagonal” muons, which are crossing multiple planes, rows, and columns. However, the performance is less good for vertical and horizontal muons. Additionally, the track-determination error distribution obtained from the Geant4 simulated sample shows that there is room for improvement. First, it was decided to change the approach to dealing with outliers. In most of the cases, these are far less energetic channels than the one hit by an actual track. Therefore, instead of performing spatial clustering, the fit method is changed to a *weighted* least squares linear fit, so that the more energetic fibres contribute more to the track reconstruction. This is a rationale similar to that advocated for the sOMP approach for the ES cluster reconstruction problem. Thus, the fit is forced to pave the way through the most energetic channels. It is convenient to represent the results of the track fit in terms of the polar angles of the track. Figure 46 displays the uncertainties on the two polar angle projections, comparing the former approach adopted in the collaboration and the energy-weighted track fit proposed in this work. A significant improvement is obtained in the definition of the track.

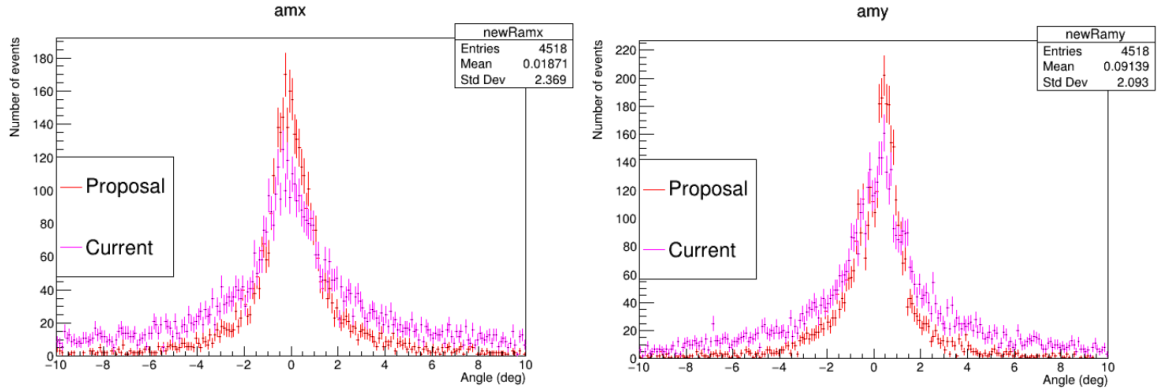


Figure 46: The comparison of performance in the horizontal muon tracks reconstruction by two different methods: spatial clustering (pink) and weighted fit (red). The performance is assessed by comparing the divergence of obtained track parameters from the Geant4-level true-information. The parameters include two polar angles in  $x - z$  (left) and  $y - z$  (right) planes. The weighted fit method shows better performance.

#### 4.1.5 Dead fibres and overflow channels

There are 4 fibres traversing each SoLi $\partial$  cube. If there is an energy deposit in it, the 4 read-out fibres are, in principle, receiving a fraction of the scintillating photons. There are, however, several scenarios for which this is not the case. The first one appears when the energy contribution is not enough for the fibre photons to meet the threshold level; since muons are depositing large energies on average, it is not the main case. Another one appears when one or several fibres are dead. Some of them are dead permanently (most of these dysfunctional fibres are concentrated in Module 5) or temporarily. The latter happens if a fibre receives too much light and the electronics is no longer able to cope with it. According to ROff studies, a single channel saturates at 15700 ADC counts. It is an unfortunate feature of the read-out electronics, but when a channel saturates, the corresponding event buffer requires to be reset in order to transmit again nominally the read-out information, and this reset can only occur at the beginning of a new run. Therefore, the "saturated" fibre remains dead until the end of the 8-minute run. Since muons deposit high energies, they are likely to produce dead fibres. The time evolution of the number of reconstructed with different number of fibres is presented in Figure 47. The fibre dying effect has two main implications. The first one is related to the calibration procedure. The cubes were reconstructed with the fewest of four active fibres, providing a less accurate energy measurement than the others. Therefore, they have to be rejected as much as possible. The only cubes which one cannot dismiss are with the permanently dead fibres. They are kept in the procedure, since otherwise there is no straightforward way to attach the calibration values to them. The second implication concerns the reconstruction and the read-out simulation. The reconstruction algorithm must correct for the dying fibre effect, regardless of its origin. In the CCube algorithm, the system matrix elements which correspond to a dying fibre during a run are switched to zero (and restored with the fibre at the beginning of the next run). The frequency of the fibre dying effect was estimated with the BiPo background sample. With that knowledge at hand, it was implemented into the ROSim in order to emulate the effect in the simulation.

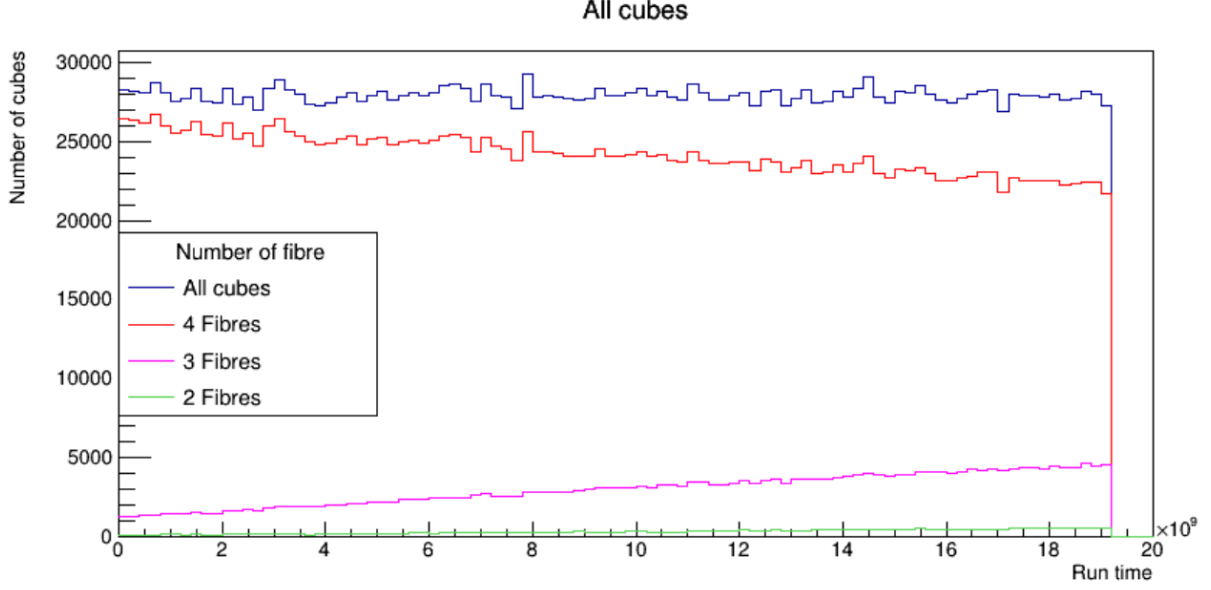


Figure 47: The time evolution of the number of cubes reconstructed with different number of fibres within one run of ROff data. The total number of cubes (blue) is shared among 4 (red), 3 (purple) and 2 (green) fibres cubes.

#### 4.1.6 KL divergence

In order to improve the quality of the light sharing evaluation, it is advantageous to define a well-behaved (hence, Gaussian) response of the detector by removing the outlier values. There is a large variety of methods available; the Kullback–Leibler (KL) divergence [99] method was chosen. Generally speaking, the KL divergence is a type of statistical distance (or dissimilarity test), quantifying how much a probability distribution  $p_1$  is different from a reference probability distribution  $p_2$ . In the case of SoLi $\partial$ , both are Poisson distributions; hence, the KL divergence is given by:

$$\begin{aligned}
 KL(p_1 \parallel p_2) &= m = \sum p_1(x) \cdot \ln \frac{p_1(x)}{p_2(x)} = \left| p_i = \frac{\lambda^x \cdot e^{-\lambda}}{x!} \right| = \\
 &\sum p_1(x) \cdot \ln \frac{\lambda_1^x \cdot e^{-\lambda_1} \cdot x!}{\lambda_2^x \cdot e^{-\lambda_2} \cdot x!} = \sum p_1(x) \cdot [\ln \lambda_1^x \cdot e^{-\lambda_1} - \ln \lambda_2^x \cdot e^{-\lambda_2}] = \\
 &\sum p_1(x) \cdot [x \ln \lambda_1 - \lambda_1 - x \ln \lambda_2 + \lambda_2] = \ln \lambda_1 \sum p_1(x) \cdot x - \lambda_1 \sum p_1(x) - \\
 &- \ln \lambda_2 \sum p_1(x) \cdot x + \lambda_2 \sum p_1(x) = \lambda_1 \cdot \ln \lambda_1 - \lambda_1 - \lambda_1 \cdot \ln \lambda_2 + \lambda_2 .
 \end{aligned} \tag{58}$$

The final expression is, hence, the following:

$$\lambda_1 \cdot \ln \lambda_1 - \lambda_1 - \lambda_1 \cdot \ln \lambda_2 + \lambda_2 - m = 0 . \tag{59}$$

This class of equations is solved with a Lambert function  $W$ . This is a multivalued function with different branches, which works only for certain values of  $\lambda_1$  and  $\lambda_2$  (which are defined as the expected values of the two Poisson distributions, considered before). To activate the principal branch for the SoLi $\partial$ -like expected values (0.25 for the light sharing in the main cube and 0.05 for LL), a slight modification to Equation 59 is performed:

$$\lambda_1 - \lambda_2 + \lambda_1 \cdot \ln \lambda_1 - \lambda_1 \cdot \ln \lambda_2 - m = 0 , \quad (60)$$

where  $m$  is the mean of the Gaussian fit of the initial  $x$  distribution,  $\lambda_1$  is considered to match the reference constant value and  $\lambda_2$  represents the distribution of the light sharing measurements. Then, Equation 59 is solved for  $\lambda_2$  as follows:

$$\lambda_2 = \lambda_1 \cdot W\left[\frac{1}{\lambda_1} \cdot \exp\left(1 + \lambda_1 \cdot \ln \lambda_1 - \frac{m}{\lambda_1}\right)\right] . \quad (61)$$

#### 4.1.7 SM derivation. Light sharing

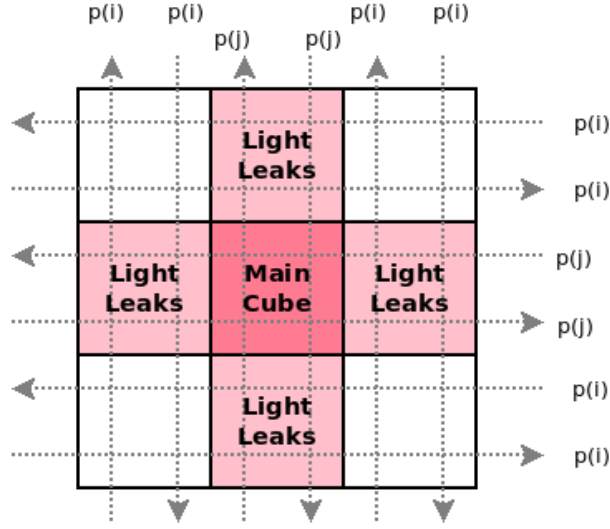


Figure 48: An illustration of the simplest calibration problem: it corresponds to a single plane and a unique cube crossed by the muon track. The total energy deposit is shared between the main cube (pink), its fibres (projections  $p_i$ ), the neighboring cubes, which are receiving light due to the LL effect (light pink) and their corresponding fibres (projections  $p_j$ ).

With all adjustments and improvements completed, an actual relative calibration procedure can be developed. The objective is to derive the SM elements. The first stage consists of filling the matrix with initial values, determined from the light sharing. At this stage, only the amplitudes of the channels attached to the muon tracks are required. For the sake of simplicity, let us consider the simplest calibration problem processed by the algorithm: there is a unique plane, crossed by the horizontal muon, and hence there is only one hit cube. From the optical simulation output it is known that the LL are propagated only to the neighbouring cubes in the  $x$  and  $y$  directions. Thereby, the region of interest is shorten up to a volume of  $3 \times 3$  cubes. It is shown in Figure 48. The energy contribution of the hit cube is shared between 12 fibres: 4 from the main cube itself (with projections denoted  $p_i$ ) and 8 (4 horizontal and 4 vertical) from the neighbouring cubes (with projections denoted  $p_j$ ). Therefore, there are 12 SM values associated with each cube. The sum of all 12 channel amplitudes provides an estimate of the total energy deposited in the plane. For each channel, the projection is composed as the multiplication of the number of photons arrived ( $n$ ) and the MPPC gain ( $g$ ). Since the detector was equalised with respect to the

gain, it is considered identical for all channels. Therefore, the light-sharing function ( $f$ ) is defined as:

$$\begin{aligned}
 p(k) &= n(k) \cdot g(k) = n(k) \cdot g \\
 n_{\text{plane}} &= \sum_k n(k) \implies E_{\text{plane}} = n_{\text{plane}} \cdot g \\
 f(k) &= \frac{p(k)}{E_{\text{plane}}} = \frac{n(k)}{n_{\text{plane}}} .
 \end{aligned} \tag{62}$$

The latter expression provides the sharing of photons between the fibres. It is conveniently defined in the same way for the main cube and the LL cubes. The number of photons  $n$  follows the Poisson statistics. Thus, the KL divergence method introduced before can be applied directly. The result of its application is shown in Figure 49.

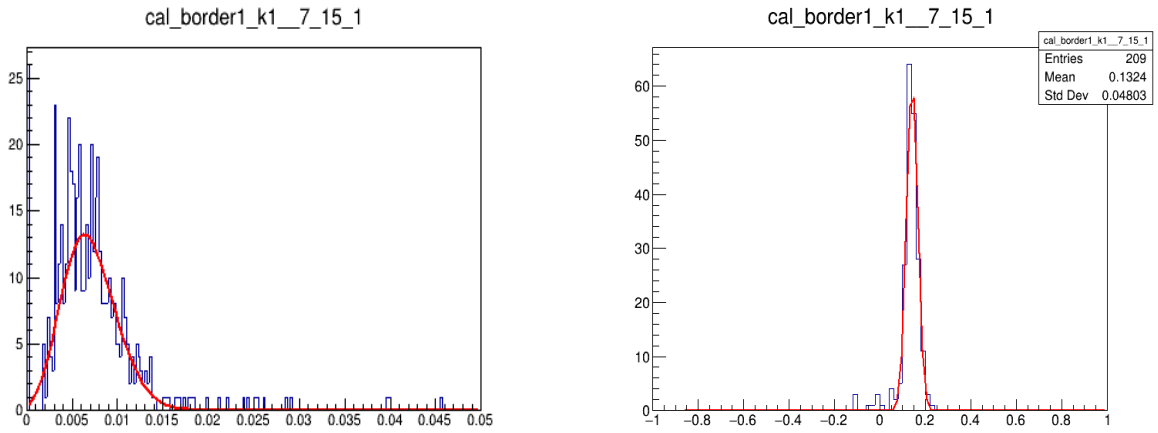


Figure 49: Left: distribution of the light fraction of the total signal deposited in cube 7, 15, 1 (in the X, Y, Z notation) and carried out by one fiber out of the 12 triggered. In this example, the fiber is from the cube adjacent to the energy deposit (hence from light leakages). The right plot exhibits the same distribution transformed with the KL divergence method. It follows a Gaussian behaviour and removes the outliers, therefore improving the center of the peak position determination.

#### 4.1.8 SM derivation. Homogenisation of the response

The second stage of the relative calibration is aimed at capturing the individual features of the cubes. They induce the variation of the detector response that must be calibrated. This is the place where the reconstructed muon track is used explicitly. It is required to evaluate the muon path length in the plane. By combining it with the total energy of this plane (the same sum of 12 fibres), the energy loss  $\frac{dE}{dx}$  is estimated as:

$$\frac{dE}{dx} = \frac{E_{\text{plane}}}{dx} . \tag{63}$$

Similarly to the light sharing derivation, let us consider a single cube for the sake of simplicity. The energy loss in the cube is calculated for all the muons that crossed it. As mentioned previously, not all the reconstructed cubes are considered to derive the SM

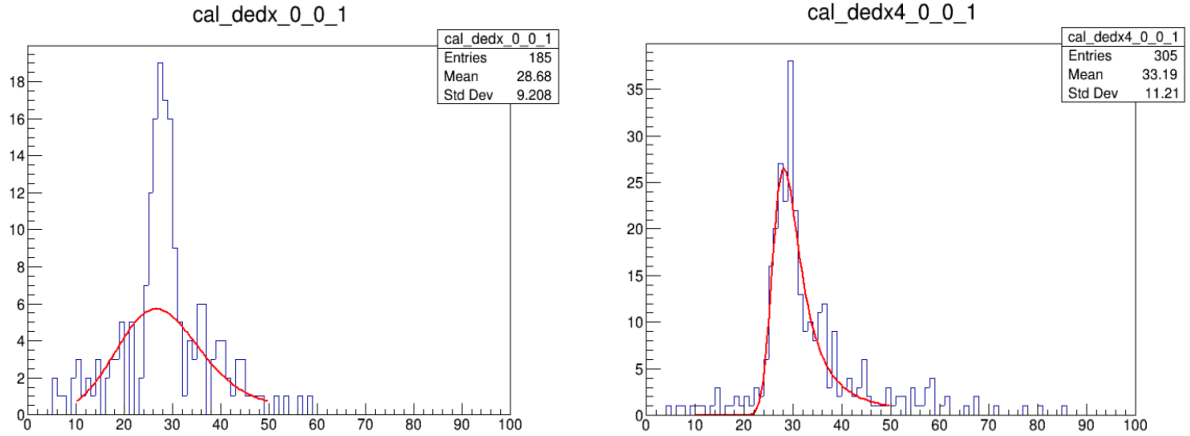


Figure 50: Left: the raw  $\frac{dE}{dx}$  distribution for the 0, 0, 1 cube (in the X, Y, Z notation) obtained from merging the values of all the horizontal muons that crossed it. Right: the exact same distribution with the implementation of the improved muon track reconstruction and application of the additional cuts (4 active fibres and no overflow channels). The fit manages to converge with these established modifications. They allow the most probable value of the distribution to be precisely determined.

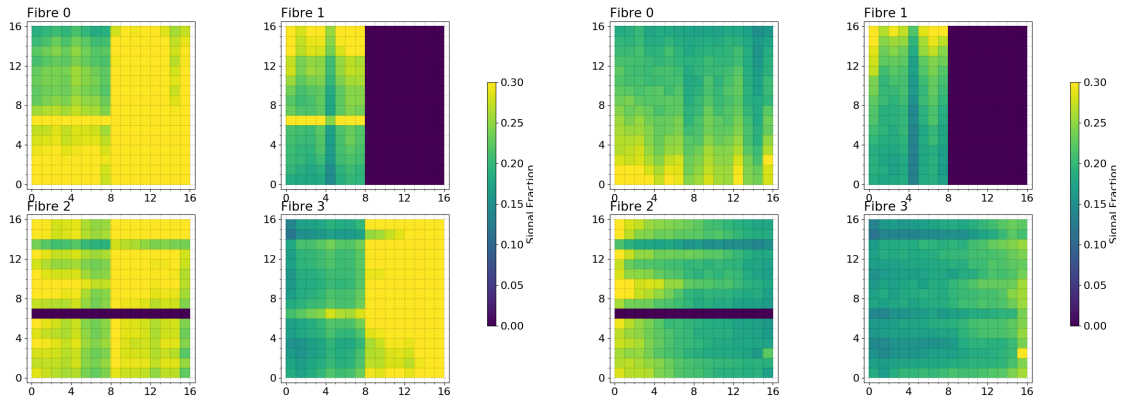


Figure 51: The light sharing distributions for the 4 main fibres of all the cubes in the plane 48 (dark blue corresponds to permanently dead fibres) before (left) and after (right) applying the homogenising procedure.

elements. If the hit cube was reconstructed with less than 4 fibres, had temporarily dead fibres, or presented an overflow channels, it is discarded. In addition, the upgraded muon track reconstruction is used and the dramatic improvement in  $\frac{dE}{dx}$  measurement can be seen in Figure 50. The resulting  $\frac{dE}{dx}$  distribution is fitted by a Landau function convoluted with a Gaussian. The model has 3 free parameters: the width of the Gaussian, the Landau scale factor, and its most probable value MPV ( $m_L$ ). The latter is the observable employed to homogenise the detector response. However, a reference is required to adjust the response of the individual cubes. It has been chosen as the average response of the detector estimated with the mean of the distribution of all values of  $m_L$ . It should be noted that other choices are possible. The light-sharing values for each of the 12 fibres attached to the hit cube are eventually weighted with respect to the average detector response:

$$f^*(k) = f(k) \cdot \frac{m_L}{\overline{m_L}} . \quad (64)$$

This transformation concludes the relative calibration of the detector and established the final values of the SM elements. The impact of the homogenisation procedure is the most pronounced for the planes with permanently dead fibres. In Figure 51 the response of the 4 fibres of each main cube in the plane 48 is represented. The dark blue area (half of the plane) corresponds to the dead channels. Even under such conditions, the relative calibration works well and allows the events appearing in that region of the detector to be reconstructed. Although their energy resolution will be degraded, these events are appropriate for further analysis.

## 4.2 Absolute calibration

The relative calibration being performed beforehand, it provides several benefits for the absolute energy scale derivation. For instance, it is enough to compute the conversion factor for a single cube, *e.g.* with the largest statistics available. In addition, multiple approaches can be tested without having to redefine simultaneously the relative calibration stage. Three of them are reported in this subsection. To begin with, it seems natural to try to employ the horizontal muons for the absolute energy calibration as well. There are several options to pick up the reference value for the conversion factor. A similar principle of calculation of  $\frac{dE}{dx}$  was selected. However, instead of fitting the Landau MPV distribution of the individual cube fits, the energy-loss measurements from all them are gathered. This distribution creates the mean energy response of an imaginary merged cube, which embodies the characteristics of all the cubes. For the reference value in MeV units, the same trick is performed for the equivalent Geant4 distribution. Yet, since all the cubes are identical in the simulation, this only results in a reduction of the statistical uncertainty. The previously introduced Landau function convoluted by a Gaussian is then fitted to both distributions. The conversion factor between the MPVs of the two fits is the definition of the absolute energy scale. In short, the absolute energy calibration procedure can be summarised as:

- $\frac{dE}{dx}$  fit for the imaginary cube at G4 level provides the data expectation in MeV/cm [1],
- $\frac{dE}{dx}$  fit for the imaginary cube to ROff distributions provides the data expectation in ADC/cm [2]
- The same assumption of the gain equalisation is considered for the whole detector, such that ADC to PA transition is established and controlled by the overvoltage settings. Therefore, the alignment of [1] and [2] provides the absolute energy scale in PA/MeV. This value is hereafter referred to as the Light Yield (LY).

The horizontal muon energy regime is high enough to claim that at the energy loss curve they live at or farther the relativistic plateau above the minimum ionisation point (see Figure 52). Without even considering high energy muons experiencing radiative energy losses in addition, the plateau is slightly rising and the average  $\frac{dE}{dx}$  is varying with the muon energy. A dedicated Geant4 study has been conducted in order to illustrate this

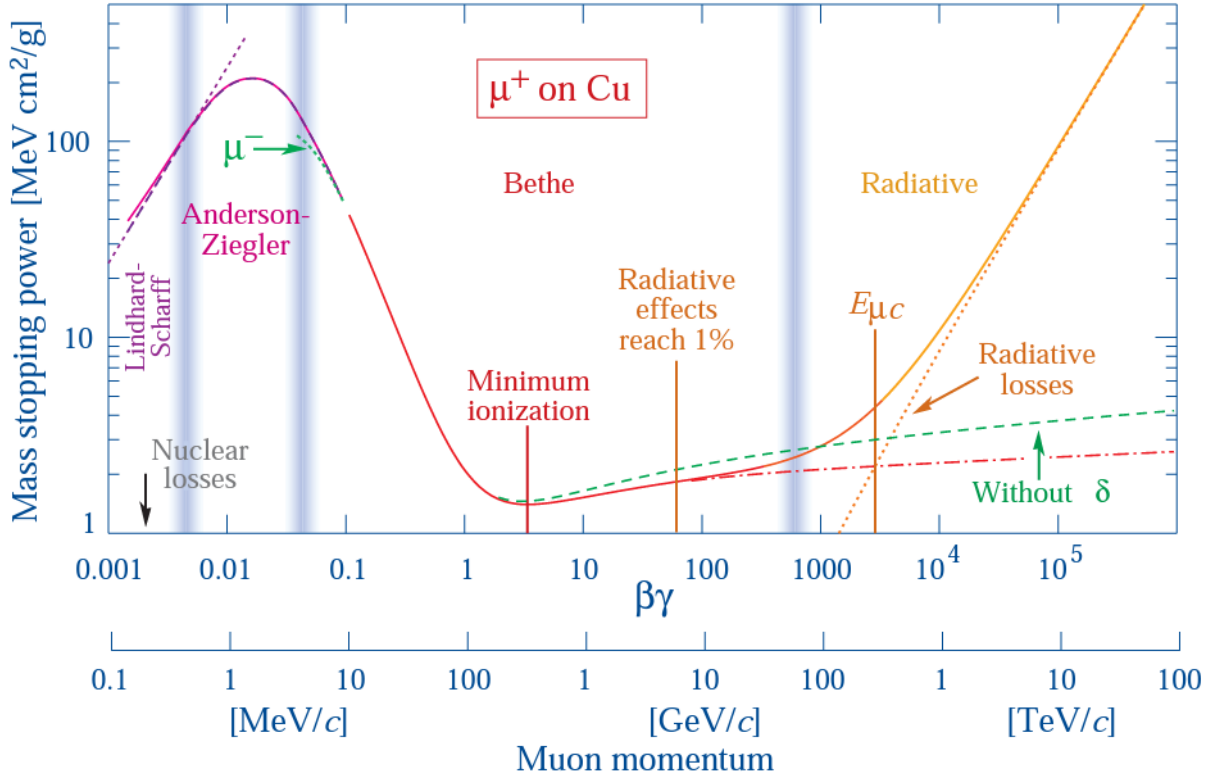


Figure 52: The mass stopping power for  $\mu^+$  in copper as a function of their momentum.

effect. To measure the stopping power, the setup had to be slightly different from the optical simulation described in Chapter 4.1.1. Firstly, it has to include all the 12 fibres between which horizontal muon is sharing the energy while crossing the plane. Second, to increase the statistics and remove outliers, the number of planes was increased to 3. Thus, the final setup sketched on the left plot of Figure 53 consists of a  $3 \times 3 \times 3$  set of cubes. Muons with three different energies are generated to cross the central cubes of the simulated setup. The distribution of simulated values of energy loss for each energy regime is summarised in the right graph of Figure 53. Variations in the average response at the level of 10% are observed. As it was touched above line, horizontal muon energies can reach the region where radiative losses become non-negligible. A more accurate knowledge of the energy distribution of horizontal muons would therefore be in order if one wants (and one does want!) to reach a precision of a few percents on the absolute energy scale. However, the obtained value is a good order of magnitude of the absolute energy scale and was a convenient choice to characterise the time evolution of the detector response presented in the document for instance. It has to be replaced by a more precise estimate, though, for the final physics analysis and two absolute calibrations with radioactive sources will be presented in the next sections.

#### 4.2.1 Calibration with $^{22}\text{Na}$

Natural candidates for the calibration of the absolute energy scale are provided with radioactive sources of known energy, handled with the CROSS system (see Chapter 2.2.5). Since CROSS places the sources between the modules (10 planes), the particles have to

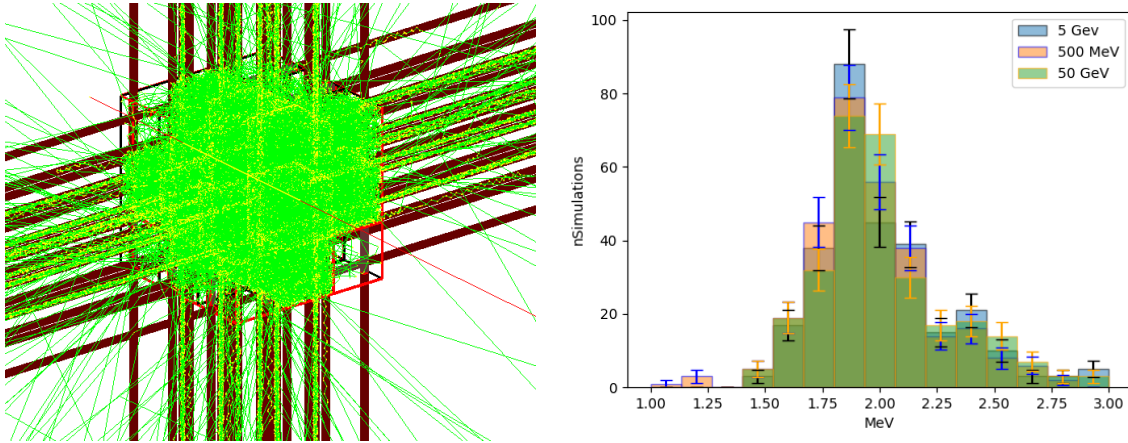


Figure 53: Left: the setup used for the muon energy loss evaluation in the Geant4 simulation. It consists of  $3 \times 3 \times 3$  PVT cubes, with Tyvek wrapping and emulates the electronics read-out; it does not include the neutron capture screens. Right: the energy loss distributions, obtained for the muons of three different energy levels - 500 MeV in pink, 5 GeV in blue and 50 GeV in green. The results are within a broad 10% agreement

penetrate at least 5 planes. This requirement imposes to use gamma calibration sources. The list of available options includes  $^{22}\text{Na}$  and  $^{207}\text{Bi}$  sources. The former offers two 511 keV annihilation gammas from  $\beta^+$  decay and a 1275 keV gamma particle from an excited state of  $^{22}\text{Ne}$ . The latter decays into one of three excited states of  $^{207}\text{Pb}$ , which provide gamma particles at 1770 keV, 1063 keV (84%) and 569 keV. Taking into account the initial energies and granularity of the SoLi $\partial$  detector, the only way to proceed is by studying the Compton edge (CE). Considering the expected energy resolution of the detector at the level of 15%, the CE fit is a complicated exercise. In collaboration, two independent methods were developed for this purpose. The Klein-Nishina analytical method relies on the evaluation of the interaction cross section convoluted by the Gaussian. It was developed at Subatech Nantes and was described in depth in the PhD thesis of David Henaff [100]. The second approach is numerical and relies on the convolution of the Geant4 reference energy distribution with a Gaussian modelling the energy resolution effects. It was designed at IJCLab in Paris and is thoroughly reported in the Ph.D thesis of Noë Roy [101]. With the previous version of the reconstruction, both methods were used in versions of the reconstruction preceding the work described in this manuscript. The numerical method was, however, used as a baseline to provide the relative and absolute calibrations of the electromagnetic signal (and the analytical method served as a cross-check. The comparison with the horizontal muons (relative calibration and absolute conversion factor) will be studied for the numerical method. Hence, a few explanatory lines about the algorithmic steps of the comparisons are given below:

- produce Geant4 simulations for each of the CROSS positions in the plane;
- process these simulated samples with the muon-induced version of both ROSim and data reconstruction;
- reject the cubes with less than 4 active fibres and events with more than a cube to

select clean events with the CE;

- apply the cuts to the processed data and check what is the combined reconstruction and selection efficiency; construct the efficiency dependence versus energy;
- create a cube template for the specific LY and energy resolution  $\sigma_0$ :
  1. consider each energy deposit  $E$  in this cube, simulated in Geant4;
  2. perform a convolution by the Gaussian with  $\sigma = \sigma_0 \cdot \sqrt{E}$ ;
  3. weight the intermediate template by the dedicated efficiency value;
  4. multiply it by the LY estimate.

The simulated templates are meant to cover all the parameter space of interest in terms of the LY output and the energy resolution. Templates must be processed under the same conditions and with the application of the same selection cuts as those applied to the calibration data. The energy distributions obtained for a given cube with different positions of the source are merged and compared to all the available templates. The one that best matches the data distribution is selected according to either a Kolmogorov-Smirnov or a  $\chi^2$  test. The values of the template parameters (LY and energy resolution) are taken as the calibration results for the given cube. Since, after the relative calibration with muons, it is enough to calibrate only the cube, the calibration procedure was performed solely for the cubes in front of the positions where CROSS can place the radioactive source. These cubes are supposed to have the largest statistics. The LY obtained are shown on the right plot of the Figure 54. The mean value of the Gaussian is obtained to be  $86.3 \pm 0.7$  PA/MeV and the width  $\sigma$  at  $11 \pm 1$  PA/MeV. The latter defines the typical expected precision of the method. Thus, it is obtained at the level of 6% for both parameters <sup>2</sup>. It can be observed that the absolute conversion factor (taken as the mean of the individual cube LY distribution) is 10% away from the value inferred by the muons. As was discussed above, this is the typical precision of the muon absolute scale prediction. It has been shown [102] with a Geant4-based optical simulation that for low-energy deposits such as those provided by <sup>22</sup>Na, the collection of the resulting light is not linear and can introduce a few percent biases in the determination of energy. These systematic effects have not been accurately quantified to date and are adding up to the statistical uncertainty. Should these <sup>22</sup>Na calibration values be taken as the absolute energy scale reference, a rigorous determination of the attached systematics is in order.

#### 4.2.2 Calibration with AmBe

The determinations of the absolute energy scale with muons and <sup>22</sup>Na presented before have one disadvantage in common. Their characteristic energy does not correspond to the typical energy of the IBD event. Despite the fact that the AmBe calibration source was initially considered solely for the neutron calibration, it can prove useful with the ES calibration as well. It is possible due to the 4.4 MeV gamma emitted by the excited <sup>12</sup>C in 60% of the cases:

---

<sup>2</sup>Additional uncertainty related to the knowledge of the relative muon calibration is assumed to be negligible, since the muon conversion factors are known with a precision better than the percent.

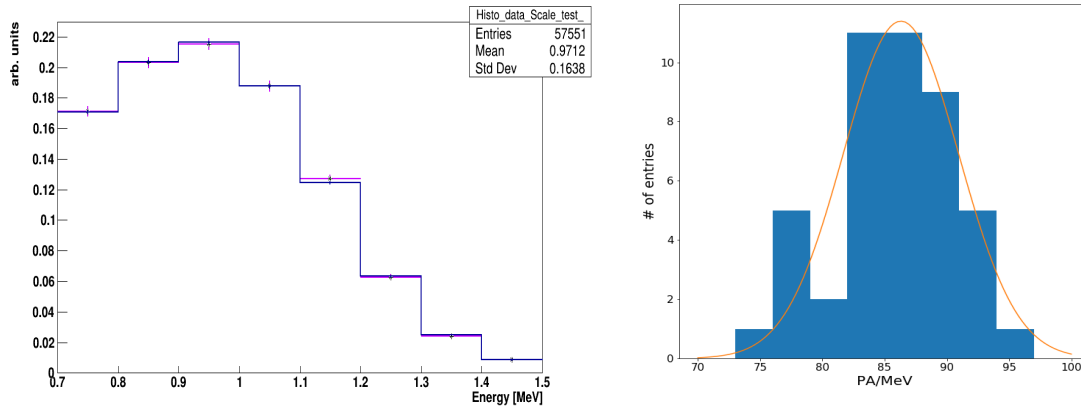
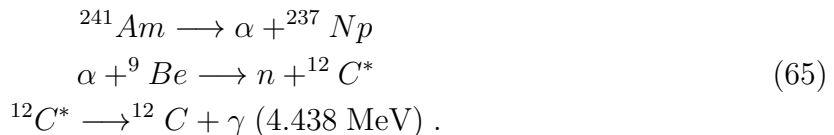


Figure 54: Left: an example of the comparison between the calibration data and the template, which provides the best result for the KS test. Right: the obtained LY for the cubes, which are placed in front of the possible calibration source positions.



Apart of being at the heart of the IBD energy regime, the AmBe gamma has another interesting feature. Because of its higher energy, it can also be induced through the creation of an electron-positron pair. The pair conversion has a non-negligible cross section for the 4.4 MeV gamma, although the interaction through Compton Scattering (CS) dominates the energy depositions. In this physics process, an energy of 1.022 MeV is spent to create the electron and positron, while the remaining energy is split between them as the kinetic energy. Regarding the sources mentioned above, the 1770 keV gamma of  ${}^{207}\text{Bi}$  could be another candidate for pair conversion calibration. However, the remaining 750 keV is too low for calibration purposes; it can also be seen that this energy level appears only in 7% of the total decays of  ${}^{207}\text{Bi}$ . Regarding the AmBe source, according to the Geant4 simulation in 3.5% of the cases, the  $e^+e^-$  pair is sharing a 3.4 MeV kinetic energy and hence lives in the heart of the IBD energy distribution. Moreover, in most of the cases, the  $e^+e^-$  pair deposit its energy in a single cube. AmBe source provides thus a mono-energetic calibration source.

Secondly, the positron annihilates after losing its energy and creates two annihilation gammas. This makes a signal signature identical to that of the IBD candidates. Thus, all the tools developed for topological identification of IBD are highly relevant and can be used to select  $e^+e^-$ . Finally, the neutron, issued by AmBe, can interact with  ${}^{12}\text{C}$  from the detector materials. The neutron is energetic enough to excite the  ${}^{12}\text{C}$  nucleus. During the further de-excitation, exactly the same 4.4 MeV gamma as in Equation 65 can emerge. This *a priori* background source becomes an additional signal, increasing the initial sample by 15%.

However, there is one significant difference compared to sodium calibration. The AmBe source does not only produce the events with pair creation. Hence, the energy region of interest is spoiled by the events caused by high-energy neutrons and gamma, which interacted

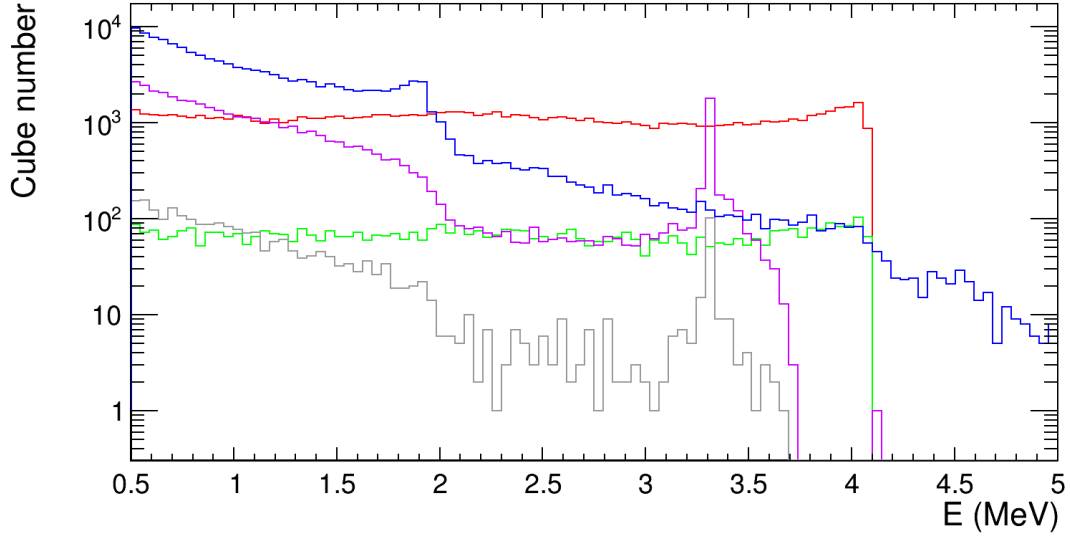


Figure 55: The Geant4 total energy corresponding to the neutron (blue), “original”  $\gamma$  (CS in red and pair creation in purple) and neutron induced  $\gamma$  (CS in green and pair creation in grey).

via the CS. Therefore, two templates are in order: signal and background. However, Geant4 level information scrutiny must be performed beforehand to gain understanding of the ES part of the signal. The events are first split according to the presence of the 4.4 MeV gamma, either the one coming directly from the AmBe source or the neutron-scattering-induced excited  $^{12}\text{C}$ . The events containing the 4.4 MeV gamma are further divided according to the process through which it interacted with the detector. That can be either Compton scattering or pair creation. To illustrate the events of interest, the total energy distribution per event is computed for all the signal sources described above and is shown in Figure 55, with the purple and grey parts being the desired signal. However, within an actual event, the neutron-induced and electromagnetic categories can overlap. The primary task is to design a selection of the cube where an  $e^+e^-$  pair has occurred and contributed dominantly to the total deposited energy in this cube. The simplest way consists of selecting the cube with the highest energy in the event. The result of such a choice is presented in Figure 56.

The red distribution represents the background sample and consists of a combination of neutron- and gamma-induced events. For the former type, one can observe the Compton edge issued from the neutron capture on hydrogen of the detector and the subsequent release of a 2.2 MeV gamma. As for the latter, these are the events where the interaction happened through a Compton scattering. The correspondent Compton Edge is found to be around 4 MeV. The green signal distribution has the expected shape, but a small knee is observed on the left-hand side of the distribution. From the size (and CE-like shape) of the additional energy contribution (further confirmed by the study of the Geant4-level true “information”), one can conclude that it appears when gamma resulting from the positron annihilation gamma makes an energy deposit in the same cube as the one where the pair was issued. Obviously, these events will not exhibit the same energy resolution. This is the place where IBD tools can be used. The categorisation of the events according to their geometrical properties is presented and justified in Chapter 5. For now, let us postulate

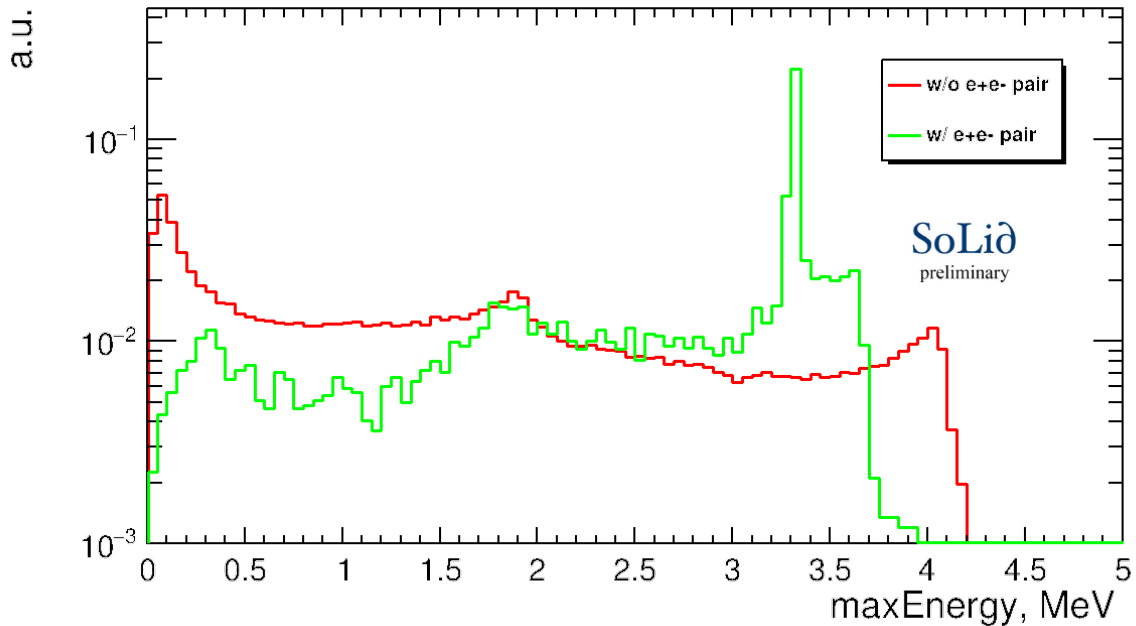


Figure 56: The energy distribution for the most energetic cube per event in the AmBe ROSim simulation sample (background and signal are superimposed). It consists of two subsets: with (in green) and without (red) the  $e^+e^-$  pair creation. The peak around 3.4 MeV corresponds to the  $e^+e^-$  pair energy deposit. The right-hand tail of the green distribution is addressed further in the text.

that only the events with a clear (*i.e.* no additional energy deposits)  $3 \times 3 \times 3$  envelope around the most energetic cube (the assumed place of the pair creation) and two additional reconstructed EM clusters (which are supposed to correspond to the annihilation gamma) are considered. These simultaneous requirements ensure that the  $e^+e^-$  pair deposited its energy in a unique cube and that this cube energy is not modified by the presence of annihilation gamma contributions<sup>3</sup>. Another advantage of this approach is that it is unlikely that the generic background sources reproduce a geometrical template with the high-energy cube in the middle of the two back-to-back gamma. This selection is hence supposed to reduce the background contamination and ensure an adequate measurement of the cube energy. To have access to the categorisation information, the Geant4 simulation was processed with Saffron2. The simulation was slightly modified to take into account the presence of an intermediate-energy neutron. The IBD neutron typical energy is at the keV scale, and thus, it is not capable of creating additional cubes via proton recoils. However, neutrons from the AmBe source can issue those significant proton recoils. To mitigate this effect from this analysis, the cubes that are at a distance less than 3 cubes from the reconstructed NS are removed from the composition of the EM clusters outside the envelope. This value is educated thanks to a dedicated Geant4 scrutiny, which shows that the neutron-triggered cubes are at distances lower than those of the annihilation gamma. Furthermore, any cube with an energy above 0.6 MeV obeys the same restriction. The processed events which comply to the geometrical pattern discussed above (referred to

<sup>3</sup>If 511 keV gamma has experienced the Compton scattering in the cube of the pair creation, it would not have enough energy to escape the envelope and create an EM cluster.

as Topology 20) are selected and traced back at the Geant4 level in order to record its initial energy. The Geant4 and ROSim signal and background distributions are shown in Figure 57.

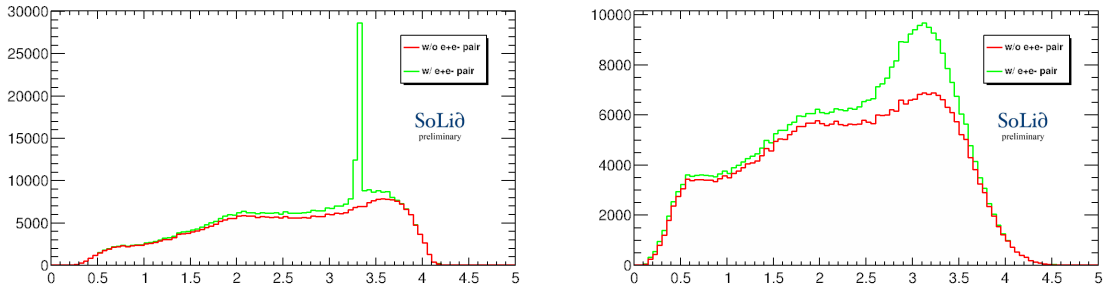


Figure 57: The stacked energy distributions for the most energetic cubes for events with (in green) and without (red) the  $e^+e^-$  pair creation. The selected events must have 2 reconstructed EM clusters and empty  $3\times 3\times 3$  envelope around the most energetic cube (aka Topology 20). The correspondent distributions are presented at Geant4 (left) and ROSim (right) levels. Both of them indicate the significance of the signal contribution.

This plot shows that signal contamination by annihilation gamma energy deposits has disappeared. Simultaneously, it shows the impact of the energy resolution on the Geant4 templates and reveals an extra complication for the template fit. The background component exhibits a structure (a bump behaviour) in the signal region. The fit method, similar to that developed for  $^{22}\text{Na}$ , is applied primarily to ROSim data samples. The first step is to search for the best pair of free parameters (scaling factor and energy resolution) independently for the signal and background. To do that, a scan over the parameter space is performed, searching for the best  $\chi^2$ . It is important to note that the meaning of the scaling factor is slightly different with respect to the  $^{22}\text{Na}$  calibration. Since the fit is performed to data already calibrated with muons, the scaling factor shows the difference between the LY defined by muons and AmBe. The comparison of the ROSim distribution with the transformed template with the best couple of parameter values is shown in Figure 58.

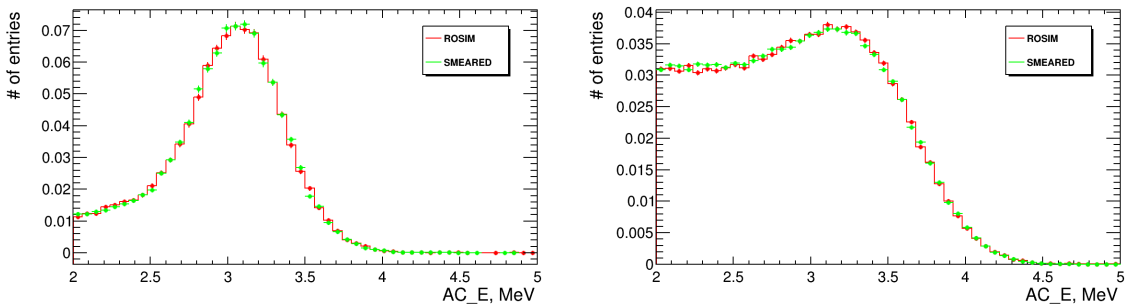


Figure 58: The comparison of the ROSim distribution with the Geant4 template transformed with the best pair of parameters (scale, resolution) obtained from the  $\chi^2$  scan. The distributions represent the energy of the most energetic cube for Topology 20 for the signal (left) and background (right) events.

Since the scans were performed independently for the signal and background samples, it was not granted to obtain the same result. This first cross-check is passed, as both samples converged on the values of the parameters (0.930, 14.7%). The latter value is indeed the energy resolution emulated in the simulation. The obtained value of the scaled factor hints at a LY value with AmBe 7% lower than what muons, which goes in a similar direction as indicated by the  $^{22}\text{Na}$  result. The next step in the setup of the approach is to perform a real fit. An unbinned event-by-event maximum likelihood fit was designed for this purpose. It is performed with the RooFit toolkit provided by ROOT software. The transformed templates are converted to probability density functions (PDFs). The signal and background yields are the free parameters of the fit. The approach used for the determination of the absolute energy scale with muons is applied to transform the calibration data. Instead of selecting the unique cube, an imaginary mean cube is generated by gathering the responses from all the cubes. Figure 59 represents an example of such a fit.

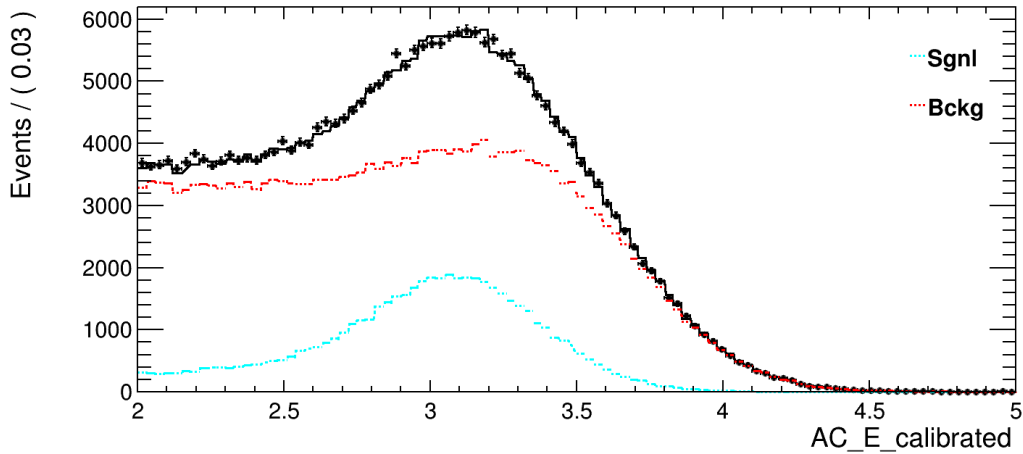


Figure 59: An example of the unbinned event-by-event ML fit. It is performed on the AmBe ROSim subset with only Topology 20 events considered (displayed as a black points). The total shape (in black) consists of signal (blue) and background (red) templates, which are defined from ROSim and further modified by shifting (light yield scaling) and blurring (energy resolution convolution). The correspondent yields remain free parameters of the fit. The best set of parameters is defined by scanning the log-likelihood and picking the minimal value. We obtain (0.933, 14.9%)

The best fit is chosen according to the value of the negative log-likelihood. It converges to the pair values of (0.933, 14.9%), which is close to the one obtained from the individual scans. This observation validates the calibration technique, and the fit of the free parameters to the actual calibration data can be performed. As mentioned above, AmBe was originally a source used for the neutron calibration. The trigger settings were thus tuned for the registration of a neutron signal. There were only two calibration campaigns during Phase I, where the trigger settings were modified to also read out the ES part. It is not the problem per se, one calibration point is enough, since the time evolution of the detector response can be controlled by the muon SM during the whole lifetime of the detector operation. However, despite the fact that the trigger settings were modified, they did not exactly match the IBD conditions. The differences in background and signal

contributions between ROSim and the calibration data are significant. Therefore, the calibration procedure cannot rely on the knowledge of the simulated signal efficiency or on an expected signal-to-background ratio. Since the simulation cannot be useful to define discriminative variables, an elementary selection based on a low cube ( $\geq 5$ ) multiplicity is then applied to the calibration data sample. Since the signal-to-background ratio cannot be inferred by the simulation, the signal and background yields are free to vary in the fit method. In order to cross-check the impact of the additional background, which might have been not simulated, the systematic study is performed. The anticipated assumption is that there is an additional contribution either in the transformed background template or in the calibration sample itself. In both cases, the linear component emulates an extra contribution with different contamination (0, 5, 10 or 20%). The results of the dedicated fits are collected in the Table 5. The table exhibits that the scale factor determination is stable irrespective of the conditions, which is not the case for the energy resolution. The fit tries to compensate unaccounted background by increasing it.

Modification level		0%	5%	10%	20%
Modified Model	Scale	93.16	93.24	93.35	93.52
	Resolution	14.45	14.10	13.96	13.90
Modified Data	Scale	93.16	92.99	92.87	92.63
	Resolution	14.45	15.35	16.02	17.45

Table 5: The fit results of the ROSim data with the modified model/data.

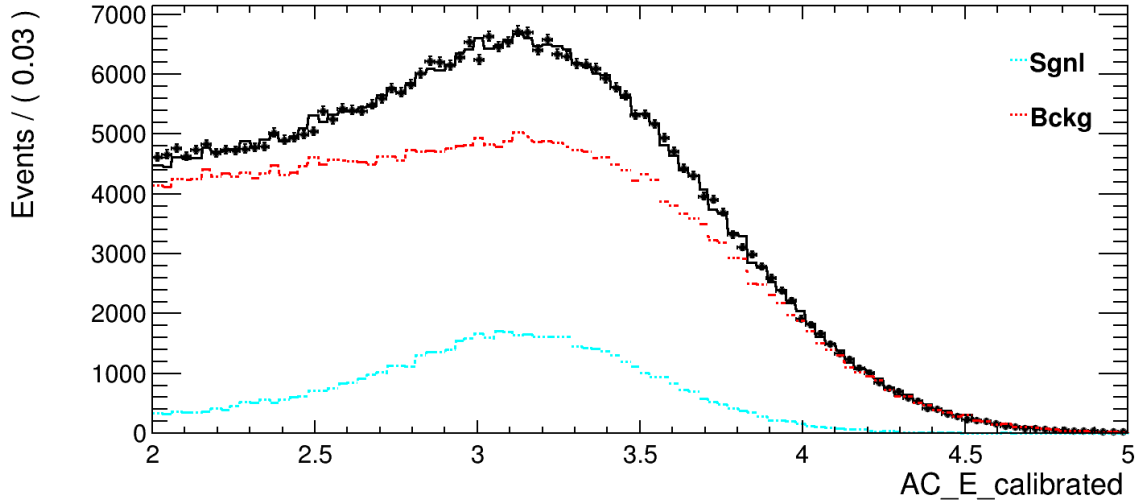


Figure 60: An example of the unboxed event-by-event ML fit. It is performed on the AmBe calibration data with only Topology 20 events considered (black points). The total shape (in black) consists of signal (blue) and background (red) templates, which are defined from ROSim and further modified by shifting (light yield scaling) and blurring (energy resolution convolution). The correspondent yields remain free parameters of the fit. The best set of parameters is obtained to be (0.955, 20.5%)

The scaling factor measurement seems stable when varying the background contributions to the AmBe calibration data sample. In turn, the systematic budget can be lower

than or close to the statistical uncertainty. A detailed systematic review is ongoing, and more sources of errors are going to be checked. Simultaneously, to improve the method, equivalent trigger conditions must be simulated with ROSim, and additional discriminative variables can be designed. For instance, it is known from the Geant4 analysis that the main source of background events are coming from multiple Compton scattering, mimicking the annihilation gamma. Thus, the cosine of the angle between the vectors (position source  $\rightarrow$  pair creation cube) and (position source  $\rightarrow$  reconstructed EM cluster barycenter) can be considered. For the background, these vectors are colinear and, hence, the cosine distribution is supposed to peak at +1, while signal events are flat. For now, the fit to the calibration data is performed with the elementary low-multiplicity requirement. The calibration data distribution and the result of the fit are shown in Figure 60. The best pair of parameters preferred by the fit is (0.955, 20.5%). The large value of the energy resolution might be a sign of the presence of an additional source of background. At the same time, the scaling factors obtained for the calibration data and ROSim differ. This deviation might hint either towards the same explanation about an unaccounted background source or to the necessity of the additional ROSim tuning.

### 4.3 Crosschecks and validations

The results of the relative and absolute calibrations obtained in this chapter can be questioned from different directions. The essential question regarding relative muon calibration is the precision of the method. In principle, one day of statistics is enough to perform it for all cubes. Practically, the results are there dominated by the statistical uncertainty, hiding the level of day-to-day variation. Thereby, it was decided to reduce the granularity and combine the data in 10-day periods (which is a compromise to align the precision with actual variations of the detector response). The statistical uncertainties in determining the light sharing for such a period are shown in Figure 61.

As it was mentioned before, the detector is a dynamic system. So, the second direction of cross-checks is an exploration of the evolution of the detector response in time. The information obtained from horizontal muons is also helpful in this respect. Firstly, the change in light sharing over time is examined. The PVT is exposed to ageing, which decreases the performance of scintillating photon generation. Moreover, it is not an isotropic process, thus some of the fibres can be more affected than others. Finally, the WLS are also exposed to ageing, but the scale of the effect is way less significant, according to the manufacturer's tolerances. To estimate it, one of the periods from the beginning of Phase I is taken as a reference and compared to the later periods: the immediately following 10 days, 6 months after, and a year after. It is presented in Figure 62. As expected, the deviation increases over time. The same behaviour is obtained for all four main fibre distributions.

Secondly, the absolute energy scale evolution can be tracked. This method is still limited by the precise knowledge of the muon energy distribution. However, since the atmospheric muon energy characteristics remain the same, the calibration values will hint at the evolution trend of the detector response. Figure 63 shows the evolution of the unique LY factor, which is currently injected into the system, versus time (one factor is enough, since the detector was homogenised). As expected, the conversion factor is decreasing due to the ageing of the PVT. The average effect is around 4-5% per year, which is slightly higher than specified on the data sheet. It could be explained by a chiller failure that occurred

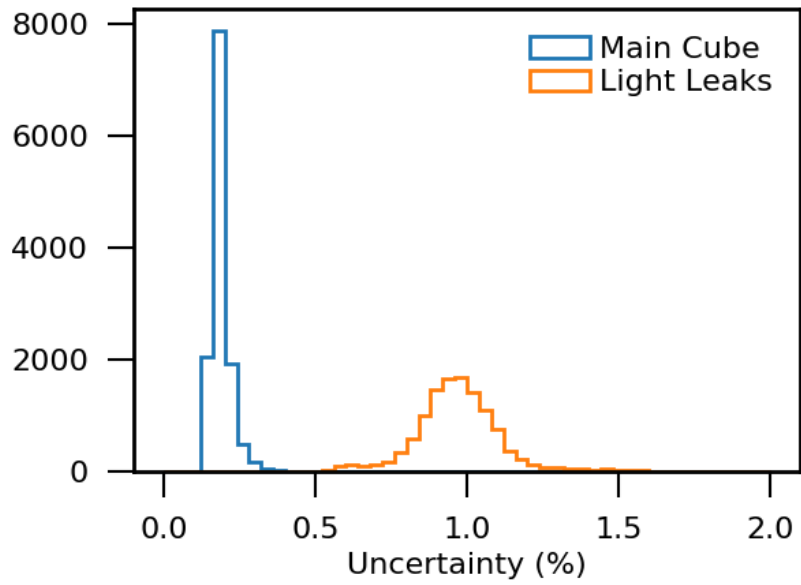


Figure 61: The distribution of the statistical uncertainty associated to the light sharing determination based on 10-days statistics of horizontal muons. The blue distribution corresponds to the main cube and the orange one to the neighboring cubes.

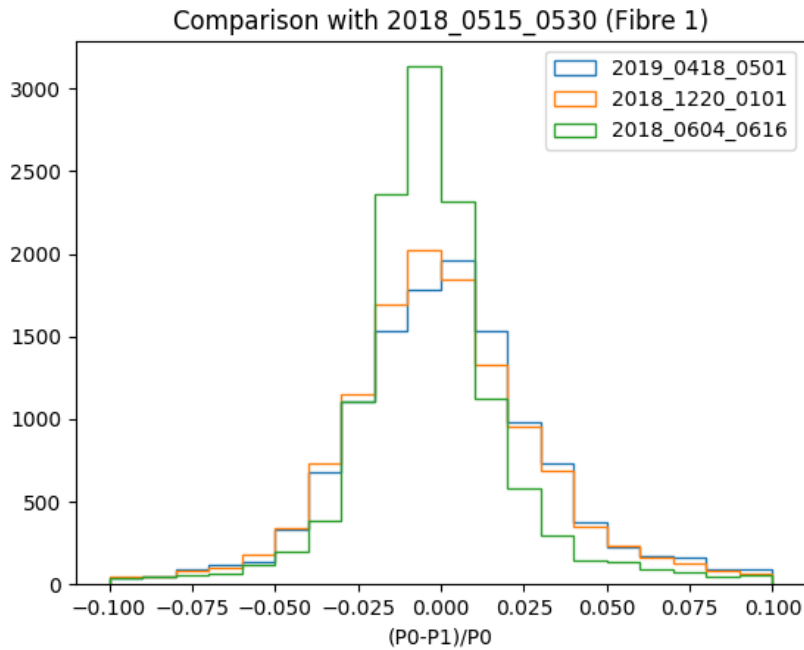


Figure 62: The relative time evolution of the light sharing in one of the vertical fibres of the main cube. The reference period is taken from the beginning of the Phase I and the others are from later by 10 days (green), 6 months (orange) and 1 year (blue).

in May 2019. The temperature in the detector container increased to  $50^\circ$  instead of the usual  $12^\circ$  in standard operation. The accident is believed to have caused a degradation

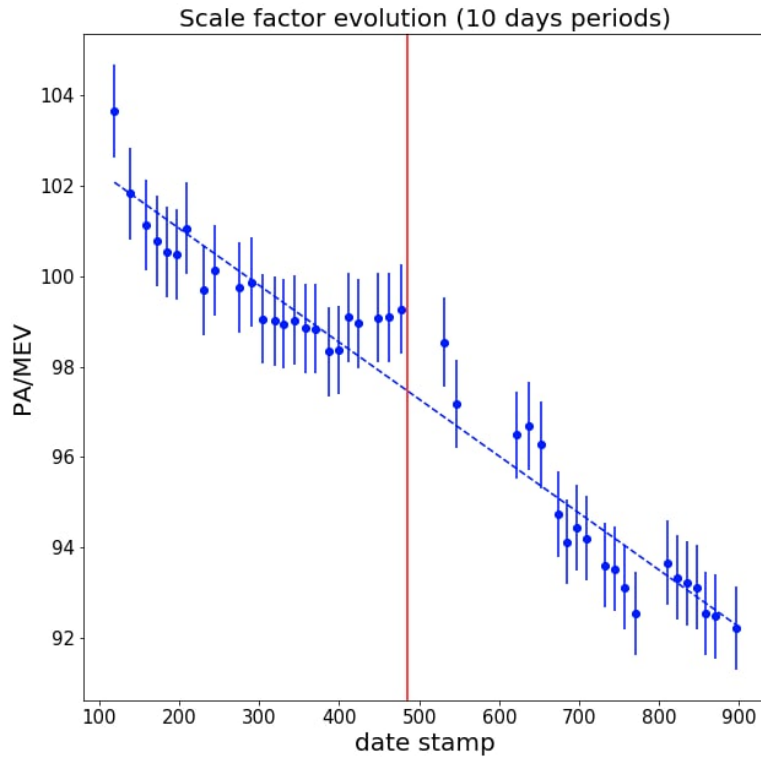


Figure 63: The absolute energy scale factor obtained with the horizontal muons calibration for the 10-days period versus time. The dashed line shows the linear fit, indicating the 4.5% PVT aging effect. The red solid line indicates the time stamp of the chiller failure.

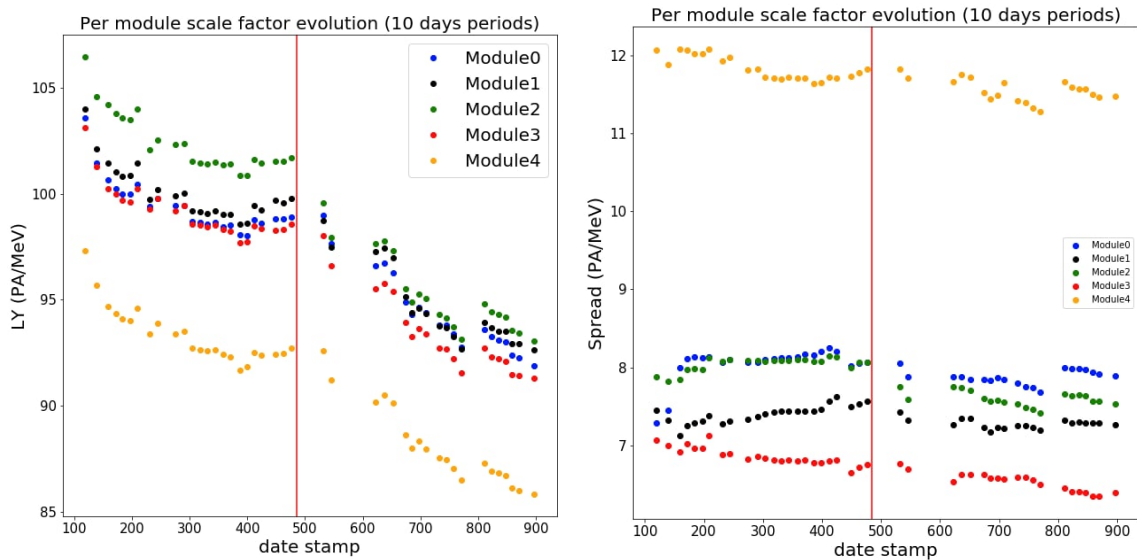


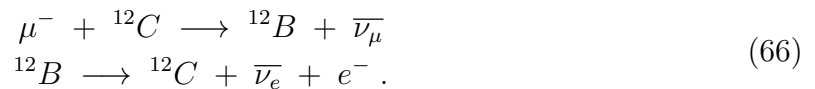
Figure 64: The average absolute energy scale factor (left) and the spread (right) per module obtained with the horizontal muons calibration for the 10 days period versus time. The red solid line indicated the time stamp of the chiller failure.

in the performance of the PVT. One step further is to increase the granularity of the cross-check and explore the evolution of the response per module. To do that, the reverse homogenisation was done to obtain access to the individual LY values of the cubes. The

result of the module-by-module check is presented in Figure 64. The last module of the detector concentrates most of the dead fibres; thus, it is expected that the average LY in the module is lower, while it is determined with a slightly worse precision. This effect is mitigated if the planes, placed after plane 45, are discarded. This is a region of the detector that accumulates most of the dead fibres. Without it, the performance of the sub-module 5 improves to an average one.

### 4.3.1 Cosmogenic background determination

An additional way to cross-check the performance of the reconstruction and calibration methods introduced in the work described by this manuscript is to consider standard background candle energy distributions if available and compare them to the Geant4 predictions. Cosmogenic muon-induced backgrounds are invaluable for this. Cosmic muons can be stopped in the detector after having issued very-high energy deposits. They are captured primarily by the  $^{12}\text{C}$  nuclei contained in the detector materials. Subsequently, it triggers the following chain of reactions:



The  $^{12}\text{B}$  nuclei are a well-known radioactive  $\beta$  source. The half-life time of the isotope is short (20.2 ms) and the end-point energy of subsequent  $\beta$  decay is 13.4 MeV. Hence, the energy distribution completely covers the IBD range. The selection is based on identifying the muon tracks that are stopping inside the detector. Then a related ES cluster is searched. This cluster has to be close in space and time to the reconstructed muon. To suppress the background, the ES cluster energy is required to be above 3 MeV. In addition, events with additional muon candidates within the  $200\mu\text{s}$  time window are removed. The yield of  $^{12}\text{B}$  is estimated from a fit of the time distance between the muon and the ES cluster. Finally, the energy spectrum is determined via the sPlot technique. The comparison between the measured spectrum and the reference one from Geant4 is shown in Figure 65. The agreement is within 5% in the entire energy range. The selection was designed and tuned by the LPC Caen collaborators. An exhaustive description can be found in the PhD thesis of Savitri Gallego [93]. These results provide very strong confidence in the horizontal-muon relative calibration. Indeed, this standard candle background was not observed in the data by collaboration prior to the use of the muon calibration.

## 4.4 Conclusion

The results of this chapter complement the previous one and finalise the tools for data processing by providing the relative and absolute calibration of the SoLi $\partial$  detector. The relative calibration is provided by the horizontal muons and offers the direct determination of the expected light sharing at the subpercent precision level without relying on any assumptions as the attenuation length. On the other hand, for the absolute energy scale evaluation, three different methods were presented. Each of them has certain disadvantages, which can be mitigated by combining all available sources. For instance, the horizontal muon approach, which is selected as the baseline for this thesis, is providing a new calibration value every 10 days and hence accounting for the time evolution of

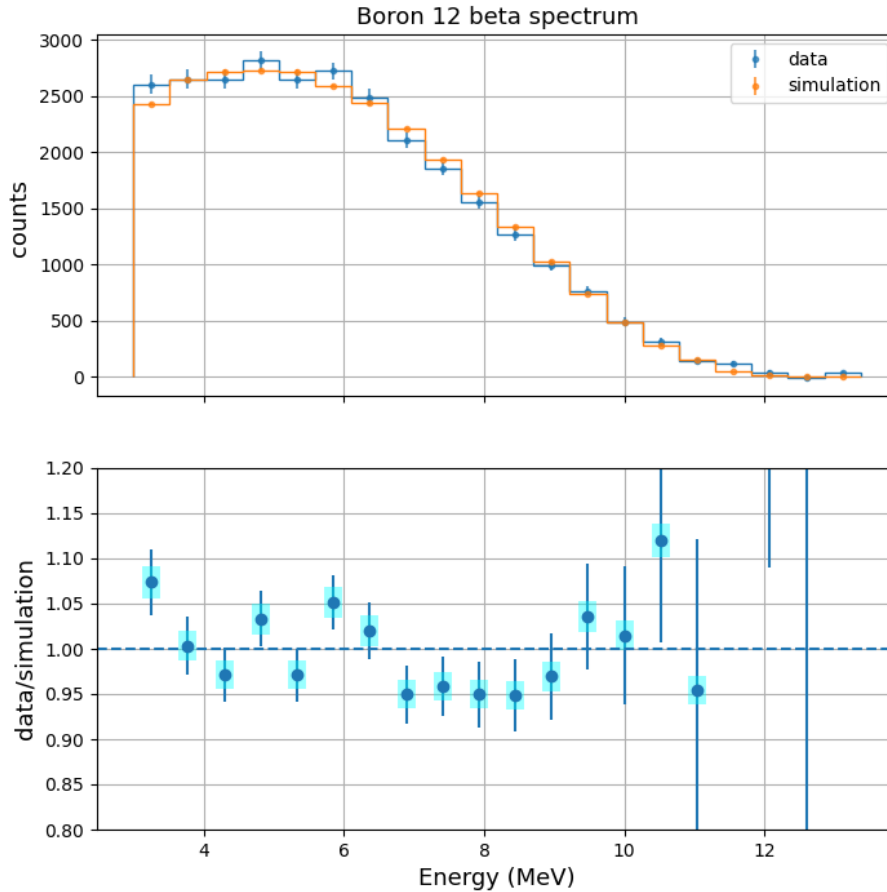


Figure 65: Top: the comparison of the  $^{12}\text{B}$  energy spectrum determined from the ROFF data (blue) and the Geant4 reference (orange). It was obtained with the implementation of the relative and absolute calibrations derived from the horizontal muons. Bottom: the relative ratio between the ROFF and Geant 4 with the statistical (blue bars) and systematic (cyan rectangles) uncertainties. It shows an agreement within 5%, which was not possible with the prior calibrations in use within the collaboration.

the detector response. However, the computation of the absolute scale is limited by the precise knowledge of the actual muon energy distribution. The radioactive AmBe source offers a promising  $e^+e^-$  pair calibration method, with the energy, which corresponds to the middle of the IBD range and, to the best of our knowledge, has a several-percent precision. It cannot be used for the accurate determination of the energy resolution of the detector. Finally, the latter can be fixed by fitting the Compton edge from the  $^{22}\text{Na}$  radioactive source. In summary, the absolute energy scale design for the final Phase I analysis has to be determined. However, with the selected baselines, all the components are in place to proceed with the antineutrino analysis, which is presented in the next chapter.

## 5 IBD analysis

The previous chapters established the required machinery for the data processing and all the necessary inputs to design the signal definition. The minimal set of components includes the neutron trigger, identified as NS, and the reconstructed ES cluster within the positive  $[0, 500]\mu\text{s}$  time window. This simplified selection was applied to 74 days of the ROFF data (purely the background) and an IBD SoLO simulation sample (purely the signal). The latter was scaled accordingly to match the same data taking time. The comparison of expected yields is shown in Figure 66. It is observed that the background sources are overwhelming the signal and that an extensive use of the physics properties of the electromagnetic part of the signal (ES cluster) is in order.

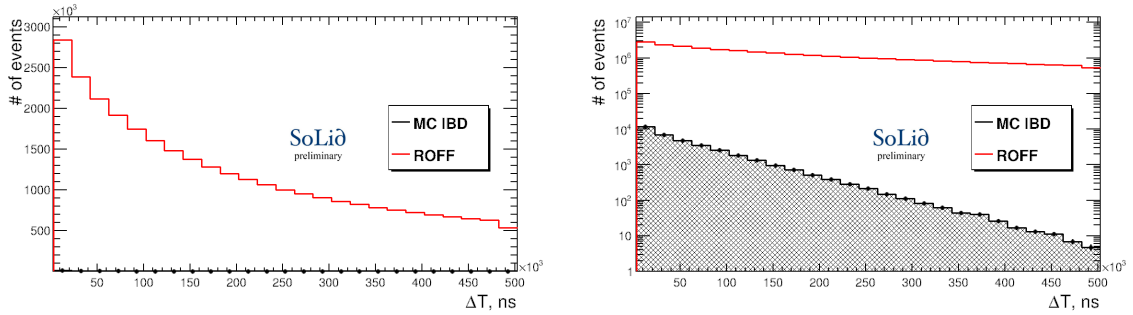


Figure 66: Left: the comparison of the raw yields expected from 74 days of the ROFF data and an accordingly scaled IBD SoLO simulation. Right: the same distribution in logarithmic scale. The plots indicate the overwhelming level of background (around 1 to 800) for the initial data set.

According to the current understanding presented in the Chapter 2.4, there are three different types of the background in the ROFF dataset sample. The analysis reported in this chapter aims at selecting geometrical properties of the signal events according to their electromagnetic characteristics to narrow down the background contribution to a sample that can potentially be comprehensively understood. To reach this understanding, it has been chosen to search for the most complex geometric patterns of the signal events with the rationale that the background sources will not likely mimic these features. A complex geometrical pattern therefore offers a larger number of discriminative variables. What is the way to define and describe the patterns? This is the place where the high granularity of the detector, combined with the CCube reconstruction algorithm, can be maximally employed. For instance, it becomes possible to separate the ionisation and annihilation contributions from the positron. The more annihilation contributions it is possible to identify, the more complex the geometrical pattern will be. Thus, three electromagnetic components can be potentially distinguished in an IBD ES cluster. One is provided by the positron ionisation processes and two by the two back-to-back annihilation  $\gamma$ . Thus, the events are categorised according to the number of components identified. The attached category of the event is referred to as *topology* in the following. Hence, events that fall into the topologies with two annihilation  $\gamma$  are supposed to be the cleanest. This statement will be validated further in this chapter. Furthermore, it will also be shown that the background sample corresponding to the  $2\gamma$  topologies can be satisfactorily understood.

## 5.1 Justification of the topologies

Understanding how a positron deposits its energy in the detector is crucial to establish the analysis design. To gain this knowledge, a Geant4 simulation of IBD events was explored. The primary purpose of the scrutiny is to compare the total energy in the cube where the annihilation has occurred with the initial energy of the positron. By default, the cube with the largest energy in the event is assumed to be the annihilation cube (AC). This assumption does not work for all events with low-energy positrons. Therefore, to select a robust sample for analysis, events with positrons below 1 MeV are rejected. Above this threshold, this assumption works in 95% of the cases (for the sake of simplicity, the last 5% were also rejected for now). However, even in the case where the cubes are matched, it does not imply that the AC energy corresponds to the initial energy of the positron. The difference between the two is described by the energy spread variable:

$$E_{\text{spread}} = \frac{E_{\text{true}} - E_{\text{AC}}}{E_{\text{true}}} . \quad (67)$$

As soon as  $E_{\text{spread}}$  is different from zero, it affects the nominal energy resolution of the detector. Therefore, the next stage of this Geant4 scrutiny is aimed at identifying the possible sources of the spread and categorising the events according to it. The first set of observations is related to the positron. Firstly, it creates a brehmstrahlung photon in about 22% of the events. It should be noted that the brehmstrahlung photons are of modest energies. When the brehmstrahlung contributions are excluded, it is observed that the positron deposits its energy in a single cube in 85% of the cases. In 12% of the cases, the energy is divided between two cubes. In the vast majority of the occurrences, these are two adjacent cubes. Hence, a  $3 \times 3 \times 3$  cubes envelope around the AC guarantees isolation of the ionisation part of the positron energy. In addition, the clean envelope (*i.e.* without additional energy deposits above the threshold) ensures that the ionisation contribution is contained in one cube and potentially allows one to perform the energy measurement without any other resolution effect than the intrinsic resolution of the detector. After losing its energy, the positron annihilates in the matter and emits two annihilation gamma particles. In around 6% of the events the annihilation occurs in flight, *i.e.* when the positron has not yet lost all of its energy. If it is matter, part of the initial energy is carried away by the photons. More importantly, the energy is not shared equivalently between them, and the angle varies. On the contrary, if the annihilation occurs at rest, *i.e.* positron is left with a negligible amount of kinetic energy, the characteristics of the annihilation gamma are predefined. In a dominating fraction of occurrences, two back-to-back 511 keV annihilation gamma are issued<sup>4</sup>. This set of observations is summarised in Figure 67. Further observations are related to the annihilation gamma contributions. According to the simulation, both of them allow the energy in the detector to be around 68% of the events. Moreover, in 29% of the cases, at least one of the annihilation gamma is experiencing a Compton interaction in the very same cube where the annihilation has appeared. In this case, the energy released is more than the kinetic energy of the positron. It was hence decided, based on the features discussed above, to focus on the explicit reconstruction of the annihilation gamma clusters outside the AC envelope. Thereby, the foreseen topologies might include events with 0, 1 or two reconstructed gamma particles

---

<sup>4</sup>It is also possible, for example, two have three gamma with a  $120^\circ$  angle (what a beautiful signal signature would it be!).

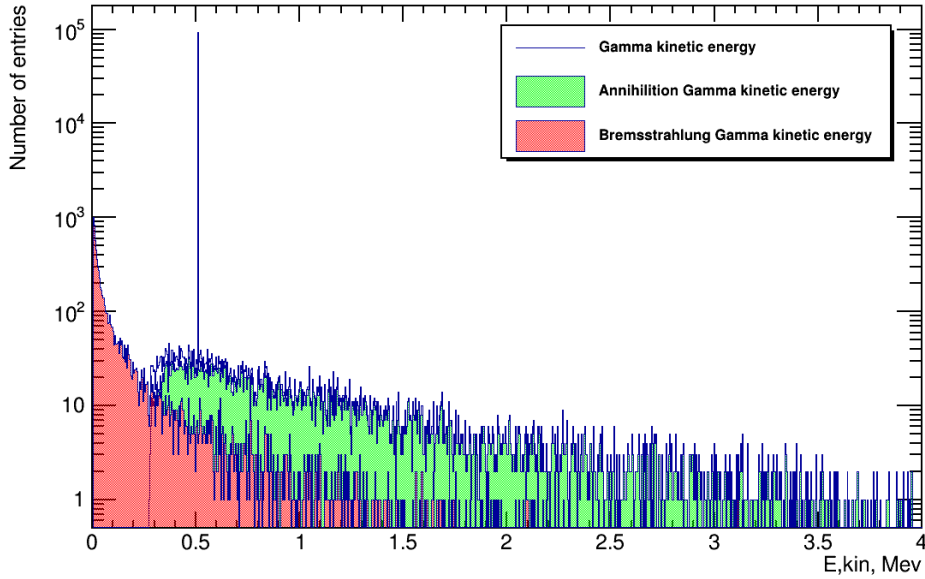


Figure 67: The initial kinetic energy distributions for the photons appearing in the IBD events: brehmstrahlung in red and annihilation gamma in green. The peak at 511 keV justifies the dominance of the positron annihilation at rest.

(which are referred to later in the text as 0, 1,  $2\gamma$  topologies and are comprehensively discussed in Chapter 5.2). The latter is therefore expected to provide the canonical energy resolution combined with the best use of the detector granularity. Moreover, the back-to-back electromagnetic clusters condition mitigates the impact of the brehmstrahlung photons. Their additional deposits will be attached to one of the annihilation clusters (or misidentified as one of them, when only one annihilation gamma makes it out of the envelope). The back-to-back condition will be violated for these clusters, since the angular distribution of brehmstrahlung is isotropic. The energy spread distribution obtained for the different topologies is shown in Figure 68. All the distributions are centred at zero, whereas very significant differences are observed in the tails. The black distribution, which represents the general case, has a pronounced left-hand part, implying that the AC energy is larger than the initial energy of the positron. It corresponds to the scenario where one annihilation gamma at least has experienced a Compton scattering within AC. This part is expectedly suppressed for  $2\gamma$  events, represented in the blue distribution. For this exploration, the  $2\gamma$  topology is defined as an event with at least 1 cube outside the envelope for each gamma particle. This cube is required to have an energy larger than 100 keV, and the annihilation gamma must be the dominant contributor to the energy deposit. The other remarkable feature of these distributions is that the energy spread differs for the events with 2 reconstructed gamma, whether the envelope is free of energy deposits or not. If one selects the events with no additional cubes above 50 keV in the envelope, the green distribution is obtained. It has reduced energy spread right-hand tails, compared to the two others. This better energy resolution is obtained because it rejects events in which the positron deposits energy in two cubes. Thereby, the topology definitions must rely on the envelope conditions since different energy estimators are in order to measure

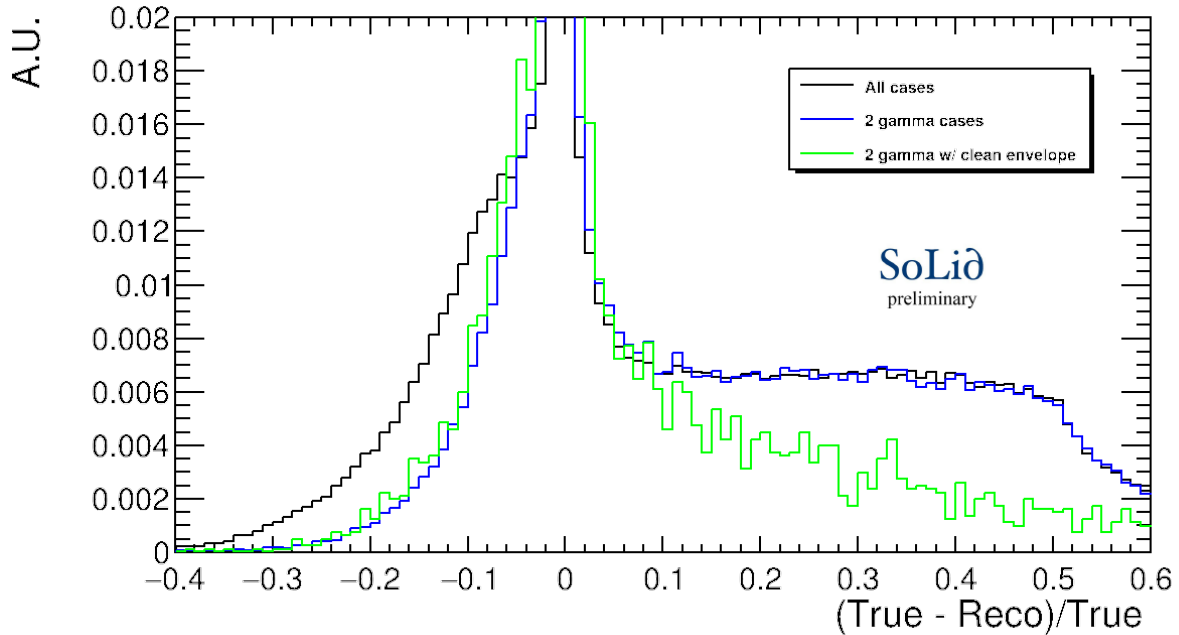


Figure 68: The superimposed energy spread distributions for several categories (topologies) of events. The energy of the most energetic cube is employed as the reconstructed energy. The black line represents all topologies combined. The blue distribution displays the topologies where 2 EM clusters are reconstructed outside of the AC envelope (aka 2 gamma topology); the left-hand tail is here removed since the annihilation photons do not contribute to AC. The green distribution corresponds to 2 gamma topology events requiring in addition a clean envelope around the AC cube. The right tail observed in the black line distribution is here removed (the rationale is that events for which the positron contributes to 2 cubes are discarded; it also indicates that such events will need special treatment in terms of energy estimator).

the actual energy of the positron. The algorithm to categorise the events into mutually exclusive topologies is presented in the following subsection.

## 5.2 Definition of the topologies

As introduced above, the definition of the event topology relies on separating the positron ionisation effects from the subsequent interactions caused by the annihilation gammas. In the events with a positron energy above 1 MeV, the dominant contribution is provided by the ionisation. This results in the definition of an annihilation cube, which is the most energetic in the event, and the envelope around, which isolates the AC. The energy deposits associated with the annihilation gammas are gathered outside of this envelope. Practically, the approach starts from the list of the cubes reconstructed by the CCube and provides the topology categorisation following the algorithm:

- the most energetic cube is identified and assigned to be the location of the positron annihilation. As before, it is denoted AC (Annihilation Cube).
- The envelope around the AC is gathering the cubes adjacent side-by-side or apex to the AC cube to isolate the ionisation deposit. This results in a volume of  $3 \times 3 \times 3$  cubes with the AC cube in the centre.

- The cubes outside of the envelope are assumed to detect the energies deposited by the two annihilation  $\gamma$ . It is supported by the following facts: The mean path of a 0.5 MeV photon is given by the equation:

$$\lambda = \frac{1}{\mu} = \frac{1}{0.09443} = 10.6 \text{ cm} , \quad (68)$$

where  $\mu$  is the attenuation coefficient. The density of PVT is taken to be  $1 \text{ g/cm}^3$ . Indeed, this mean path exceeds the envelope distance. Furthermore, the study at the Geant4 level of the origin of the energy deposits shows that about 99% of the actual cubes outside the envelope receive an energy deposit from one of the annihilation  $\gamma$ .

- The rest of the procedure follows with the logical selection of the actual reconstructed geometries:
  - if there is no cube outside the envelope, Topology 00 (only AC in the envelope), Topology 01 (AC and 1 cube), Topology 02 (AC and 2+ cubes). For these events there is no annihilation  $\gamma$  detected, and the algorithm is over.
  - If there is at least one cube outside of the envelope, the algorithm proceeds to a further categorisation.
- The most energetic cube outside the envelope EM1 is identified. It is the core of the electromagnetic cluster associated with the first annihilation  $\gamma$ .
- For all the other cubes outside the envelope, the cosine of the angle defined by the vectors (AC  $\rightarrow$  EM1) and (AC  $\rightarrow$  Cube) is computed. If the cosine is positive, the cube is associated with the same gamma as EM1. Otherwise, the cube is associated to the second electromagnetic cluster. This matching is driven by the fact that annihilation  $\gamma$  is back-to-back when the positron is annihilated at rest. The list of cubes associated with each reconstructed  $\gamma$  is used to build the barycenter (weighted in energy) of this electromagnetic signal. The assignment of the cubes to an hemisphere is repeated for all cubes taking the barycenter position corresponding to EM1 as the reference. The barycenter position and energy of EM1 and EM2 (when applicable) are eventually recomputed to form the reconstructed  $\gamma$  candidates.
- Two outcomes are possible:
  - There is no cube associated to the second EM cluster  $\implies$  this will define the topologies with only one reconstructed annihilation  $\gamma$ . This topological configuration corresponds to Topology 10 (only AC in the envelope), Topology 11 (AC and 1 cube), and Topology 12 (AC and 2+ cubes).
  - There is at least one cube associated to the second EM cluster  $\implies$  this topological configuration corresponds to 2 reconstructed annihilation  $\gamma$ , namely Topology 20 (only AC in the envelope), Topology 21 (AC and 1 cube) and Topology 22 (AC and 2+ cubes).

The set of topological configurations is gathered in Table 6. The first number represents the number of reconstructed EM clusters and the second the number of additional cubes in the envelope. The Figure 69 aims at displaying the logical steps to construct the most complex topology to illustrate each step of the algorithm.

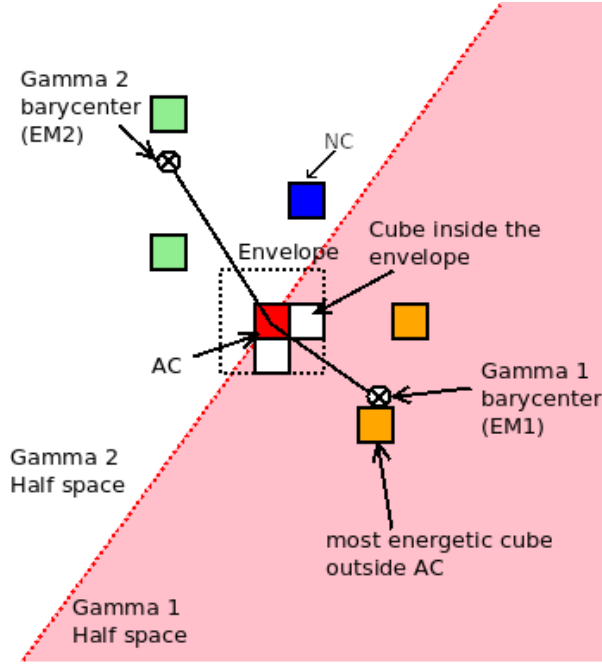


Figure 69: An example of building the most involved Topology 22. It has additional cubes in the envelope and both annihilation  $\gamma$ .

Envelope condition	$0\gamma$	$1\gamma$	$2\gamma$
Only AC	Topology 00	Topology 10	Topology 20
AC and 1 cube	Topology 01	Topology 11	Topology 21
AC and 2+ cubes	Topology 02	Topology 12	Topology 22

Table 6: The rationale behind the topological categorisation based on the quantity of the reconstructed electromagnetic clusters and the envelope condition.

### 5.2.1 Further search for the annihilation $\gamma$ contributions

The analysis work focusses on the  $2\gamma$  events. By default, the selected topologies are 20, 21 and 22. The simulation indicates, however, that very few IBD candidates fall into the latter topology and it can be safely removed (Further ROFF studies will indicate that the level of the background is overwhelming as well for this category). However, to fully address the  $2\gamma$  topologies, an additional exploration was performed. It was aimed at the isolation of candidates that can contain the energy deposit of the second  $\gamma$ . The only possible source of it implies cubes inside the envelope. Topology 11, which contains only one extra cube (candidate) around the AC, is a convenient sample to tackle the problem. Firstly, the event processed with Saffron2 is connected to the correspondent event in the Geant4 simulation. If the candidate cube is a ghost (*i.e.* it is not found back in the simulation), the event is rejected. The remaining cases are split into groups according to the origin of the extra energy deposit, positron, the reconstructed annihilation gamma or the second unreconstructed annihilation gamma. All categories are investigated with respect to two key parameters: the distance from AC to the candidate and the cosine of the angle between the vectors ( $AC \rightarrow EM1$  Barycenter) and ( $AC \rightarrow \gamma$  Candidate). The

latter is assumed to be positive if the candidate is provided by the already reconstructed gamma, negative if it is issued by the second gamma, and shall have a flat distribution if issued by the positron. The top plots in Figure 70 show that if the extra cube in the envelope comes from the splitting of the positron contribution, it shares the  $x$  or  $y$  coordinate with the AC. Thereby, the dominant distance is 1 (the metric is here the cube side). On the contrary, the candidates originating from the annihilation gamma reach the corners of the envelope. Therefore, the distance obtained can be either  $\sqrt{2}$  or  $\sqrt{3}$ . This additional  $2\gamma$  topology is therefore defined with the following requirements:

- Energy of the Candidate  $< 0.6$  MeV (to match annihilation  $\gamma$  regime);
- Distance (AC  $\rightarrow$  Candidate)  $> 1$ ;
- Cosine b/w the vectors (AC  $\rightarrow$  EM1 Barycenter) and (AC  $\rightarrow$  Candidate)  $< 0$ ;

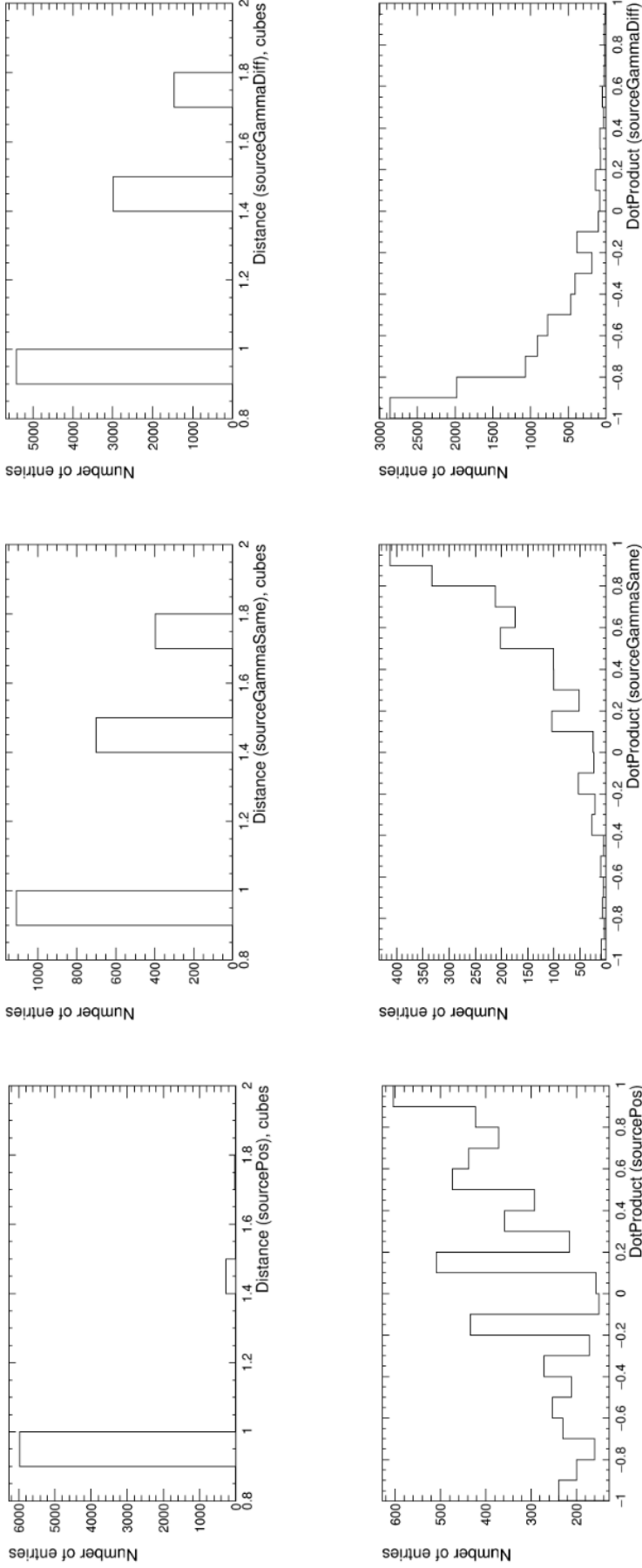
The obtained category will be referred to as Topology 23. A similar approach is applicable to Topology 12. Since the combinatorics of the envelope cubes is larger, there might be several cubes matching the conditions listed above. If that is the case, the cube with the largest energy is selected as the candidate. The 2 gamma events, originated from Topology 12, are referred to as Topology 24. The 0 gamma topologies are processed afterward in a similar way. Since there is only one cube in the envelope in Topology 01, it cannot provide the candidates for both gamma. Thus, the search is aimed at the extra deposit at the angle of the envelope. If one is found, the event is marked as Topology 13. Finally, the envelope combinatorics in Topology 02 allows one to dig deeper. First, the highest-energy candidate at a distance of  $\sqrt{2}$  or  $\sqrt{3}$  from AC is searched. If none is found, the event remains in its topological category; otherwise, the algorithm tries to search for the second gamma corner candidate with a negative cosine. If there is none, the event is tagged as Topology 14. If one is found, the event is tagged as Topology 25. The final set of accepted topologies is summarised in Table 7.

Envelope condition	$0\gamma$	$1\gamma$	$1\gamma^*$	$2\gamma$	$2\gamma^*$	$2\gamma^{**}$
Only AC	Topo00	Topo10	Topo13	<b>Topo20</b>	<b>Topo23</b>	
AC & 1 cube	Topo01	Topo11	Topo14	<b>Topo21</b>	<b>Topo24</b>	<b>Topo25</b>
AC & 1+ cubes	Topo02	Topo12		Topo22		

Table 7: The definition of the topologies, including the case where the  $\gamma$  deposit is found inside the envelope (tagged with \*). Topologies marked in bold are considered for further analysis.

To summarise, TopologyMN is defined as the following:

- For classical Topologies (not tagged with \* in Table 7) including: Topo00, 01, 02, 10, 11, 12, 20, 21, 22): M represents the number of reconstructed annihilation photons and N represents the number of extra (to AC) cubes in the envelope.
- For enhanced topologies (tagged with \* in Table 7) including: Topo13, 14, 23, 24, 25): M still represents the number of reconstructed annihilation photons. However, since the additional annihilation photon was searched inside the envelope, N now tags the original Topology in which the search has been performed, starting at the first available index:



## Positron

## Reconstructed $\gamma_1$

## Reconstructed $\gamma_2$

Figure 70: The events from IBD ROSim in Topology 11 (1 $\gamma$  and 1 extra cube in the envelope) are further examined. The origin of the extra cube is tracked via Geant4 information. The events are divided into three groups according to origin of the extra cluster:  $e^+$  (left), reconstructed  $\gamma$  (middle) and unreconstructed  $\gamma$  (right). Two distributions are made for each group: the distance from the extra cube to AC (top) and the cosine of an angle between the vectors [AC  $\rightarrow$  EM1 barycenter] and [AC  $\rightarrow$  Extra Cube] (bottom). To select the extra cube triggered by unreconstructed  $\gamma$  one must select cubes at the distance of  $\sqrt{2}$  or  $\sqrt{3}$  from AC and negative cosine.

- Topo 01  $\rightarrow$  Topo 13, Topo 02  $\rightarrow$  Topo 14
- Topo 11  $\rightarrow$  Topo 23, Topo 12  $\rightarrow$  Topo 24, Topo 02  $\rightarrow$  Topo 25

### 5.2.2 Cube level energy threshold

There is no cube-level energy threshold introduced in the CCube algorithm. The distribution of the events in the topology categories strongly depends on the cube energy threshold. Therefore, it is of prime importance to establish that energy threshold along with the signal definition. Since the topological approach is mainly focused on the  $2\gamma$  topologies, the tuning of the cut is aimed at optimising the purity and efficiency of these specific events. In order to do that, the Geant4 level information is used one more time. The starting point is to process the IBD MC simulated sample with Saffron2 multiple times by modifying the threshold value each time with a step of 5 keV. The same logic as introduced in Chapter 5.1 applies here: only events with AC energy in the [1, 6] MeV range are considered. Several figures of merit (FoM) are designed in order to find the adequate quality estimator for each  $E_{\text{cut}}$ :

$$\begin{aligned}
 \text{FoM}_1^{\text{old}} &= \text{Purity} \cdot F_{2\gamma}; \quad \text{FoM}_1^{\text{new}} = \epsilon \cdot (1 - \hat{\mathcal{L}}), \\
 \text{FoM}_2 &= \text{FoM}_1 \cdot S/B, \\
 \text{FoM}_3 &= \text{FoM}_1 \cdot S/\sqrt{B}.
 \end{aligned}
 \tag{69}$$

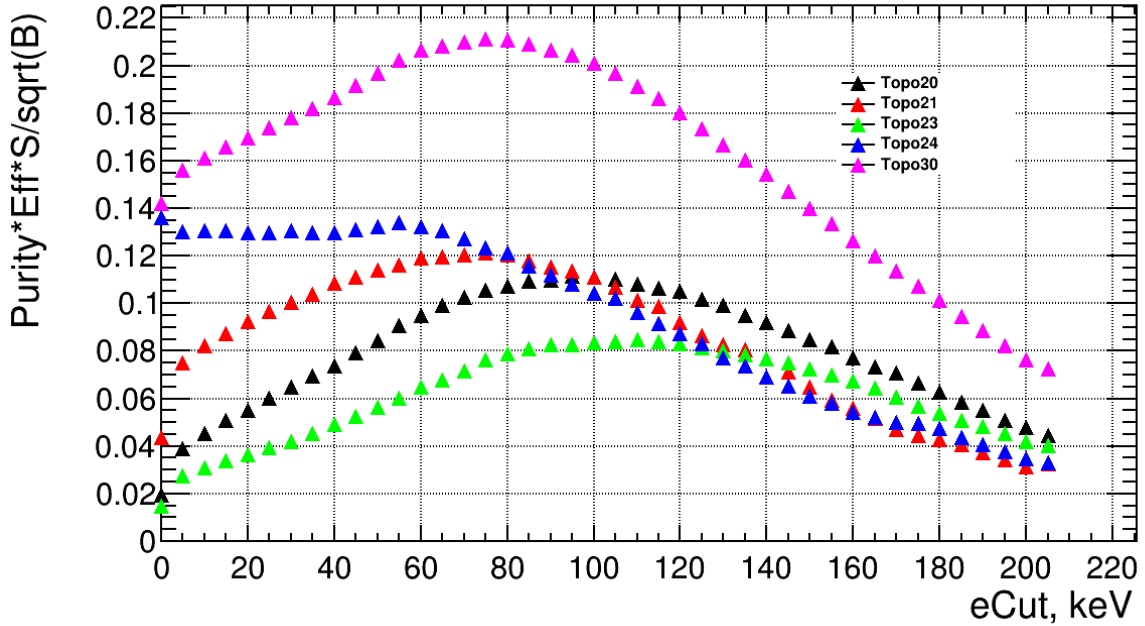


Figure 71: Evolution of the  $\text{FoM}_3$  value as a function of the cube energy threshold value. It is displayed per individual  $2\gamma$  topology and the combined sample noted as Topology 30 (pink).

The definition of proposed FoMs is based on the synergy between Geant4 truth and ROSim output information. It allows the accuracy of the two-gamma reconstruction to be assessed. Before the novel reconstruction and calibration procedures were implemented, it

was based on the values of  $Purity$  and  $F_{2\gamma}$ . The first factor quantifies in which fraction of events falling in the  $2\gamma$  topologies it is possible to identify three EM clusters in the Geant4 simulation. Hence, it measures the content of the true two  $\gamma$  topology in the selected sample. The factor  $F_{2\gamma}$  represents the fraction of occurrences of a given topology in the total number of events in the MC simulation. The accuracy of the gamma identification can be probed directly with the CCube algorithm estimators. Therefore, the updated estimator FoM<sub>1</sub> involves cube reconstruction efficiency and ghost rate. In both cases, the second and third figures of merit consider the multiplication of FoM<sub>1</sub> by the signal-over-background ratio ( $S/B$ ) or the  $S/\sqrt{B}$  ratio accordingly. The yield  $S$  ( $B$ ) is defined as the number of events in a given topology in the appropriately scaled signal (background) sample, respectively. The purpose of the modification of the FoM<sub>1</sub> is to include the ROff data composition per topology. Since the background overwhelms the signal (see Figure 66), it has been chosen to give preference to FoM<sub>3</sub>. Figure 71 shows its distribution. The maximum of the figure of merit is obtained at  $E_{cut} = 75$  keV. This value is used from hereafter to define the list of actual cubes participating in an ES cluster and hence construct the topology.

### 5.2.3 CCube efficiency per topology

The final piece of information on the topologies is provided by the estimation of the performance of the CCube algorithm. To address the question, the same set of estimators introduced in Chapter 3.2.1 is used. This set is complemented by the accuracy of assigning the positron annihilation cube (for the same [1, 6] MeV range):

- The AC identification efficiency;
- The cube reconstruction efficiency  $\epsilon$ , as defined in the Equation 50;
- The ghost rate  $\hat{\mathcal{L}}$ , as defined in the Equation 51.

	Topo00	Topo01	Topo02	Topo10	Topo11	Topo12	Topo13
$AC_{match}$	99.2(0.9)	97.2(0.9)	95.8(1.3)	98.1(0.7)	96.1(0.7)	93.8(1.1)	99.4(1.5)
$\epsilon$ (%)	68.7(0.4)	76.8(0.4)	84.3(0.5)	79.8(0.3)	83.7(0.3)	87.4(0.4)	79.5(0.6)
$\hat{\mathcal{L}}$ (%)	0.9(0.1)	12.7(0.2)	22.1(0.3)	10.9(0.1)	17.9(0.1)	24.7(0.2)	1.9(0.1)
	Topo14	Topo20	Topo21	Topo22	Topo23	Topo24	Topo25
$AC_{match}$	96.1(1.1)	98.5(1.4)	96.4(1.5)	94.5(2.1)	99.4(1.9)	96.2(1.4)	98.0(3.0)
$\epsilon$ (%)	85.1(0.5)	85.9(0.5)	87.4(0.6)	89.0(0.8)	86.4(0.8)	89.0(0.5)	90.0(1.2)
$\hat{\mathcal{L}}$ (%)	16.9(0.2)	15.4(0.2)	21.3(0.3)	27.3(0.4)	8.9(0.2)	20.4(0.2)	13.2(0.4)

Table 8: Performance of the CCube algorithm for the different topologies

To compute the AC identification efficiency, the position of the most energetic cube reconstructed by the CCube algorithm is compared to the cube where the positron has contributed most of its ionisation energy loss in the Geant4 simulation. It is then determined as the fraction of events processed through Saffron2 where the positions are matching. The performance per topology is summarised in Table 8. The overall response

is similar across the different topologies. However, one can note a slight increase in  $\hat{\mathcal{L}}$  for the events with a higher cube multiplicity (Topology 02, 12 and 22).

### 5.3 Identification of the background sources

A sample of ROff data was analysed corresponding to 74 days of data collection to identify contamination coming from different sources of background. Four sources of background contributions are identified in the SoLi $\partial$  detector: they include accidentals, BiPo and atmospheric neutrons, further split into fast and nominal components. The level of presence of each background source is strongly dependent on the topologies. To provide a quantitative measure of these fractions, an extended unbinned maximum likelihood event-per-event fit to the  $\Delta T$  distribution of the events is performed. The fit machine is provided by the RooFit toolkit [103], which is a part of the ROOT data analysis framework [104]. The model considered in the fit reads:

$$\Delta T = N_{\text{acc}} + N_{\text{BiPo}} \cdot e^{-\frac{\Delta T}{235.8 \mu\text{s}}} + N_{\text{fNeu}} \cdot e^{-\frac{\Delta T}{8.5 \mu\text{s}}} + N_{\text{Neu}} \cdot e^{-\frac{\Delta T}{62 \mu\text{s}}}, \text{ where} \quad (70)$$

- $N_{\text{acc}}$  is the number of accidental events (Acc). It is restricted from the FPNT sample. The accidental distribution is assumed to be represented by a constant function.
- The BiPo component is modelled by means of an exponential probability density function (p.d.f.) of fixed parameter  $235.8 \mu\text{s}$  [105]. Its floated yield is denoted  $N_{\text{BiPo}}$ .
- The third and fourth terms of the equation represent the model for the atmospheric neutron contribution. It consists of two parts:
  1. Falls rapidly with  $\Delta T$  [79]. It might correspond to non-thermalised atmospheric neutrons. It is modelled by an exponential p.d.f. of parameter  $8.5 \mu\text{s}$ ;
  2. The “nominal” fraction of the atmospheric neutrons, corresponding to thermalised neutrons. An exponential p.d.f. of parameter  $62 \mu\text{s}$  is used.

The latter is particularly toxic, since it shares an identical neutron moderation time with the signal events. Therefore, it is not possible to distinguish these contributions solely with the  $\Delta T$  fit. The moderation time for both atmospheric components is restricted from the value determined by a  $\Delta T$  fit to simulated MC IBD events. Moreover, this fit also fixes the proportion of the fast component ( $f_{\text{fNeu}}$ ). The total yield  $N_{\text{Atm}}$  is a free parameter of the fit. It is connected to the individual yields as:

$$N_{\text{fNeu}} = f_{\text{fNeu}} \cdot N_{\text{Atm}} ; N_{\text{Neu}} = (1 - f_{\text{fNeu}}) \cdot N_{\text{Atm}} . \quad (71)$$

#### 5.3.1 Background sources distribution across topologies

The  $\Delta T$  fit was made for all topologies in the ROff data. The background composition for each of them is summarised in Table 12. It shows that the way the background sources are distributed varies widely among the topologies. When no  $\gamma$  is explicitly reconstructed, the number of BiPo and accidentals are competing. With an increase in the number of reconstructed  $\gamma$ , the contamination of BiPo increases, while the level of accidentals is decreasing. Interestingly enough, the fraction of atmospheric neutrons remains at an equivalent level. Hence, when both annihilation  $\gamma$  are reconstructed, BiPo becomes the

dominant background source. To highlight the variation of the background fractions upon the topologies, one example was selected per number of reconstructed  $\gamma$ : Topology 00 ( $0\gamma$ ), Topology 10 ( $1\gamma$ ), and Topology 20 ( $2\gamma$ ). The results of the corresponding fits are collected in Figures figs. 72 to 74. The introduction of the  $2\gamma$  topologies provides a significant reduction of the background prior to any additional selection.

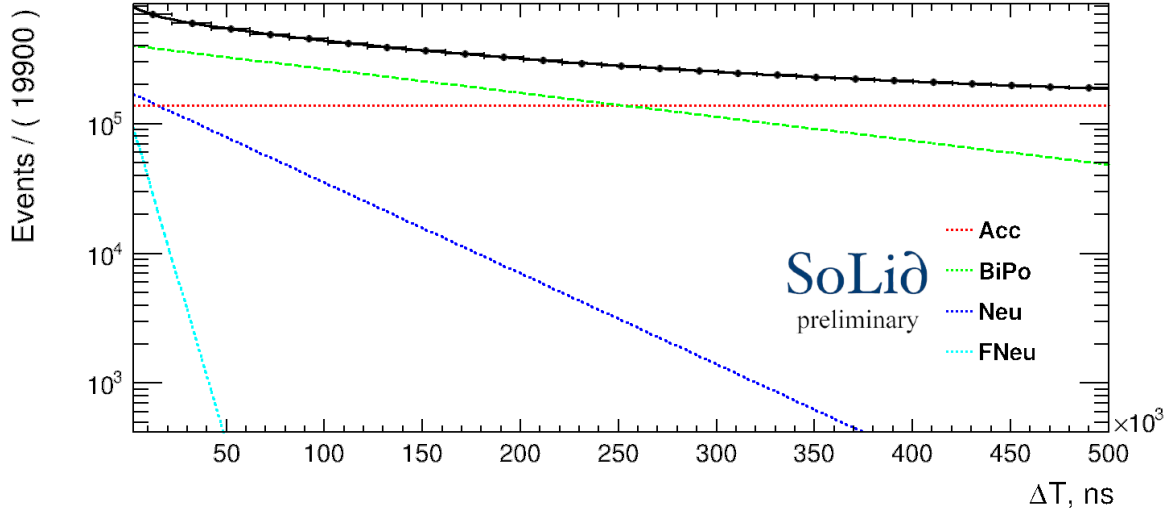


Figure 72: An example of the unbinned extended ML event-per-event fit to distance in time between the nuclear and electromagnetic components of ROff events (black data points) where no annihilation gamma was reconstructed (in particular Topology 00). The resulting shape (black solid line) is composed of three background shapes: accidentals (red), bismuth-polonium natural radiation decay chain (green) and atmospherics (fast component in light blue and normal in dark). The sample is dominated by BiPo and accidental contributions.

Topology 00	Acc	BiPo	Neu	fNeu $\cdot 10^2$
Yields $\cdot 10^6$	$3.44 \pm 0.01$	$4.17 \pm 0.01$	$0.53 \pm 0.01$	$3.93 \pm 0.11$

Table 9: The background sources yields from the  $\Delta T$  fit for Topology 00.

Topology 10	Acc	BiPo	Neu	fNeu $\cdot 10^2$
Yields $\cdot 10^6$	$2.26 \pm 0.01$	$4.73 \pm 0.01$	$0.48 \pm 0.01$	$3.52 \pm 0.11$

Table 10: The background sources yields as determined from a  $\Delta T$  fit for Topology 10

In addition to the difference between the 0, 1 and  $2\gamma$  topologies, the results obtained indicate the deviations within each of those categories. Atmospheric contamination is increasing with the number of cubes in the envelope. Topology 22 is of particular illustrative interest for highlighting this feature. This is the rationale behind the design of a specific signal selection for each individual topology.

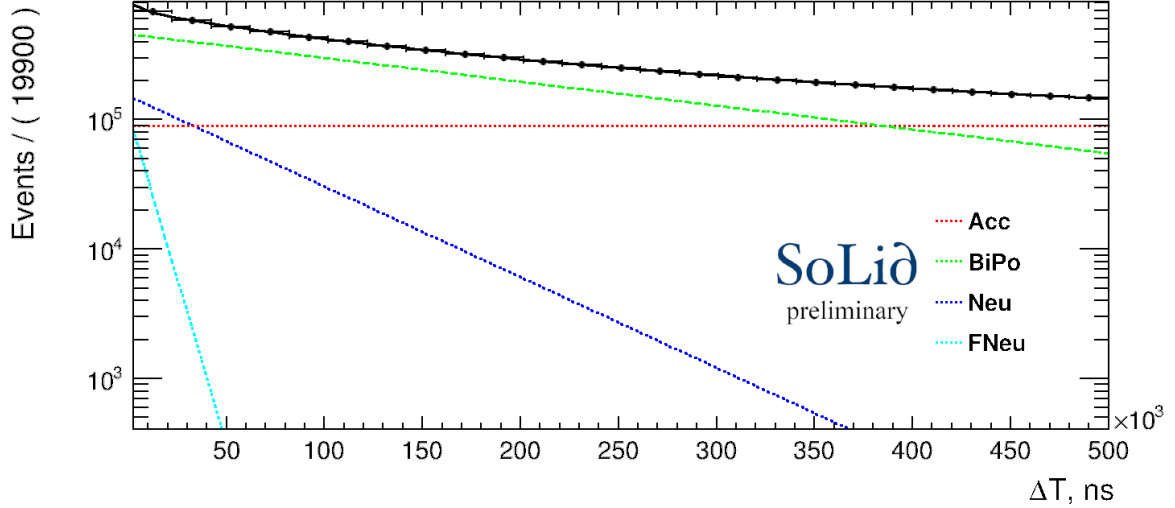


Figure 73: An example of the unbinned extended ML event-per-event fit to distance in time between the nuclear and electromagnetic components of the even for the ROff events (black data points) where 1 annihilation gamma was reconstructed (in particular Topology 10). The resulting shape (black solid line) is composed of three background shapes: accidentals (red), BiPo (green) and atmospherics (fast component in light blue and normal in dark). The BiPo domination is more pronounced than for Topology 00.

<b>Topology 20</b>	Acc	BiPo	Neu	fNeu · 10 <sup>2</sup>
Yields · 10 <sup>5</sup>	1.41 ± 0.02	7.11 ± 0.04	0.52 ± 0.02	6.01 ± 0.40

Table 11: The background sources yields determined from the  $\Delta T$  fit for Topology 20.

	Topo00	Topo01	Topo02	Topo10	Topo11	Topo12	Topo13
Acc,%	42.1(0.1)	40.0(0.2)	28.7(0.3)	30.2(0.1)	23.5(0.1)	17.2(0.2)	39.8(0.3)
BiPo,%	51.0(0.2)	51.5(0.3)	57.4(0.5)	63.3(0.2)	68.0(0.2)	67.8(0.4)	52.7(0.5)
Atm,%	6.5(0.1)	7.9(0.1)	12.9(0.2)	6.1(0.1)	7.9(0.1)	13.7(0.2)	7.0(0.2)
fAtm,%	0.5(0.1)	0.6(0.1)	1.0(0.1)	0.5(0.1)	0.7(0.1)	1.3(0.1)	0.5(0.1)
	Topo14	Topo20	Topo21	Topo22	Topo23	Topo24	Topo25
Acc,%	31.6(0.3)	15.5(0.3)	11.8(0.3)	10.2(0.5)	16.4(0.4)	13.4(0.4)	16.1(1.0)
BiPo,%	60.0(0.5)	78.1(0.6)	77.2(0.8)	65.7(1.1)	79.1(0.9)	77.1(0.8)	79.1(2.2)
Atm,%	7.7(0.2)	5.7(0.2)	10.2(0.3)	21.7(0.5)	4.1(0.3)	8.7(0.3)	4.2(0.8)
fAtm,%	0.6(0.1)	0.7(0.1)	0.8(0.1)	2.4(0.1)	0.4(0.1)	0.8(0.1)	0.5(0.2)

Table 12: Background source fractions determined from the  $\Delta T$  fits for all topologies.

## 5.4 Preselection cuts

The selection and analysis stages for the background rejection are summarised in Figure 75. As emphasised in the previous subsections, the analysis effort focusses on the  $2\gamma$  events

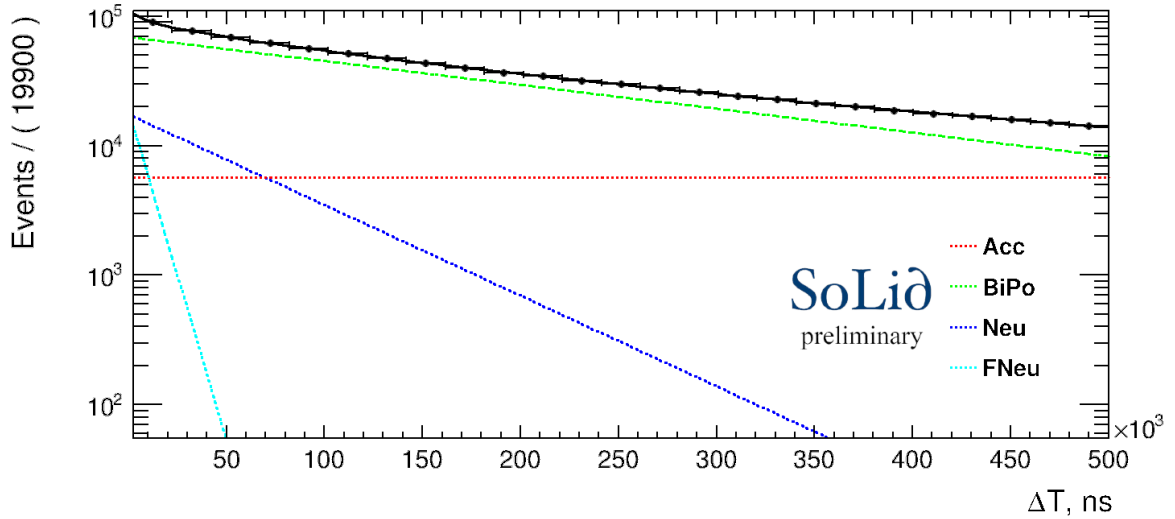


Figure 74: An example of the unbinned extended ML event-per-event fit to distance in time between the nuclear and electromagnetic components of the events for the ROFF events (black data points) where 2 annihilation gammas were reconstructed (in particular Topology 20). The resulting shape (black solid line) is composed of: accidentals (red), BiPo (green) and atmospherics (fast component in light blue and normal in dark). The BiPo domination is even more pronounced here than what we observed for Topology 00 and Topology 10.

selection, as the cleanest way to understand the background and hence spot a signal. The corresponding topologies are 20, 21, 23, 24 and 25.

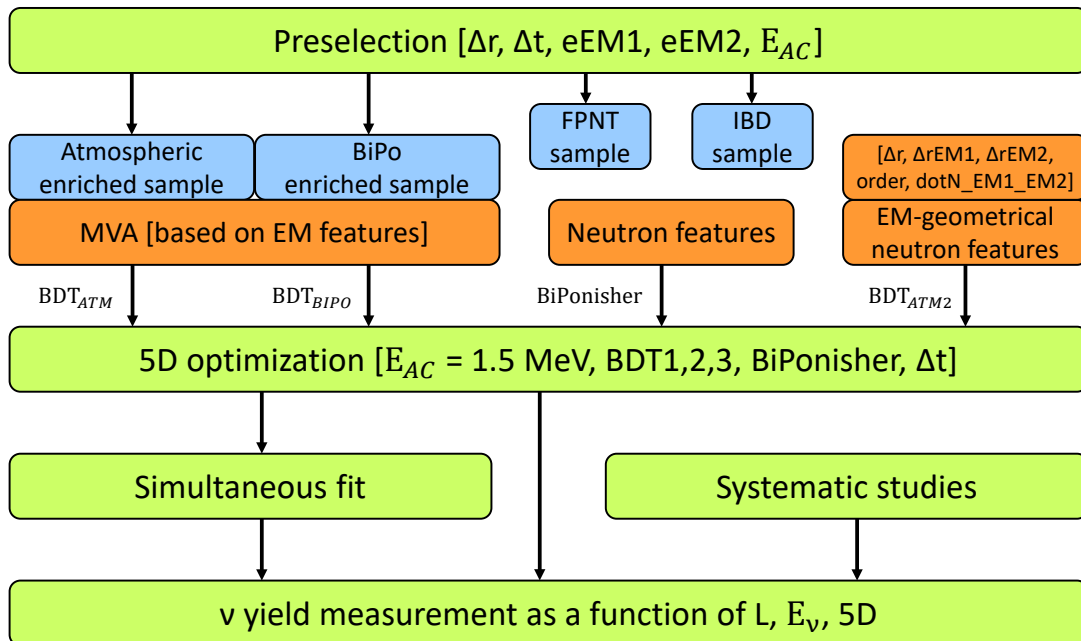


Figure 75: The topological analysis workflow.

The first action is to design a set of preselection cuts to cope with the overwhelming level of background, even if the use of topologies significantly reduces its amount. Preselection

is composed to provide a significant rejection of background events while keeping the signal efficiency as large as possible. Figure 76 gathers the main electromagnetic characteristics of the events, which drive the preselection requirements. For example, the typical total energy of annihilation  $\gamma$  does not exceed 511 keV. Hence, events with an annihilation gamma candidate EM cluster energy above 0.6 MeV (to account for the resolution effects) are rejected. Another feature is that the region of AC energy below 1 MeV is populated by a gigantic level of background, making it difficult to perform an analysis there. Moreover, the identification of AC in this energy regime is complex. Thereby, the events with the highest energy deposit below 1 MeV are safely removed. Finally, the preselection includes the  $\Delta R$  variable, which is the spatial distance between the NS and the AC. Most of the IBD events prefer the region with low values of  $\Delta R$ . The imposed requirement  $\Delta R < 5$  does not affect the signal efficiency at all. At the same time, it removes part of the background contribution mainly caused by accidental and atmospheric sources. No further requirement is imposed for the distance in time  $\Delta T$ , which constitutes a control variable to measure the signal and background yields. In the end, the set of preselection cuts is the following:

- The AC energy in the range [1, 6] MeV;
- the total energy of the annihilation gamma candidates  $< 0.6$  MeV;
- spatial distance between the NS and AC ( $\Delta R$ )  $< 5$  cubes;

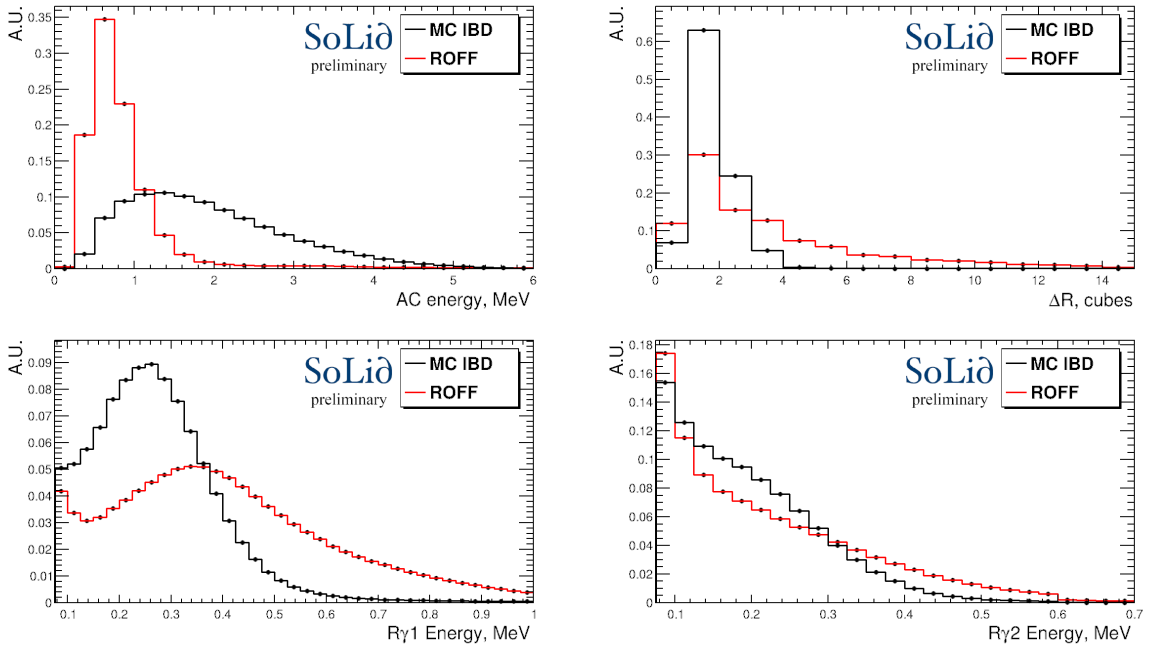


Figure 76: Distributions of (top left) the energy of the most energetic cube, (top right) spatial distance between NS and ES, (bottom left) the energy of the first reconstructed gamma and (bottom right) the energy of the second reconstructed gamma. Signal (black) and background (red) are superimposed.

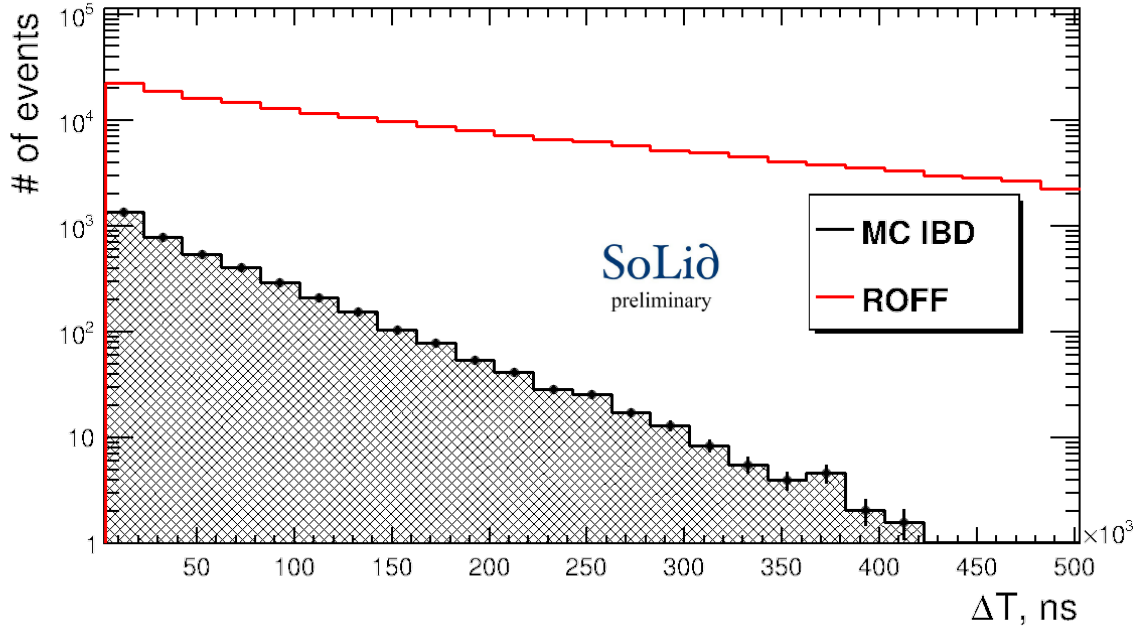


Figure 77: The comparison of the yields in the preselected  $2\gamma$  topology expected from 74 days of the ROFF data and an accordingly scaled IBD SoLO simulation in logarithmic scale. The plot is indicating a level of signal to background around 1/50).

The Figure 77 illustrates the effect of the preselection. Signal efficiency is at the level of 80%, while background contamination is reduced by more than a factor 10. Compared to Figure 66, the signal yield decreases by factor  $6^5$  and provides 60 expected IBD events per day, while the signal-to-background ratio is improved by more than a factor 15! The preselection requirements also impact the background composition in the topology categories, and it is useful to assess it. Figure 78 displays the  $\Delta T$  fit for the  $2\gamma$  topologies collection. The BiPo contribution is measured to be more significant (around 85%) than before the preselection, reinforcing the necessity to design a selection aimed at rejecting it maximally.

<b>20+21+23+24</b>	Acc	BiPo	Neu	fNeu
Yields $\cdot 10^4$	$1.1 \pm 0.01$	$16 \pm 0.1$	$1.8 \pm 0.1$	$0.2 \pm 0.02$

Table 13: The background sources yields determined from the  $\Delta T$  fit for the combined preselected  $2\gamma$  sample.

#### 5.4.1 Normalisation factor determination

The presented yields determined from the  $\Delta T$  fits are the number of events in the total sample considered. It is much more convenient to represent the yields per day in order to provide results independent of the size of the considered samples. It is hence necessary to

<sup>5</sup>this reduction factor accounts for the selection of the topologies of interest.

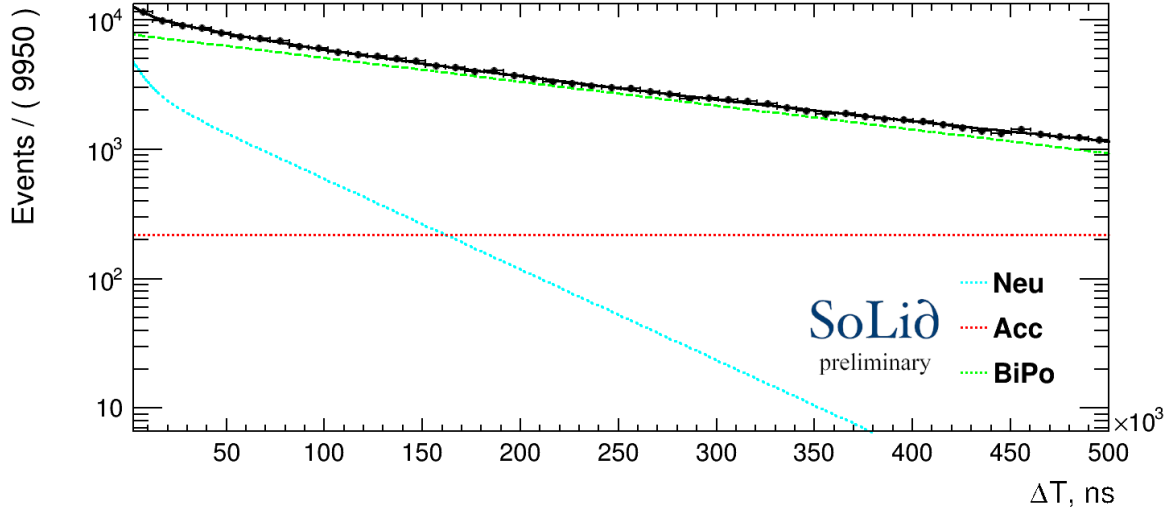


Figure 78: The  $\Delta T$  distribution in the ROFF data sample for the preselected  $2\gamma$  topologies collection. The fit result is superimposed as well as the individual components of the fit model.

derive the normalisation factor of this conversion. For the ROFF and RON datasets, it is simple. Each data file processed with Saffron2 contains the *runDuration* variable. The value of this variable indicates the time (in seconds) for which the data was taken. It is further complemented with information about the dead time of the run. The summation of the run lengths, corrected for the dead time, therefore, provides the total duration of the data taking within the sample. The number of events per day is then provided by a simple division. For the MC IBD simulation, the factor is composed of fractions. The initial number of events in the Geant4 simulation sample serves as a denominator and the number of events after Saffron2 processing and application of the cuts as a numerator. Such a definition accounts for the effects of the detector (*i.e.* neutron capture, trigger, reconstruction) and the effect of each stage of the analysis (*i.e.* preselection cuts and optimisation). In order to obtain the number of events per day, this fraction is further multiplied by the total number of expected neutrinos experiencing an IBD in the detector. This number is taken to be 1200, evaluated as the mean value of  $\bar{\nu}$  per day calculated out of the number of fissions in the reactor core for the first 5 cycles of data collection [85].

## 5.5 Discriminative variables

The signal-to-background ratio after the preselection is at the level of 1 to 50. Therefore, additional features are identified to further suppress background contributions. The following list of variables dedicated to the  $2\gamma$  topologies is defined based on the signal characteristics and the properties of the background events observed in the ROFF sample considered in this analysis.

- The main signature of the events, with two clearly separated annihilation photons, consists of their back-to-back characteristic. Therefore, the cosine of the angle between the vectors  $(\vec{A}_{\gamma 1}, \vec{A}_{\gamma 2})$  is computed; the  $2\gamma$  events are more likely to be found at values of cosine close to -1.

- The reconstructed energy of the annihilation photons  $R\gamma_1$  and  $R\gamma_2$ , denoted  $eEM1$  and  $eEM2$ , respectively, is characteristic of the annihilation process. They are peaking for signal events at the Compton edge value of a 511 keV photon. Since the two photons are hierarchised by energy in the reconstruction, the discriminative power of the  $eEM1$  variable is stronger.
- A larger multiplicity of cubes in the electromagnetic signal is characteristic of IBD candidates. This variable is denoted `promptNCCube`.
- The numbers of cubes involved in the electromagnetic clusters  $R\gamma_1$  and  $R\gamma_2$  do not exhibit an obvious discriminative power per se, but carry information through their correlations with other discriminative variables.
- A similar comment is in order when it comes to the separation distance between AC and the reconstructed positions of  $\gamma$ , denoted `distAC-EM1` and `distAC-EM2`, as well as the distance between the two *gamma*  $\gamma_1$ ,  $AC\gamma_2$  and  $\gamma_1\gamma_2$ ; those variables are useful through correlations with the others.

The characteristics of the atmospheric-induced background differs from the BiPo natural radiation. Hence, it is useful to establish an additional set of variables to discriminate this particular source of background. It is also necessary since there are no extra handle to reject it as is the BiPonator in the case of the natural radiation. Generally speaking, an atmospheric-induced background event consists of a fast neutron, which is creating several proton recoils, recognized by the categorisation algorithm as EM clusters. The neutron thermalises and is then captured and issues the NS. The following set of variables is defined to capture the geometrical neutron features:

- If the neutron trajectory is interpreted as a track<sup>6</sup>, then the NC is assumed to be in the end in most cases. Thus, the cosine of the angle between the vectors  $(N\vec{C}\gamma_1, N\vec{C}\gamma_2)$  is computed; the atmospheric induced events are more likely to be found at the positive values of the cosine;
- The set of the spatial distances between the NC and the reconstructed EM clusters is calculated. They are denoted as `delr`, `delrEM1` and `delrEM2` respectively;
- There is no practical reasoning to justify that a particular proton recoil is attached to the AC,  $R\gamma_1$  or  $R\gamma_2$ . If one searches for the smallest spatial distance between the three introduced above, a flat distribution will be obtained. On the contrary, the 2  $\gamma$  events are more likely to be closer to the NS. The dedicated variable is denoted as `order`. It shows which of the spatial distances is the smallest.

Finally, one additional control variable (*i.e.* it is not expected to have any discriminative power), is introduced. It takes the most energetic cube for the envelope,  $R\gamma_1$  and  $R\gamma_2$  and searches for the number of fibres used for its reconstruction. As introduced in Chapter 4.1.5, the number of fibres directly impacts the quality of energy evaluation. If the most energetic cube for one of the clusters is reconstructed with only two fibres, the event is rejected. Leaves two options available for each of the clusters: 3 or 4 fibres. Such that 8 categories are defined with this variable, which is denoted as `eventType`.

---

<sup>6</sup>This is a bold concept! It is used here to define the average properties of fast neutron scatterings.

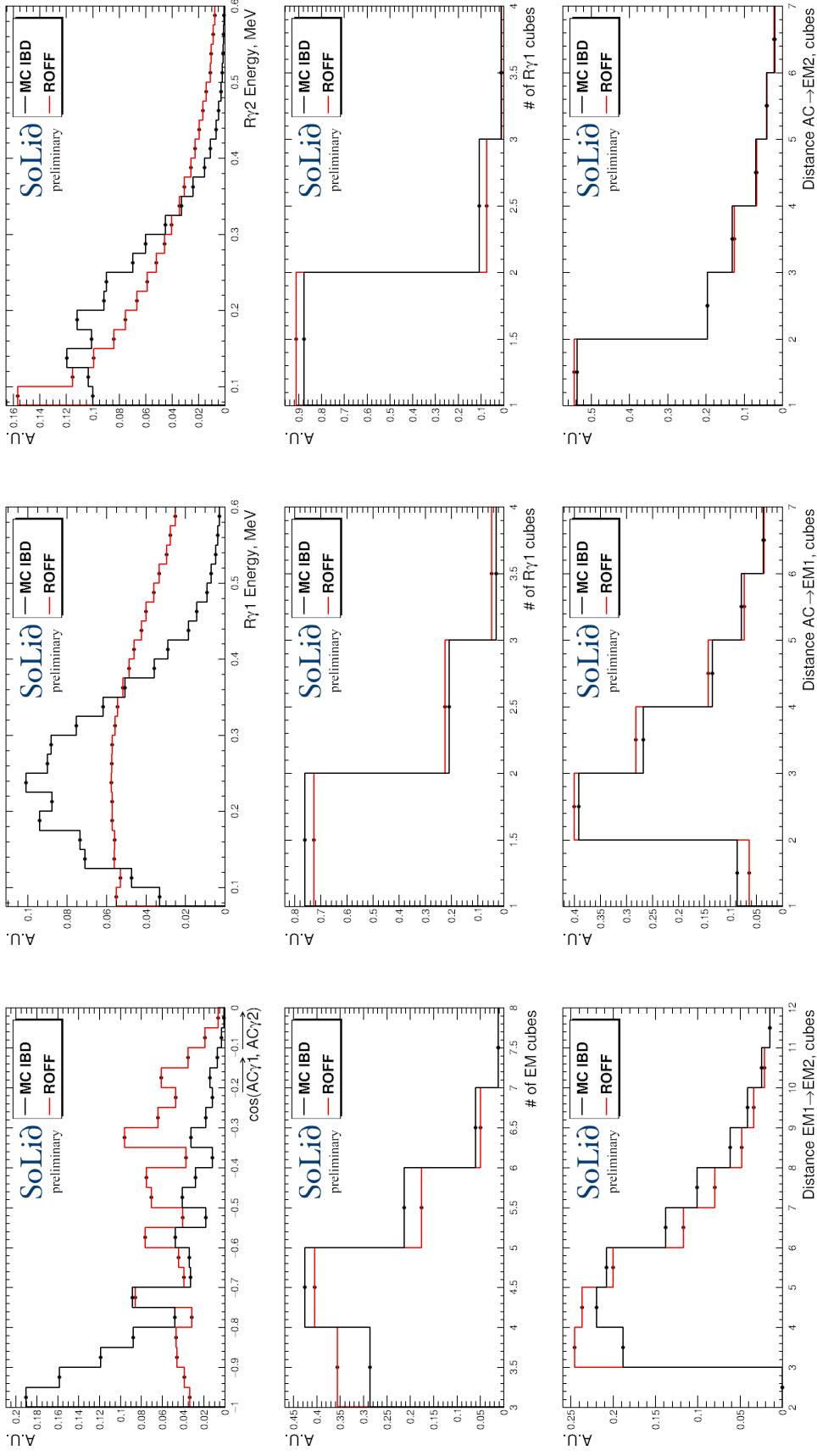


Figure 79: Distribution of (top left) the cosine of the angle between the  $\vec{AC}\gamma_1$  vectors for signal (black) and background (red). It is supplemented with the distributions of other discriminative variables such as the reconstructed energies of the first (top middle) and second (top left) reconstructed  $\gamma$ , the multiplicity of the event and of the reconstructed  $\gamma$  (set of middle plots) and the spatial distances between AC and the reconstructed  $\gamma$  (set of bottom plots).

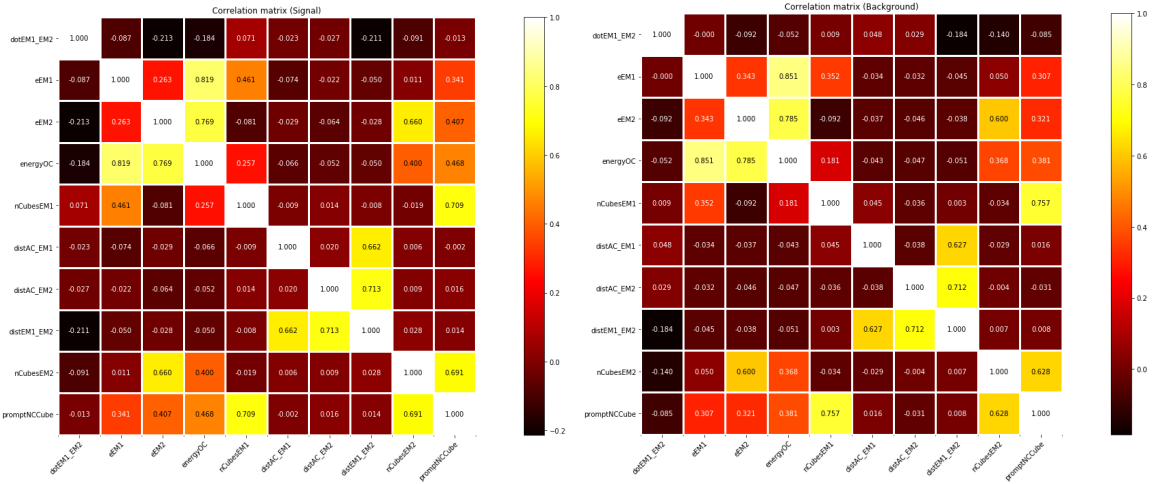


Figure 80: An example of the correlation matrices for the discriminative variables. The matrices were derived for a subset (Topology 20 only) of MC IBD (left) and ROff (right). There are several variables showing different correlation patterns for signal and background. It justifies the use of a nonlinear MVA tool to optimise the background rejection.

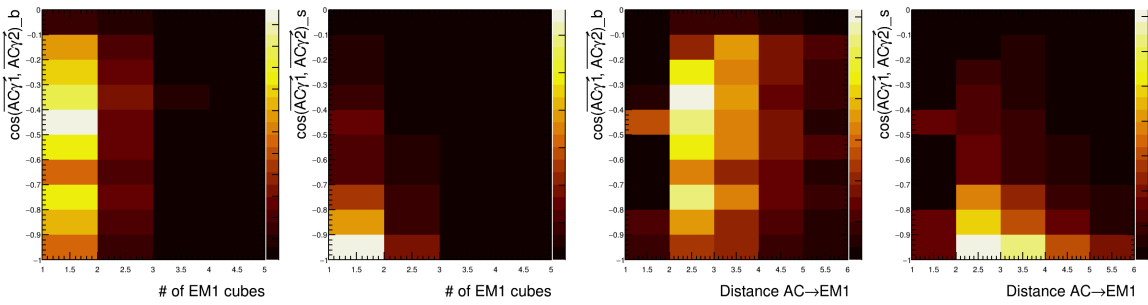


Figure 81: Correlation patterns in the ROff data (index B) and MC IBD (index S) for the variables with low discriminative power.

The Figure 79 displays the normalised distributions of some discriminative variables for the simulated events of IBD and candidates of the preselected ROff data. Beyond the direct discriminative power of each variable, it is important to consider the correlation patterns. Figure 80 provides two examples of scatter plots, where different patterns of correlations are observed for signal and background events. Significant non-linear correlations are present for most of the defined variables and motivate therefore the use of a multivariate classifier accounting for them. Since the complexity of the problem is modest, it was decided to use a vastly established and commissioned tool based on a Boosted Decision Tree algorithm [106]. Anticipating the next two subsections, the relevance of the simulation of this set of variables as well as the reproducibility of their correlations will be first tested on data calibration samples of the most dominant background source (BiPo events). The training of the multivariate classifiers for signal events will be performed with IBD simulated events as signal events against enriched samples of BiPo and atmospheric events, preselected on the ROff data sample at hand in this analysis.

## 5.6 Datasets

The MC IBD and the ROff samples define the signal and background data sets accordingly. However, the previous subsection has postulated, however, the necessity for each source of background to have the dedicated sample, which will dominantly contain the events issued by this source. The correspondent samples are called enriched samples and are defined for the BiPo and atmospheric sources. The accidental background source does not require an additional data set, since the FPNT control sample is already in use and sufficient to constrain these contributions.

### 5.6.1 BiPo enriched sample

The BiPo events dominate the background in the ROff data after the preselection. Therefore, the composition of a high-purity sample is straightforward. Its selection is based on variables that are not used in the set of discriminative variables, namely  $\Delta T$  and BiPonisher (because of the overwhelming contamination, the full power of BiPonator is not required in this selection. In addition, it does not increase the purity of the sample):

- $\Delta T > 120\mu\text{s}$
- BiPonisher  $< 1.5$
- + preselection cuts

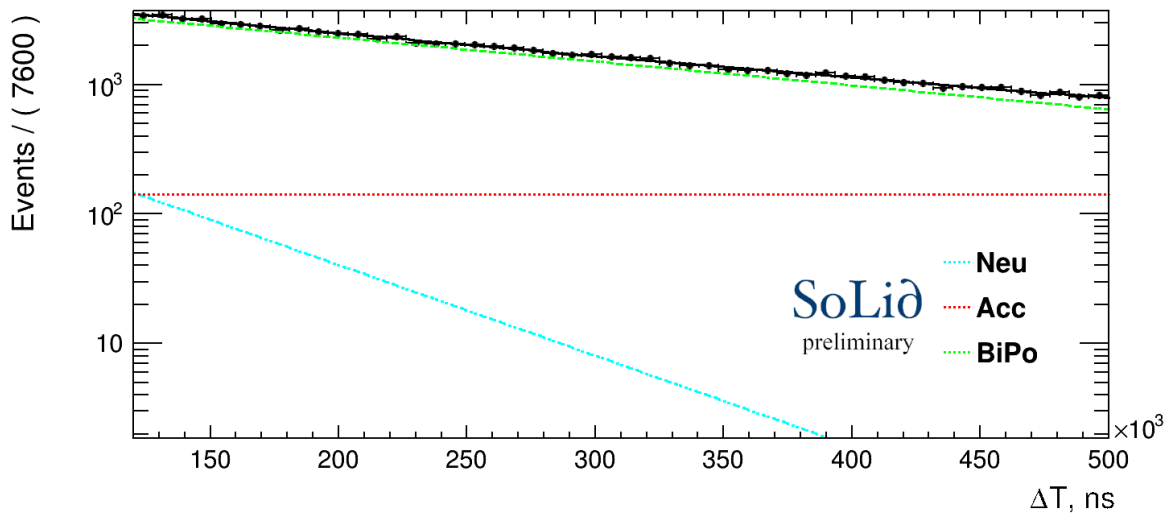


Figure 82: Distribution of the  $\Delta T$  variable (black dots) for the BiPo enriched  $2\gamma$  collection sample. The  $\Delta T$  fit result is superimposed (solid black line). The BiPo contribution shown with the green dotted line is dominant and composes 90% of the enriched sample.

The composition of the enriched sample is assessed by performing the  $\Delta T$  fit for the selected events. Its results are shown in Figure 82 and Table 14. The data are well described by the sum of BiPo and accidental backgrounds, indicating that the atmospheric neutron contribution is vanishing. The purity of the BiPo sample is measured to be  $\sim 90\%$ . The prepared sample is further employed to validate the accuracy of the simulation of the discriminative variables for BiPo events.

20+21+23+24	Acc	BiPo	Neu	fNeu
Yields per day	$100 \pm 1$	$1100 \pm 5$	$15 \pm 5$	0

Table 14: The background sources yields determined from the  $\Delta T$  fit to the combined BiPo enriched  $2\gamma$  data sample

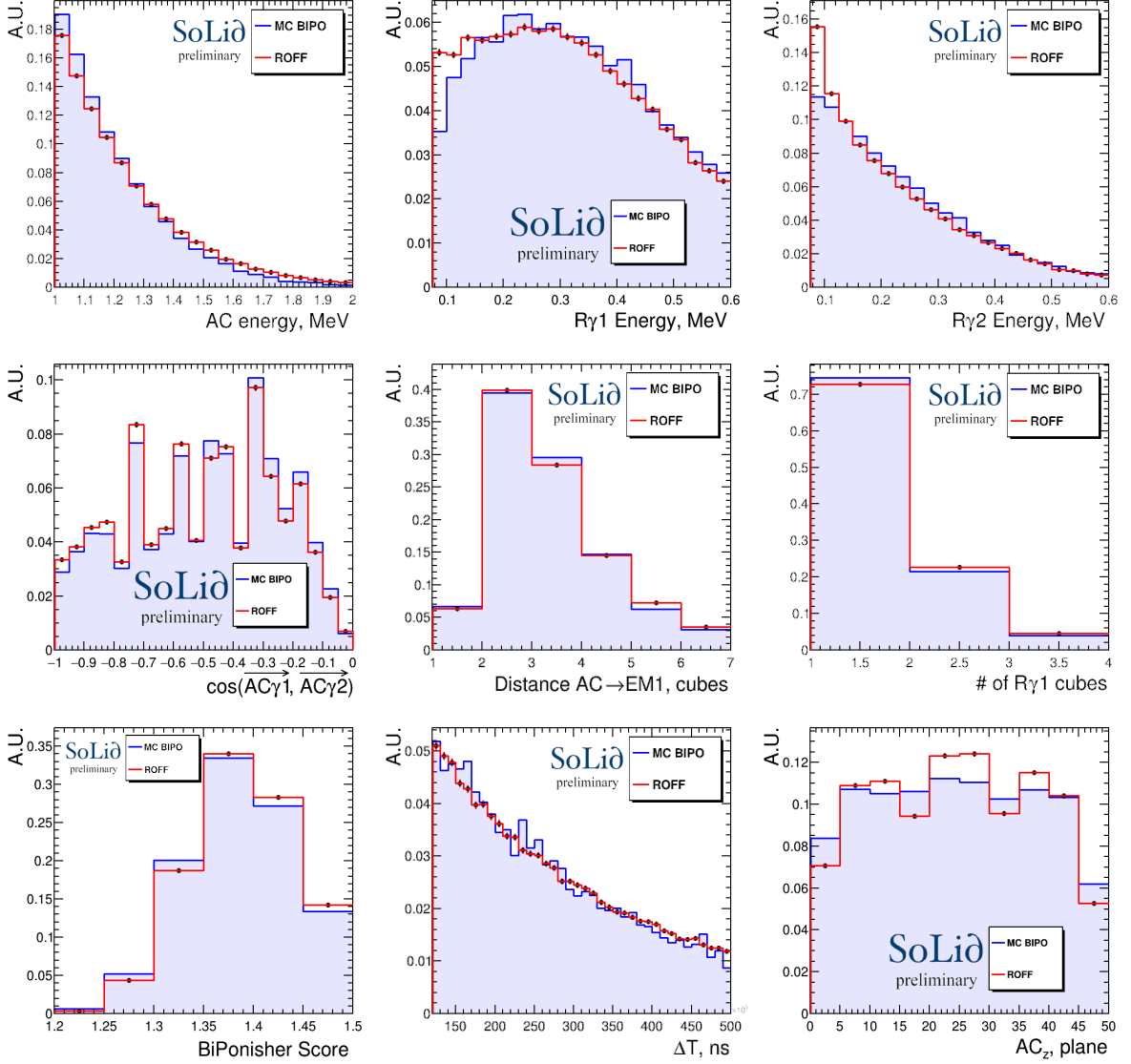


Figure 83: Comparison of some discriminative variables distributions obtained from the ROFF data BiPo enriched sample (red histogram with black data points) and from the BiPo MC simulation (blue filled histogram). The overall agreement is acceptable. The spatial distance between AC and NS, however, shows significant discrepancies, making impossible to model the  $\Delta R$  BiPo shape from the simulation.

### 5.6.2 BiPo-enriched sample validation

The sample of selected BiPo events in the ROff data is compared to a sample of 5 million simulated events. Figure 83 shows the superposition of each discriminative variable determined in the simulation and ROff data. The overall agreement is satisfactory though some discrepancies at the level of 10 % can be observed in the reconstructed  $\gamma$  energies and the cosine of the angle of their lines of flight. These mismodelings can be explained by the accidental contamination of the BiPo enriched sample and by the fact that the PVT cubes on the edges of the detector have much less BiPo contamination. This detector feature is not implemented in the Geant4 geometry simulation. It is also important to check the correlation patterns exhibited in Chapter 5.5. Figure 84 shows that the features shown in Figure 81 are satisfactorily reproduced in the simulation.

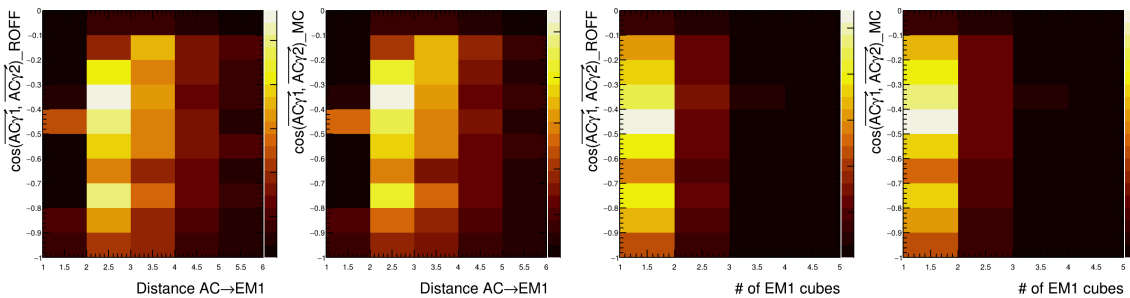


Figure 84: Comparison of the correlation patterns for two variables obtained from the ROff BiPo-enriched sample and from the MC simulation.

### 5.6.3 Atmospherics-enriched sample

Significantly lower statistics compared to BiPo events and the absence of a  $\Delta T$  region where this source could be uniquely identified makes the composition of a high-purity atmospheric sample much more complex. Indeed, even for low values of  $\Delta T$ , the contamination by BiPo can not be neglected. There is no convenient way to proceed. The discrimination power provided solely by the BiPonisher is not enough. It therefore has to be complemented either by the  $\Delta T$  variable, which makes it impossible to precisely determine the background composition of the sample, or with the AC energy (atmospherics prefer larger energies compared to the BiPo), which will have implications for the oscillation analysis. For the time being, it was decided to proceed with the latter option. The aim of the exploration is to select the best pair of parameters (BiPonisher,  $AC_E$ ). The search is performed individually per topology and the goodness of the pair is defined by the fit results or more precisely the fraction of atmospheric background in the selected sample. This fraction has to be maximised under the condition of the minimal size of the enriched sample of 1000 events per topology. Otherwise, there are not enough statistics to properly train the MVA tool. The  $\Delta T$  fit of the combined  $2\gamma$  collection sample with the optimal cuts applied is presented in Figure 85 and Table 15.

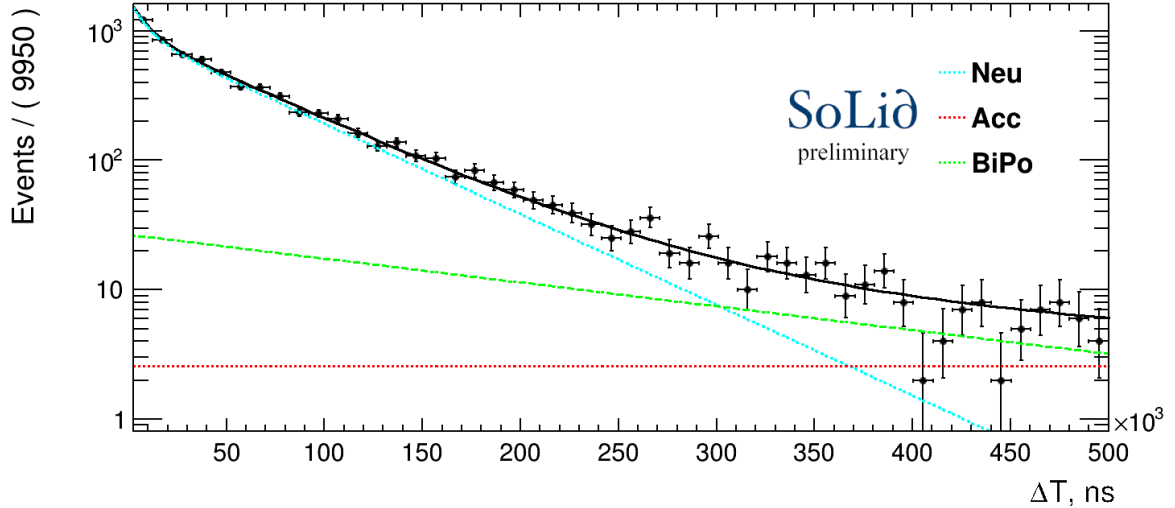


Figure 85: Distribution of the  $\Delta T$  variable (black dots) for the atmospheric-enriched  $2\gamma$  collection sample. The  $\Delta T$  fit result is superimposed (black solid line). The combined atmospheric contribution (blue dotted line) is dominant and composes 90% of the enriched sample.

<b>20+21+23+24</b>	Acc	BiPo	Neu	fNeu
Yields per day	$2 \pm 0.2$	$7 \pm 1$	$78 \pm 2$	$7 \pm 1$

Table 15: The background sources yields determined from the  $\Delta T$  fit to the combined atmospheric-enriched  $2\gamma$  sample

## 5.7 Multivariate analysis and 5D optimisation

The set of discriminative selection variables is defined, and it has been checked that the BiPo simulation data is reproducing correctly both the distributions and the correlation patterns. The design of the classifier algorithm can then proceed with a training of signal events from a sample of preselected IBD simulated candidates against the enriched background samples. In total, three BDT classifiers are trained against the following:

1. BiPo-enriched sample with the EM set of variables (BDT<sub>1</sub>);
2. atmospheric-enriched sample with the EM set of variables (BDT<sub>2</sub>);
3. atmospheric-enriched sample with the neutron-driven set of variables (BDT<sub>3</sub>).

ROOT analysis framework provides all the required machinery via the Toolkit for Multivariate Data Analysis (TMVA) [107]. To maximise the use of available statistics (which is especially critical for the atmospheric background), a k(10)-folding strategy [108] is employed:

- All events are enumerated (independently in each topology);
- The test and training samples are split according to:

- For ( int  $j = 0; j < 10; j++$  ):
  - If (number%10) !=  $j \Rightarrow$  train sample (which means 90% of events);
  - if (number%10) ==  $j \Rightarrow$  test sample (which means 10% of events)
- The BDT trained on a given sub-sample of ROff data is applied to the events which have not been used in the training:  
For the event with (number%10) ==  $j \Rightarrow$  BDT number  $j$  is used

It is mandatory to check that the classifiers are properly trained. Figure 86 is gathering for each of the four topologies considered in this work the comparison of the 10 BDT responses for the trained and test samples. The agreement is remarkable and indicates that there is no overtraining of the tool.

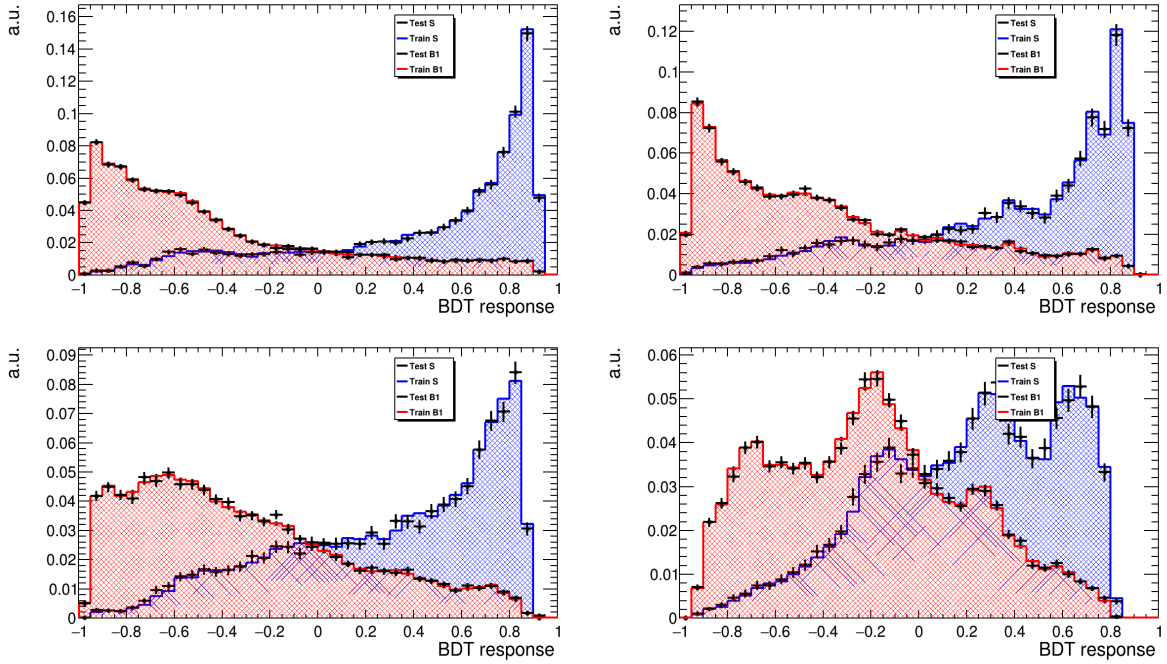


Figure 86: The results of the overtraining check for the set of  $2\gamma$  Topologies: 20 (top left), 21 (top right), 23 (bottom left) and 24 (bottom right). For each of the 10-foldings, the BDT scores are displayed for the training (filled histograms) and test (black data points) samples, as well as for the signal (blue) and background (red) datasets. The results of the different foldings are further combined. None of the distributions indicates overtraining.

It has been chosen to proceed with a five-dimensional optimisation of the three discriminant values of the BDT, the BiPonator variable and  $\Delta T$ , which are basically uncorrelated with the EM variables used in the BDT. It is complemented with the static  $AC_E$  cut, which rejects events with a value below the threshold of 1.5 MeV. The best set of parameters is searched via a scan over all of the parameter space. It is aimed at maximising the significance of the signal used as a figure of merit (FoM):

$$\text{FoM} = \frac{\text{Signal}}{\sqrt{\text{Signal} + \text{Background}}}. \quad (72)$$

	BDT <sub>1</sub>	BDT <sub>2</sub>	BDT <sub>3</sub>	BiPonator	$\Delta T$	FoM
Topology 20	-0.2	0	0.05	0.49	302500	2.1
Topology 21	-0.25	-0.15	-0.15	0.44	242500	1.8
Topology 23	-0.25	0.1	-0.3	0.49	282500	1.4
Topology 24	-0.25	0.2	0.05	0.69	282500	1.4
Topology 25	0.15	0.1	-0.1	0.49	152500	0.7

Table 16: The output of the 5D optimisation cuts for the  $2\gamma$  topology collection.

This optimisation is performed for each topology of interest independently. Table 16 gathers the optimal cuts obtained for the  $2\gamma$  topologies. Not all cuts are applied simultaneously. At the first stage, only the  $AC_E$ , BiPonator, BDT<sub>1</sub> and BDT<sub>2</sub> cuts are employed. The sample which underwent this subset of cuts is referred to as the 3D-optimised. Similarly, the sample, which underwent all the cuts, is denoted as the 5D-optimised. The cuts  $\Delta T$  and BDT<sub>3</sub> are kept for a later stage to keep the spatial and time distance distributions between the NS and ES clusters untouched. They are, however, identified at the same time, since it allows the cuts on the other parameters to be relaxed, by anticipating that some of the background events are rejected later. An additional reasoning behind this staged approach in the application of the cuts is introduced in the next subsection. The modified comparison of signal and background yields, after the application of the first set of cuts, is shown in Figure 87. The signal-to-background ratio is predicted to be 1 to 2 with 23 antineutrino events expected per day.

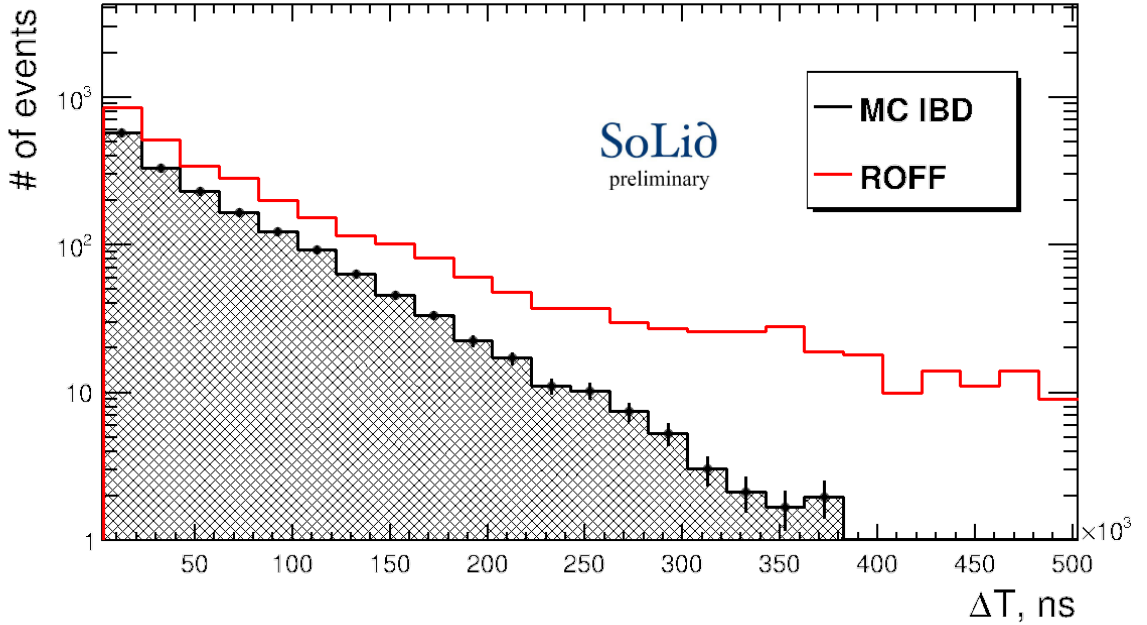


Figure 87: The comparison of the yields in the 3D-optimised (no  $\Delta T$ , no BDT<sub>3</sub> cuts applied)  $2\gamma$  topology sample expected from 74 days of ROFF data and an accordingly scaled IBD SoLO simulation in logarithmic scale. The plot is indicating a significant decrease of background level (S/B ratio is 1 to 2, which is an improvement by factor 25 comparing to the preselected sample).

## 5.8 Simultaneous fit technique

The background contamination, which remained after the application of the multivariate analysis tool, cannot be distinguished solely by the  $\Delta T$  fit. It is due to the fact that both components of the atmospheric background are sharing the same neutron moderation time with the signal events. The fraction of the fast component in the total atmospheric yield is even constrained from that determined in the IBD MC sample. Hence, it is only possible to estimate the combined contribution of the atmospheric and the signal candidates. Then an additional variable distribution has to be considered and fitted simultaneously with the  $\Delta T$  distribution. The idea is to employ the spatial distance  $\Delta R$  between the NS and the AC. This variable is included in the BDT<sub>3</sub> training that is not used in the selection of the 3D optimisation. The background fit model to describe the  $\Delta R$  distribution is defined similarly to Equation 70:

$$\Delta R = N_{\text{acc}} \cdot S_{\text{acc}} + N_{\text{BiPo}} \cdot S_{\text{BiPo}} + N_{\text{Atm}} \cdot S_{\text{Atm}} , \quad (73)$$

where:

- $N_i$  denotes the yield of the background component  $i$ . It is a free parameter of the fit, defined exactly the same way as for the  $\Delta T$  model, such that the results can be shared afterward in a simultaneous fit with  $\Delta T$ . The only difference is that  $N_{\text{Atm}}$  is not split between fast and nominal component and hence is presented as a total yield;
- $S_i$  denotes the  $\Delta R$  shape for the background component  $i$ . Their shape is taken from the distributions obtained in the enriched samples (or the control sample for accidentals). Technically, the discrete character of  $\Delta R$  is best represented by histograms that are transformed into a probability density function (RooHistPdf). In principle, since the  $\Delta R$ - $\Delta T$  fit is performed on the 3D optimized sample it makes sense to define the corresponding shapes from the 3D optimised enriched samples. Practically, the statistics of these samples is modest, and hence the knowledge of the shape is subjected to the statistical fluctuations. The situation improves once the larger amount of the ROff data (*e.g.* the full Phase I) is considered for the analysis;
- The accidentals are constrained in yields and shape from the preselected FPNT sample in use;
- The BiPo is modelled with the enriched sample. It owns a large enough statistics after application of the BDT<sub>1</sub> and BDT<sub>2</sub> cuts. However, the statistics starts to be scarce once the BiPonator cut is introduced. The  $S_{\text{BiPo}}$  BiPonator cut is therefore not applied. Since the BiPonator tool uses information that is completely uncorrelated with the  $\Delta R$  distribution, no bias is expected. Finally, accidental contamination has to be subtracted. It is done with the  $S_{\text{acc}}$  and the yields defined from the FPNT sample;
- The modelling of the atmospheric  $\Delta R$  shape is the most complicated. The two concurrent approaches that were considered are discussed below.

The atmospheric background  $\Delta R$  shape can be defined either from the preselected enriched ROff sample or the 3D optimised ROff sample. In both cases, accidental

contamination is subtracted by considering the yields provided by the FPNT and the  $S_{\text{Atm}}$  shape defined above. The remaining contamination comes from BiPo events. In both cases, this contamination is determined with the fit to the  $\Delta T$  distribution and is subsequently subtracted considering the  $S_{\text{BiPo}}$  p.d.f. defined above. The 3D-optimised ROFF sample has larger statistics, hence the identification of the BiPo yield is more precise and the final shape is less exposed to statistical variations. The situation might change when a larger enriched background sample is available, but for now, the 3D-optimised ROFF sample is the retained choice.

This choice makes the  $\Delta R$  fit for the ROFF data to automatically converge. Therefore, it has to be validated. In order to do that, the k-fold splitting that was used for the MVA tool is also employed in this context. This time, 9 out of 10 samples are used to compose  $S_{\text{Atm}}$  and the remaining one undergoes the  $\Delta T$  and simultaneous  $\Delta R$ - $\Delta T$  fit. The comparison of the results obtained for subsets of the folds is summarised in Tables 17 and 18.

Fold	0	1	2	3	4	5
Acc	$9.4 \pm 6.0$	$7.5 \pm 4.6$	$12.0 \pm 7.1$	$18.9 \pm 6.7$	$16.2 \pm 7.5$	$21.1 \pm 8.4$
BiPo	$54.7 \pm 18.5$	$27.1 \pm 15.6$	$64.9 \pm 20.0$	$27.3 \pm 18.4$	$43.7 \pm 19.8$	$42.1 \pm 20.7$
Atm	$209.2 \pm 19.7$	$242.3 \pm 19.2$	$234.7 \pm 20.9$	$249.1 \pm 19.8$	$240.3 \pm 20.6$	$213.8 \pm 19.9$

Table 17: The background compositions obtained from the  $\Delta T$  fit for some of the 10 ROFF equally split sub-samples.

Fold	0	1	2	3	4	5
Acc	$11.5 \pm 5.3$	$5.1 \pm 4.2$	$11.3 \pm 6.3$	$17.8 \pm 5.5$	$16.8 \pm 6.3$	$20.3 \pm 6.8$
BiPo	$48.4 \pm 11.8$	$44.7 \pm 10.2$	$66.8 \pm 13.0$	$24.5 \pm 10.7$	$40.3 \pm 11.6$	$47.9 \pm 11.9$
Atm	$213.0 \pm 14.1$	$227.3 \pm 13.6$	$233.3 \pm 15.0$	$254.1 \pm 14.0$	$242.8 \pm 14.5$	$208.9 \pm 13.9$

Table 18: The background compositions obtained from the  $\Delta R$ - $\Delta T$  fit for some of the 10 ROFF equally split sub-samples.

Based on the background compositions evaluated, three important conclusions can be drawn. Firstly, the obtained yields are in agreement within their statistical uncertainties. Secondly, the simultaneous fitting improves the attached uncertainty on the yield determination. These two facts validate that the fitting procedure can be conducted with the atmospheric  $\Delta R$  shape determined directly from the ROFF data sample. As a side note one can see that after 3D optimisation the atmospheric are becoming the dominant source of the background. It justifies *a posteriori* the development of a selection too trained specifically against this type of background. The results are supplemented with Figure 88. It shows the difference between  $S_{\text{Atm}}$  and  $S_{\text{IBD}}$ , which justifies the relevance of variable selection to distinguish the two components. Moreover, the  $S_{\text{Atm}}$  distribution obtained for each iteration in the k-folding approach is seen in agreement with their uncertainties.

## 5.9 Systematic studies

All the methods and techniques used in the analysis were presented and validated. Before proceeding to establish the yield predictions, a thorough review of the systematic



and LL), one thousand SM are sampled within their associated uncertainty. The original sample of MC IBD events (*i.e.* without the reconstruction) is processed with each of the generated SM. The uncertainty is defined as the spread of the yields determined with each of the alternative generated SM. Let us note that the second stage of the determination is provided in this document for the light sharing and the first one for the absolute energy scale, since the final factor is yet to be chosen by the collaboration. The fixed parameters of the  $\Delta R$ - $\Delta T$  fit model are known with a given uncertainty. They are varied in the simultaneous fit according to one standard deviation of their uncertainty, and the variation in the measured yields is reported as a systematic uncertainty estimate. This is in particular the case for the characteristic moderation time of the neutron or BiPo lifetime. It is more important to obtain a credible systematic uncertainty related to knowledge of the  $\Delta R$  shapes. They are mostly determined from the ROff data sample of reference and suffer from statistical fluctuation. The p.d.f.  $\Delta R$  shapes used are sampled according to this statistical uncertainty and the generated distribution is used as the new baseline model in the simultaneous fit. The procedure is reproduced 100 times to obtain a 10% precision on the uncertainty. The spread of the obtained yields results distribution is taken as the corresponding systematic estimate. For now, the largest systematic uncertainty is expectedly associated with the  $\Delta R$  shape of the atmospheric background source, which suffers from the smaller size of the sample used to determine the shape. The situation will improve as we anticipate a larger background data set in the next stage of this analysis. Obviously, the list of mentioned systematics is incomplete and the dedicated search for the new sources is permanently ongoing. The current state of the art is summarised in Table 19. It is worth mentioning here that this analysis has been conducted without using the signal data (blind analysis). The determination of these systematic estimates has also been determined without the use of the ROn data. This approach will allow us to evaluate *comprehensively* the agreement between the prediction of antineutrino yield and the actual measurement on the open small ROn dataset.

## 5.10 Construction of the predictions

Table 20 summarises the number of IBD candidates expected per day for the 3D and 5D optimised samples. The expected number of background events, as determined from the ROff sample, is provided as well. The FoM that fills the fourth and last columns of the table is directly the signal significance. It can be used to define the size of the ROn sample to be opened to validate the topological reconstruction approach. The evidence is obtained for one day. Five days of ROn are close to the usual observation level of five standard deviations. The proof of principle of the approach was performed in 5 days. The results presented below correspond to the 21 days (the full open data set available in collaboration) of the ROn data.

It is also important to have predictions in terms of distributions of control variables to better qualify the observed signal. Control variables are chosen so that they are not part of the discriminative variables. Some of them can, however, be used to further select events in a posterior phase of the analysis. Four of them were considered:  $AC_E$ ,  $\Delta T$ ,  $\Delta R$ , and the position  $z$  of AC. Figure 89 displays the selection predictions in terms of background, determined from the ROff sample, and the number of IBD candidate signal events using the simulated signal sample. These predictions are normalised to a sample of candidates corresponding to 21 days of ROn data. No information from ROn data set has

Syst source	Nominal	$\delta$	$\sigma_{Y\bar{\nu}}$	$\sigma_{Y\bar{\nu}}, \%$	Comment
Light sharing	Saffron2 induced	Sampled	0.23	0.98	
Absolute energy scale	Saffron2 induced	+3.0% -3.0%	+1.09 -1.02	4.57 4.29	To be improved with the SM sampling
$\Delta\tau$ BiPo	235.8 $\mu s$	+1.2 $\mu s$ -1.2 $\mu s$	+0.01 -0.02	0.04 0.08	
$\Delta\tau$ Atm	62.0 $\mu s$	+0.5 $\mu s$ -0.5 $\mu s$	+0.13 -0.14	0.54 0.58	
$\Delta\tau$ fAtm	8.5 $\mu s$	+0.8 $\mu s$ -0.8 $\mu s$	-0.03 +0.02	0.12 0.08	
$\Delta R$ Acc shape	FPNTs sample p.d.f.	Sampled	0.21	0.88	Uncertainty scales with the ROff data statistics
$\Delta R$ Atm shape	Enr. sample driven p.d.f.	Sampled	0.50	2.10	Uncertainty scales with the ROff data statistics
$\Delta R$ BiPo shape	Enr. sample driven p.d.f.	Sampled	0.15	0.63	Uncertainty scales with the ROff data statistics
$\Delta R$ IBD shape	ROSim p.d.f.	Sampled	0.59	0.37	

Table 19: List of the currently considered systematic sources, sizes of variations of the initial values and the impact on the antineutrino yield determination.

	3D			5D		
	Signal/day	Bckg/day	FoM	Signal/day	Bckg/day	FoM
Topology20	6.8(44.5%)	8.1(0.9%)	1.8	6.0(39.2%)	2.2(0.2%)	2.1
Topology21	6.4(51.5%)	12.6(2.8%)	1.5	5.7(45.3%)	3.9(0.8%)	1.8
Topology23	3.7(42.5%)	5.6(1.0%)	1.2	3.4(38.6%)	2.3(0.4%)	1.4
Topology24	5.3(33.6%)	12.9(2.0%)	1.2	4.2(26.5%)	4.4(0.7%)	1.4
Topology25	1.3(35.3%)	1.9(1.6%)	0.7	1.0(27.8%)	0.8(0.7%)	0.8
Total	23.5(42.1%)	41.1(1.5%)	2.9	20.1(36.2%)	13.6(0.5%)	3.5

Table 20: Predictions of each  $2\gamma$  topology for the optimised cuts (**efficiencies claimed in parenthesis are calculated w.r.t. the numbers of preselected events in each topology category**)

been used to design the analysis. The unblinding of the ROn data set will be described in the next Section.

In order to complete this set of predictions, the background composition of the selected sample of ROff data has been analysed by means of the simultaneous  $\Delta R$ - $\Delta T$  fit. Figure 90 displays the result of the fit and the components of the fit model. The Table 21 gathers the measured fraction of each background source. The background yields per day correspond to the 3D optimisation. They will be further reduced by the application of the additional requirements present in the 5D optimisation.

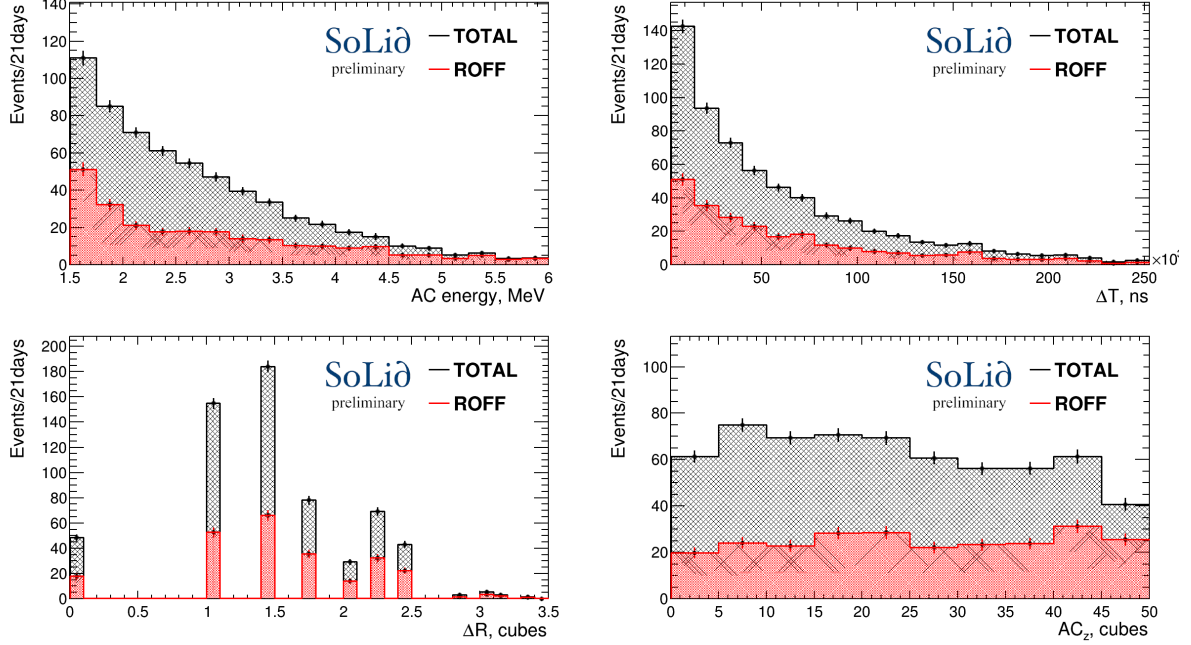


Figure 89: The control plot of AC energy (top left) displayed as stacked histograms of the background (red) and signal (grey) predictions. It is complemented with spatial (bottom left) and time (top right) distances between NS and AC, and the  $z$  position of the AC (bottom left).

<b>20+21+23+24</b>	Acc	BiPo	Atm
ROFF	$1.9 \pm 0.3$	$6.8 \pm 0.5$	$30.6 \pm 0.6$
MC IBD			$23.5 \pm 0.2$
Total	$1.9 \pm 0.3$	$6.8 \pm 0.5$	$54.1 \pm 0.6$

Table 21: Yield predictions for the MC IBD and ROff data per 1 day.

## 5.11 Unblinding strategy validation with the open data set

The set of predictions obtained in the previous subsection was designed following a blind analysis strategy. To verify the proposed approach and the dedicated predictions, a subsample of the ROn data has to be opened. Closing it again can be very costly; hence, the unblinding conditions have to be rigorously thought in advance. To begin with, any further interpretations of the results obtained with the opened ROn data are done under two assumptions. Firstly, it is required that the background compositions in ROff and ROn samples are equivalent, or if they are not, that the difference can be accounted for by an additional background source coming from the reactor physics. Second, the background composition among the different cycles of data collection must be stable. Anticipating the full Phase I analysis strategy, the latter condition has to be validated for each of the ROff cycles entering the analysis. The proposed way to perform the cross-check is by means of a  $\Delta T$  fit that allows the BiPo and atmospheric fractions to be measured. The results for the 10 ROff cycles, used in this analysis, are summarised in Table 22.

The obtained mean values for the merged sample are:  $\overline{BiPo} = 2170$ ;  $\overline{Atm} = 260$ ;  $\overline{Acc} = 150$ . The yields evaluated are in agreement with the mean values, and hence the stability

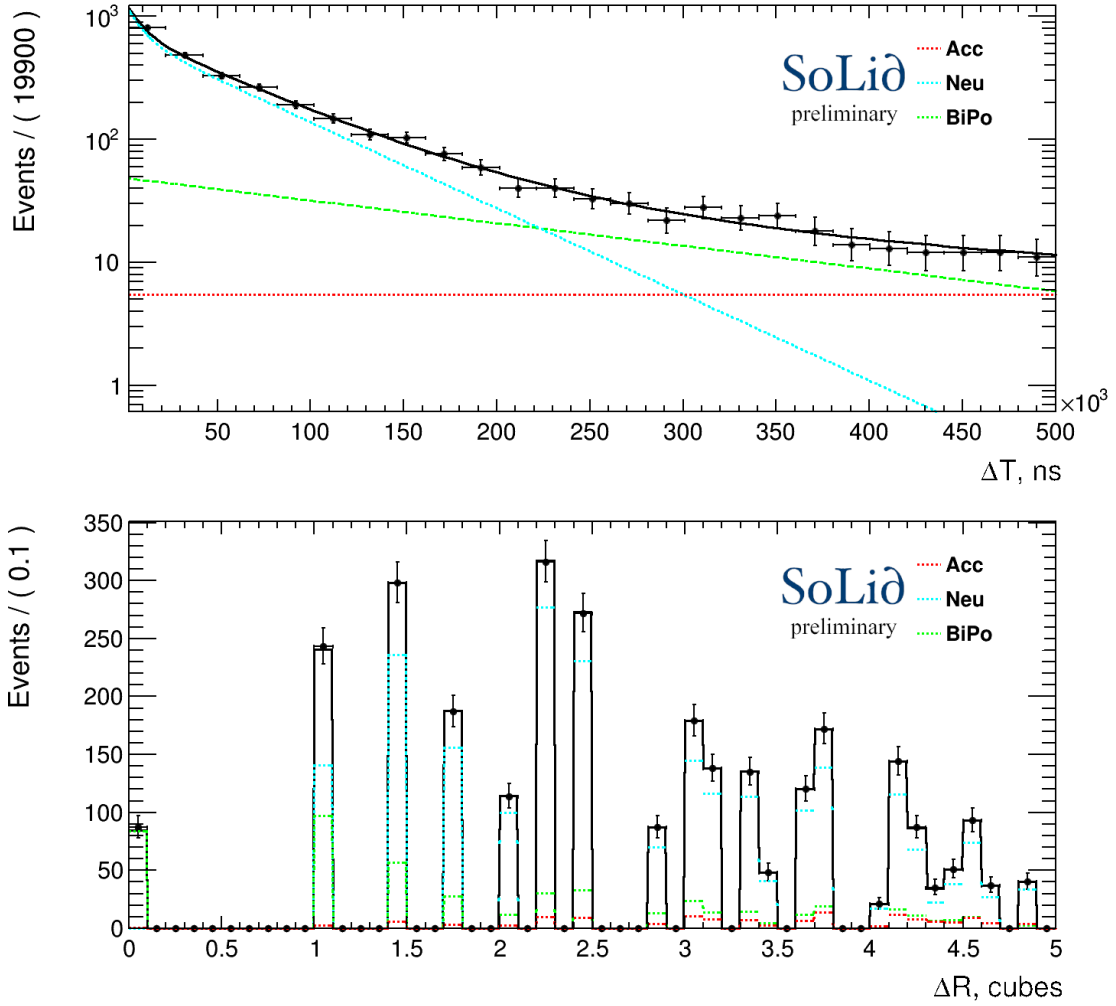


Figure 90: Distribution of the  $\Delta T$  and  $\Delta R$  variables (black data points) for 75 days of ROFF 3D optimised  $2\gamma$  collection sample. The simultaneous  $\Delta R$ - $\Delta T$  fit result is superimposed (black solid line) with the correspondent components (BiPo in green, Accidentals in red and Atmospherics in blue). The simultaneous fit method is established from hereafter as a baseline tool to identify signal and background yields.

	P1	P2	P3	P4	P5
BiPo	2130±30	2280±30	2160±30	2140±30	2210±30
Atm	260±30	270±30	235±30	285±30	275±30
Acc	145±5	155±5	150±5	145±5	150±5
	P6	P7	P8	P9	P10
BiPo	2150±30	2180±30	2120±30	2200±30	2110±30
Atm	270±30	215±30	235±30	260±30	320±30
Acc	150±5	150±5	140±5	160±5	145±5

Table 22: The normalized background per day compositions of the 10 preselected ROFF cycles used in the analysis.

	NS	ES	Coincidences	Coincidences ( $2\gamma$ )
ROff	1.43e+07	2.5e+07	4.1e+05	2700 $\pm$ 10
ROn	1.41e+06	3.6e+07	5.4e+05	2800 $\pm$ 10

Table 23: The ROff/ROn initial characteristics comparison scaled to 1 day.

of the background compositions of the different ROff samples is conserved for the  $2\gamma$  topologies. As for opening the ROn sample, the approach is divided into stages in order to maximally reduce the probability of burning the data. Each stage has a condition to pass further, and the unblinding procedure is stopped once there is a stage where the condition is not met. The first step of the unblinding consists of comparing the yields of NS, ES, and NS/ES coincidences in the samples of ROff and ROn. The comparison of normalised yields is summarised in Table 23. If the number of NS signals is consistent in both samples, an increase in the number of ES signals is observed in the ROn sample. It is remarkable to note that this increase is topologically dependent and that a consistent number of ES is obtained between the two reactor status samples for topologies involving two reconstructed  $\gamma$ . The increase in ES signals for the other topologies is likely related to airborne nuclei induced by the reactor that are also measured by dedicated ancillary detectors at BR2.

### 5.11.1 BiPo component comparison

The next step is related to the background composition comparison and particularly BiPo enriched  $2\gamma$  samples. Because it is a dominant source of the background for the preselected ROff data, it is crucial to check that the BiPo fraction remains the same for the ROn samples. As a natural radiation issued to the detector by the detector, the reactor conditions are not expected to change its rate. Its stability will be invaluable information to assess the robustness of the background model in this analysis. The same requirements used to select the BiPo-enriched sample in the ROff dataset (described in Chapter 5.6.1) are applied to the ROn dataset. The fit to the  $\Delta T$  distribution is performed, and its results are compared between the two. The Table 24 is displaying the results of the comparison normalised to the size of the ROn data set for all the  $2\gamma$  topologies included. The level of accidentals is observed to increase, supporting the hypothesis that an airborne background contribution actually occurs when the reactor is powered. It also confirms that the level of BiPo is found to be the same as that measured in the ROff data set. It is useful to compare these samples not only with respect to the numbers but also in terms of the electromagnetic characteristics. The comparison of the control variables in the two data sets is provided in Figure 91, where all distributions are found to be in good agreement.

	ROff	ROn	ROff (BiPo)	ROn (BiPo)
BiPo	2165 $\pm$ 10	2160 $\pm$ 20	1090 $\pm$ 5	1080 $\pm$ 15
Atm	260 $\pm$ 10	320 $\pm$ 20	15 $\pm$ 5	20 $\pm$ 10
Acc	150 $\pm$ 1	195 $\pm$ 5	95 $\pm$ 1	130 $\pm$ 5

Table 24: ROff vs ROn background composition (preselected and BiPo-enriched samples)

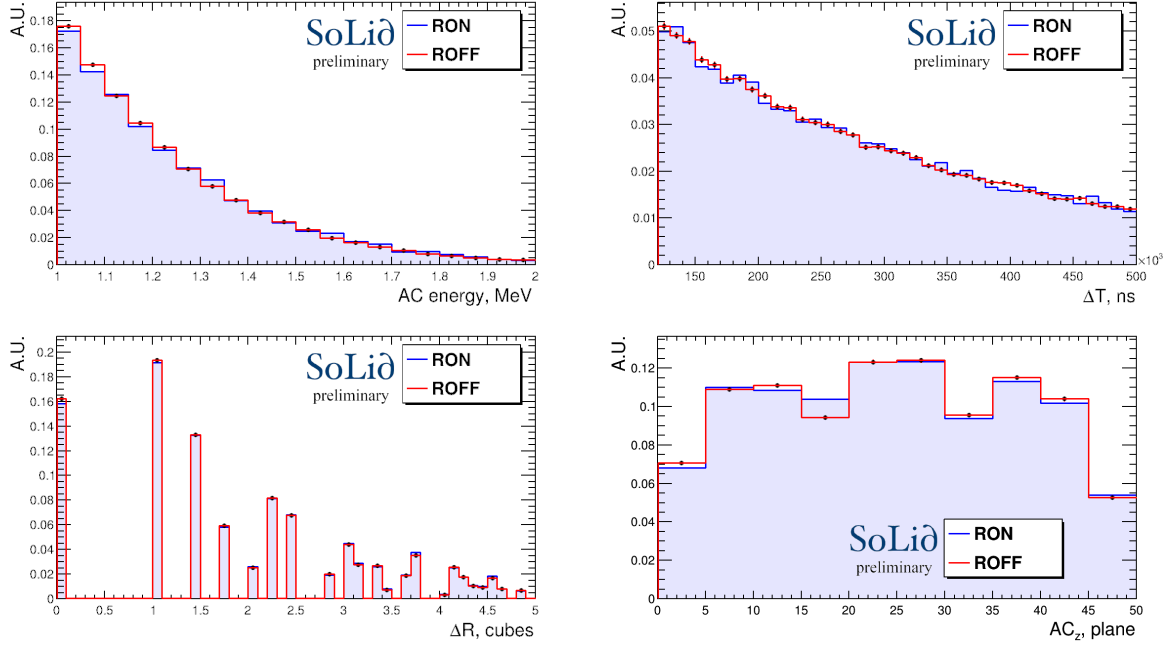


Figure 91: The comparison of the AC energy distribution (top left) for the BiPo enriched components (which is assumed to be constant). The comparison was made for the preselected  $2\gamma$  combined ROFF and ROn samples. It is complemented with another control plot distributions (time (top right) and spatial (bottom left) distance between NS and ES, and  $z$  position of the AC) with the ROFF sample displayed as a filled blue histogram and ROn as a red histogram. All distributions agree within the statistical uncertainties and therefore justify the equivalence of the BiPo components in the background compositions of ROFF and ROn.

This exploration points therefore towards a correct understanding of the background sources (at least no inconsistency with the models is noticed) and allows the number of IBD candidates in the ROn data set under consideration to be unveiled.

### 5.11.2 Predictions versus ROn measurements

The exact same selection requirements used to select the ROFF and simulated IBD candidates are applied to the ROn data set. The number of selected events is presented in the control plots in Figure 92. The selected ROn candidates are shown with the blue data points. The predicted number of IBD events (in shaded grey) and the expected backgrounds as determined from the ROFF dataset are superimposed on the ROn measurement. Good statistical agreement is obtained in the four proposed projections. This is a clear indication of an excess of events consistent with the IBD hypothesis.

The comparison is complemented by the  $\Delta R$ - $\Delta T$  fit to the candidates distribution selected in the ROn dataset. Figure 93 displays the result of the fit. The Table 25 gathers the yield measurements obtained in this fit and the predictions established in the sub-section 5.10. The measured yields for the different components of the samples were also found to be in satisfactory agreement with those predicted.

To obtain the final signal and background yield, the efficiency of the two additional cuts (BDT $_3$  and  $\Delta T$ ) from the 5D optimisation must be taken into account. It is done by introducing a scaling factor, based on information from Table 20. It is defined as the

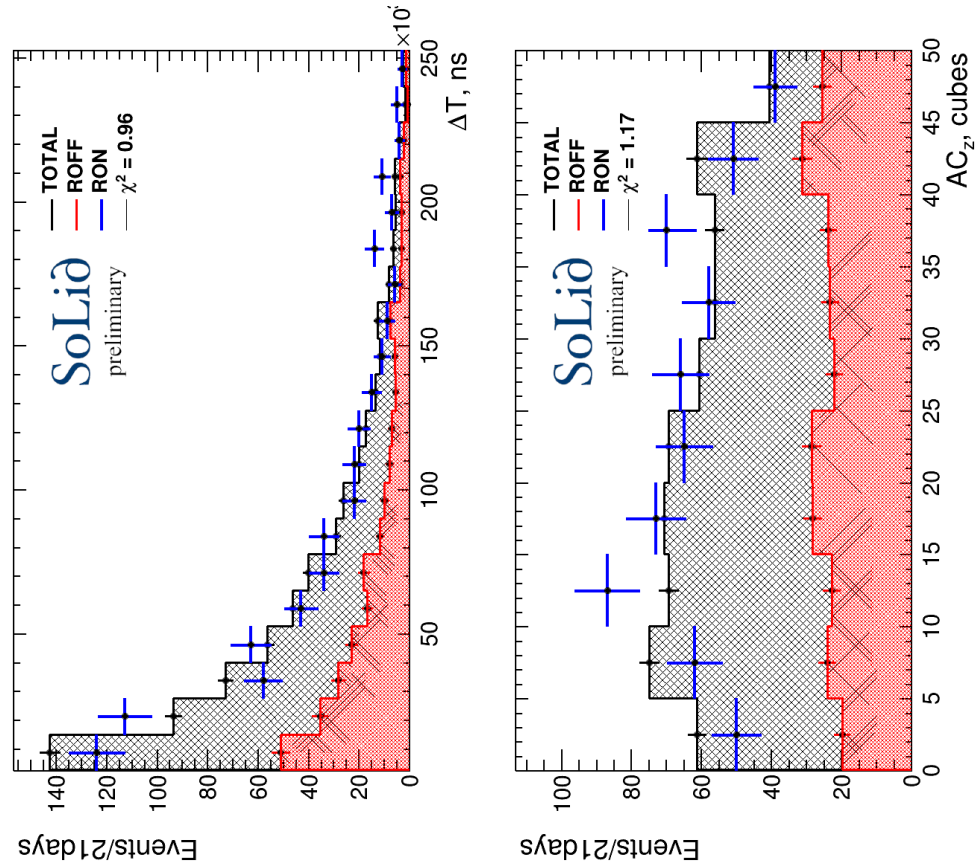


Figure 92: The first stage of assessments of the predictions with respect to the RON data which consists of comparison of the control plots for the 5D optimised data samples. Each plot contains the stacked and accordingly scaled predictions from the ROFF data (in red) and the MC IBD (in grey), which are compared with the RON (blue data points). The excess of events compared to the ROFF predictions can be clearly seen. In addition, within the statistical uncertainties it is in agreement with the prediction.

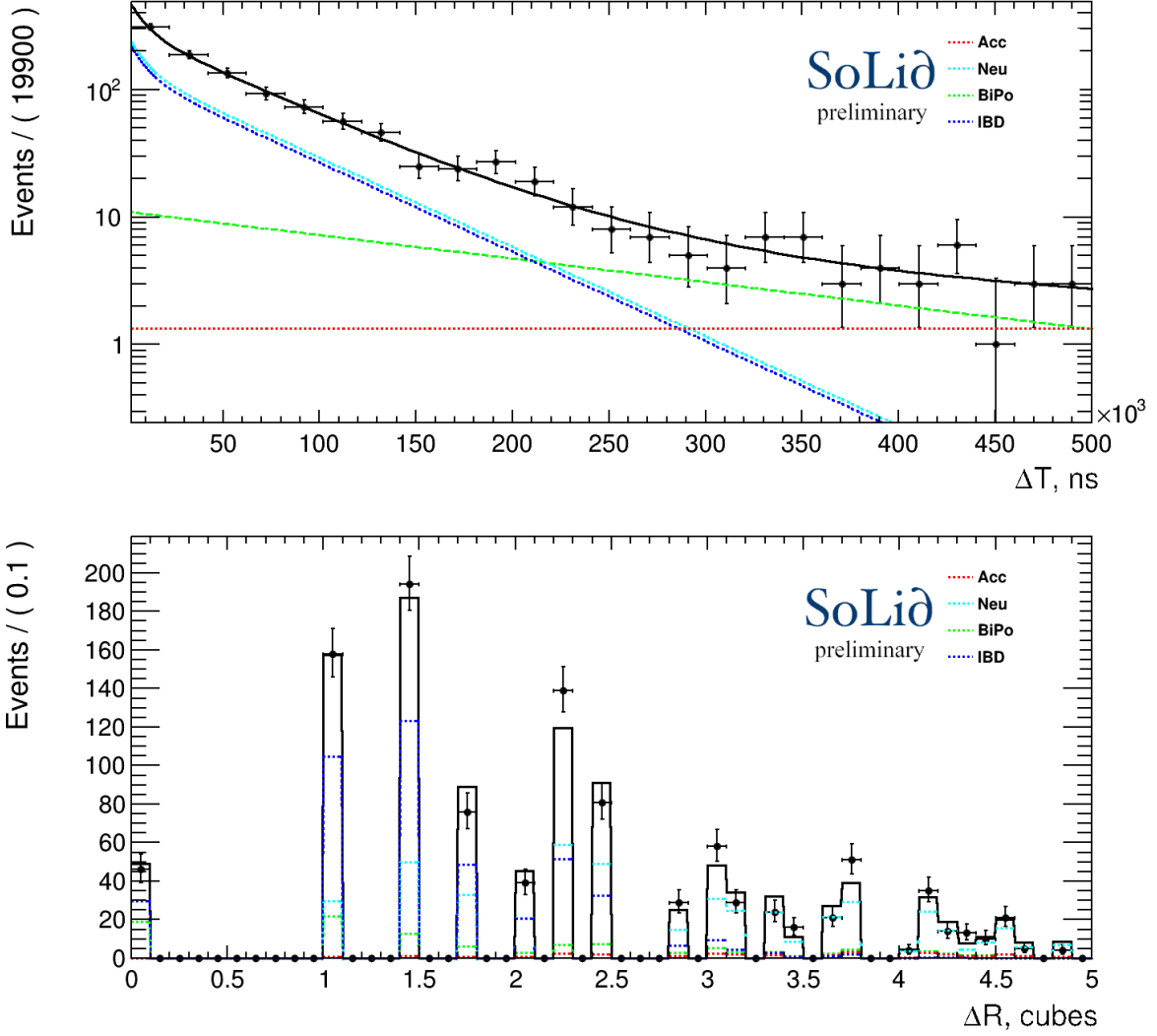


Figure 93: Distribution of the  $\Delta T$  and  $\Delta R$  variables (black data points) for the 3D optimised  $2\gamma$  collection ROn open dataset. The simultaneous  $\Delta R$ - $\Delta T$  fit result is superimposed (black solid line) with the correspondent background (BiPo in green, Accidentals in red and Atmospherics in blue) and signal (in dark blue) components. The fit has converged and the extracted yields are in agreement with the prediction within the statistical uncertainties.

<b>20+21+23+24</b>	Acc	BiPo	Atm	IBD
Prediction	$1.9 \pm 0.3$	$6.8 \pm 0.5$	$30.6 \pm 0.6$	$23.5 \pm 0.2$
Total	$1.9 \pm 0.6$	$6.6 \pm 1.6$	$27.8 \pm 2.0$	$25.5 \pm 2.1$

Table 25: The comparison of the scaled-per-day  $\Delta R$ - $\Delta T$  fit yields obtained from the combined MC IBD and ROff predictions versus ROn data.

fraction of the yields after the 5D optimisation to the yield after the 3D optimisation. By combining the results of the simultaneous fit, the newly defined scaling factor and the systematic estimation (which is for now just a sum in quadrature of the individual contributions), the final measurement on the ROn open dataset is obtained:

$$Y_{\bar{\nu}}^{2\gamma} = 21.8 \pm 2.1 \pm 1.5 \frac{\bar{\nu}}{\text{day}} \quad ; \quad S/B = 1.2 \pm 0.2 \quad (74)$$

The Figure 94 concludes the scrutiny of the results obtained from the open data set by providing an additional projection. The yield of Equation 74 is superimposed on the predicted performance and the selected working point.

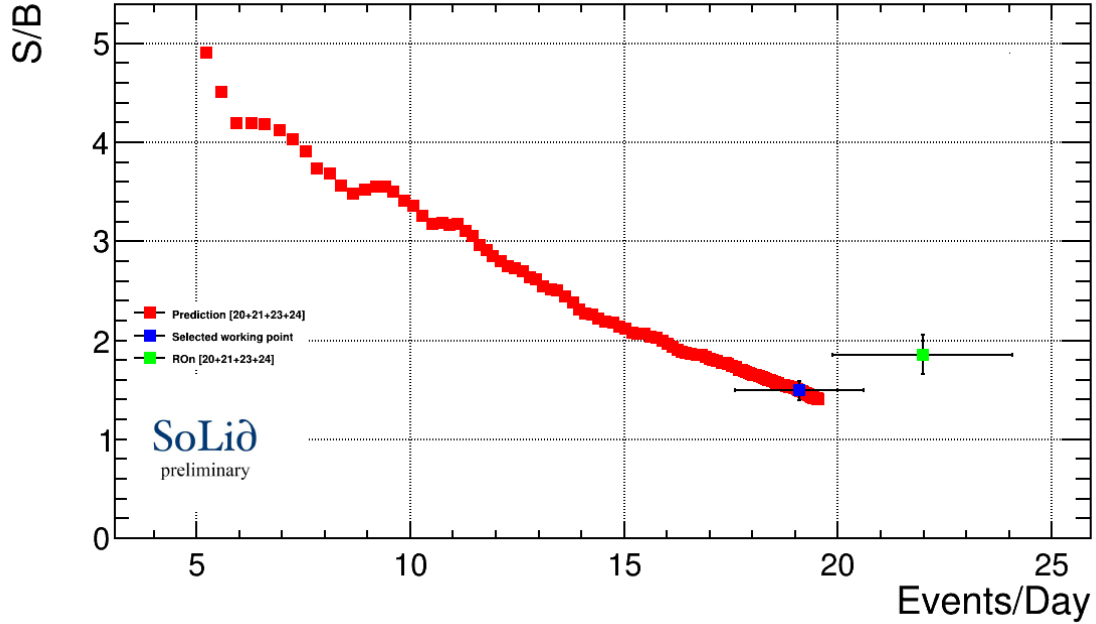


Figure 94: The performance of the topological analysis in signal-to-background ratio as the function of the excess per day. The red points correspond to the expectation, obtained by varying the  $BDT_1$  cut. The blue point shows the selected working point and only systematic uncertainty attached. Finally, the green point is representing the result, obtained with the open dataset with an attached statistical uncertainty.

## 6 Summary and outlook

The topological analysis presented in this thesis gathered developments related to the electromagnetic signal reconstruction, their calibration and a selection of antineutrinos based on the characteristics and assets of the *Soli $\partial$*  detector. Chapter 5 provides the proof of principle of the topological reconstruction analysis, based on a blind analysis, obtained with 21 days of the open data set available in the collaboration. There is still the open question of the final choice of the absolute energy scale to be taken. However, no show-stoppers are identified and this analysis can proceed to the full Phase I analysis and the subsequent oscillation analysis. It should be noted that preliminary oscillation parameters sensitivity studies have been performed based on the selection performance of this analysis. They are reported in [93]. In order to reach the next step, the full available statistics has to be gathered. The pieces of the unblinding strategy were already mentioned here and there in this document. Let us gather them under the proposal:

- There is a unique requirement for the ROff data: only consider cycles, with background compositions as determined by the  $(\Delta R)\Delta T$  fit consistent within 2.5 standard deviations;
- The ROn data, on the other hand, has to fulfil a set of conditions. First, it was observed that the BiPo contamination remains unchanged for the ROn periods for the  $2\gamma$  topologies. Hence, the BiPo-enriched yields can be compared directly with those of the ROff in use. A cycle is considered further if the two results are agreeing within 2.5 standard deviations;
- In contrast with BiPo, the fraction of accidentals is larger in ROn samples. Thus, a relative comparison of the yields can be foreseen. Each ROn cycle is surrounded by the two ROff periods [before (b) and after (a)]. The cycle is selected if the comparison of the accidental rates (ROn - ROff<sub>b</sub>) and (ROn - ROff<sub>a</sub>) are agreeing within 2.5 standard deviations;
- If the background composition of the considered ROn period is consistent, the algorithm proceeds to the control plots. The comparison has to be kept blind with solely goodness of fit being verified. It can be done with *e.g.* a  $\chi^2$  goodness-of-fit test that will be passed if  $\chi^2/\text{degree of freedom} < 1.6$ .
- Proceed with the  $\Delta R\text{-}\Delta T$  simultaneous fit in order to determine the signal and background yields. As previously, the plots are kept blind. Pass if the obtained yields for the individual components agree within 2.5 standard deviations with the predicted background composition.

In addition, to improve the statistics available, other signal topologies might be re-visited for analysis. However, the  $0\gamma$  case is hopeless with a too high level of background. Most of the previously defined discriminative variables are not available. On the other hand, the  $1\gamma$  events, which are in the middle position, looked promising in a first attempt to include them. Though several discriminative handles are not present, including the cosine between the annihilation  $\gamma$ , the remaining can still provide valuable discrimination power. For instance, the Figure 95 gathering the overtraining plots of the BDTs trained against BiPo and atmospheric-enriched samples for Topology 10 exhibits such a discriminative

power. Preliminary studies show that  $1\gamma$  topologies can provide an antineutrino sample of an equivalent size as that obtained with the  $2\gamma$  analysis at the price of a degraded signal-to-background ratio of 1 to 3.

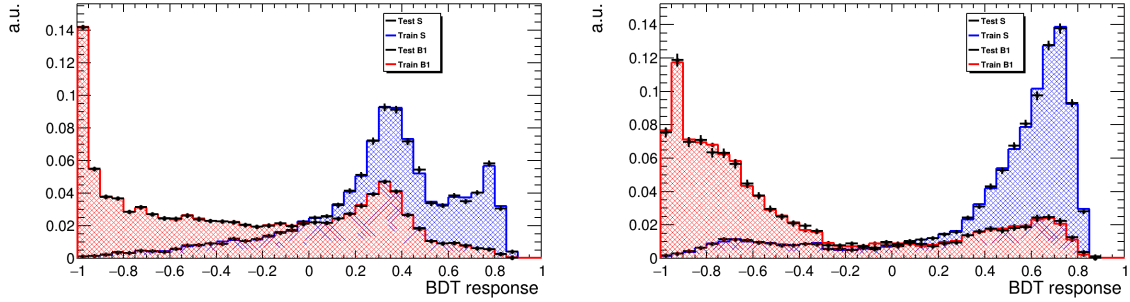


Figure 95: The results of the two overtraining crosschecks (MVA tools trained against BiPo (left) and Atmospheric (right) enriched samples) for  $1\gamma$  Topology 10. For each of the 10-foldings, the BDT scores are displayed for the training (filled histograms) and test (black data points) samples, as well as for the signal (blue) and background (red) data sets. The results of the different foldings are further combined. None of the distributions indicates overtraining.

All the merged statistics from Phase I data will be used to perform first the complete sensitivity study to the oscillation analysis. It will indicate if the selected sample is enough to spot a modulation of the flux issued by an oscillation to a sterile flavour, reject the hypothesis, or none of the two (in such case, only part of the parameter space will be constrained). There are two concurrent approaches developed in the SoLi $\theta$  collaboration. The baseline method is a frequentist method which relies on the construction of a covariance matrix. By relating the theoretical prediction and the measured data, it allows the  $\chi^2$  test to be defined for a given couple of oscillation parameters. To obtain the exclusion contour, the approach is based on the Feldman and Cousins technique combined with a so-called raster scan [85]. An alternative method has been introduced based on Bayesian inference [93]. It relies on the Metropolis–Hastings algorithm, which is a Markov-Chain Monte-Carlo method for obtaining a sequence of random samples from a probability distribution. It is combined with the response matrix, which comprises the predictions in the reconstruction space based on the information available from the Geant4 simulation in the true space.

The initial studies for the performance of topological selection presented in this manuscript have been started for both of the available methods. They are still ongoing, and the expected sensitivity contours should be available in the near future.

## A Appendix

Several additional characteristics of the topological analysis performance can be further investigated. An evolution of the event selection efficiency with 5D-optimised cuts is one of them. The absence of the dependency will postulate that the selection is unbiased, which is particularly important for the oscillation analysis input. As installed in Chapter 1.3, the probability of the oscillation depends on the variables  $L$  and  $E$ . The latter one approximated with the energy estimator and it is up to the analysis to define it. The distance travelled in the SoLi $\partial$  experiment is estimated with the  $z$  coordinate of the AC. The evolution with respect to both of these parameters is represented in Figure 96. It is computed as follows:

- Only preselected sample with  $AC_E > 1.5$  MeV for each topology is considered;
- The efficiency bins are designed to contain the same number of events;
- The fraction of the events which passed the 5D-optimised cuts to the total number of events in each bin is calculated.

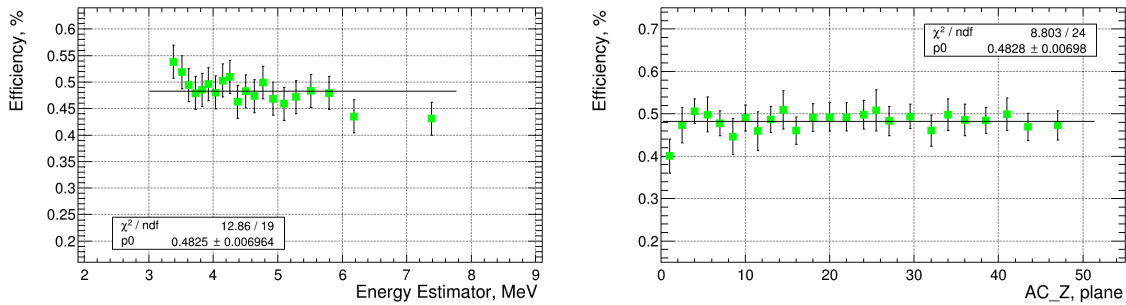


Figure 96: An evolution of the topological selection performance for the  $2\gamma$  sample collection as the function of energy estimator (left) and the  $z$  coordinate of the AC (right). In both cases the distribution is in agreement with a straight line fit within the statistical uncertainties. It indicates that there is no dependency between MVA performance and oscillation parameters.

In order to define the positron (antineutrino) energy estimator, the characteristics of the individual topologies must be taken into account. The simplest estimator comes with Topology 20 and Topology 23. The estimator for them is simply  $AC_E$ , since for Topology 20 both annihilation  $\gamma$  are clearly identified outside the envelope and for Topology 23 the additional cube in the envelope is assumed to be the second annihilation  $\gamma$ . For Topology 21 there is an additional cube in the envelope. Since both annihilation  $\gamma$  are associated outside of it anyway, it is assumed that the extra cube is also provided by the positron. Thus, to design energy estimator, the energy of the 2 cubes in the envelope are summed. Topology 24 is the most complicated because of the combinatorics of the envelope. There is more than one additional cube in there, and it is assumed that only one of them will be attached to the second annihilation  $\gamma$ . Hence, all the other cubes in the envelope are assumed to be provided by a positron, and their energy needs to be summed to provide the energy estimator.

In order to evaluate the performance of each energy estimator, the energy spread is explored with respect to the initial energy of the positron. These studies are kept on the

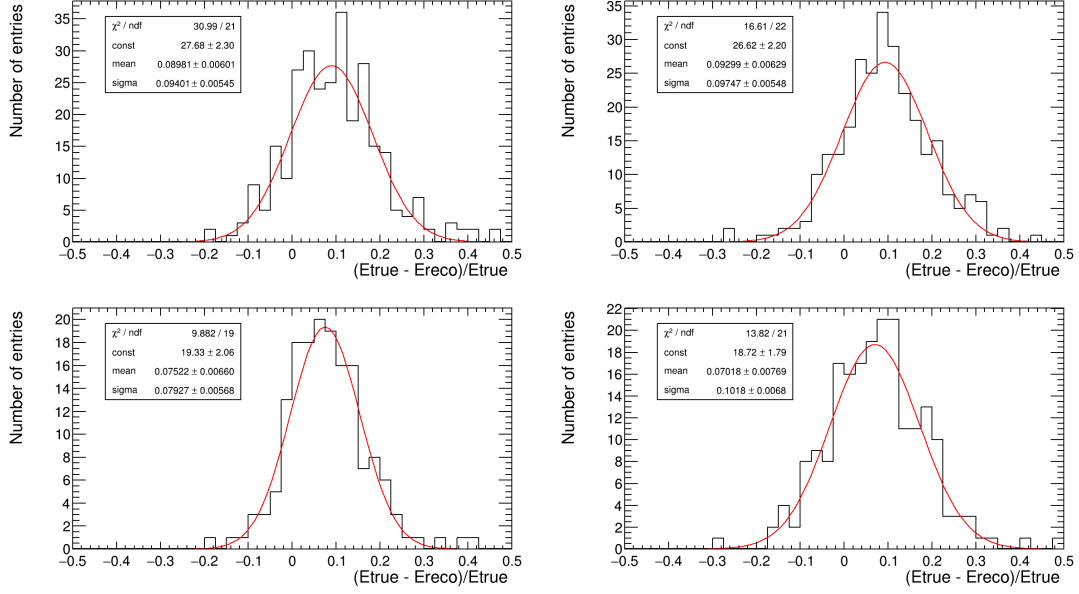


Figure 97: The energy spread distribution defined by the energy estimator and the initial positron energy for the set of  $2\gamma$  Topologies: 20 (top left), 21 (top right), 23 (bottom left) and 24 (bottom right). To construct these distributions, the energy space is split into 10 bins with the equivalent statistics. The results are shown for the same bin along all the topologies, which corresponds to the average energy of 2.5 MeV. The energy resolution and biases are extracted using the Gaussian fit for the further exploration.

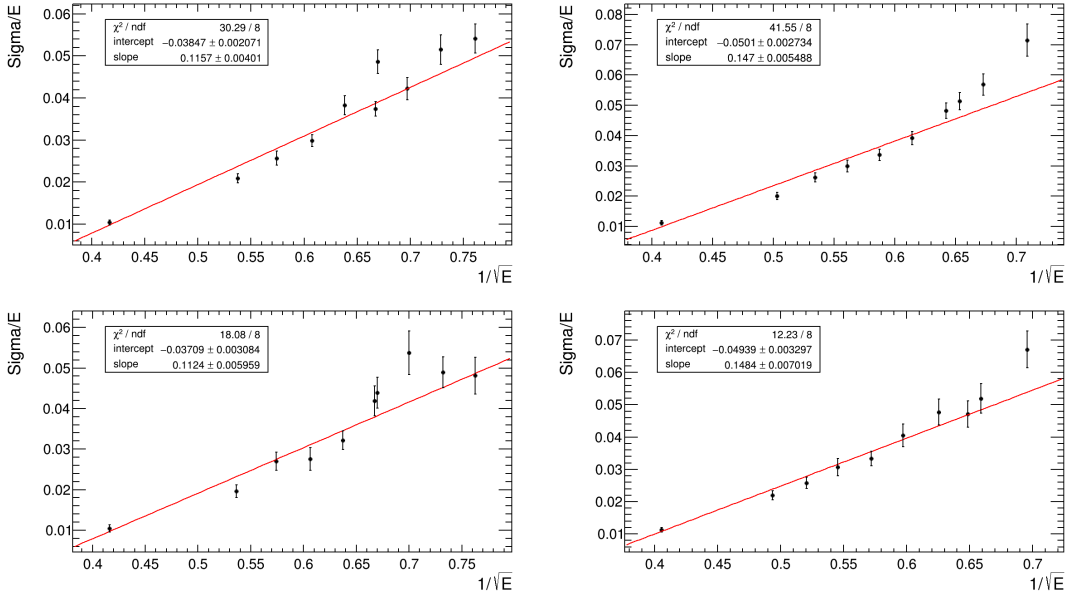


Figure 98: The energy  $\sigma/E$  distribution as the function of the  $1/\sqrt{E}$  for the set of  $2\gamma$  Topologies: 20 (top left), 21 (top right), 23 (bottom left) and 24 (bottom right). Each point corresponds to the bin in the energy space with equivalent statistics and displays the energy resolution value extracted via the Gaussian fit. All distributions agree with the linear fit model within the statistical uncertainties.

5D-optimised MC IBD. The same trick, with designing bin edges to secure the equivalent statistics, as for the efficiency evolution distribution, is used. The Figure 97 is showing the energy spread distribution for one of the bins in each topology, superimposed with the result of a simple Gaussian model fit. The method has been used to estimate the mean of the spread and, more importantly, the width, which hints at the value of the energy resolution. The distribution of  $\sigma/E$  as a function  $1/\sqrt{E}$  is represented in Figure 98.

## References

- [1] P. Mermod, *Right-handed neutrinos: the hunt is on!*, 2017. doi: 10.48550/ARXIV.1704.08635.
- [2] W. Pauli, *Dear radioactive ladies and gentlemen*, Phys. Today **31N9** (1978) 27.
- [3] F. L. Wilson, *Fermi's Theory of Beta Decay*, Am. J. Phys. **36** (1968) 1150.
- [4] H. Bethe and R. Peierls, *The 'neutrino'*, Nature **133** (1934) 532.
- [5] F. Reines and C. L. Cowan, *A Proposed experiment to detect the free neutrino*, Phys. Rev. **90** (1953) 492.
- [6] C. L. Cowan *et al.*, *Detection of the free neutrino: A Confirmation*, Science **124** (1956) 103.
- [7] F. Reines *et al.*, *Detection of the free anti-neutrino*, Phys. Rev. **117** (1960) 159.
- [8] G. Danby *et al.*, *Observation of High-Energy Neutrino Reactions and the Existence of Two Kinds of Neutrinos*, Phys. Rev. Lett. **9** (1962) 36.
- [9] M. L. Perl *et al.*, *Evidence for Anomalous Lepton Production in  $e^+ - e^-$  Annihilation*, Phys. Rev. Lett. **35** (1975) 1489.
- [10] ALEPH Collaboration *et al.*, *Combination procedure for the precise determination of  $z$  boson parameters from results of the lep experiments*, 2001. doi: 10.48550/ARXIV.HEP-EX/0101027.
- [11] K. Kodama *et al.*, *Observation of tau neutrino interactions*, Physics Letters B **504** (2001) 218.
- [12] K. Kodama *et al.*, *Final tau-neutrino results from the DONuT experiment*, Physical Review D **78** (2008) .
- [13] J. N. Bahcall *et al.*, *Standard Solar Models and the Uncertainties in Predicted Capture Rates of Solar Neutrinos*, Rev. Mod. Phys. **54** (1982) 767.
- [14] B. T. Cleveland *et al.*, *Measurement of the solar electron neutrino flux with the homestake chlorine detector*, The Astrophysical Journal **496** (1998) 505.
- [15] Heidelberg-Karlsruhe-Milan-Munich-Nice-Rehovoth-Rome-Saclay, D. Vignaud, *THE GALLIUM SOLAR NEUTRINO EXPERIMENT GALLEX*, in *5th Moriond Astrophysics Meeting: Nucleosynthesis & its Implications on Nuclear and Particle Physics*, 453–461, 1985.
- [16] SAGE, J. N. Abdurashitov *et al.*, *Measurement of the solar neutrino capture rate with gallium metal*, Phys. Rev. C **60** (1999) 055801, arXiv:astro-ph/9907113.
- [17] F. Kaether *et al.*, *Reanalysis of the gallex solar neutrino flux and source experiments*, Physics Letters B **685** (2010) 47.

- [18] Super-Kamiokande, S. Fukuda *et al.*, *Determination of solar neutrino oscillation parameters using 1496 days of Super-Kamiokande I data*, Phys. Lett. B **539** (2002) 179, arXiv:hep-ex/0205075.
- [19] Y. Fukuda *et al.*, *Measurements of the solar neutrino flux from super-kamiokande's first 300 days*, Physical Review Letters **81** (1998) 1158.
- [20] T. Nakaya, *Atmospheric and long baseline neutrino*, .
- [21] SNO, J. Boger *et al.*, *The Sudbury neutrino observatory*, Nucl. Instrum. Meth. A **449** (2000) 172, arXiv:nucl-ex/9910016.
- [22] SNO, S. N. Ahmed *et al.*, *Measurement of the total active B-8 solar neutrino flux at the Sudbury Neutrino Observatory with enhanced neutral current sensitivity*, Phys. Rev. Lett. **92** (2004) 181301, arXiv:nucl-ex/0309004.
- [23] B. Pontecorvo, *Neutrino Experiments and the Problem of Conservation of Leptonic Charge*, Zh. Eksp. Teor. Fiz. **53** (1967) 1717.
- [24] Z. Maki, M. Nakagawa, and S. Sakata, *Remarks on the unified model of elementary particles*, Prog. Theor. Phys. **28** (1962) 870.
- [25] Super-Kamiokande, Y. Ashie *et al.*, *A Measurement of atmospheric neutrino oscillation parameters by SUPER-KAMIOKANDE I*, Phys. Rev. D **71** (2005) 112005, arXiv:hep-ex/0501064.
- [26] T2K, K. Abe *et al.*, *Precise Measurement of the Neutrino Mixing Parameter  $\theta_{23}$  from Muon Neutrino Disappearance in an Off-Axis Beam*, Phys. Rev. Lett. **112** (2014) 181801, arXiv:1403.1532.
- [27] N. Agafonova *et al.*, *Final results of the opera experiment on  $\nu \tau$  appearance in the cngs neutrino beam*, Physical Review Letters **120** (2018) .
- [28] I. Esteban *et al.*, *The fate of hints: updated global analysis of three-flavor neutrino oscillations*, Journal of High Energy Physics **2020** (2020) .
- [29] A. Y. Smirnov, *The msw effect and solar neutrinos*, 2003. doi: 10.48550/ARXIV.HEP-PH/0305106.
- [30] KamLAND, K. Eguchi *et al.*, *First results from KamLAND: Evidence for reactor anti-neutrino disappearance*, Phys. Rev. Lett. **90** (2003) 021802, arXiv:hep-ex/0212021.
- [31] Daya Bay, F. P. An *et al.*, *Observation of electron-antineutrino disappearance at Daya Bay*, Phys. Rev. Lett. **108** (2012) 171803, arXiv:1203.1669.
- [32] Double Chooz, Y. Abe *et al.*, *Indication of Reactor  $\bar{\nu}_e$  Disappearance in the Double Chooz Experiment*, Phys. Rev. Lett. **108** (2012) 131801, arXiv:1112.6353.
- [33] RENO, J. K. Ahn *et al.*, *Observation of Reactor Electron Antineutrino Disappearance in the RENO Experiment*, Phys. Rev. Lett. **108** (2012) 191802, arXiv:1204.0626.
- [34] T2K, K. Abe *et al.*, *Observation of Electron Neutrino Appearance in a Muon Neutrino Beam*, Phys. Rev. Lett. **112** (2014) 061802, arXiv:1311.4750.

- [35] A. de Gouvea *et al.*, *Neutrinos*, 2013. doi: 10.48550/ARXIV.1310.4340.
- [36] S. Davidson, E. Nardi, and Y. Nir, *Leptogenesis*, Phys. Rept. **466** (2008) 105, arXiv:0802.2962.
- [37] L. Cremonesi, *Sensitivity to the neutrino oscillation parameters in the hyperkamiokande experiment*, Journal of Physics: Conference Series **598** (2015) 012017.
- [38] DUNE, R. Acciarri *et al.*, *Long-Baseline Neutrino Facility (LBNF) and Deep Underground Neutrino Experiment (DUNE): Conceptual Design Report, Volume 2: The Physics Program for DUNE at LBNF*, arXiv:1512.06148.
- [39] C. Athanassopoulos *et al.*, *The liquid scintillator neutrino detector and LAMPF neutrino source*, Nuclear Instruments and Methods in Physics Research Section A: Accelerators, Spectrometers, Detectors and Associated Equipment **388** (1997) 149.
- [40] LSND Collaboration, A. Aguilar *et al.*, *Evidence for neutrino oscillations from the observation of  $\bar{\nu}_e$  appearance in a  $\bar{\nu}_\mu$  beam*, Phys. Rev. D **64** (2001) 112007.
- [41] K. Eitel, *Latest results of the KARMEN2 experiment*, Nuclear Physics B - Proceedings Supplements **91** (2001) 191.
- [42] A. A. Aguilar-Arevalo *et al.*, *The MiniBooNE detector*, Nuclear Instruments and Methods in Physics Research Section A: Accelerators, Spectrometers, Detectors and Associated Equipment **599** (2009) 28.
- [43] MiniBooNE Collaboration, A. A. Aguilar-Arevalo *et al.*, *First measurement of the muon neutrino charged current quasielastic double differential cross section*, Phys. Rev. D **81** (2010) 092005.
- [44] S. KOPP, *Accelerator neutrino beams*, Physics Reports **439** (2007) 101.
- [45] MiniBooNE Collaboration, A. A. Aguilar-Arevalo *et al.*, *Search for electron neutrino appearance at the  $\Delta m^2 \sim 1 \text{ eV}^2$  scale*, Phys. Rev. Lett. **98** (2007) 231801.
- [46] MiniBooNE Collaboration, A. A. Aguilar-Arevalo *et al.*, *Updated miniboone neutrino oscillation results with increased data and new background studies*, Phys. Rev. D **103** (2021) 052002.
- [47] MicroBooNE Collaboration *et al.*, *Search for an excess of electron neutrino interactions in microboone using multiple final state topologies*, 2021. doi: 10.48550/ARXIV.2110.14054.
- [48] M. Cribier *et al.*, *Production of a 62-PBq Cr-51 low-energy neutrino source for GALLEX*, Nucl. Instrum. Meth. A **378** (1996) 233.
- [49] V. V. Barinov *et al.*, *Search for electron-neutrino transitions to sterile states in the BEST experiment*, Physical Review C **105** (2022) .
- [50] J. M. Berryman *et al.*, *Statistical significance of the sterile-neutrino hypothesis in the context of reactor and gallium data*, Journal of High Energy Physics **2022** (2022) .

- [51] T. A. Mueller *et al.*, *Improved predictions of reactor antineutrino spectra*, Physical Review C **83** (2011) .
- [52] G. Mention *et al.*, *Reactor antineutrino anomaly*, Physical Review D **83** (2011) .
- [53] RENO, S.-H. Seo, *New Results from RENO and The 5 MeV Excess*, AIP Conf. Proc. **1666** (2015) 080002, [arXiv:1410.7987](#).
- [54] L. Hayen, J. Kostensalo, N. Severijns, and J. Suhonen, *First-forbidden transitions in the reactor anomaly*, Phys. Rev. C **100** (2019) 054323.
- [55] PROSPECT Collaboration and STEREO Collaboration, H. Almazán *et al.*, *Joint measurement of the  $^{235}\text{U}$  antineutrino spectrum by prospect and stereo*, Phys. Rev. Lett. **128** (2022) 081802.
- [56] Double Chooz, H. de Kerret *et al.*, *Double Chooz  $\theta_{13}$  measurement via total neutron capture detection*, Nature Phys. **16** (2020) 558, [arXiv:1901.09445](#).
- [57] C. Giunti, Y. F. Li, C. A. Ternes, and Z. Xin, *Reactor antineutrino anomaly in light of recent flux model refinements*, Physics Letters B **829** (2022) 137054.
- [58] K. N. Abazajian *et al.*, *Light Sterile Neutrinos: A White Paper*, [arXiv:1204.5379](#).
- [59] M. Aker *et al.*, *Katrin: status and prospects for the neutrino mass and beyond*, Journal of Physics G: Nuclear and Particle Physics **49** (2022) 100501.
- [60] ANTARES, M. Ageron *et al.*, *ANTARES: the first undersea neutrino telescope*, Nucl. Instrum. Meth. A **656** (2011) 11, [arXiv:1104.1607](#).
- [61] IceCube Collaboration, M. G. Aartsen *et al.*, *Searching for  $e\nu$ -scale sterile neutrinos with eight years of atmospheric neutrinos at the icecube neutrino telescope*, Phys. Rev. D **102** (2020) 052009.
- [62] Z. Atif *et al.*, *Search for sterile neutrino oscillations using RENO and NEOS data*, Physical Review D **105** (2022) .
- [63] A. P. Serebrov *et al.*, *Search for sterile neutrinos with the neutrino-4 experiment and measurement results*, Phys. Rev. D **104** (2021) 032003.
- [64] Neutrino-4, A. P. Serebrov and R. M. Samoilov, *A Comment on the note [arXiv:2006.13147](#) on [arXiv:2005.05301](#), "Preparation of the Neutrino-4 experiment on search for sterile neutrino and the obtained results of measurements"*, [arXiv:2006.13639](#).
- [65] PROSPECT, M. Andriamirado *et al.*, *Improved short-baseline neutrino oscillation search and energy spectrum measurement with the PROSPECT experiment at HFIR*, Phys. Rev. D **103** (2021) 032001, [arXiv:2006.11210](#).
- [66] Daya Bay Collaboration and PROSPECT Collaboration, F. P. An *et al.*, *Joint determination of reactor antineutrino spectra from  $^{235}\text{U}$  and  $^{239}\text{Pu}$  fission by daya bay and prospect*, Phys. Rev. Lett. **128** (2022) 081801.

- [67] STEREO, H. Almazán *et al.*, *Interpreting Reactor Antineutrino Anomalies with STEREO data*, arXiv:2210.07664.
- [68] T. Katori, *Short baseline neutrino oscillation experiments*, Journal of Physics: Conference Series **598** (2015) 012006.
- [69] Y. Abreu *et al.*, *SoLid: a short baseline reactor neutrino experiment*, Journal of Instrumentation **16** (2021) P02025.
- [70] *Sckcen br2 website*, <https://www.sckcen.be/en/about-sck-cen/corporate-information/infrastructure>. Accessed: 01-12-2022.
- [71] *Eljen technology website*, <https://eljentechnology.com/products/plastic-scintillators/ej-200-ej-204-ej-208-ej-212>. Accessed: 01-12-2022.
- [72] *Scintacor neuron screen data-sheet*, <https://scintacor.com/wp-content/uploads/2015/09/Datasheet-Neutron-Screens-High-Res.pdf>. Accessed: 01-12-2022.
- [73] *Dupont backing data-sheet*, <https://usa.dupontteijinfilms.com/wp-content/uploads/2017/01/339-Datasheet.pdf>. Accessed: 01-12-2022.
- [74] *Dupont wrapping data-sheet*, [https://www.dupont.com/content/dam/dupont/amer/us/en/microsites/tyvek-design/images/documents/2019-C&I\\_Tyvek\\_1082D\\_Datasheet.pdf](https://www.dupont.com/content/dam/dupont/amer/us/en/microsites/tyvek-design/images/documents/2019-C&I_Tyvek_1082D_Datasheet.pdf). Accessed: 01-12-2022.
- [75] *Saint-gobain data-sheet*, <https://www.crystals.saint-gobain.com/sites/hps-mac3-cma-crystals/files/2021-11/Fiber-Product-Sheet.pdf>. Accessed: 01-12-2022.
- [76] *Hammamatsu data-sheet*, <https://seltokphotonics.com/upload/iblock/118/1186141f87bc6da48efe2c465195e38d.pdf>. Accessed: 01-12-2022.
- [77] M. Caresana *et al.*, *Real-time measurements of radon activity with the Timepix-based RADONLITE and RADONPIX detectors*, JINST **9** (2014) P11023.
- [78] GEANT4, S. Agostinelli *et al.*, *GEANT4—a simulation toolkit*, Nucl. Instrum. Meth. A **506** (2003) 250.
- [79] V. Pestel, *Détection de neutrinos auprès du réacteur BR2 : analyse des premières données de l'expérience SoLid*, theses, Normandie Université, 2019.
- [80] Y. Abreu *et al.*, *Commissioning and operation of the readout system for the SoLid neutrino detector*, Journal of Instrumentation **14** (2019) P11003.
- [81] L. S. Waters *et al.*, *The MCNPX Monte Carlo radiation transport code*, AIP Conf. Proc. **896** (2007) 81.

- [82] S. Kalcheva *et al.*, *Reactor Core Simulations for Determination of the Antineutrino Spectrum for the SoLid Experiment at BR2 Reactor*, in *M&C 2017 - International Conference on Mathematics & Computational Methods Applied to Nuclear Science & Engineering*, Proceeding Meeting International Conference on Mathematics & Computational Methods Applied to Nuclear Science & Engineering, Jeju, Korea, April 16-20, 2017,, (Jeju, South Korea), 2017.
- [83] O. Méplan *et al.*, *MURE : MCNP Utility for Reactor Evolution - Description of the methods, first applications and results*, ENC 2005 - European Nuclear Conference. Nuclear Power for the XXIst Century : From basic research to high-tech industry, 2005. Poster - PACS.
- [84] P. Vogel and J. F. Beacom, *Angular distribution of neutron inverse beta decay*,  $\bar{\nu}_e + \vec{p} \rightarrow e^+ + n$ , Phys. Rev. D **60** (1999) 053003.
- [85] Michiels, Ianthe, *Development of the oscillation analysis framework for the SoLid experiment*, PhD thesis, Ghent University, 2020.
- [86] S. Abe *et al.*, *Production of radioactive isotopes through cosmic muon spallation in KamLAND*, Physical Review C **81** (2010) .
- [87] M. Guan *et al.*, *A parametrization of the cosmic-ray muon flux at sea-level*, 2015. doi: 10.48550/ARXIV.1509.06176.
- [88] M. S. Gordon *et al.*, *Measurement of the flux and energy spectrum of cosmic-ray induced neutrons on the ground*, IEEE Transactions on Nuclear Science **51** (2004) 3427.
- [89] C. Hagmann, D. Lange, and D. Wright, *Cosmic-ray shower generator (cry) for monte carlo transport codes*, **2** 1143 – 1146, 2007.
- [90] J. B. Birks and F. A. Black, *Deterioration of anthracene under /cap alpha/-particle irradiation*, Proc. Phys. Soc. (London) **Vol: 64A** (1951) .
- [91] Verstraeten, Maja, *Search for sterile neutrinos in the eV and MeV mass range with the SoLid detector*, PhD thesis, University of Antwerp, 2021.
- [92] Vandierendonck, Giel, *The SoLid neutrino experiment : stabilising, operating, understanding and upgrading the detector*, PhD thesis, Ghent University, 2022.
- [93] Gallego, Savitri, *Analyse des données de l'expérience SoLiD : mesure du spectre antineutrino à BR2 et recherche d'oscillations vers un neutrino stérile*, PhD thesis, 2022.
- [94] A. N. Tikhonov and V. Y. Arsenin, *Solutions of ill-posed problems*, V. H. Winston & Sons, Washington, D.C.: John Wiley & Sons, New York, 1977. Translated from the Russian, Preface by translation editor Fritz John, Scripta Series in Mathematics.
- [95] M. A. T. Figueiredo, R. D. Nowak, and S. J. Wright, *Gradient projection for sparse reconstruction: Application to compressed sensing and other inverse problems*, IEEE Journal of Selected Topics in Signal Processing **1** (2007) 586.

- [96] M. A. T. Figueiredo and R. D. Nowak, *An em algorithm for wavelet-based image restoration*, IEEE Transactions on Image Processing **12** (2003) 906.
- [97] A. Beck and M. Teboulle, *A fast iterative shrinkage-thresholding algorithm for linear inverse problems*, SIAM Journal on Imaging Sciences **2** (2009) 183, arXiv:<https://doi.org/10.1137/080716542>.
- [98] Y. Zhu, A. K. Jha, D. F. Wong, and A. Rahmim, *Image reconstruction in fluorescence molecular tomography with sparsity-initialized maximum-likelihood expectation maximization*, Biomed. Opt. Express **9** (2018) 3106.
- [99] S. Kullback and R. A. Leibler, *On Information and Sufficiency*, The Annals of Mathematical Statistics **22** (1951) 79 .
- [100] D. Henaff, *Toward the search of a sterile neutrino with the SoLid experiment at the SCK-CEN BR2 reactor : detector calibration and design of a multivariate topological selection of antineutrino events*, theses, Ecole nationale supérieure Mines-Télécom Atlantique, 2021.
- [101] N. Roy, *Search for sterile neutrino oscillations with the SoLid experiment at BR2 reactor : Energy calibration of the detector and antineutrino signal extraction*, theses, Université Paris-Saclay, 2021.
- [102] Y. Querlioz. M1 internship report, personal communication.
- [103] W. Verkerke and D. P. Kirkby, *The RooFit toolkit for data modeling*, eConf **C0303241** (2003) MOLT007, arXiv:[physics/0306116](https://arxiv.org/abs/physics/0306116).
- [104] R. Brun and F. Rademakers, *ROOT: An object oriented data analysis framework*, Nucl. Instrum. Meth. A **389** (1997) 81.
- [105] E. N. Alexeyev *et al.*, *Results of a search for daily and annual variations of the  $^{214}\text{Po}$  half-life at the two year observation period*, Phys. Part. Nucl. **47** (2016) 986, arXiv:[1505.01752](https://arxiv.org/abs/1505.01752).
- [106] B. P. Roe *et al.*, *Boosted decision trees, an alternative to artificial neural networks*, Nucl. Instrum. Meth. A **543** (2005) 577, arXiv:[physics/0408124](https://arxiv.org/abs/physics/0408124).
- [107] A. Hocker *et al.*, *TMVA - Toolkit for Multivariate Data Analysis*, arXiv:[physics/0703039](https://arxiv.org/abs/physics/0703039).
- [108] S. Arlot and A. Celisse, *A survey of cross-validation procedures for model selection*, Statistics Surveys **4** (2010) .